Ernesto da Silveira Goulart Guimarães

Engenharia tecidual hepática utilizando células tronco pluripotentes induzidas

Liver tissue engineering using induced pluripotent stem cells

São Paulo

2019

Ernesto da Silveira Goulart Guimarães

Engenharia tecidual hepática utilizando células tronco pluripotentes induzidas

Liver tissue engineering using induced pluripontent stem cells

Tese apresentada ao Instituto de Biociências da Universidade de São Paulo, para a obtenção de Título de Doutor em Ciências, na Área de Genética e Biologia Evolutiva.

Orientadora: Profa. Dra. Mayana Zatz

São Paulo

2019

Ficha Catalográfica

da Silveira Goulart Guimarães, Ernesto

Engenharia tecidual hepática utilizando células tronco pluripotentes induzidas / Ernesto da Silveira Goulart Guimarães; orientadora Mayana Zatz. São Paulo, 2019.

208 f.

Tese (Doutorado) - Instituto de Biociências da Universidade de São Paulo, Departamento de Genética e Biologia Evolutiva.

1. Engenharia tecidual. 2. Células tronco pluripotentes induzidas. 3. Fígado. 4. Bioimpressão 3D. 5. Organóide.

Comissão Julgadora:

_____ _____

Prof(a). Dr(a). Prof(a). Dr(a).

_____ _____

Prof(a). Dr(a). Prof(a). Dr(a).

_____

Profa. Dra. Mayana Zatz

Orientadora

Dedicado à Raúl Marcel González Garcia (*in memoriam*)

Epígrafe

“O que existe de Minas em mim é este sonho

de subir montanhas e garimpar estrelas”

Wilson Pereira

Agradecimentos

Primeiramente agradeço à Profa. Mayana Zatz pela confiança em meu trabalho, pelo aprendizado e por ser um grande exemplo de brilhantismo, elegância profissional, dedicação, caráter e amor pela ciência. Agradeço também pela amizade que construímos nos últimos anos.

Agradeço, pelos mesmo motivos, ao Prof. Silvano Raia. Tenho uma imensurável admiração pela sua história e pelo seu ímpeto vanguardista, que muito me inspiram. Ao Prof. Peter Lelkes, agradeço por todo ensinamento, confiança, carinho e paciência comigo. Minha estadia em seu laboratório foi um divisor de águas na minha carreira.

Este trabalho é dedicado ao meu querido Prof. Raúl Garcia, da UFJF, meu primeiro mentor, a quem eu esperava entregar em mãos, a cópia desta tese. Por força do destino isso não foi possível. Confesso que sinto uma tristeza muito grande por não ter te agradecido o suficiente por tudo o que fez por mim. A felicidade no seu olhar toda a vez você via minha evolução é algo que sentirei muita falta, pois era a mais pura e transcendente força humana. De certa forma, fica aqui registrado meu agradecimento eterno.

Aproveito para agradecer ao meu grande amigo e irmão de bancada por mais de 11 anos, Luiz Carlos de Caires Júnior. Agradeço pelos ensinamentos, paciência, dedicação, e principalmente pela sua confiança e amizade. Admiro sua força e vontade de fazer mais e melhor e de aproveitar as oportunidades da vida. Agradeço ao meu querido amigo e aluno de iniciação científica, Kayque Telles-Silva por todo apoio e paciência ao longo do desenvolvimento deste trabalho. Tenho muito orgulho do seu desenvolvimento e de ter participado (de forma modesta) no seu aprendizado ao longo destes quase 4 anos.

Agradeço aos professores Oswaldo Keith Okamoto, Maria Rita de Passos-Bueno e Mariz Vainzof, pelos inúmeros ensinamentos e pela amizade. Agradeço pela paciência, acolhimento, confiaça e pelos incontáveis momentos de alegria que dividi com todos os meus brilhantes amigos, contemporâneos de meu período de doutoramento: Bruno Torres, Uirá Melo, Camila Musso, Gerson Kobayashi, Danyllo Oliveira, Lucas Alvizi, Luciano Brito, Amanda Assoni, Carolini Kaid, Felipe Leite, Joyce Esposito e Antônio.

Agradeço especialmente à Profa. Elia Caldini e às técnicas de seu laboratório de Biologia Celular, Nilsa e Sueli, pela confiança, parceria nas análises histológicas e, sobretudo, pelo lindo trabalho que realizam. Agradeço em especial o Dr. Bruno Torres e a Dra. Fernanda Paes Leme e equipe do LNBio, em especial à Sami Yokoo, do Laboratório de Espectrometria de Massas do LNBio. Agradeço também à Dra. Silvana Rocco, Dra. Irene e Dr. Maurício do Laboratório de Ressonância Magnética Nuclear do LNBio. Agradeço ao professor Alberto e o técnico de seu Laboratório de Microscopia do IB-USP, Márcio, pelo apoio nas análises de microscopia eletrônica de varredura. Agradeço ao Rafael, Priscila e Cleonice do LIM29, pelos ensaios preliminares em animais. Agradeço também ao LIM 61, coordenado pelo Prof. Paulo Pêgo, e sua aluna Karina. Por fim, mas não menos importante, agradeço a todos que, com sua dedicação, competência, carinho e respeito pelo trabalho, me fizeram apaixonar pelo meu local de trabalho, o Centro de Estudos do Genoma Humano e Células Tronco da USP.

Nada na minha vida seria possível sem o amor incondicional e sacrifício da minha querida mãe, Ana, a quem sou eternamente grato. Da mesma forma, agradeço a minha querida companheira, Tábata Guerra, pelo seu amor, paciência e dedicação.

Agradeço à FAPESP pelo apoio e financiamento. Da mesma forma, agradeço à CAPES, CNPQ, SES-SP, CNPEM, FINEP e Universidade de São Paulo.

Índice

Apresentação da Tese de Doutorado

Índice de Abreviações

3D = Três dimensões

2D = Duas dimensões

DAMPS = Móleculas associadas à dano celular/tecidual

dpMSC = Células tronco mesenquimais derivadas de polpa de dente

EMT = Transição epitélio-mesenquima

HAECs =Células endoteliais arteriais

HepG2 = Linhagem celular de hepatoblastoma

HUVEC = Células endoteliais derivadas de veia umbilical

ICG = Indocianina verde

iNCC = Células de crista neural obtidas de células iPS

iPS = células tronco pluripotentes induzidas

m/v = massa/volume

MSC = Células tronco mesenquimais

NCBI = Centro nacional para informação em biotecnologia

NPC = Células não-parenquimáticas

PAS = Ácido periódico de Schiff

UV = Luz ultra-violeta

v/v = volume/volume

Índice de Tabelas

Índice de Figuras

Apresentação da tese de doutorado

A engenharia tecidual hepática é uma abordagem da medicina regenerativa que visa criar tecidos funcionais para pacientes acometidos por doenças hepaticas graves. O objetivo desta tese foi avaliar, por estratégias diferentes, a potencial aplicação de células tronco de pluripotência induzida na produção de tecidos hepáticos funcionais *in vitro*.

Este trabalho foi desenvolvido no Centro de Estudos do Genoma Humano e Células Tronco (CEGH-CEL) do Instituto de Biociências da Universidade de São Paulo (USP) desde 2015 sob coordenação da Profa. Dra. Mayana Zatz, com apoio nos desenhos exprimentais e discussão dos resultados do Prof. Dr. Peter I. Lelkes da *Temple University – Philadelphia* e do Prof. Dr. Silvano Raia, da Faculdade de Medicina da USP.

A introdução da tese, Capítulo 1, é uma revisão da literatura e exposição do estado atual da arte sobre a fisiologia, embriogênese, principais patologias hepáticas e a utilização de células tronco no contexto de terapias regenerativas. Além disso, a introdução descreve as principais abordagens e desafios atuais da engenharia tecidual hepática, foco principal desta tese. Os três capítulos subsequentes estão escritos na forma de artigos científicos, consistindo na descrição dos resultados obtidos em cada abordagem testada para a produção de um tecido hepático funtional *in vitro.* Nessa seção, encontram-se os manuscritos submetidos para publicação (Capítulos 2 e 3) e em preparação (Capítulo 4). Por fim, a última seção da tese (Capítulo 5) realiza uma ampla discussão dos reultados obtidos e projeta perspectivas futuras relativas à continuação dos estudos e desenvolvimentos tecnológicos, objeto desta tese de doutoramento.

Além disso, resultados adicionais e/ou preliminares, assim como as publicações científicas, fruto de colaborações e projetos paralelos realizados durante o período do desenvolvimento deste trabalho, estão anexadas ao final da tese.

Capítulo 1:
Introdução e objetivos

Capítulo 1: Introdução e objetivos

1.1. Fisiologia Hepática

O fígado é o órgão interno de maior massa do corpo humano e possui um papel central na regulação de diversas funções fisiológicas, com destacada participação em processos metabólicos no organismo, tais como: o metabolismo enzimático de compostos absorvidos e distribuídos pelo sistema enterohepático (xenobióticos) pelo complexo do citocrômo P450 (CYP450), e/ou metabólitos oriundos de diversas vias metabólicas convergentes, produção e excreção da bile, produção de albumina sérica, produção de importantes fatores da cascata de coagulação, realização do metabolismo do grupo heme, metabolismo de compostos nitrogenados, lipídeos, açúcares (sendo um dos maiores reservatórios de glicogênio do corpo), entre outros (Corless *et al*., 1983).

A estrutura anatômica primordial do fígado é o lóbulo hepático. Esta estrutura possui a forma de um hexágono, tendo em seu centro a veia hepática (também chamada de veia central) e em seus vértices a tríade hepática, composta pela veia porta (responsável por suprir 75-80% do volume de perfusão do órgão, carregando o sangue desoxigenado, porém rico em nutrientes absorvidos pelo intestino), artéria hepática e ducto biliar (Eipel *et al*., 2010). Apesar de representar aproximadamente 2,5% da massa total do corpo humano, o fígado recebe por volta de 25% do débito cardíaco (Eipel *et al*., 2010). A artéria hepática supre a demanda de sangue oxigenado ao tecido, porém é pobre em nutrientes. O conjunto de ductos biliares formam a árvore biliar, responsável pela produção e secreção biliar. A bile é uma secreção rica em moléculas anfipáticas (i.e. sais biliares), derivadas do metabolismo hepático do colesterol, que facilitam a absorção intestinal de lipídeos pela emulsificação da gordura dos alimentos (Maldonado-Valderrama *et al*., 2011).

A junção de dois lóbulos hepáticos adjacentes, formando uma estrutura composta por duas veias centrais e duas tríades hepáticas adjacentes, formando um losango imaginário, é chamado de ácino hepático, onde, por gradiente de difusão de nutrientes, são designadas três zonas distintas. Estas zonas possuem funções metabólicas diferenciadas (Kietzmann, 2017). A figura 1 representa as estruturas anatômicas e fisiológicas hepáticas, descritas anteriormente.

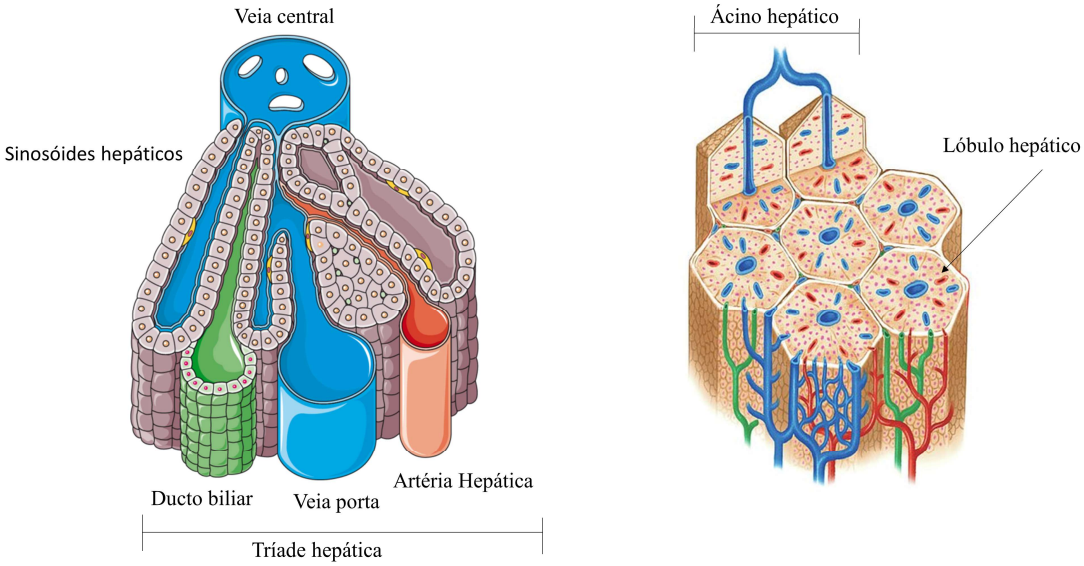

Figura 1: Estrutura anotômica-funcional hepática. À esquerda, a representação de uma tríade hepática e a representação das cordas hepáticas e leitos sinusoidais. À direita, estão indicadas as estruturas de lóbulo e ácino hepático. Ilustrações obtidas de banco público de imagens (https://smart.servier.com/, acesso em 24/03/2019), ou produzidas pelo autor desta tese.

A unidade celular funcional do tecido hepático é o hepatócito, maior componente do parênquima, que inclui também células endoteliais especializadas (i.e. sinusoidais), células estelares, células de Kupffer, células epiteliais biliares e colangiócitos (Zeilinger *et al*., 2016).

Os hepatócitos são células epiteliais especializadas que se alinham sobre uma fina membrana basal, formando uma estrutura chamada corda hepática, separados das células endoteliais sinosoidais (assim chamadas pela presença de uma membrana celular

e basal incompleta) por um espaço, também chamado de espaço perisinusoidal (ou espaço de Disse) (Zeilinger *et al*., 2016). Este espaço é preenchido pelo plasma sanguíneo e contém extensões das microvilosidades dos hepatócitos, o que facilita a absorção de nutrientes e xenobióticos. Os hepatócitos realizam também o transporte basolateral e apical, através da formação de canalículos nas junções célula-célula, que em conjunto formam os ductos biliares e posteriormente a árvore biliar, responsáveis pelo transporte da bile (Diaz, 2000). As células epiteliais que formam a parede dos ductos biliares são chamadas de colangiócitos.

O transporte de xenobióticos pelos hepatócitos é crítico na cinética de metabolização hepática, que inclui também a expressão de diversas enzimas do citocromo P450, transaminases e enzimas de conjugação (Sevior *et al*., 2012). O metabolismo hepático de xenobióticos aumenta a polaridade das moléculas, visando facilitar sua excreção renal. O metabolismo de xenobióticos pode ser dividido em três fases. O metabolismo de fase I envolve reações de oxirredução em cadeias laterais, normalmente realizado pelas enzimas do citocromo P450 microssomais, muitas delas NADH redutases ou mono-oxigenases, e por transaminases, que realizam a transferência de grupamentos amino (Sevior *et al*., 2012). Já a fase II é a fase de conjugação, onde são adicionadas moléculas polares como ácido glicurônico (como no caso da conjugação da bilirrubina) e glutationa a sítios específicos, como carboxílicos, hidroxílicos, aminas ou sulfídricos (Sevior *et al*., 2012). A fase III compreende todas as modificações subsequentes em xenobióticos visando sua excreção (Sevior *et al*., 2012). É importante ressaltar que o controle da expressão dos genes envolvidos no metabolismo hepático se dá através de receptores nucleares, co-fatores de transcrição, como o PXR, CAR e AHR, que induzem e/ou reprimem a expressão dos genes relacionados à biotransformação (Sevior *et al*., 2012). Várias drogas são capazes de

induzir ou reprimir a expressão de enzimas do metabolismo de xenobióticos através da modulação da atividade dos receptores nucleares. Este processo é chamado de indução ou repressão metabólica, sendo extremamente relevante no estudo de interações medicamentosas.

As células de Kupfer são macrófagos residentes do tecido hepático, responsáveis pela resposta inflamatória local (importante frente a injúrias teciduais agudas e crônicas), defesa contra patógenos e fagocitose de eritrócitos e posterior quebra da hemoglobina e liberação do grupamento heme (Dixon *et al*., 2013).

Outro componente importante para a fisiologia hepática são as células estelares. Localizadas no espaço perisinusoidal, permanecem quiesentes e participam da absorção e armazenamento de lipídios e vitamina D, porém, quando ativadas, começam a secretar colágeno e realizar o remodelamento da matriz extracelular hepática, iniciando o processo fibrótico (Weiskirchen & Tacke, 2014).

A albumina, a proteína sérica mais abundante é produzida exclusivamente no fígado, desempenha um papel importante no equilíbrio ácido-base sanguíneo, no transporte de íons e moléculas e na manutenção da pressão intravascular (pressão oncótica, ou coloidal) (Levitt & Levit, 2016). O fígado também exerce um papel fundamental no controle hemostático, visto que é responsável pela produção dos fatores II, V, VII, IX, X e XI da cascata de coagulação, além da produção de fibrinogênio e protrombina (Senzolo *et al*., 2006). Outra função primordial do fígado é a biossíntese e regulação dos níveis de colesterol e lipoproteínas circulantes (Ramasamy, 2014).

1.2. Embriologia e desenvolvimento hepático

De origem endodérmica ventral, a especificação hepática começa com a formação da endoderme definitiva, formada a partir da porção posterior da fissura primitiva, durante os primeiros momentos da gastrulação (Loh *et al*., 2014). Nesta etapa, as principais vias de sinalização que definem o fenótipo de endoderme definitiva são as atividades das vias de TGF-β e Wnt e baixa atividade das vias de BMP (Loh *et al*., 2014). Para a posterior especificação em endoderme ventral, é necessária a atividade de BMP e ácido retinóico (Loh *et al*., 2014). Neste estágio, a porção posterior do intestino primitivo ventral já possui a capacidade de se diferenciar em tecido hepático ou pancreático. Para adquirir o comprometimento com tecido hepático, é necessária a participação efetiva de fatores produzidos pela mesoderme circundante (Loh *et al*., 2014).

Após adquirir a especificação hepática (aproximadamente 25 dias de gestação) o fígado inicia sua organogênese tissular através da formação do divertículo hepático e posterior formação do corpúsculo hepático primitivo (aproximadamente 40 dias de gestação), induzido por fatores secretados pela mesoderme cardíaca e do *septum striadum* circundante (Camp *et al*., 2017). Os principais fatores secretados são BMP4, BMP6, FGF-4 e HGF (Ang *et al*., 2018). O fígado fetal é um importante centro de hematopoese (Mikkola & Orkin, 2006). Este centro hematopoiético local e temporário é responsável pela produção de Oncostatina M, um dos fatores necessários para a diferenciação terminal dos hepatoblastos (células progenitoras embrionárias bipotentes com comprometimento hepático, capazes de se diferenciar em hepatócitos e colangiócitos) em hepatócitos (Miyajima *et al*., 2000).

Neste momento, os hepatoblastos iniciam o processo de de-laminação do lúmen do intestino primitivo. O divertículo hepático formado começa então a ser invadido por células endoteliais (que posteriormente formarão os sinusóides hepáticos) e

mesenquimais vindas da mesoderme circundante (Si-Tayebe *et al*., 2010). Assim, inicia-se a formação das placas hepáticas e ductos intrahepáticos. Este processo se estenderá até o terceiro trimestre da gestação, quando as estruturas hepáticas estão devidamente formadas. (Si-Tayebe *et al*., 2010).

A figura 2, a seguir, resume o processo de diferenciação e organogênese hepática, paralelamente, descritos anteriormente nesta seção.

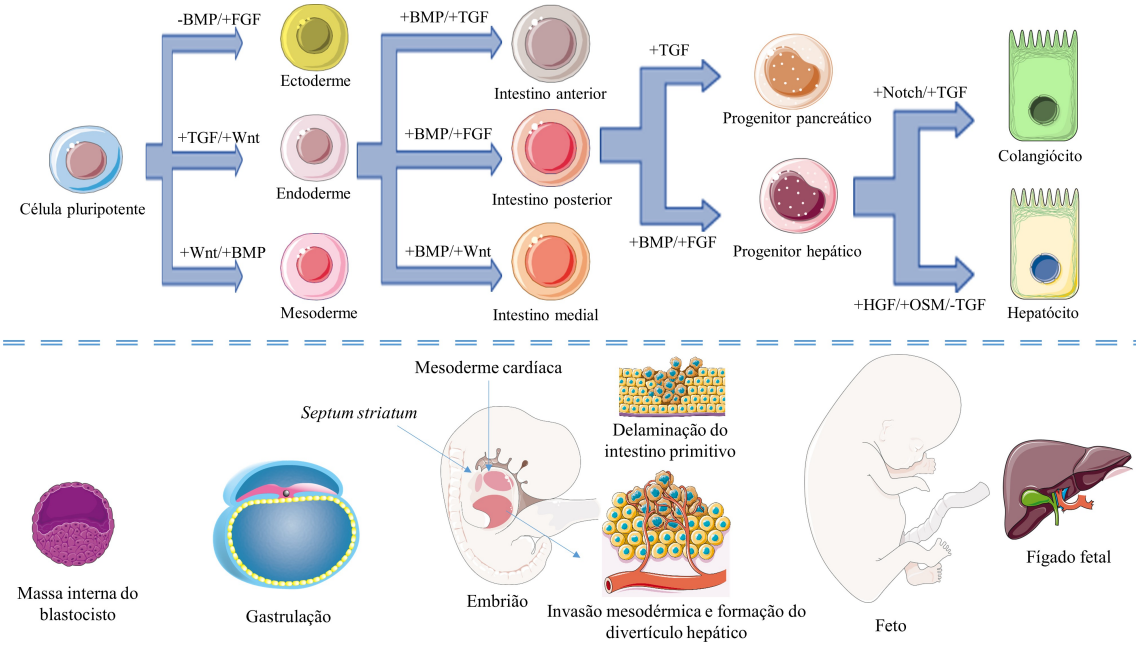

Figura 2: Diferenciação e organogênese hepática. Figura esquemática representativa da rota de diferenciação hepática (parte superior) e da organogênese hepática (parte inferior)**.** Ilustrações obtidas de banco público de imagens (https://smart.servier.com/, acesso em 24/03/2019), ou produzidas pelo autor desta tese.

Ainda durante o desenvolvimento embrionário, o fígado já possui muitas de suas atividades metabólicas funcionais, como a expressão da maioria das enzimas do complexo do citocromo P450, capacidade de estocar glicogênio e produção de sais biliares. Entretanto, a maturação final hepática, e o pleno exercício de suas funções só é alcançado semanas após o nascimento, como por exemplo a produção de albumina, dos fatores de coagulação em concentrações fisiológicas, e a atividade enzimática

fisiologicamente suficiente de conjugação da bilirrubina, realizada pela enzima UGT-1A (muitas vezes causando o quadro de icterícia pós-natal) (Grijalva & Vakili, 2013).

1.3. Patogênese e epidemiologia das doenças hepáticas

Sabe-se que o fígado apresenta uma incrível capacidade regenerativa. Em procedimentos de hepatectomia parcial, onde 70% do fígado é removido, o tecido remanescente aumenta significativamente de tamanho em apenas 7 dias, tornando-se capaz de prover todas as funções hepáticas normalmente (Michalopoulos, 2007). Injurías teciduais severas iniciam um rápido processo proliferativo de hepatócitos, seguido de uma etapa de maturação terminal, visando reposição do tecido lesado. Hepatócitos localizados nas regiões circundantes à veia central, com alta ativação da via Wnt (AXIN2+) são responsáveis pela regeneração fisiológica (i.e. *turnover* celular) (Wang *et al*., 2015), já os hepatócitos da região periportal (SOX9+) são responsáveis pela reposição tecidual frente a lesões crônicas (Font-Burgada *et al*., 2015). A região periportal é um nicho de hepatócitos quiescentes, aptos a iniciarem um processo proliferativo frente a diversas formas de injuria tecidual.

Apesar da inerente capacidade regenerativa, em condições patológicas severas, o processo regenerativo é insuficiente. A agressão tecidual crônica ou aguda do parênquima pode levar à perda substancial de função hepática, condição chamada de hepatopatia grave. A agressão ao parênquima hepático pode ocorrer de diversas formas. A exposição a agentes citotóxicos hepáticos (i.e. hepatotóxicos), como por exemplo o paracetamol, etanol e aflotoxina, podem induzir a necrose de hepatócitos e, a depender da concentração introduzida, induzir a falência hepática aguda (que pode levar o paciente ao óbito em poucos dias). Agentes virais, como os vírus da hepatite B e C, são

agressivos ao parênquima hepático, onde se replicam, causando um processo inflamatório crônico, quando não tratado (Bhatia *et al*., 2014). O consumo abusivo de álcool gera, além de uma inflamação local devido a sua toxicidade, um processo de acúmulo de vesículas gordurosas nos hepatócitos, chamado de esteatose, que assim como a estatose não alcoólica (i.e. esteatose induzida por dietas ricas em ácidos graxos associado ou não a um quadro de diabetes com glicemia não controlada), induzem uma inflamação local do parênquima hepático (Bhatia *et al*., 2014). Além disso, doenças genéticas, como a síndrome de Crigler-Najjar (doença autossômica recessiva em que o paciente é incapaz de conjugar a bilirrubina por deficiência da enzima UGT-1A) também podem evoluir para um quadro hepático degenerativo. Da mesma forma, as doenças colestáticas (interrupção do fluxo biliar) também são capazes de iniciar um grave processo degenerativo no fígado (Bhatia *et al*., 2014).

A lesão hepática crônica inicia um processo fibrótico progressivo em resposta à inflamação local, chamado de cirrose hepática. O remodelamento da matriz extracelular hepática é promovido pelas células estelares, que sob estimulação das vias inflamatórias e por indução das vias de PDGF e TGF-β iniciam a deposição de colágeno tipo I (fibrogênese), aumentam sua taxa de proliferação e iniciam a então chamada fase de progressão (Seki & Kim, 2015). Sem os devidos estímulos inflamatórios, estas células entram em apoptose e iniciam a fase de regressão, onde diminuem a deposição de colágeno (Seki & Kim, 2015).

A deposição excessiva de tecido fibrótico não funcional tem duas consequências fundamentais: déficit de função hepática (devido à substituição de tecido funcional) e hiper-pressurização do sistema porta-hepático. A hipertensão hepática é caracterizada pelo aumento do gradiente de pressão da veia hepática superior a 10 mmHg, medido pela diferença da pressão sinusoidal obstruída e pressão venosa central (Suk & Kim,

2015). Pacientes com hipertensão portal podem apresentar varizes gastro-esofágicas, decorrentes da resposta vascular visando diminuir o débito portal via *backup* vascular, devido ao aumento da resistência de perfusão sinusoidal. As varizes gastro-esofágicas, por possuírem paredes frágeis, podem se romper e causar sangramentos abdominais graves. Além disso, devido ao déficit de função hepática normalmente associada ao quadro cirrótico, a deficiência de produção de albumina sérica leva a episódios de extravasamento de líquido na cavidade abdominal, chamado de ascite (Suk & Kim, 2015).

A hepatite C ainda é um dos grandes causadores da cirrose hepática. Existem no mundo aproximadamente 150 milhões de pacientes infectados, 1,5 milhões destes no Brasil, sendo responsável por aproximadamente 350 mil mortes por ano (Kretzer *et al*., 2014). De modo geral, as hepatopatias severas (cirrose hepática e hepatocarcinoma celular), representam graves problemas de saúde pública, responsáveis por mais de 2 milhões de mortes por ano, com impacto direto na qualidade de vida da população e economia dos países (Rowe, 2017). Estima-se aproximadamente 60 milhões de pacientes cirróticos apenas nos Estados Unidos e União Europeia. Calcula-se que 2% das mortes no mundo estão associadas com diagnóstico clínico de cirrose hepática (Angus *et al*., 2018). Por outro lado, estima-se que a esteatose hepática não alcoólica afeta mais de 25% da população mundial, sendo um dos fatores de risco para o desenvolvimento da cirrose hepática (Rowe, 2017). Esta alta incidência se deve ao aumento progressivo da incidência de obesidade e diabetes na população mundial nas últimas décadas.

A velocidade de progressão da doença hepática varia de acordo com a origem etiológica, porém, de maneira geral, se não tratada, prejudica a funcionalidade do órgão, resultando em um quadro clínico geral grave. O estágio final de progressão é a falência

hepática e posterior evolução ao óbito em curto período de tempo. A Figura 3, a seguir, resume as formas de lesão hepáticas descritas nesta seção.

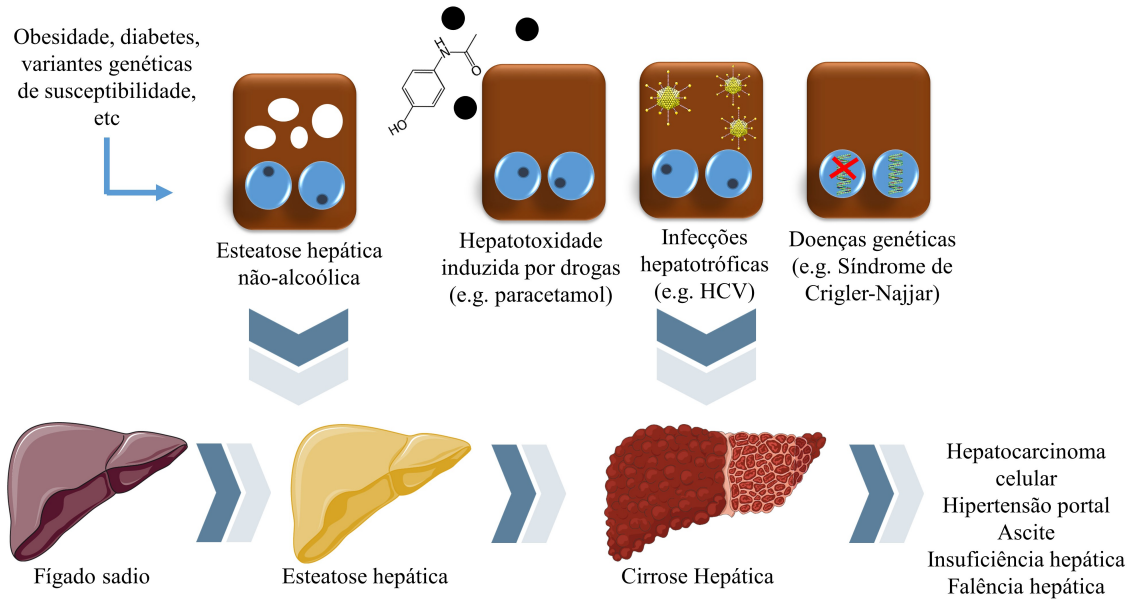

Figura 3: Diferentes formas de lesão hepática. Figura representativa e esquemática das diferentes formas de indução de lesão ao parênquima hepático. Ilustrações obtidas de banco público de imagens (https://smart.servier.com/, acesso em 24/03/2019), ou produzidas pelo autor desta tese.

Atualmente, o transplante de fígado constitui a única terapia definitiva para pacientes em estágio final de doença crônica hepática e/ou quando não existem terapias efetivas disponíveis (Wiegand & Berg, 2013). Este cenário é extremamente complexo devido à limitada disponibilidade de doadores. Além disso, outros complicadores impactantes na efetividade de transplantes de órgãos residem na manutenção, preservação e transporte do órgão a ser doado, a rejeição imunológica e dificuldade de ser obter pacientes compatíveis para o transplante (Jadlowiec & Taner, 2016).

De acordo com o último relatório anual publicado pela Associação Brasileira de Transplante de Órgãos (ABTO), referente ao ano de 2017, existe uma necessidade estimada de aproximadamente 5152 fígados para transplante. Foram realizados no ano de 2017 apenas 2109 procedimentos (ABTO, 2018). A lista de espera para transplante

de fígado fechou o ano de 2017 com 1101 pacientes ativos inscritos, tendo ingressado, no mesmo ano, 2829 pacientes, com uma mortalidade de 539 (ABTO, 2018).

Assim, observa-se que é evidente a necessidade do desenvolvimento de novas abordagens e tecnologias visando mitigar os problemas contemporâneos e crescentes enfrentados na clínica e no atendimento a pacientes nas filas de espera para transplante de órgãos.

1.4. Engenharia tecidual hepática

Uma solução potencial para os atuais problemas de déficit de órgãos disponíveis para transplantes são as abordagens de engenharia tecidual. A engenharia tecidual é uma ciência multidisciplinar que engloba aspectos das ciências de materiais, engenharia mecânica, engenharia elétrica, biologia celular, fisiologia, entre outras. Conceitualmente, a engenharia tecidual é uma das abordagens utilizadas pela medicina regenerativa. De maneira geral, a medicina regenerativa busca alternativas eficientes para pacientes que possuem uma lesão ou perda tecidual significativa onde a capacidade regenerativa do tecido lesado não é mais capaz de recuperar a homeostase e função tecidual (Katari *et al*., 2015).

O objetivo da abordagem de engenharia tecidual é a produção de tecidos biológicos, ou biomateriais, em laboratório, capazes de prover funções fisiológicas básicas a pacientes que necessitam de reposição funcional (Langer & Vacanti, 1993). De maneira geral, estas abordagens visam evitar ou diminuir a necessidade de doadores de órgãos, criar estratégias que consigam aumentar a sobrevida de pacientes em fila de espera, ou até mesmo soluções definitivas para estes problemas (Katari *et al*., 2015).

Para desenvolver um órgão e/ou tecido funcional passível de ser transplantado, é necessário ter acesso a uma fonte de células adequada, bem como desenvolver o melhor substrato, ou matriz estrutural, com o qual essas células irão crescer, se organizar e interagir com sinais indutivos necessários para a neoformação tecidual. Estes materiais podem possuir origem natural ou sintética. Os materiais utilizados para engenharia tecidual devem, necessariamente, cumprir os seguintes requisitos: não serem citotóxicos, não induzirem a reposta imune, possuírem propriedades mecânicas compatíveis com o tecido alvo e serem bio-absorvível ou integrativos (Atala & Yoo, 2011).

Dentre as várias abordagens de medicina regenerativa para tratamento de pacientes com doenças hepáticas, destaca-se o transplante de células, utilizando hepatócitos de doadores cadavéricos ou até mesmo de células derivadas de células tronco (Bhatia *et al*., 2014). Esta abordagem seria utilizada principalmente em pacientes com falência hepática aguda. Entretanto, a dificuldade de enxertia e vascularização no microambiente hepático inflamado é um dos grandes desafios desta abordagem. Por isso, nos últimos anos, a enxertia ectópica vem sendo estudada (Bhatia *et al*., 2014).

Outra possível abordagem seria a utilização de equipamentos extracorpóreos bio-artificiais, onde o plasma do paciente seria perfundido e detoxificado, no que é chamado de diálise de toxinas ligadas à albumina. Estudos com os equipamentos mais recentes mostraram que tal abordagem pode ser eficiente como um modelo de *bridge transplantation*, ou seja, uma forma de conseguir aumentar a sobrevida de pacientes críticos em fila de espera para transplante de fígado (Bhatia *et al*., 2014). Entretanto, a viabilidade dos hepatócitos utilizados nestes equipamentos, por estarem fora de seu microambiente tecidual natural, é reduzida ao longo do tempo. Além disso, os equipamentos apresentam dificuldade em prover um gradiente e oxigênio ideal e de

contornar os problemas com a força de cisalhamento gerada durante a perfusão plasmática, o que dificulta o escalonamento clínico da tecnologia (Bhatia *et al*., 2014).

Por isso, tem-se investido muito no desenvolvimento de tecidos hepáticos *in vitro,* por meio de técnicas de engenharia tecidual, como uma forma eficiente de produzir um substituto tecidual viável, capaz de prover função hepática por longos períodos de tempo e de fácil enxertia. Nos próximos tópicos, serão discutidas as principais estratégias e tecnologias que vêm sendo utilizadas em estudos de engenharia tecidual hepática. Para isso, serão abordados os conceitos principais das tecnologias e uma discussão do atual estado da arte em cada matéria.

1.4.1. Bioimpressão 3D

A impressão em três dimensões (3D) é um processo, ou conjunto de processos, no qual um material é produzido em 3D, geralmente a partir de um processo de deposição sucessiva de múltiplas camadas, baseado em um arquivo projetado em computador. A maioria das impressoras 3D disponíveis no mercado realizam este processo pelo derretimento de um polímero plástico (e.g. ácido poli-lático) e posterior secagem de camadas do material, formando ao final a forma desejada. O bico de extrusão do material é aquecido a temperaturas próximas de 200ºC e, por um jogo de polias e/ou esteiras, o bico é movimentado nos três eixos (x, y e z), dando forma volumétrica à estrutura. Apesar de ter ganhado notoriedade nos últimos anos, principalmente devido à drástica redução dos preços dos equipamentos e reagentes, a impressão 3D existe desde a década de 80 (Yao *et al*., 2016).

Nos últimos anos, técnicas que possibilitam a impressão de tecidos vivos (i.e. matrizes contendo células vivas) têm ganhando destaque. A maioria dos métodos

disponíveis para impressão de tecidos vivos usa uma imersão/dispersão celular em hidrogéis, também chamados de biotintas (Derakhshanfar *et al*., 2018). Os hidrogéis utilizados devem possuir uma viscosidade ideal para o processo de impressão e, normalmente, necessitam de um tratamento (químico ou físico) ao final do processo visando aumentar a sua dureza e preservar a forma impressa.

Dentre os principais hidrogéis utilizados para esta finalidade temos os hidrogéis acrilados (e.g. gelatina, ácido hialurônico, colágeno I, etc, que possuem radicais acril conjugados à sua cadeia lateral), onde, na presença de catalizadores (e.g. Irgacure 2959) e radiação ultra-violeta (UV), polimerizam e enrijecem. Outros materiais usados como biotintas incluem o alginato e nanocelulose. O alginato é um dos materiais mais utilizados atualmente na composição de biotintas, devido ao fato de ser um material que possue alta viscosidade (que facilita o processo de impressão), de fácil polimerização e biocompatível. O alginato é um polissacarídeo extraído de algas que, na presença de íons cálcio, se polimeriza e enrijece.

Observa-se que, independentemente da composição da biotinta, a formação neo-tecidual depende da capacidade das células impressas de migrarem, interagirem e desenvolverem com o microambiente e a matriz extracelular circundante (Derakhshanfar *et al*., 2018). A formulação de biotintas deve prover um ambiente mecânico ideal para as células crescerem, além de reproduzirem características importantes do tecido a ser mimetizado, como a dureza e elasticidade.

Tão importante quanto a formulação da biotinta é a técnica de impressão, ou seja, o método com que o material contendo as células formará a sua estrutura 3D desejada. A técnica de impressão define aspectos importantes do tecido gerado, como a densidade celular máxima na matriz, a resolução de impressão (i.e. o menor tamanho possível de imprimir duas formas capazes de serem distinguidas), etc. A seguir, a Figura

4 resume as etapas de pré-impressão, impressão e pós-impressão dos protocolos mais utilizados de bioimpressão.

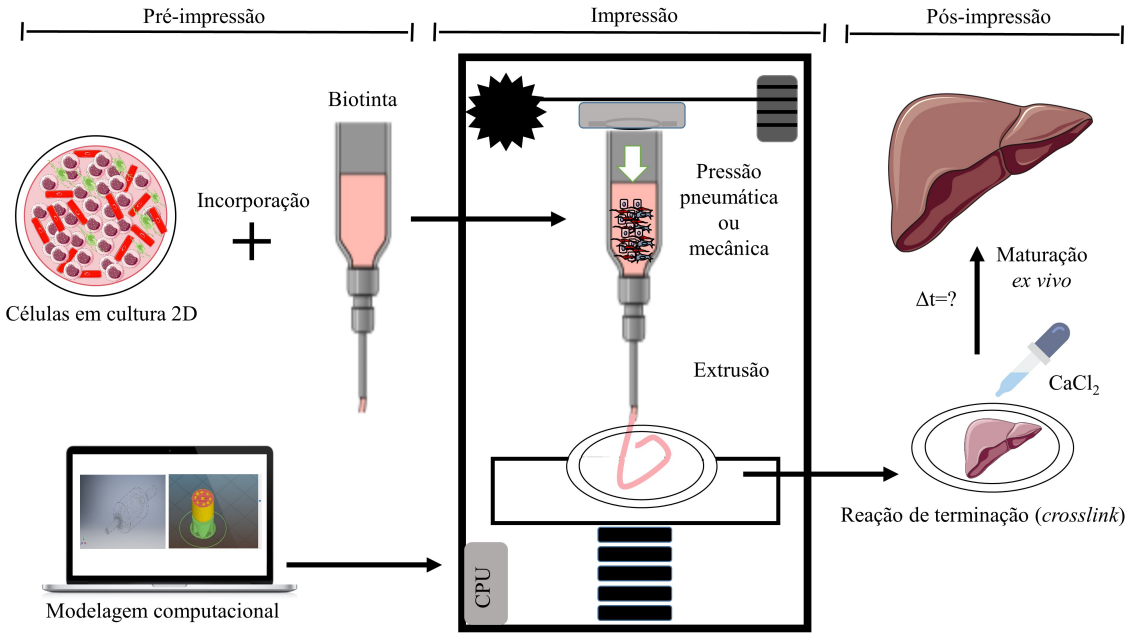

Figura 4: Representação esquemática do processo de bioimpressão. Figura representativa e esquemática indicando as etapas do processo de bioimpressão, descritos nesta seção. Ilustrações obtidas de banco público de imagens (https://smart.servier.com/, acesso em 24/03/2019), ou produzidas pelo autor desta tese.

A principal técnica de bioimpressão 3D consiste na extrussão (pneumática ou mecânica) da biotinta contendo as células pré-incorporadas e dispersas em sua formulação. Normalmente, o proesso de incorporação é um processo mecânico, obtido pela mistura de uma suspensão de células em alta concentração com a biotinta, até se obter uma dispersão homogênea. O resultante final é impresso e polimerizado ao final do processo. Este protocolo de bioimpressão é o mais utilizado devido ao fato de produzir tecidos com alta viabilidade celular ao final do processo, possuir baixo custo operacional e pela facilidade de manuseio.

Mais recentemente, vários grupos têm se dedicado a desenvolver novas técnicas de impressão que possibilitam maior resolução e compactação tecidual. A seguir, vamos

comentar as principais técnicas de impressão que foram desenvolvidas recentemente e que já foram utilizadas para impressão de tecido hepático.

Outras abordagens de bioimpressão 3D, por exemplo, envolvem a focalização de radiações ionizantes, como a ultravioleta, normalemente utilizadas para induzir a polimerização de alguns materiais conjugados com radicais metacrilados (Ma *et al*., 2016). No trabalho de Ma e colaboradores (Ma *et al*., 2016), os autores conseguiram imprimir uma estrutura de um corte de um lóbulo hepático em tamanho real composto por uma camada de hepatócitos derivados de células pluripotentes induzidas (iPS), impresso sobre uma camada de células tronco mesenquimais (MSC) humanas derivadas de tecido adiposo que foi impressa sobre o negativo da estrutura anterior. A construção final foi capaz de manter a secreção de albumina por mais de 20 dias, além de manter a expressão de enzimas do citocromo P450 como o os CYP3A4, 1A2, 2B6, 2C9 e 2C19. Entretanto, esta tecnologia ainda não é capaz de produzir tecidos com altura/espessura significativa, devido aos limites de resolução óptica dos equipamentos disponíveis.

Outra técnica que vem sendo estudada é a impressão tecidual via agregação 3D de esferóides celulares perfurados e suspensos em uma plataforma, de maneira que as distâncias entre as esferas individuais possibilitam a agregação de toda a estrutura, como já demonstrado para a produção de um tecido hepático, a partir de hepatócitos primários (Yanagi *et al*., 2017). A vantagem desta tecnologia se deve ao fato de dispensar utilização de hidrogel como matriz de impressão, isto é, não utiliza biotintas, o que garante a produção de um tecido completamente compacto e com junções célula-célula preservadas, importante para a manutenção de fenótipos epiteliais. Entretanto, o equipamento disponível atualmente para empregar esta técnica possui alto custo para aquisição e manutenção, diferentemente das outras técnicas citadas.

Com os desenvolvimentos recentes nas tecnologias de bioimpressão 3D, muitas publicações mostraram que a impressão de um tecido funcional hepático pode ser uma abordagem viável (Kizawa *et al*., 2017; Faulkner-Jones *et al*., 2015). No entanto, a impressão de hepatócitos, de maneira geral, ainda é um grande desafio devido às limitações associadas à passagem e à cultura celular a longo prazo, mesmo com os recentes avanços em protocolos de cultura (Hu & Li, 2015). Outra questão desafiadora para a evolução desta tecnologia reside no fato de que os hepatócitos são células epiteliais, ou seja, possuem uma polarização apical/basal específica e bem definida, além de uma forte junção célula-célula formado por *tight-junctions*. Logo, a dispersão tridimensional de hepatócitos em biotintas deve possibilitar o reagrupamento destas células no novo micro-ambiente. Por este e outros motivos, a maioria dos trabalhos publicados até então não conseguiram produzir um tecido hepático funcional estável por longos períodos de tempo em cultura.

Desta forma, fazendo uma análise crítica, observa-se que há uma necessidade inerente de se avaliar protocolos de impressão capazes de produzir tecidos hepáticos que preservem a funcionalidade epitelial do tecido por longos períodos de tempo. Para tal, é importante avaliar se as técnicas convencionais de impressão por extrusão seriam capazes de cumprir tais objetivos. A Tabela 1 resume todos os trabalhos publicados (encontrados em busca no NCBI) que utilizaram a técnica de bioimpressão com células hepáticas. Observa-se que a grande maioria dos trabalhos utilizaram a técnica de extrusão associada a uma composição de biotinta de alginato. Além disso, a grande maioria dos trabalhos utilizaram linhagens tumorais (HepG2) ou hepatócitos primários.

Tabela 1: Revisão bibliográfica dos artigos publicados com o tema de bioimpressão de células hepáticas.

Autor	Biotinta	Técnica de Impressão	Células	Resultado
Skardal *et al*., 2010	Polietileno glicol tetraédrico	Extrusão	HepG2 e NIH3T3	Sobrevida aumentada por quatro semanas
Chang *et al*., 2010	Gelatina	Extrusão co-axial	HepG2	Aumento do metabolismo hepático em cultura microfluídica
Matsusaki *et al*. 2013	Multicamadas de gelatina e fibronectina	Injeção celular a jato	HepG2 e HUVEC	Responsividade a drogas hepatotóxicas em duas semanas de cultivo
Bertassoni *et al*., 2014	Gelatina-metacrilato	Extrusão e polimerização simultânea	HepG2 e NIH3T3	Sobrevida aumentada por até oito dias
Faulker-Jones *et al*., 2015	Alginato	Extrusão co-axial com cloreto de cálcio	Células embrionárias humanas	Diferenciação *in situ* em hepatócitos
Zhong *et al*., 2016	Colágeno-quitosana	Extrusão	Hepatócitos primários humano	Aumento da sobrevida em modelo murino de lesão hepática
Nguyen *et al*., 2016	NovoGel®	Extrusão	HUVECs (células endoteliais), Hepatócitos e células estelares primárias humanas	Responsividade a drogas hepatotóxicas em duas semanas de cultivo
Ma *et al*., 2016	Gelatina-metacrilato	Espelhamento de forma e focalização de luz UV	Hepatócitos derivados de células iPS	Impressão de formas pequenas (e.g. lóbulo hepático) com boa resolução
Snyder *et al*., 2016	Alginato	Extrusão co-axial	HepG2 e HUVEC	Melhor resolução em impressões co-axiais, promovendo aumento da difusão de nutrientes
Kang *et al*., 2017	Alginato	Extrusão	Fibroblasto fetais murinos transdiferenciados em hepatócitos	Enxertia com sucesso em modelo murino

Jeon *et al*., 2017	Alginato	Extrusão	HepG2	Uniformidade nas estruturas impressas
Yanagi *et al*., 2017	-	Agregação de esferoides	Hepatócitos primários	Produção de um tecido compacto e funcional, com densa junção celular.
Lee *et al*., 2018	Hidrogel de matriz decelularizada de fígado de porcos	Extrusão	HepG2 (hepatoblastoma) e BMMSCs	Aumento da função hepática da linhagem HepG2
Wang *et al*., 2018	Gelatina-Alginato	Extrusão com auxilio tomográfico óptico	C3A (hepacarcinoma celular)	Maior uniformidade nas estruturas impressas
Kang *et al*., 2018	Alginato e colágeno I	Extrusão com padrão pre-definido	HepG2 e EA.hy 926 (células endoteliais)	Impressão de formas pequenas (e.g. lóbulo hepático) com boa resolução
Mazzocchi *et al*., 2018	Colágeno I e ácido hialurônico	Extrusão com padrão pre-definido	Hepatócitos e células estelares primárias humanas	Responsividade a drogas hepatotóxicas em duas semanas de cultivo
Kim *et al*. 2018	Alginato	Extrssão	Hepatócitos primários e MSC	Aumento da viabildiade da impressão de hepatócitos com células MSC
Yu *et al*., 2019	Hidrogel de matriz descelularizada de fígado de porcos + Gelatina-Metracrilato	Espelhamento de forma e focalização de luz UV	Hepatócitos derivados de células iPS	Impressão de formas pequenas (e.g. lóbulo hepático) com boa resolução

1.4.2. Organóides

A organogênese hepática pode ser recapitulada, em parte, usando a tecnologia de organóide (Takebe *et al*., 2013). A combinação de células progenitoras parenquimatosas (i.e. hepatoblastos) com proporções definidas de células não parenquimáticas (i.e. células endoteliais e células mesenquimais) (NPC) recria um microambiente celular análogo aos estágios iniciais do desenvolvimento do corpúsculo hepático e permite uma formação tecidual espontânea, possuindo um micro-sistema vascular interno, ou seja, um "mini-fígado" (Camp *et al*., 2017). Estas estruturas, quando transplantadas, conseguem fundir seu sistema vascular com o do hospedeiro, provendo função hepática (Takebe *et al*., 2013). As primeiras tentativas de produção de organóides hepáticos usaram hepatoblastos derivados de células-tronco pluripotentes e células primárias humanas não parenquimatosas, como células endoteliais derivadas da veia umbilical (HUVEC) e MSC derivadas de tecido adiposo, ambos derivados de diferentes doadores (Takebe *et al*., 2013). A Figura 5 resume o protocolo e as etapas de produção de organóides hepáticos.

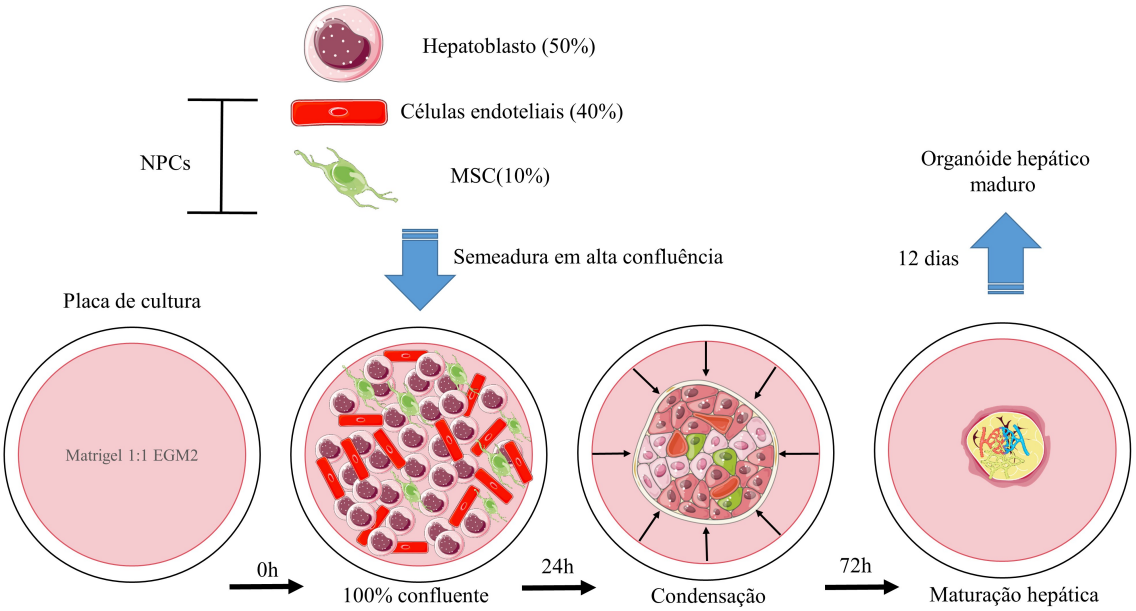

Figura 5: Produção de organóides hepáticos. Representação do protocolo de produção de organoides hepáticos (Takebe *et al.*, 2013). Ilustrações obtidas de banco público de imagens (https://smart.servier.com/, acesso em 24/03/2019), ou produzidas pelo autor desta tese.

A produção de organóides hepáticos consiste numa abordagem de engenharia tecidual que dispensa-se a utilização de um biomaterial, ou arcabouço. Além da potencial aplicação em estratégias de medicina regenerativa, tais tecidos podem ser utilizados em ensaios de avaliação de toxicidade hepática de novos fármacos, dispensando ou diminuindo a utilização de animais e ou células tumorais, sistemas que não possuem alta representatividade da fisiologia hepática humana.

Como dito anteriormente, NPCs contribuem para o desenvolvimento hepático e homeostase tecidual pela secreção de fatores de crescimento como TNF-α, IL-6, HGF, TGF-β e BMP2, 4 e 6 que regulam a proliferação de hepatócitos, síntese de DNA e formação de cordas hepáticas (Gordillo *et al*., 2015; Shin & Monga, 2013; Loh *et al*., 2014). Asai e colaboradores (Asai *et al*., 2017) mostraram as contribuições individuais e aditivas do secretoma de células endoteliais e células mesenquimais para o desenvolvimento de organoides hepáticos *in vitro*. Mais recentemente, alguns grupos relataram uma série de protocolos que foram capazes de gerar organóides hepáticos usando células parenquimatosas e NPC, todas derivadas de células-tronco pluripotentes induzidas (iPS) obtidas do mesmo doador, ou NPC primária também obtida do mesmo doador (i.e. tecido isogênico) (Takebe *et al*., 2017; Koui *et al*., 2017; Nie *et al*., 2018). No trabalho de Takebe e colaboradores (Takebe *et al*., 2017), os autores geraram com sucesso organoides hepáticos de doadores humanos em larga escala, que poderiam ser potencialmente utilizados em plataformas personalizadas de avaliação de toxicidade hepática no desenvolvimento de fármacos, levando em consideração um *background* genético de base populacional.

A produção de um organóide hepático isogênico evitaria complicações de rejeição imunológica em casos de transplantes em humanos, um objetivo muito importante para futuras aplicações de medicina regenerativa. É possível considerar que esta tecnologia seja usada em combinação com as atuais técnicas moleculares de edição gênica, onde mutações em genes relacionados a vias metabólicas hepáticas (e.g. distúrbios do ciclo da urea, erros inatos do metabolismo, doenças de estoque lissosomal, etc), que normalmente acometem crianças e que podem evoluir para uma necessidade de transplante hepático, podem ser corrigidas e transplantadas de volta ao paciente doador, recuperando o déficit metabólico do mesmo e evitando acúmulos tóxicos de intermediários.

No entanto, a diferenciação em larga escala de iPS em várias linhagens celulares pode ser desafiadora em termos de custo e eficiência. Desta forma, as linhagens celulares primárias podem ser mais atraentes, em termos de custo-benefício. É digno de nota que o uso de NPC primárias comerciais gera organóides quiméricos, o que poderia gerar rejeição tecidual no caso da aplicação em pacientes imuno-competentes. Pouco se sabe sobre a influência na fisiologia e na maturação de organóides hepáticos da utilização de cada componente das NPC (i.e. células endoteliais ou mesenquimais) obtidas de explantes teciduais do próprio potencial receptor ou através do estabelecimento de linhagens de iPS e posterior diferenciação nos fenótipos desejados.

A Tabela 2 resume os principais achados de todos os trabalhos publicados (encontrados em busca no NCBI) que utilizaram a técnica de organóides hepáticos. Para a pesquisa não foram considerados os protocolos de formação de organóides com células tumorais ou protocolos de formação de esferóides compostos por apenas um tipo celular. Observa-se que a grande maioria dos trabalhos utilizaram a combinação de hepatoblastos e células MSC e endoteliais de linhagens primárias comerciais.

Tabela 2: Revisão bibliográfica dos artigos publicados com o tema de organóides hepáticos.

Autor	Células	Avaliação
Takebe *et al*., 2013.	Hepatoblastos derivados de iPS, MSC e HUVEC	Formação de organóide por condensação mesenquimal
Ramachandran *et al*., 2015.	Hepatócito, MSC e células sinusoidais humanas primárais	Formação de organóide por condensação mesenquimal
Schepers *et al*., 2016.	Hepatoblastos derivados de iPS	Diferenciação em microfluídica de hepatócitos
Guye *et al*., 2016.	iPS	Formação de organoide pela manipulação da expressão gênica de *GATA6*
Takebe *et al*., 2017.	Hepatoblastos derivados de iPS, MSC e HUVEC	Formação de microrganóides em larga escala
Asai *et al*., 2017.	Hepatoblastos derivados de iPS, MSC e HUVEC	Participação de HUVEC e MSC na diferenciação terminal de hepatoblastos de organóides
Camp *et al*., 2017.	Hepatoblastos derivados de iPS, MSC e HUVEC	Formação de organóide por condensação mesenquimal
Koui *et al*., 2017.	Hepatoblastos, células endoteliais e mesenquimais derivadas de iPS	Formação de organóide por condensação mesenquimal
Nie *et al*., 2018.	Hepatoblastos derivados de iPS, MSC e endotelial de um mesmo doador	Formação de organoide por condensação mesenquimal
Li *et al*. 2018.	Hepatoblastos derivados de iPS, células estelares endoteliais sinusoidais humanas, hepatócitos derivados de MSC	Variação da proporção de células para cada combinação contendo células hepática
Ayebe *et al*., 2018.	Hepatoblastos derivados de iPS, MSC e HUVEC	Tensão de $O2_{(g)}$ e inibição de TGF-β influenciam a formação de organoides hepáticos
Ng *et al*. 2018.	Hepatoblastos derivados de iPS	Formação de hepatoesferas é influenciadoa pela quantidade de TGF-β e Hh
Zhang *et al*., 2018.	Progenitor de intestino primitivo anterior, MSC e HUVEC	Formação de organóide por condensação mesenquimal
Wu *et al*., 2019.	Hepatoblastos e células endoteliais derivadas de iPS	Protocolo de para formação de esturturas biliares

1.4.3. Descelularização

A obtenção ou produção de arcabouços para serem utilizados em abordagens de engenharia tecidual, como descrito anteriormente, deve levar em consideração a complexidade natural do órgão/tecido a ser produzido. Uma técnica promissora que vem sendo utilizada no desenvolvimento de órgãos transplantáveis não imunogênicos é a descelularização de matrizes biológicas. A descelularização de órgãos é capaz de produzir uma matriz biológica tridimensional acelular não imunogênica, usando apenas a matriz extracelular do tecido doador, preservando a complexa organização tridimensional e arquitetura do mesmo (Uygun *et al*., 2010; Badylak, 2007; Ott *et al*., 2008).

Dentre as diversas formas para remoção de células de um tecido biológico, destaca-se a perfusão de soluções com detergentes. Os detergentes solubilizam a bicamada lipídica da membrana plasmática das células, removendo-as gentilmente de sua matriz extracelular. Ao final do protocolo de descelularização, o que resta são as proteínas fibrosas e reticulares da matriz extracelular (e.g. colágeno I, III, V, elastina, etc) e também as proteínas de lâmina basal (e.g. colágeno IV, fibronectina, lamininas, etc) (Hoshiba *et al*., 2016).

As proteínas de matriz extracelular são bastante conservadas entre indivíduos da mesma espécie e até mesmo entre indivíduos de outras espécies de mamíferos (Ozbek *et al*., 2010). É sabido que as proteínas de matriz extracelular não induzem resposta imunológica. Logo, os tecidos descelularizados são uma excelente fonte de arcabouços para serem utilizados em abordagens de engenharia tecidual.

O objetivo desta tecnologia é utilizar esta matriz acelular para posteriormente ser recelularizada utilizando células saudáveis e maduras oriundas do próprio paciente que

será o receptor final do órgão, eliminando assim o risco de rejeição do mesmo. A Figura 6, a seguir, resume a estratégia da técnica de descelularização/recelularização.

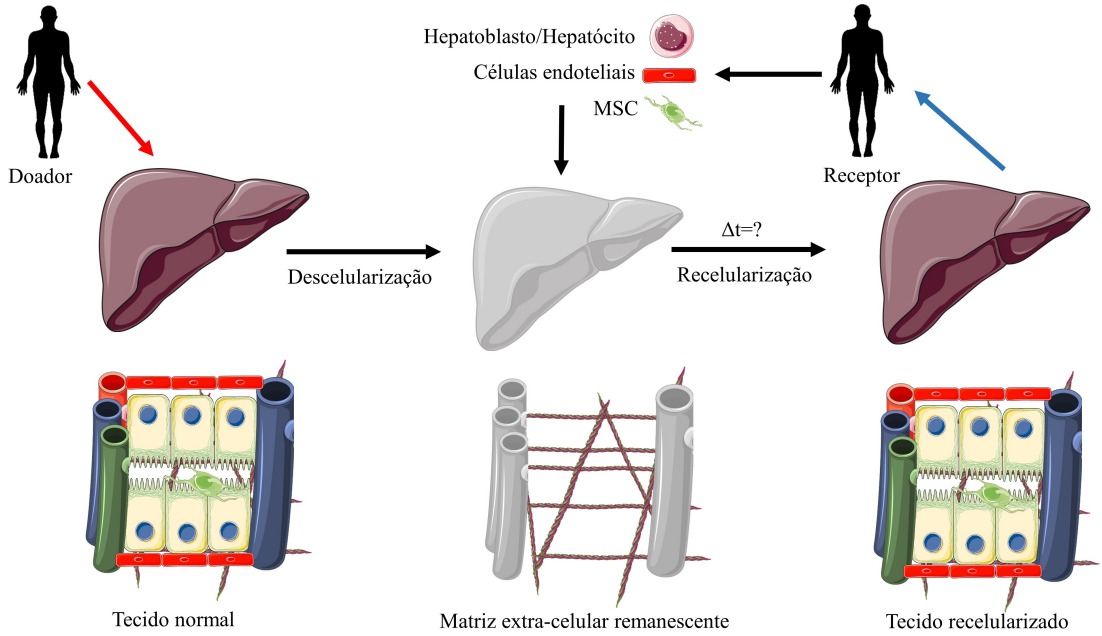

Figura 6: Abordagem de descelularização/recelularização de fígado. Representação do protocolo de descelularização/recelularização de fígado inteiro. Ilustrações obtidas de banco público de imagens (https://smart.servier.com/, acesso em 24/03/2019), ou produzidas pelo autor desta tese. A seta vermelha indica a remoção cirúrgica do órgão do doardor a ser utilizado no processo de descelularização. A seta azul indica a etapa final da estratégia, ou seja, o transplante do órgão "reconstruído" com células do próprio receptor.

É importante ressaltar que, após remover o componente celular dos tecidos, remanescentes da lise celular (e.g. DNA, vesículas celulares, etc) podem induzir uma ativação imunológica. Os DAMPs (*damage-associated molecular pattern*), como o DNA livre, são capazes de induzir uma resposta imunológica via ativação dos receptores do tipo *Toll-like* e subsequente ativação de NF-κβ e produção de citocinas pró-inflamatórias (Piccinini & Midwood, 2010), quando transplantado para o receptor. Para evitar tal resposta, os protocolos de descelularização precisam incluir múltiplas etapas de lavagem e perfusão de soluções hipertônicas, que ajudam a precipitar e remover remanescentes celulares.

Outra vantagem desta tecnologia se baseia na capacidade de, após descelularizados, os tecidos produzidos serem capazes de serem amazenados em baixa temperatura por longos períodos de tempo, sem prejuízo significativo para a ultra-estrutura tecidual e resistência mecânica dos mesmos (Poornejad *et al*., 2015.). Desta forma, imagina-se que seria possível o estabelecimento de bancos de órgãos descelularizados, aptos a receber as células de acordo com a demanda para tal.

Para a etapa subsequente, a etapa de recelularização das matrizes produzidas, é necessário um trabalho prévio de obtenção, expansão e/ou diferenciação dos diferentes tipos celulares que compõem o tecido alvo a partir de células progenitoras/tronco do paciente receptor. O protocolo de recelularização deve contemplar ainda a forma adequada de perfusão das células visando a correta distribuição celular no tecido.

Autores que utilizaram desta tecnologia descrevem que um dos facilitadores para as células perfundidas encontrarem seu correto nicho no microambiente tecidual seria seu próprio perfil de expressão de integrinas (proteínas responsáveis pelo reconhecimento e adesão celular a proteínas de matriz extracelular) observado em cada fenótipo celular. As integrinas são proteínas constituídas por duas subunidades, alfa e beta, que podem ser combinadas de diversas formas. Como existem 18 subunidades alfa e 8 subunidades beta diferentes, possibilitando 144 combinações diferentes, é improvável que células de fenótipos celulares distintos possuam exatamente o mesmo perfil de expressão de integrinas (Bilkin & Stepp, 2010).

Estudos prévios já utilizaram hepatócitos primários, linhagens celulares estabelecidas e/ou comercializadas, células progenitoras e/ou células-tronco embrionárias para repovoar o arcabouço hepático descelularizado (Ren *et al*., 2013; Baptista *et al*., 2011). Tais trabalhos não obtiveram sucesso no transplante devido a falhas na revascularização do órgão, ocorrendo edema, extravasamento vascular, e

eventos tromboembolísticos severos. Até o momento, nenhum sucesso com a descelularização/recelularização de órgãos inteiros foi obtido em modelos animais em procedimentos envolvendo o transplante do órgão gerado. Tal insucesso se deve principalmente à dificuldade de reestabelecer a integridade da parede vascular nos leitos capilares e sinusoidais. Para o devido sucesso da revascularização e recelularização hepática, é necessário um trabalho prévio de recondicionamento da matriz acelular, visando prover ao tecido remanescente, pobre em moléculas adjuvantes do processo de adesão celular (e.g. heparina, glicosaminoglicanos, etc.) (Lecht *et al*., 2014), com os constituintes mínimos necessários para uma adesão e migração celular, suficiente para o preenchimento do parênquima.

Uma possibilidade para contornar as dificuldades de recelularização de matrizes complexas como do fígado, conforme descrito anteriormente, seria a utilização de um outro tecido doador para o processo de descelularização, de anatomia mais simples, que possibilite uma organização tecidual eficiente e que funcionaria como um tecido hepático funcional, porém acessório, visto que não seria capaz de prover a totalidade da função hepática por si só. Algumas abordagens já utilizaram como arcabouço tecidos decelularizados de baço (que também apresenta um leito vascular sinusoidal, assim como o fígado, porém sem a organização lobular e com um sistema vascular mais simples) (Gao *et al*., 2015) e também da placenta (Kakabadze *et al*. 2018).

A Tabela 3 resume os principais achados de todos os trabalhos publicados (encontrados em busca no NCBI) que utilizaram a técnica de descelulariação/recelularização de diversas matrizes para a produção de tecido hepático. Observa-se que a grande maioria dos trabalhos utilizaram a recelularização de fígados inteiros descelularizados e utilizaram células primárias como fonte celular para o protocolo de recelularização.

Tabela 3: Revisão bibliográfica dos artigos publicados com o tema de descelulariação/recelularização para produção de tecido hepático.

Autor	Arcabouço descelularizado	Estratégia	Células	Transplante *in vivo*
Uygun *et al*., 2010.	Fígado de Rato	Recelularização de fígado inteiro	Hepatócitos primários de rato	8 horas
Baptista *et al*., 2011.	Fígado de Rato	Recelularização de fígado inteiro	Hepatócitos primários de rato	72 horas
Bao *et al*., 2011.	Fígado de Fuinha	Recelularização de fígado inteiro	Hepatócitos fetais humanas + HUVEC	-
Gutierrez *et al*., 2011.	Fígado de Camundongo	Recelularização de fígado inteiro	Hepatócitos primários de camundongos	-
Barakat *et al*. 2012.	Fígado de Porco	Recelularização de fígado inteiro	Hepatócitos e células estelares fetais humanas	-
Yagi *et al*., 2013.	Fígado de Porco	Recelularização de fígado inteiro	Hepatócitos primários de porcos	-
Kadota *et al*., 2014.	Fígado de Rato	Recelularização de fígado inteiro	Hepatócitos primários de rato + MSC de medula óssea	1 hora
Jiang *et al*., 2014.	Fígado de Camundongo	Recelularização de fígado inteiro	MSC de medula óssea	-
Navarro-Tableros *et al*., 2015.	Fígado de Camundongo	Recelularização de fígado inteiro	Células progenitoras hepáticas humanas	-
Ko *et al*., 2015.	Fígado de Porco	Recelularização de fígado inteiro	Células endoteliais de camundongos	24 horas
Bruinsma *et al*., 2015.	Fígado de Rato	Recelularização de fígado inteiro	Hepatócitos primários de rato	24 horas
Xiang *et al*., 2015.	Baço de Rato	Recelularização de Baço Inteiro	MSC de medula óssea	Subcutâneo - 24 dias
Zhou *et al*., 2016.	Fígado de Rato	Recelularização de fígado inteiro	Hepatócitos primários de rato + células progenitoras endoteliais	-

Park *et al*., 2016.	Fígado de Camundongo	Recelularização de fígado inteiro	Hepatócito derivados de iPS de porcos	1-8 horas
Hussein *et al*., 2016.	Fígado de Porco	Recelularização de fígado inteiro	HepG2 + células endoteliais	1 hora
Ogiso *et al*., 2016.	Fígado de Rato	Recelularização de fígado inteiro	Hepatócitos fetais de camundongos	-
Wen *et al*., 2016.	Fígado de Camundongo	Recelularização de fígado inteiro	Hepatócitos fetais de camundongos	-
Butter *et al*., 2017.	Fígado de Rato	Recelularização de fígado inteiro	Hepatócitos primários de rato	-
Hassanein *et al*., 2017.	Fígado de Rato	Recelularização de fígado inteiro	HepG2 + HUVEC	-
Yang *et al*., 2018.	Fígado de Camundongo	Recelularização de lóbulo hepático	Hepatócitos primários de camundongos	-
Robertson *et al*., 2018.	Fígado de Rato	Recelularização de fígado inteiro	HepG2	-
Devalliere *et al*., 2018.	Fígado de Rato	Recelularização de fígado inteiro	Células endoteliais	-
Kojima *et al*., 2018.	Fígado de Rato	Recelularização de fígado inteiro	Hepatócitos e células endoteliais sinusoidais primáriais de ratos	-
Kakabadze *et al*., 2018.	Placenta de Ovelha	Recelularização de placenta inteira	Fragmentos hepáticos digeridos de ovelhas	20 dias

1.5. Células tronco iPS

Abordagens de engenharia tecidual hepática necessitam de uma fonte de células adequada, capaz de prover quantidade suficiente e um fenótipo celular compatível com o tecido a ser gerado. Como discutido nos itens anteriores, existem diversas potenciais fontes celulares que poderiam ser utilizadas para a produção de tecidos hepáticos em laboratório, como: hepatócitos primários ou progenitores hepáticos bipotentes (isolados de doadores cadavéricos), hepatócitos obtidos a partir da transdiferenciação de células primárias do potencial receptor (e.g. fibroblastos dérmicos) e hepatócitos diferenciados a partir de células embrionárias ou de iPS (Goldmann & Gouon-Evans, 2016).

Como o fígado é o órgão interno de maior massa do nosso corpo, um pré-requisito fundamental para uma potencial fonte celular é prover uma quantidade significativa de células para conseguir repor as funções fisiológicas básicas do órgão. Logo, as células a serem utilizadas devem ser de fácil acesso e terem uma alta capacidade proliferativa *in vitro* antes de entrarem em senescência.

Hepatócitos primários, apesar de apresentarem o melhor fenótipo celular para este tipo de aplicação, possuem baixíssima capacidade proliferativa (2-3 passagens antes de entrarem em senescência), além de serem uma fonte limitada, devido à escassez de doadores de tecidos (Levy *et al*., 2015).

Hepatócitos produzidos a partir da transdiferenciação, ou seja, obtidos a partir da super-expressão de fatores de transcrição hepáticos como ATF5, PROX1, FOXA2, FOXA3, e HNF4A em células primárias, possuem uma capacidade proliferativa maior, dependendo da fonte celular inicial que será transformada em cultura, além de serem capazes de produzir um fenótipo hepático de alta qualidade (Nakamori *et al*., 2017). Porém, as células normalmente utilizadas para este fim (fibroblastos) são capazes de

proliferar em média 10 passagens até atingirem a senescência, o que pode ser um limitador para a produção de órgão ou tecido para um indivíduo adulto, ou que necessite de uma reposição substancial de função hepática.

Já as células embrionárias possuem uma capacidade proliferativa elevada, se mantêm estáveis por em média 50-60 passagens em cultura e são capazes de se diferenciar em hepatócitos e outros fenótipos celulares importantes na constituição de tecidos hepáticos, como células endoteliais e mesenquimais (Koui *et al*., 2017). Porém, não é possível estabelecer linhagens de células embrionárias de indivíduos adultos, e, portanto, a utilização de linhagens estabelecidas e/ou comerciais poderia gerar rejeição tecidual em futuros transplantes.

As iPS, por sua vez, podem ser obtidas de indivíduos adultos (potencialmente o próprio receptor) através de um processo de reprogramação somática. É importante ressaltar, entretanto, que as células iPS apresentam marcas epigenéticas das células de origem, o que pode afetar o rendimento das diferenciações e o fenótipo celular final (Goldmann & Gouon-Evans, 2016). Tanto os hepatócitos derivados de células embrionárias quanto de iPS apresentam um fenótipo fetal ao final da diferenciação, o que significa que elas não são metabolicamente ativas da mesma forma que um hepatócito adulto/primário (Goldmann & Gouon-Evans, 2016). Esta característica das células embrionárias e iPS não se limita apenas à diferenciação hepática. Muitos tecidos adquirem sua maturação final meses ou até anos após o nascimento.

A descoberta e produção das primeiras células iPS mudou o paradigma e as projeções futuras para pesquisas envolvendo engenharia tecidual e células-tronco. As células iPS tradicionalmente têm sido geradas a partir de fibroblastos humanos através da indução da expressão de fatores de reprogramação definidos (OCT3/4, SOX2, KLF4, c-MYC, etc) (Takahashi *et al*., 2007).

A diferenciação das células iPS em hepatócitos, células endoteliais e mesenquimais tem sido realizada por administração de fatores de crescimento, superexpressão de fatores de transcrição (vetores virais) ou co-cultura com outros tipos celulares (Kondo *et al*., 2014). Protocolos para diferenciação de iPS em hepatócitos maduros, células endoteliais funcionais e mesenquimais vêm sendo extensivamente desenvolvidos (Shan *et al*., 2013). Especificamente, entre os mais recentes trabalhos destacam-se protocolos que conseguiram em dezoito dias produzir hepatócitos maduros, que apresentavam a formação espontânea de estruturas de ductos biliares, além da expressão de genes característicos de progenitores hepáticos (AFP e HNF4), hepatócitos (CK18 e ALB), enzimas de metabolização do complexo do citocromo P450 e secreção de proteínas características de um fenótipo celular maduro de hepatócitos, como ureia e albumina (Shan *et al*., 2013).

Quanto à diferenciação de linhagens funcionais de células endoteliais, vários protocolos já conseguiram isolar linhagens responsivas a estímulos humorais, mecânicos e farmacológicos, além da expressão de marcadores característicos de tecido endotelial maduro (CD31, VE-caderina, Fator de Von-Willebrand, etc) e formação espontânea de vasos sanguíneos em cultura tridimensional (Adams *et al*., 2013).

Nosso grupo desenvolveu um protocolo para diferenciação de células mesenquimais, a partir de células de crista neural diferenciadas de iPS (iNCC) (Miller *et al*., 2017), que possuem a expressão de marcadores característicos como CD73, CD90 e CD105 e possuem o potencial em se diferenciar em múltiplos tecidos como ósseo, cartilaginoso e adiposo, quando devidamente estimuladas.

A Figura 7, a seguir, realiza um resumo da análise crítica e discussão sobre as potenciais fontes celulares descritas anteriormente.

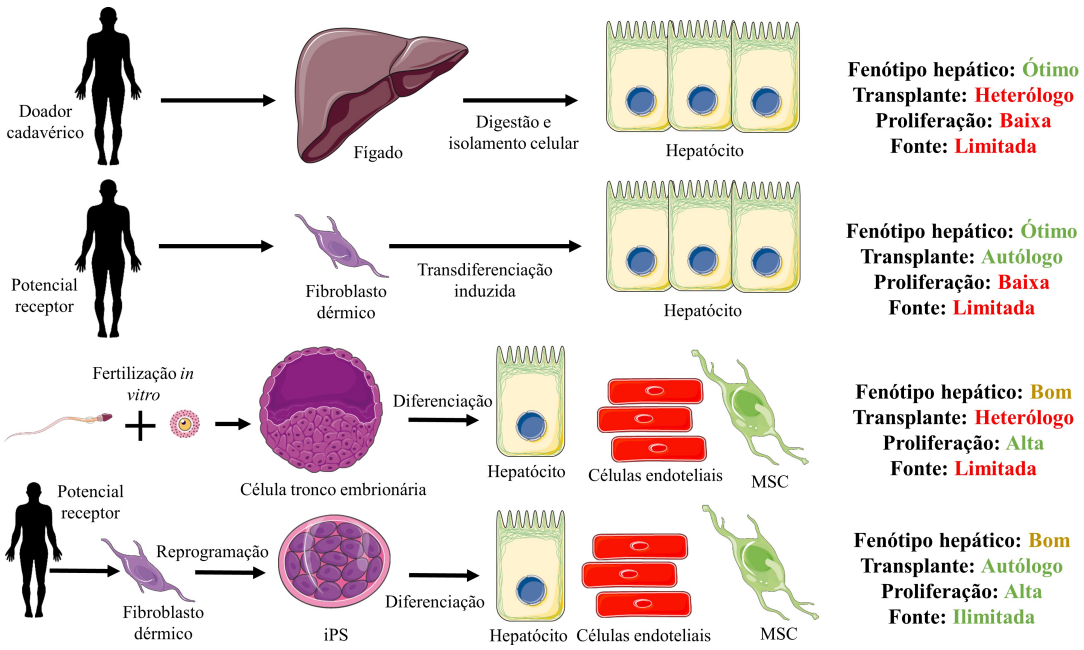

Figura 7: Análise das fontes celulares para produção de tecido hepático. Representação esquemática e análise das vantagens e desevantagens das seguintes fontes celulares para produção de tecido hepático, em ordem: Hepatócitos primários, hepatócitos transdiferenciados, hepatócitos diferenciados de células embrionárias, hepatócitos diferenciados de iPS. Ilustrações obtidas de banco público de imagens (https://smart.servier.com/, acesso em 24/03/2019), ou produzidas pelo autor desta tese.

Em conclusão, as células iPS apresentam melhor potencial de aplicação, considerando as vantagens e desvantagens das fontes celulares disponíveis para a produção de tecido hepático em laboratório em combinação com tecnologias de engenharia tecidual. Entretanto, a utilização destas células é desafiadora devido à necessidade de uma profunda validação da eficiência dos fenótipos celulares obtidos.

1.6. Objetivos

O objetivo geral desta tese de doutorado foi de avaliar novas abordagens que possibilitem superar alguns dos principais desafios no desenvolvimento das tecnologias contemporâneas de engenharia tecidual hepática, como a bioimpressão 3D, organóides hepáticos e descelularização/recelularização de matrizes biológicas, utilizando células tronco iPS, obtidas de doadores saudáveis, como fonte celular. De forma geral, este trabalho buscou identificar os principais gargalos tecnológicos, procurando esclarecer dúvidas e propor soluções inovadoras para tal.

1.7. Objetivos específicos

a) Bioimpressão 3D

Testar a eficiência da bioimpressão 3D comparando a forma de dispersão celular em esferoides hepáticos derivados de iPS ou hepatócitos dissociados, utilizando uma biotinta de Alginato/Plurônico F-127, ambos em associação com células NPC (i.e. endoteliais e mesenquimais), todas derivadas do mesmo doador.

b) Organóides hepáticos

Avaliar o impacto da utilização de NPCs primárias adultas ou derivadas de iPS de um mesmo doador para o desenvolvimento/maturação e funcionalidade de organóides hepáticos.

c) Fígado acessório aórtico

Obtenção e avaliação funcional de um tecido hepático acessório formado em arcabouço acelular vascular aórtico de rato como potencial *by-pass* porta-cava funcional utilizando células diferenciadas a partir de uma linhagem de iPS humana.

Referências

ABTO. Dimensionamento dos transplantes no Brasil e em cada estado 2010-2017. Registro brasileiro de transplantes. Ano XXIII, n.4. 2018

Adams, W. J., Zhang, Y., Cloutier, J., Kuchimanchi, P., Newton, G., Sehrawat, S., Aird, W. C., Mayadas, T. N., Luscinskas, F. W., *et al*. Functional vascular endothelium derived from human induced pluripotent stem cells. Stem Cell Reports, v.1, n.2, p105-13. 2013.

Ang, L. T., Tan, A. K. Y., Autio, M. I., Goh S. H. H., Lee, K. L., Tan, J., Pan, B., Lee, J. J. H. A., *et al*. Roadmap for Human Liver Differentiation from Pluripotent Stem Cells. Cell Rep, v.22, n.8, p2190-2205. 2018.

Angus, C., Meier, P., Holmes, J. Liver disease mortality trends: a response to the editor. Lancet. v.391, n.10127, p1258-1259. 2018.

Asai, A., Aihara, E., Watson, C., Mourya, R., Mizuochi, T., Shivakumar, P., Phelan, K., Mayhew, C., Helmrath, M., Takebe, T., Wells, J, Bezerra, J. A. Paracrine signals regulate human liver organoid maturation from induced pluripotent stem cells. Development. v.144, n.6, p1056-1064. 2017.

Atala, A. & Yoo, J. J. Tissue engineering: current strategies and future directions. Chonnam Med J, v.47, n.1, p1-13. 2011.

Ayabe, H., Anada, T., Kamoya, T., Sato, T., Kimura, M., Yoshizawa, E., Optimal Hypoxia Regulates Human iPSC-Derived Liver Bud Differentiation through Intercellular TGFB Signaling. Stem Cell Reports, v.11, n.2, p306–316. 2018.

Badylak, S. F. The extracellular matrix as a biologic scaffold material. Biomaterials. v.28, n.25, p3587-93. 2007.

Bao, J., Shi, Y., Sun, H., Yin, X., Yang, R., Li, L., *et al*. Construction of a Portal Implantable Functional Tissue-Engineered Liver Using Perfusion-Decellularized Matrix and Hepatocytes in Rats. Cell Transplantation, v.20, n.5, p753–766. 2011.

Baptista, P. M., Siddiqui, M. M., Lozier, G., Rodriguez, S. R., Atala, A, Soker, S. The use of whole organ decellularization for the generation of a vascularized liver organoid. Hepatology, v.53, n.2, p.604-17. 2011.

Barakat, O., Abbasi, S., Rodriguez, G., Rios, J., Wood, R. P., Ozaki, C., *et al*. Use of decellularized porcine liver for engineering humanized liver organ. J Surg Res, v.173, e11-e25. 2011.

Belkin, A. M. & Stepp, M. A. Integrins as receptors for laminins. Microsc Res Tech, v.51, n.3, p280-301. 2000.

Bertassoni, L. E., Cardoso, J. C., Manoharan, V., Cristino, A. L., Bhise, N. S., Araujo, W. A., *et al*. Direct-write bioprinting of cell-laden methacrylated gelatin hydrogels. Biofabrication, v.6, n2, 024105. 2014

Bhatia S. N., Underhill, G. H., Zaret, K. S., Fox, I. J. Cell and Tissue Engineering for Liver Disease. Sci Transl Med, v.6, n.245, 245sr2. 2014.

Bruinsma, B. G., Kim, Y., Berendsen, T. A., Ozer, S., Yarmush, M. L., Uygun, B. E. Layer-by-layer heparinization of decellularized liver matrices to reduce thrombogenicity of tissue engineered grafts. J Clin Transl Res v1.pii:04. 2015.

Butter, A., Aliyev, K., Hillebrandt, K.-H., Raschzok, N., Kluge, M., Seiffert, N., *et al*. Evolution of graft morphology and function after recellularization of decellularized rat livers. Journal of Tissue Engineering and Regenerative Medicine, v.12, n.2, e807–e816. 2017.

Camp, J. G., Sekine, K., Gerber, T., Loeffler-Wirth, H., Binder, H., Gac, M., Kanton, S., Kageyama, J., Damm, G., *et al*. Multilineage communication regulates human liver bud development from pluripotency. Nature, v.546, n.7659, p533-538. 2017.

Chang, R., Emami, K., Wu, H., Sun, W. Biofabrication of a three-dimensional liver micro-organ as anin vitrodrug metabolism model. Biofabrication, v.2, n.4, 045004. 2010.

Corless, J. K., Middleton III, H. M. Normal Liver FunctionA Basis for Understanding Hepatic Disease. Arch Intern Med, v.143, n.12, p2291-4. 1983.

Derakhshanfar, S., Mbeleck, R., Xu, K., Zhang, X., Zhong, W., Xing, M. 3D bioprinting for biomedical devices and tissue engineering: A review of recent trends and advances. Bioact Mater. v.3, n.2, p144-156. 2018.

Devalliere, J., Chen, Y., Dooley, K., Yarmush, M. L., Uygun, B. E. Improving functional re-endothelialization of acellular liver scaffold using REDV cell-binding domain. Acta Biomaterialia, v.15, n.78, p151-164. 2018.

Diaz G. J. Basolateral and canalicular transport of xenobiotics in the hepatocyte: A review. Cytotechnology, v.34, n.3, p225-35. 2000.

Dixon, L. J., Barnes, M., Tang, H., Pritchard, M. T., Nagy L. E. Kupffer cells in the liver. Compr Physiol. v.3, n.2, p785-97. 2013.

Eipel C., Abshagen, K., Vollmar, B. Regulation of hepatic blood flow: The hepatic arterial buffer response revisited. World J Gastroenterol, v.16, n.48, p6046–57. 2010.

Faulkner-Jones, A., Fyfe, C., Cornelissen, D. J., Gardner, J., King, J., Courtney, A., Shu, W. Bioprinting of human pluripotent stem cells and their directed differentiation into hepatocyte-like cells for the generation of mini-livers in 3D. Biofabrication, v.7, n.4, p044102. 2015

Font-Burgada J, Shalapour S, Ramaswamy S, Hsueh B, Rossell D, Umemura A, Taniguchi K, Nakagawa H, et at. Hybrid Periportal Hepatocytes Regenerate the Injured Liver without Giving Rise to Cancer. Cell, v. 162, n.4, p766-79. 2015.

Gao, R., Wu, W., Xiang, J., Lv, Y., Zheng, X., Chen, Q., Wang, H., Wang, B., Liu, Z., Ma, F. Hepatocyte culture in autologous decellularized spleen matrix. Organogenesis. v.11, n.1, p16-29. 2015.

Goldman, O. & Gouon-Evans, V. Human Pluripotent Stem Cells: Myths and Future Realities for Liver Cell Therapy. Cell Stem Cell, v.18, n.6, p703-6. 2016.

Gordillo, M., Evans, T., Gouon-Evans, V. Orchestrating liver development. Development. v.142, n.12, p2094-108. 2015.

Grijalva, J., Vakili, K. Neonatal liver physiology. Semin Pediatr Surg, v.22, n.4, p185-9. 2013.

Guye, P., Ebrahimkhani, M. R., Kipniss, N., Velazquez, J. J., Schoenfeld, E., Kiani, S., *et al*. Genetically engineering self-organization of human pluripotent stem cells into a liver bud-like tissue using Gata6. Nature Communications, v.7, 10243. 2016.

Hassanein, W., Uluer, M. C., Langford, J., Woodall, J. D., Cimeno, A., Dhru, U., *et al*. Recellularization via the bile duct supports functional allogenic and xenogenic cell growth on a decellularized rat liver scaffold. Organogenesis, v.13, n.1, 16–27. 2016.

Hoshiba T., Chen, G., Endo, C., Maruyama, H., Wakui, M., Nemoto, E., Kawazoe, N., Tanaka, M. Decellularized Extracellular Matrix as an In Vitro Model to Study the Comprehensive Roles of the ECM in Stem Cell Differentiation. Stem Cells Int, v.2016:6397820. 2016.

Hu, C. & Li, L. In vitro culture of isolated primary hepatocytes and stem cell-derived hepatocyte-like cells for liver regeneration. Protein Cell. v.6, n.8, p562-74. 2015.

Hussein, K. H., Park, K. M., Kang, K. S., Woo, H. M. Heparin-gelatin mixture improves vascular reconstruction efficiency and hepatic function in bioengineered livers. Acta Biomater, v.38, p82-93. 2016.

Jadlowiec, C. C. & Taner, T. Liver transplantation: Current status and challenges. World J Gastroenterol, v.22, n.18, p4438-45. 2016.

Jeon, H., Kang, K., Park, S. A., Kim, W. D., Paik, S. S., Lee, S.-H., *et al*. Generation of Multilayered 3D Structures of HepG2 Cells Using a Bio-printing Technique. Gut and Liver, v.11, n.1, p121–128. 2017.

Jiang, W. C., Cheng, Y. H., Yen, M. H., Chang, Y., Yang, V. W., Lee, O. K. Cryo-chemical decellularization of the whole liver for mesenchymal stem cells-based functional hepatic tissue engineering. Biomaterials v.35, p3607-3617. 2014.

Kadota, Y., Yagi, H., Inomata, K., Matsubara, K., Hibi, T., Abe, Y., *et al*. Mesenchymal stem cells support hepatocyte function in engineered liver grafts. Organogenesis, v.10, p268-277. 2014.

Kakabadze, Z., Kakabadze, A., Chakhunashvili, D., Karalashvili, L., Berishvili, E., Sharma, Y., Gupta, S. Decellularized human placenta supports hepatic tissue and allows rescue in acute liver failure. Hepatology, v.67, n.5, p1956-1969. 2018.

Kang, D., Ahn, G., Kim, D., Kang, H.-W., Yun, S., Yun, W.-S., *et al*. Pre-set extrusion bioprinting for multiscale heterogeneous tissue structure fabrication. Biofabrication, v.10, n.3, 035008. 2018.

Kang, K., Kim, Y., Jeon, H., Lee, S. B., Kim, J. S., Park, S. A., *et al*. Three-Dimensional Bioprinting of Hepatic Structures with Directly Converted Hepatocyte-Like Cells. Tissue Engineering Part A, v.24, n.7-8, p576–583. 2018.

Katari, R., Peloso, A., Orlando, G. Tissue engineering and regenerative medicine: semantic considerations for an evolving paradigm. Front Bioeng Biotechnol, v.2, p57. 2015.

Kietzmann, T. Metabolic zonation of the liver: The oxygen gradient revisited. Redox Biol. v.11, p622-630. 2017.

Kim, Y., Kang, K., Yoon, S., Kim, J. S., Park, S. A., Kim, W. D., *et al*. Prolongation of liver-specific function for primary hepatocytes maintenance in 3D printed architectures. Organogenesis, v.14, n.1, p1–12. 2018.

Kizawa, H, Nagao, E, Shimamura, M, Zhang, G., Torii, H. Scaffold-free 3D bio-printed human liver tissue stably maintains metabolic functions useful for drug discovery. Biochem Biophys Rep, v.10, p186-191. 2017.

Kizawa, H., Nagao, E., Shimamura, M., Zhang, G., Torii, H. Scaffold-free 3D bio-printed human liver tissue stably maintains metabolic functions useful for drug discovery. Biochemistry and Biophysics Reports, v.10, p186–191. 2017.

Ko, I. K., Peng, L., Peloso, A., Smith, C. J., Dhal, A., Deegan, D. B., *et al*. Bioengineered transplantable porcine livers with reendothelialized vasculature. Biomaterials, v.40, p72-79. 2015.

Kojima, H., Yasuchika, K., Fukumitsu, K., Ishii, T., Ogiso, S., Miyauchi, Y., *et al*. Establishment of practical recellularized liver graft for blood perfusion using primary rat hepatocytes and liver sinusoidal endothelial cells. American Journal of Transplantation, v.18, n.6, p1351–1359. 2018.doi:10.1111/ajt.14666

Kondo, Y., Yoshihashi, S., Mimori, K., Ogihara, R., Kanehama, Y., Maki, Y., Enosawa, S., Kurose, K., Iwao, T., *et al*. Selective culture method for hepatocyte-like cells differentiated from human induced pluripotent stem cells. Drug Metab Pharmacokinet. v.29, n.5, p407-13. 2014.

Koui, Y., Kido, T., Ito, T., Oyama, H., Chen, S. W., Katou, Y., Shirahige, K., Miyajima, A. An In Vitro Human Liver Model by iPSC-Derived Parenchymal and Non-parenchymal Cells. Stem Cell Reports, v.9, n.2, p490-498. 2017.

Kretzer I. F., do Livramento, A., da Cunha, J., Gonçalves, S., Tosin, I., Spada, C., Treitinger, A. Hepatitis C worldwide and in Brazil: silent epidemic--data on disease including incidence, transmission, prevention, and treatment. ScientificWorldJournal. 827849. 2014.

Langer, R. & Vacanti J. P. Tissue engineering. Science. v.260, n.5110, p920-6. 1993.

Lecht, S., Stabler, C. T., Rylander, A. L., Chiaverelli, R., Schulman, E. S., Marcinkiewicz, C., Lelkes, P. I. Enhanced reseeding of decellularized rodent lungs with mouse embryonic stem cells. Biomaterials, v.35, n.10, p.3252–3262. 2014.

Lee, H., Han, W., Kim, H., Ha, D.H., Jang, J., Kim, B. S., Cho, D.W. Development of Liver Decellularized Extracellular Matrix Bioink for Three-Dimensional Cell Printing-Based Liver Tissue Engineering. Biomacromolecules, v.18, n.4, p1229–1237. 2017.

Levitt, D. G. & Levitt, M. D. Human serum albumin homeostasis: a new look at the roles of synthesis, catabolism, renal and gastrointestinal excretion, and the clinical value of serum albumin measurements. Int J Gen Med, v.15, n.9, p229-55. 2016.

Levy, G., Bomze. D., Heinz, S., Ramachandran, S. D., Noerenberg, A., Cohen, M., Shibolet, O., Sklan, E., Braspenning, J., *et al*.Long-term culture and expansion of primary human hepatocytes, Nat Biotechnol, v.33, n.12, p1264-1271. 2015.

Li, J., Xing, F., Chen, F., He, L., So, K.F., Liu, Y., Xiao, J. Functional 3D Human Liver Bud Assembled from MSC-Derived Multiple Liver Cell Lineages. Cell Transplantation, 096368971878033. 2018.

Loh, K. M., Ang, L. T., Zhang, J., Kumar, V., Ang, J., Auyeong, J. Q., Lee, K. L., Choo, S. H., Lim, C.Y., *et al*. Efficient endoderm induction from human pluripotent stem cells by logically directing signals controlling lineage bifurcations. Cell Stem Cell, v.14, n.2, p237-52. 2014.

Ma, X., Qu, X., Zhu, W., Li, Y. S., Yuan, S., Zhang, H., Liu, J., Wang, P., Lai, C. S., *et al*. Deterministically patterned biomimetic human iPSC-derived hepatic model via rapid 3D bioprinting. Proc Natl Acad Sci USA, v.113, n.8, p2206-11. 2016.

Ma, X., Qu, X., Zhu, W., Li, Y.-S., Yuan, S., Zhang, H., *et al*. Deterministically patterned biomimetic human iPSC-derived hepatic model via rapid 3D bioprinting. Proceedings of the National Academy of Sciences, v.113, n.8, p2206–2211. 2016.

Maldonado-Valderrama, J., Wilde, P., Macierzanka A., Mackie A. The role of bile salts in digestion. , v.165, n.1, p36-46. 2011.

Matsusaki, M., Sakaue, K., Kadowaki, K., Akashi, M. Three-Dimensional Human Tissue Chips Fabricated by Rapid and Automatic Inkjet Cell Printing. Advanced Healthcare Materials, v.2, n.4, p534–539. 2012.

Michalopoulos, G. K. Liver Regeneration, J Cell Physiol, v.213, n.2, p286–300. 2007.

Mikkola, H. K. & Orkin, S. H. The journey of developing hematopoietic stem cells. Development, v.133, n.19, p3733-44. 2006.

Miller, E. E. , Kobayashi, G. S., Musso, C. M., Allen, M., Ishiy, F. A. A., de Caires, L. C. Jr., Goulart, E., Griesi-Oliveira, K., Zechi-Ceide, R. M., *et al*. EIF4A3 deficient human iPSCs and mouse models demonstrate neural crest defects that underlie Richieri-Costa-Pereira syndrome. Hum Mol Genet, v.26, n.12, p2177-2191. 2017.

Miyajima, A., Kinoshita, T., Tanaka, M., Kamiya, A., Mukouyama, Y., Hara, T. Role of Oncostatin M in hematopoiesis and liver development. Cytokine Growth Factor Rev, v.11, n.3, p177-83. 2000.

Nakamori, D., Akamine, H., Takayama, K., Sakurai, F., Mizuguchi, H. Direct conversion of human fibroblasts into hepatocyte-like cells by ATF5, PROX1, FOXA2, FOXA3, and HNF4A transduction. Sci Rep, v.7, n.1, p16675. 2017.

Navarro-Tableros, V., Herrera Sanchez, M. B., Figliolini, F., Romagnoli, R., Tetta, C., Camussi, G. Recellularization of rat liverscaffolds by human liver stem cells. Tissue Eng Part A, v.21, p1929-1939. 2015.

Ng, S. S., Saeb-Parsy, K., Segal, J. M., Serra, M. P., Blackford, S. J. I., Lopez, M. H., *et al*. Human iPS derived progenitors bioengineered into liver organoids using an inverted colloidal crystal poly (ethylene glycol) scaffold. Biomaterials, v.182, p299-311. 2018.

Nguyen, D. G., Funk, J., Robbins, J. B., Crogan-Grundy, C., Presnell, S. C., Singer, T., Roth, A. B. Bioprinted 3D Primary Liver Tissues Allow Assessment of Organ-Level Response to Clinical Drug Induced Toxicity In Vitro. Plos One, v.11, n.7, e0158674. 2016.

Nie, Y.-Z., Zheng, Y.-W., Ogawa, M., Miyagi, E., Taniguchi, H. Human liver organoids generated with single donor-derived multiple cells rescue mice from acute liver failure. Stem Cell Research & Therapy, v.9, n.1. 2018.

Nie, Y., Zheng., Y, Ogawa, M., Miyagi, E., Taniguchi, H. Human liver organoids generated with single donor-derived multiple cells rescue mice from acute liver failure. Stem Cell Res Ther, v.9, n.5. 2018.

Ogiso, S., Yasuchika, K., Fukumitsu, K., Ishii, T., Kojima, H., Miyauchi, Y., *et al*. Efficient recellularisation of decellularized whole-liver grafts using biliary tree and foetal hepatocytes. Sci Rep, v.6, n.35887. 2016.

Ott, H. C., Matthiesen, T. S., Goh, S. K., Black, L. D., Kren, S. M., Netoff, T. I., Taylor, D. A. Perfusion-decellularized matrix: using nature's platform to engineer a bioartificial heart. Nat Med, v.14 n.2, p.213-21. 2008.

Ozbek, S., Balasubramanian, P. G., Chiquet-Ehrismann R., Tucker, R. P., Adams, J. C. The evolution of extracellular matrix. Mol Biol Cell, v.21, n.24, p4300-5. 2010.

Park, K. M., Hussein, K. H., Hong, S. H., Ahn, C., Yang, S. R., Park, S. M., *et al*. Decellularized liver extracellular matrix as promising tools for transplantable bioengineered liver promotes hepatic lineage commitments of induced pluripotent stem cells. Tissue Eng Part A, v.22, p449-460. 2016.

Piccinini, A. M. & Midwood, K. S. DAMPening inflammation by modulating TLR signalling. Mediators Inflamm, n.672395. 2010.

Poornejad, N., Frost, T. S., Scott, D. R., Elton, B. B., Reynolds, P. R., Roeder, B. L., Cook, A. D. Freezing/Thawing without Cryoprotectant Damages Native but not Decellularized Porcine Renal Tissue. Organogenesis, v.11, n.1, p30-45. 2015.

Ramachandran, S. D., Schirmer, K., Münst, B., Heinz, S., Ghafoory, S., Wölfl, S., *et al*. In Vitro Generation of Functional Liver Organoid-Like Structures Using Adult Human Cells. Plos One, v.10, n.10, e0139345. 2015.

Ramasamy, I. Recent advances in physiological lipoprotein metabolism. Clin Chem Lab Med, v.12, p.1695-727. 2014.

Ren, H., Shi, X., Tao, L., Xiao, J., Han, B., Zhang, Y., Yuan, X., Ding, Y. Evaluation of two decellularization methods in the development of a whole-organ decellularized rat liver scaffold. Liver Int, v.33, n.3, p448-58. 2013.

Robertson, M. J., Soibam, B., O'Leary, J. G., Sampaio, L. C., Taylor, D. A. Recellularization of rat liver: An in vitro model for assessing human drug metabolism and liver biology. Plos One, v.13, n.1, e0191892. 2018.

Roth, A. D., Lama, P., Dunn, S., Hong, S., Lee, M.Y. Polymer coating on a micropillar chip for robust attachment of PuraMatrix peptide hydrogel for 3D hepatic cell culture. Materials Science and Engineering: C, v.90, p634–644. 2018.

Rowe I. A. Lessons from Epidemiology: The Burden of Liver Disease. Dig Dis. v.35, n.4, p304-309. 2017

Schepers, A., Li, C., Chhabra, A., Seney, B. T., Bhatia, S. Engineering a perfusable 3D human liver platform from iPS cells. Lab on a Chip, v.16, n.14, p2644–2653. 2016.

Seki, E. & Brenner, D. A.Recent advancement of molecular mechanisms of liver fibrosis. J Hepatobiliary Pancreat Sci, v.22, n.7, p512-8. 2015.

Senzolo, M., Burra, P., Cholongitas, E., Burroughs, A. K. New insights into the coagulopathy of liver disease and liver transplantation. World J Gastroenterol, v.12, n.48, p7725–7736. 2006.

Sevior, D. K., Pelkonen, O., Ahokas, J. T. Hepatocytes: the powerhouse of biotransformation. Int J Biochem Cell Biol, v.44, n.2, p257-61. 2012.

Shan, J., Schwartz, R. E., Ross, N. T., Logan, D. J., Thomas, D., Duncan, S. A., North, T. E., Goessling, W., Carpenter, A. E., *et al*. Identification of small molecules for human hepatocyte expansion and iPS differentiation. Nat Chem Biol, v.9, n.8, p514-20. 2013.

Shin, D. & Monga, S. P. Cellular and molecular basis of liver development. Compr Physiol, v.3, n.2, p799-815. 2013.

Si-Tayeb, K., Lemaigre, F. P., Duncan, S. A. Organogenesis and development of the liver. Dev Cell, v.18, n.2, p175-89. 2010.

Skardal, A., Zhang, J., Prestwich, G. D. Bioprinting vessel-like constructs using hyaluronan hydrogels crosslinked with tetrahedral polyethylene glycol tetracrylates. Biomaterials, v.31, n.24, p6173–6181. 2010.

Snyder, J., Son, A. R., Hamid, Q., Wu, H., Sun, W. Hetero-cellular prototyping by synchronized multi-material bioprinting for rotary cell culture system. Biofabrication, v.8, n.1, 015002. 2016.

Soto-Gutierrez, A., Zhang, L., Medberry, C., Fukumitsu, K., Faulk, D., Jiang, H., *et al*. A whole-organ regenerative medicine approach for liver replacement. Tissue Eng Part C Methods, v.17, p677-686. 2011.

Suk, K. T. & Kim, D. J. Staging of liver fibrosis or cirrhosis: The role of hepatic venous pressure gradient measurement. World J Hepatol, v.7, n.3, p607–615. 2015.

Takahashi, K., Tanabe, K., Ohnuki, M., Narita, M., Ichisaka, T., Tomoda, K., Yamanaka, S. Induction of pluripotent stem cells from adult human fibroblasts by defined factors. Cell, v.131, n.5, p861-72. 2007.

Takebe, T., Sekine, K., Enomura, M., Koike, H., Kimura, M., Ogaeri, T., Zhang, R. R., Ueno, Y., Zheng, Y.W., *et al*. Vascularized and functional human liver from an iPSC-derived organ bud transplant. Nature, v.499, n.7459, p481-4. 2013.

Takebe, T., Sekine, K., Kimura, M., Yoshizawa, E., Ayano, S., Koido, M., Funayama, S., Nakanishi, N., Hisai, T., *et al*. Massive and Reproducible Production of Liver Buds Entirely from Human Pluripotent Stem Cells. Cell Rep, v.21, n.10, p2661-2670. 2017.

Uygun, B. E., Soto-Gutierrez, A., Yagi, H., Izamis, M. L., Guzzardi, M. A., Shulman, C., Milwid, J., Kobayashi, N., Tilles, A. Organ reengineering through development of a transplantable recellularized liver graft using decellularized liver matrix. Nat Med. v.7, p814-20. 2010.

Wang, B., Zhao, L., Fish, M., Logan, C. Y., Nusse, R. Self-renewing diploid Axin2(+) cells fuel homeostatic renewal of the liver. Nature,v.524, n.7564, p180-5. 2015.

Wang, L., Xu, M., Luo, L., Zhou, Y., Si, P. Iterative feedback bio-printing-derived cell-laden hydrogel scaffolds with optimal geometrical fidelity and cellular controllability. Scientific Reports, v.8, n.1. 2018.

Weiskirchen, R & Tacke, F. Cellular and molecular functions of hepatic stellate cells in inflammatory responses and liver immunology. Hepatobiliary Surg Nutr, v.3, n.6, p344-63. 2014.

Wen, X., Huan, H., Wang, X., Chen, X., Wu, L., Zhang, Y., *et al*. Sympathetic neurotransmitters promote the process of recellulari- zation in decellularized liver matrix via activating the IL-6/Stat3 pathway. Biomed Mater, v.11, n.065007. 2016.

Wiegand, J. & Berg, T. The etiology, diagnosis and prevention of liver cirrhosis: part 1 of a series on liver cirrhosis. Dtsch Arztebl Int, v.110, n.6, p85-91. 2013.

Wu, F., Wu, D., Ren, Y., Huang, Y., Feng, B., Zhao, N., *et al*., Generation of hepato-biliary organoids from human induced pluripotent stem cells. Journal of Hepatology, v.19, p30002-9. 2019.

Xiang, J. X., Zheng, X. L., Gao, R., Wu, W. Q., Zhu, X. L., Li, J. H., Lv, Y. Liver regeneration using decellularized splenic scaffold: a novel approach in tissue engineering. Hepatobiliary & Pancreatic Diseases International, v.14, n.5, p502–508. 2015.

Yagi, H., Fukumitsu, K., Fukuda, K., Kitago, M., Shinoda, M., Obara, H., *et al*. Human-scale whole-organ bioengineering for liver transplantation: a regenerative medicine approach. Cell Transplant, v.22, p231-242. 2013.

Yanagi, Y., Nakayama, K., Taguchi, T., Enosawa, S., Tamura, T., Yoshimaru, K., Matsuura, T., Hayashida, M., Kohashi, K., *et al*. In vivo and ex vivo methods of growing a liver bud through tissue connection. Sci Rep, v.7, n.1, p14085. 2017.

Yang, W., Chen, Q., Xia, R., Zhang, Y., Shuai, L., Lai, J., *et al*. A novel bioscaffold with naturally-occurring extracellular matrix promotes hepatocyte survival and vessel patency in mouse models of heterologous transplantation. Biomaterials, v.177, p52–66. 2018.

Yao, R., Xu, G., Mao, S. S., Yang, H. Y., Sang, X. T., Sun, W., Mao, Y. L. Three-dimensional printing: review of application in medicine and hepatic surgery. Cancer Biol Med, v.4, p443-451. 2016.

Yu, C., Ma, X., Zhu, W., Wang, P., Miller, K. L., Stupin, J., *et al*. Scanningless and continuous 3D bioprinting of human tissues with decellularized extracellular matrix. Biomaterials, v.194, p1-13. 2018.

Zeilinger, K., Freyer, N., Damm, G., Seehofer, D., Knöspel, F. Cell sources for in vitro human liver cell culture models. Exp Biol Med (Maywood), v.241, n. 15, p1684-98. 2016.

Zhang, R. R., Koido, M., Tadokoro, T., Ouchi, R., Matsuno, T., Ueno, Y. Human iPSC-Derived Posterior Gut Progenitors Are Expandable and Capable of Forming Gut and Liver Organoids. Stem Cell Reports, v.10, n.3, p780–793

Zhong, C., Xie, H.-Y., Zhou, L., Xu, X., Zheng, S.S. Human hepatocytes loaded in 3D bioprinting generate mini-liver. Hepatobiliary & Pancreatic Diseases International, v.15, n.5, p512–518. 2016.

Zhou, P., Huang, Y., Guo, Y., Wang, L., Ling, C., Guo, Q., *et al*. Decellularization and recellularization of rat livers with hepato- cytes and endothelial progenitor cells. Artif Organs v.40, E25-E38. 2016

Capítulo 2:

3D bioprinting of liver spheroids derived from human induced pluripotent stem cells enhance liver function and viability *in vitro.*

Capítulo 2: Artigo submetido – Bioimpressão 3D

Submetido para a Revista: *Biofabrication*

3D bioprinting of liver spheroids derived from human induced pluripotent stem cells enhance liver function and viability *in vitro.*

Authors: Ernesto Goulart[1], Luiz Carlos de Caires-Junior[1], Kayque Teles Alves-Silva[1], Bruno Henrique Silva Araujo[2], Silvana Aparecida Rocco[2], Mauricio Sforca[2], Irene Layane de Sousa[2], Gerson S. Kobayashi[1], Camila Manso Musso[1], Amanda Faria Assoni[1], Danyllo Oliveira[1], Elia Caldini[3], Maria Rita Passos-Bueno[1], Silvano Raia[4], Peter I. Lelkes[5], Mayana Zatz[1]*.

Affiliations:

[1]Centro de Estudos do Genoma Humano e Células Tronco, Departamento de Genética e Biologia Evolutiva, Instituto de Biociências, Universidade de São Paulo (USP), São Paulo, SP, Brazil.

[2]Brazilian Biosciences National Laboratory (LNBio), Brazilian Center for Research in Energy and Materials (CNPEM), Zip Code 13083-970, Campinas, São Paulo, Brazil.

[3]Laboratório de Biologia Celular, Departamento de Patologia, Faculdade de Medicina, Universidade de São Paulo – (USP), São Paulo, SP, Brazil.

[4]Unidade do Fígado, Departamento de Cirurgia, Faculdade de Medicina, Universidade de São Paulo – (USP), São Paulo, SP, Brazil

[5]Department of Bioengineering, Temple University, Philadelphia, PA, United States

***Corresponding author:** mayazatz@usp.br

Abstract

The use of iPS-derived cells generating autologous grafts in combination with modern 3D bioprinting technologies could represent a relevant alternative for hepatic tissue replacement in end stage liver disease patients. However, the best methodology to recapitulate the liver epithelial parenchyma in bioprinted constructs is still under investigation. Here we tested the influence of bioprinting single cell dispersion of liver parenchymal and non-parenchymal cells as compared to printing hepatocyte spheroids, all derived from iPS cell lines. *In vitro* follow-up for 18 days after bioprinting, single cell dispersion showed reduced cell survival and hepatic function as compared to spheroid printed constructs. Single cell printed constructs induced epithelial-mesenchyme transition that resulted in rapidly loss of hepatocyte phenotype. These results contribute to 3D bioprinting technologies enhancement aiming future applications in patients with liver pathologies that require hepatic function replacement therapy.

Keywords: Bioprinting, Liver, iPS, Hepatocyte, 3D culture, Spheroids

Resumo

A bioimpressão 3D de um tecido hepático pode ser, no futuro, uma alternativa para pacientes com doença hepática terminal. O uso de células derivadas de células tronco pluripotentes induzidas (iPS) é capaz de produzir enxertos autólogos, em combinação com modernas tecnologias de bioimpressão 3D. No entanto, ainda não está claro como reproduzir o parênquima epitelial hepático em construções bio-impressas. Neste

trabalho, nós testamos a influência da dispersão de células individualizadas na bioimpressão de células do parênquima hepático, associadas a células não-parenquimatosas, frente à impressão de esferóides hepáticos, todos derivados de linhagens de células iPS. Após 18 dias de cultura *in vitro* após a impressão, a dispersão de células individualizadas apresenta uma redução significativa da sobrevida celular e da função hepática, em comparação com as construções impressas em esferóides. Construções impressas em células isoladas induzem a transição epitelial-mesênquima que resulta em rápida perda do fenótipo hepático. Esses dados contribuem para o desenvolvimento da tecnologia de bioimpressão 3D e para futuras aplicações em pacientes comprometidos com patologias hepáticas que demandam terapia de reposição funcional.

Palavras-chave: Bioimpressão, Fígado, iPS, Hepatócitos, Cultura 3D.

1. Introduction

The liver is a pivotal metabolic hub and regulator of blood homeostasis. Chronic exposure to toxic xenobiotics can lead to a persistent inflammation of liver parenchyma and formation of scar tissue, known as liver cirrhosis (Ge & Runyon, 2016). Many genetically inherited diseases, e.g. inborn errors of metabolism, hemochromatosis, etc., can also cause severe hepatic damage. Ultimately, patients that evolve to critically impaired liver function have to undergo total or partial liver transplantation as the only available option. Due to unmet donor shortage and complications associated with graft rejection and life-long immunosuppression, the development of new therapeutic approaches is highly relevant.

With the recent developments of 3D bioprinting technologies, several studies have shown that bioprinting functional liver tissue can be a feasible approach (Faulker-Jones *et al*., 2015; Ma *et al*., 2016; Kizawa, 2017). Most available methods for printing living tissues use cell immersion and dispersion within hydrogels (Bishop *et al*., 2017). Thus, neo-tissue formation relies on the ability of printed cells to migrate, interact and recapitulate liver microenvironment and surrounding extracellular matrix (ECM).

Human induced pluripotent stem cells (iPS) are a valuable cell source for liver tissue engineering since they can generate autologous grafts (i.e. avoiding potential immune responses), differentiate into all liver cell types and can be easily expanded (Palakkan et a., 2013; Bhatia *et al*., 2014; Goldman *et al*., 2016). Furthermore, with gene editing technologies, such as CRISPR-Cas9, cells from patients, who are carriers of disease causing mutations associated with liver pathologies and/or function, can now be edited before returning them into the patient (Lyu *et al*., 2018; Ruiz de Galarreta & Lujambio, 2017; Tang *et al*., 2018). In addition, the genetic background in hiPS-derived tissues influences their function and homeostasis and consequently drug toxicity screening results.

Despite recent advances in culture protools, bioprinting hepatocytes still represents a major challenge due to limitations associated with passaging and long-term cell culture (Levy *et al*., 2015). Here we tested the efficacy of bioprinting hiPS-derived hepatic spheroids within an alginate/Pluronic F-127 blend bioink formulation in association with iPS-derived non-parenchymal cells (i.e. endothelial and mesenchymal) as compared to single cell dispersions, all derived from the same donor.

2. Methods

2.1. Ethics and samples

The present study, including experimental procedures involving samples from human subjects, was approved by the ethics committee of the Instituto de Biociências at Universidade de São Paulo, Brazil (Protocol number 1.294.118). The protocol for the teratoma formation assay was approved by the ethics committee for animal studies of the Instituto de Biociências at Universidade de São Paulo, Brazil (Protocol number 229/2015).

2.2. iPS cell line generation and culture

Human induced pluripotent stem-cells (iPS) were generated from three healthy human individuals (F9048 = Male, 26; F8799 = Female, 28; F7405 = Male, 23). The iPS used in this study have been characterized previously (Miller *et al*., 2017). For more details, see Supplementary Methods.

2.3. iPS differentiation

Hepatocyte differentiation in monolayer was performed according previous published protocols (Cameron *et al*., 2015; Wang *et al*., 2017). Briefly, naive iPS cells were first cultured for three days, with daily media changes, in endodermal induction media (RPMI 1640, supplemented with 2% B27, 1% GlutaMAX – all from Gibco, 100 ng/mL of Activin A, 25 ng/mL of Wnt3a – all from R&D, and 100 µg/mL of Normocin - Invivogen). For the next 6 days, cells were cultured in hepatoblast induction media, with media changes every other day (KO-DMEM - Gibco, with 20% knockout serum replacement, 1% DMSO, 1% Glutamax and 100 ng/mL of normocin). The hepatocyte induction was carried out for 9 days with media changes every other day, and the media

was composed of Hepatozyme (Gibco), supplemented with 10 ng/mL of HGF, 20 ng/mL (R&D) of Oncostatin M (R&D), 10 nM of hydrocortisone (Sigma-Aldrich) and 1% GlutaMAX.

3D hepatic differentiation was performed according to a recently published protocol (Rashidi *et al*., 2018). This protocol closely resembles the 2D hepatic differentiation protocol. iPS cells were plated onto Matrigel (Corning) coated plates at 20,000 cells/cm^2. After three days of culture, cells were washed for 5 min in PBS, incubated again with E8 media, and mechanically lifted from the plates. The cells were cultured for 24h in E8 under orbital shaking (100 RPM). The next day, the media was replaced with definitive endodermal differentiation media and then cultured for 18 days, following the same protocol (media changes and composition) for 2D hepatic differentiation, under continuous shaking, at 100 RPM.

Endothelial differentiation was carried out according to Cao and collaborators (Cao *et al*., 2015), with minor modifications. First, iPS were plated at 1.5×10^4 /cm^2 and cultured for three days in E8 medium. For the next 5 days, basal media was composed of supplemented Stempro 34 Medium (Gibco) supplemented with various differentiation factors, as described below. The media was changed daily. On the first day, the basal media was supplemented with 5 μM of CHIR99021. On the second day, CHIR was replaced by 50 ng/mL of FGF-2. On the following three days, FGF-2 was replaced by 50 ng/mL of VEGF and 25 ng/mL of BMP4. All recombinant factors were obtained from RandD systems. On the last day of differentiation, cells were magnetically sorted using anti-CD31 microbeads (Miltenyi), following the manufacturer's instructions. CD31-positive cells were plated into 60mm Matrigel coated dishes (Corning) and cultured for no more than 6 passages in serum-free human

endothelial media (Gibco) supplemented with 10 ng/mL of VEGF, 20 ng/mL of FGF-2, 10 ng/mL of EGF and 1% of human platelet lysate.

The protocol for iPS-derived neural crest cells (iNCC) differentiation was based on previously published methodology (Miller *et al*., 2017). In brief, single iPS cells were seeded onto 60mm Matrigel-coated dishes at a density of 1×10^4 cells/cm^2 and cultured with E8 medium. Two days post-seeding, the medium was changed to iNCC differentiation medium, composed of E6 Medium (Life Technologies) supplemented with 8 ng/ml FGF-2, 20 μM SB431542 (TOCRIS), 1 μM CHIR99021 and 100 μg/ml Normocin; this differentiation medium was changed daily. After ∼2–4 days, neural crest-like cells were observed detaching from colony borders. The cells were split when reached 80% confluency, using Accutase and re-seeded into new Matrigel-coated 60-mm dishes in fresh iNCC differentiation medium. Cells were cultured for 15 days and passaged whenever the cultures reached 80% confluence. Differentiated iNCCs were cultivated for up to eight passages in iNCC differentiation medium, which was replenished daily.

Neural-crest derived msenchymal stem cell (nMSC) populations were obtained by culturing iNCCs in mesenchymal stem cell medium, as previously described (Miller et al 2017). In brief, iNCCs were seeded at 2×10^4 cells/cm^2 onto non-coated 60-mm tissue culture dishes in nMSC medium (DMEM/F12 supplemented with 10% FBS, 2 mM GlutaMAX, 0.1 mM non-essential aminoacids – all from Gibcom, and 100 μg/ml Normocin). Cells were differentiated for 6 days and passaged with TrypLE Express (Gibco), when reached 80% confluency. nMSC cultures were expanded in nMSC medium for up to 6 passages, with medium changes every 3 days. Details of the methodology for the various differentiation characterization assays are described in Supplemental Methods

2.4. Bioink formulation.

For Bioink formulation, low viscosity (15-25 cP, 1% in water) alginate (Sigma, Cat. 180947) was dissolved in distilled water at 60°C for 24h to a final concentration of 20% w/v. The alginate gel was mixed with calcium chloride solution in various concentrations, as shown in Figure 3A, using a syringe-to-syringe mixing technique for 5 minutes. Pluronic F-127 (Sigma) was dissolved in distilled water in an ice bath for 48h for a final concentration of 38% w/v. The alginate/calcium gel was mixed with Pluronic F-127 at various concentrations, as shown in Figure 3A, and mixed. For cellular experiments the final used formulation was: alginate 15%/ Pluronic F-127 6%, polymerized with 1.5% $CaCl_2$ solution for 5 minutes and washed three times with PBS before placing in culture media.

2.5. 3D-bioprinting

All bioprinting was carried out at room temperature in a Cellink (Gothenburg, Sweden) INKREDIBLE+ 3D bioprinter®. A donut-shaped construct of 5mm high and 10mm of diameter was designed using Autodesk Inventor software. The shape was chosen in order to fit in 24 well plates. The final processing prior to 3D-printing was performed using a Cellink modified version of the Slic3r software. The extrusion pressure was adjusted depending of the printability of tested hydrogels, ranging from 5-60 kPa. Printing was performed using a 20-gauge straight tip needle. The cells were resuspended in 300 µL of a 1:1 mixture of Matrigel (Corning) and EGM-2 (Lonza) media and mechanically dispersed in 1.5 mL of the resulting bioink, using a syringe-to-

syringe mixing technique for 5 minutes. For single cell printing a final concentration of $1x10^7$ cells/mL of bioink was obtained from a mixture of 75% single cells hepatoblast, 20% iEC and 10% nMSC. For hepatic spheroid printing, we used the corresponding same cell number hepatoblasts used in single cell printing.

2.6. Proteomics

For proteomics analysis, the samples were processed as previously described (Carnielle *et al*., 2018).). More detailed information can be found in the Supplemental Methods section. Pathway annotation of protein IDs was performed using the EnrichR (Kuleshov *et al*., 2016; Chen *et al*., 2013) applying Reactome (Fabregat *et al*., 2018) and Panther (Mi & Thomas, 2009) categorization with the threshold for significance set at a $p < 0.05$. Interactome was performed using String (Szklarczyk *et al*., 2017) with k-means clusterization in 3 groups. The mass spectrometry proteomics data have been deposited in the ProteomeXchange Consortium via the PRIDE partner repository with the dataset identifier PDX013191

2.7. Metabolomics

For determination of metabolite concentrations, we used the Varian-Agilent Inova Spectrometer (Agilent Technologies Inc.™, Santa Clara, USA). ^{1}H NMR spectra of the samples were acquired using a Nuclear Magnetic Resonance Spectrometer equipped with a triple resonance cryogenic probe operating at the ^{1}H frequency of 600 MHz and constant temperature of 298 K (25 °C). Depending on the concentration of the metabolites, a total of 512 scans were collected with 32000 dots and 4s acquisition time

in a spectral width of 16 ppm. A 1.5s waiting time was incorporated between the scans, during which a continuous pre-saturation radiofrequency field of water was applied. Corrections of the spectral phase baseline, as well as identification and quantification of the metabolites present in the samples were performed with the help of Chenomx NMR Suite® software (Chenomx Inc. ™, Edmonton, Canada). Pathway enrichment analysis was performed using Metaboanalyst (Chong *et al*., 2018)

2.8. Statistical Analysis

Statistical analyses were performed using GraphPad Prism (Carlsbad, San Diego) software and two-tailed unpaired Student's t tests. Data is shown as means ± SEM with n = 3, biological replicates. Values of $p < 0.05$ were considered statistically significant in statistical analysis.

3. Results

3.1. 2D and Spheroid hepatic differentiation of iPS cells

The purpose of this work was to address the importance of cellular dispersion in bioprinting hydrogels for hepatic constructs. To better evaluate the effect of 3D cellular aggregation and/or single-cell dispersion in bioink formulations, we first validated our iPS-hepatic differentiation protocol in both 2D and 3D. All data displayed in Figure 1 are related to the cell line F9048 since the other cell lines (i.e. F8799 and F7405) yielded similar results (Supplementary Figure 1C). The characterization of all human iPS cell lines used in this study are displayed in Supplemental Figure 1A-C. All 2D cellular differentiation protocols are summarized in Figure 1A. Following a robust

protocol for 2D hepatocyte differentiation, the cells expressed typical hepatic markers *CK18*, *G6PC*, *ALB* and *UGT1A1* (Figure 1B). After 18 days, 79.7% of the cell population was ALB+/UGT1A1+ (Figure 1C). Hepatocytes-derived cells stained positive for CYP3A4, ECAD, A1AT and expressed CK18, G6PC, UGT1A1 and ALB (Figure 1D). Hepatic basal-lateral transportation was tested by uptake and release of ICG (Figure 1E). The genes for liver phase I metabolism enzymes *GSTA1* and *GSTA4* were expressed at the end of hepatic differentiation (FIG1F). Treatment of the hepatocytes with Omeprazol and Rifampicin differentially modulated the expression of the genes for *CYP1A2* and *CYP3A4* (Figure 1G), confirming enzymatic induction properties of derived hepatocytes.

The phenotype of iPS-derived endothelial cells was confirmed by flow cytometry with 72% of the cell population double positive for CD31+/VECAD+ (Figure 1H). Endothelial cells (passage 5-7) stained uniformly positive for CD31/VECAD, which were co-localized at the cell boundaries, and also for Von-Willebrand Factor (Figure 1I). Functional analysis confirmed the cell's potential to form tube-like assemblies, when cultured on Matrigel (Figure 1J) and the ability to uptake acetylated-LDL in culture (Figure 1K), confirming endothelial-like scavenger activity. Gene expression analysis for vascular markers *PECAM1*, *NOTCH4*, *EFNB2* and *KDR* towards the end of the differentiation protocol confirmed an arterial-like phenotype (Figure 1L). When treated for 24h with TNF-α, the endothelial cells significantly upregulated the ICAM1, simulating endothelial-neutrophil adhesion (Figure 1M).

iPS-derived mesenchymal cells were 97.4% double positive for CD90+/CD73+ and only 1.3% were double positive for CD31+/CD45+ (Figure 1N). iMSC express the mesenchymal marker CD105 (Figure 1O). The multipotency of these iMSCs cells is demonstrated in figure 1P and figure 1Q. After 28 days of differentiation towards

osteogenic lineages, the cultures stained positive for Alizarin Red (i.e. stain for calcium deposition) and the cells expressed the important osteogenic marker *BGLAP* (Figure 1P and Q). When differentiated towards chondrogenic lineages, the cells stained positive for Alcian blue (stain for glycosaminoglycans) and expressed late chondrogenic marker *COL2A1* (Figure 1P and Q). Finally, when differentiated towards adipogenic lineages, the cells stained positive for Oil Red O (stain for lipid droplets) and expressed the late adipogenesis marker *LPL* (Figure 1P and Q).

Hepatic differentiation in 3D was checked step-by-step (Figure 2A and B). The gene expression panel revealed increased expression of endodermal and hepatic markers during the differentiation protocol (Figure 2C). Size distribution of cellular spheroids (n=50) at day 18 shows and mean diameter of 222 ± 33.37 μm (Figure 2D). Histological (H&E) and picrosirius staining revealed that spheroids are hollow and have an internal thin layer of ECM, where a single column of hepatocytes are sited (Figure 2E). The cells expressed pluripotency markers OCT4 and SSEA4 at day 0 (Figure 2F). Cells express pluripotency markers OCT4 and SSEA4 at day 0. After day 3, some cells expressed CXCR4 and FOXA2 (Figure 2G) and at day 9 a majority of the cells expressed AFP and ECAD (Figure 2H). At day 18, the cells in the cellular spheroids overwhelmingly stained positive for hepatic markers such as ALB, CYP3A4, A1AT, HNF4, CK18, and CK19 (Figure 2I-K).

3.2. Alginate-Pluronic F127 blend produces printable bioink formulation

Different blend compositions of Alginate and Pluronic F-127 were tested for their printability (Figure 3A). Hydrogels containing > 15% alginate and crosslinked with at least 1% calcium chloride were printable as were blends of alginates mixed with

3% Pluronic F-127 at alginate concentrations > 10% and at least 1.5% calcium chloride. Furthermore, alginate blends containing 6% of Pluronic F-127 were printable with alginate concentrations > 10% with at least 1.0% calcium chloride. After printing, the ability to sustain a 3D form was tested for 120h in solutions containing 1 mM calcium. All constructs retained their shapes at the end of the experiment (Figure 3B). Scanning electron microscopy analysis showed that the porosity of the alginate/pluronic blends increased as compared to alginate hydrogels (Figure 3C and D).

3.3. Hepatic spheroid bioprinting display prolonged hepatic and metabolic function

The cellular viability of the printed liver constructs decreased overtime in both groups but significantly more in single cell printed constructs. As seen in Figure 4B, after 18 days the viability of culture spheroid-printed organoids was significantly higher (80%) than that of the single-cell printed constructs (60%). In line with this observation, after 6 days of culture, LDH activity in culture supernatants of single-cells-printed constructs was significantly greater than that in the spheroid printed organoids right after printing (Figure 4C). Ki67 positive cells showed no difference among tested conditions over time (Figure 4D).). Liver-specific function assessed in the culture supernatant showed that spheroid-printed groups produced significantly more urea at day 6, 12 and 18 (Figure 4E). In contrast, AFP production was similarly reduced overtime in both groups (Figure 4F). Albumin production was significantly higher in spheroid-printed group only at day 18 (Figure 4G), as ALB production in single cell printed tissues started to decline. A1AT concentration in culture supernatants was significantly higher in spheroid-printed group at days 6 and 12 but not at day 18 (Figure

4H). Analysis by real time RT-PCR at day 18 showed that spheroid-printed tissues had significantly increased expression of hepatic phase I enzymes such as *CYP3A4*, *CYP1A2* and *CYP1A1,* phase II enzyme *GSTA1,* and important hepatocyte proteins such as *NR1/2* and *ALB* (Figure 4I). No significant difference was observed for *TDO2*, *AHR*, *CK18* and *MRP1* gene expression (Figure 4I)

3.4. Metabolomics

The quantification of cell culture metabolites at day 18 revealed a divergent clustering of single cell printed tissue versus spheroid-printed tissue (Figure 5A). Enrichment analysis showed top enriched pathways related to urea cycle and nitrogen metabolism (Figure 5B and C). Concentration of top hits within the altered pathways (i.e. aspartate, formate, glycine, hystidine and tryptophan) was significantly higher in the spheroid-based printed constructs than in the single cell-printed spheroids (Figure 5D).

3.5. Proteomics

Shotgun proteomics showed that the majority of protein ID are shared between single cell printed SC and spheroid printed tissue SP (Figure 5E). Principal component analysis showed that single cell printed constructs clustered together, differently from spheroid printed tissue where variation between cells lines was greater (Figure 5E). Applying t-test ($p<0.05$), a list of 128 differentially expressed proteins was obtained (Figure 5F). Interactome map of differently expressed proteins was filtered by major cluster of proteins and highlights the mitochondrial (blue) amino acid or fatty acid

catabolism (red) (Figure 5g). Pathway enrichment analysis confirmed interactome analysis and showed top 10 enriched pathways, where top 4 are related to amino-acids and fatty acid metabolism (Figure 5G). Also, ECM–receptor interaction and focal adhesion were highlighted as enriched pathways. Additionally, collagen type I content, an important marker of liver fibrosis, was significantly higher in single cell printed constructs as compared to spheroid counterpart (Figure 5H).

3.6. 3D single-cell dispersion induces epithelial-mesenchymal-transition (EMT).

At day 18, RT-qPCR analysis showed that constructs printed using single cell dispersion of hepatocytes had significantly reduced expression of *CDH1* and *CDH2* and significantly increased expression of *VIM* and *SNAIL2* as compared to hepatic spheroid printed tissue. However, for other genes related to EMT process, such as *CDH6*, *CDH7*, *CDH11*, *TWIST1* and *SNAIL1* (Figure 5I), the difference was not significant.

4. Discussion

In order to compare the role of 3D cellular spacing in iPS-derived liver bioprinting constructs we first characterized the cell source composition. Using standard protocols we were able to generate fully functional hepatocyte (in 2D and in 3D), endothelial cells and MSC, all derived from iPS that were derived from the same three donors. Notably, both 2D and 3D hepatic differentiation shared similar gene and protein expression profiling expression throughout the protocol. Hepatic differentiation in 2D was accompanied by the gradual increase in the expression of typical markers, such as

CK18, *G6PC*, *ALB* and *UT1A1* (Figure 1B). Flow cytometric analysis for ALB and UGT1A1, confirmed the commitment of the majority of cell population for hepatocyte phenotype (Figure 1C). Additionally, IF staining for CYP3A4 and A1AT confirmed previous findings (Figure 1D). The ability to intake and export ICG from the media confirmed bile basolateral-apical transport activity in culture (Figure 1E). Expression of hepatic phase one enzyme *GSTA1* and *GSTA4* during differentiation indicates metabolic functional hepatocytes (Figure 1F). This was also confirmed by the induction assay in the presence of Omeprazol and Rifampicin, inducers of *CYP1A2* and *CYP3A4*, respectively (Figure 1G).

Endothelial differentiation was demonstrated by flow-cytometry and IF staining for VECAD and CD31 (Figure 1H and I), showing that the vast population majority was positive for these markers. Differentiated endothelial cells expressed Von-Willebrand factor (Figure 1i) and were able, when plated on Matrigel, to form capillary like structures, which were sustained after 48h (Figure 1J). Also, iPS-derived endothelial cells were able to take up acetylated LDL, confirming vascular scavenger activity. RT-qPCR for *CD31*, *EFNB2* and *KDR* confirmed endothelial commitment over the differentiation steps (Figure 1L). When exposed to TNF-α, endothelial cells up-regulated ICAM1 (figure 1m), confirming a rapid response to inflammatory stimuli and the ability to activate neutrophils recruitment.

Mesenchymal differentiation was confirmed by flow-cytometry, with vast majority of population double positive for CD90 and CD73 and negative for endothelial/hematopoietic markers CD31 and CD45 (Figure 1N). Furthermore, MSCs expressed the mesenchymal marker CD105 (Figure 1O). When properly induced, MSCs were able to differentiate towards the osteogenic lineage (confirmed by expression of BGLAP and positive staining for Allizarin Red, confirming calcium storage ability), the

chondrogenic lineage (confirmed by expression of *COL2A1*, and positive staining for Alcian Blue (confirming accumulation of glycosaminoglycan) and adipogenic lineage (as inferred from the expression expression of LPL and positive staining for Oil Red, confirming lipid droplets accumulation), shown here in figure 1P and Q.

To generate hepatic spheroids, we used an agitation protocol, described in figure 2A and B. Expression of endodermal markers (*FOXA2* and *CXCR4*), hepatoblast markers (*AFP* and *HNF4A*) and hepatocyte markers (*ALB*, *UGT1A1* and *CK19*) confirmed the differentiation towards a hepatic phenotype (Figure 2C). The mean diameter of the spheroids was 222 ± 33.37 μm, which renders them printable using a 20 gauge needle with an inner diameter of 603 μm. As described in the literature (Rashidi *et al*., 2018), hepatic spheroids generated using this protocol are hollow structures with an inner thin ECM layer generated for the hepatic epithelia (Figure 2E). Immune fluorescence staining showed in Figure 2F-K confirmed the gene expression pattern observed in figure 2C.

Since terminally differentiated hepatocyte in 2D are not viable after passaging and have a very poor ability to migrate, we decided to print the liver constructs using hepatoblasts. Terminal differentiation was achieved during the following *in vitro* culture of these printed constructs.

Alginate/pluronic hydrogel blends produced a stable matrix with higher porosity than alginate hydrogels, as previously also described in the literature (Amstrong *et al*., 2016). Blending the two polymers increased the printability of the constructs requiring reduced concentrations of calcium and polymers (Figure 3A and retained their shapes in an aqueous solution (Figure 3b). Scanning electron microscopy revealed that the alginate/pluronic blend has increased porosity as compared to alginate by itself (Figure

3C and D). Thus, we chose to use a blend of 15% alginate/6% pluronic F-127 6% as our bioink. We printed the same cell number and ratios of hepatocyte (figure 2d and 3d),

When 3D-printed in hepatic-spheroids, liver constructs displays prolonged survival, reduced cell death after printing, increased urea production and prolonged secretion of albumin and A1AT over time (Figure 4A-C). By comparison, single cell printed constructs had reduced expression of important hepatic markers and functional enzymes which indicates a significant loss of hepatocyte functionality (Figure 4I). Specifically, in single cell printed tissue, the expression of genes for phase one enzymes (*CYP1A1*, *CYP1A2*, *CYP3A4* and *GSTA1*) was reduced, as was the expression of genes for the nuclear receptors NR1/2, also known as PXR, and AHR, transcription activators of CYP3A4 and CYP1A1 and CYP1A2, respectively (Kim *et al*., 2016) (Figure 4I). Finally, the reduced gene expression of *ALB* was in line with the reduced secretion of ALB observed in culture supernatants.

Metabolomics analysis revealed a distinguished pattern of metabolites in culture supernatant at day 18. Most enriched pathways were related to the hepatic urea cycle and nitrogen metabolism, indicating reduced hepatic metabolic activity in single-cell printed constructs. Aspartate levels were significantly higher in spheroids (Figure 5C). This could indicate an increased activity of hepatic aspartate transaminase, which could explain the increased urea secretion observed in Figure 4E, since aspartate is key in the urea cycle (Husson *et al*., 2003).

Proteomics analysis revealed a number of differently expressed proteins related to protein/amino acid metabolism, confirming metabolomics analysis. Together, this data indicates an increase in protein degradation ratio, resulting from cell death within printed tissue, corroborating the findings of increased LDH activity in culture supernatants and reduced cell viability at day 18 (Figure 3B and C). The increase in

focal adhesion markers and collagen I content in single cell printed constructs might indicate a fibrotic process (Baiocchini *et al.*, 2016). Also, collagen IV was significantly higher in single cell printed constructs, which is used as a serum marker for severe liver fibrotic process (Attallah *et al.,* 2007).

In order to evaluate how single cell printed constructs quickly lose their hepatic phenotype we analyzed the expression of selected, important EMT genes by RT-qPCR. At day 18, single cell printed hepatic constructs had reduced expression of epithelial markers *CDH1* and *CDH2* and increased expression of Vimentin and *SNAIL2*, which indicates a loss of epithelial phenotype during terminal differentiation and an increase in mesenchymal phenotype. Although mesenchymal cadherin's *CDH6*, *CDH7* and *CDH11* did not achieve statistical significance, the increased expression of Vimentin and *SNAIL2* is indicative of an increase of mesenchymal cellular phenotype within the printed constructs (Lamouille *et al.*, 2014). It is known that upon different chronic injuries to the liver, hepatocytes might undergo partial or complete EMT initiating fibrogenesis (Lamouille *et al.*, 2014; *Xue et al.*, 2013; Choi *et al*., 2009; Zeisberg *et al*., 2007). This process contributes to the development of liver cirrhosis and reduced hepatic function (Zhao *et al.*, 2016).

Together these data indicate that bioprinting hepatic tissues using spheroids yields organoids with prolonged cellular function, as compared to 3D printed spheroids generated from single cell dispersions. Our data corroborates previous findings, which demonstrated that liver progenitor cells can survive longer in vascularized perfusion chambers when implanted as spheroids (Yap *et al.*, 2013). Our data also corroborate the findings of Rashidi and collaborators (Rashid *et al*., 2018) who demonstrated that 3D hepatic spheroids can sustain hepatic function in culture for more than a year. Although it is still not clear how hepatic spheroids can sustain cell phenotype for so long, we

believe that our work reinforces the notion that for epithelial parenchyma function, providing a microenvironment, which maintains the epithelial phenotype of the hepatic cells is crucial (Cicchini *et al.*, 2015; Li *et al*., 2017). The present work indicates that iPS-derived hepatic cells, when cultured at low cell density in a 3D microenvironment that does not allow cell contact-dependent signaling, induces EMT and a pro-fibrotic phenotype, which impedes proper hepatic functionality and reduces cell viability overtime.

5. Conclusion

In short, using an alginate/pluronic hydrogel blend we were able to demonstrate that 3D printing of human liver iPS-derived parenchymal in spheroid aggregates and non-parenchymal cells in single cells significantly increases liver function and prolonged tissue survival over a long period of time *in vitro*. In addition, single cell dispersion of liver parenchymal cells induces EMT and a pro-fibrotic phenotype. This study provides important insights that could significantly improve the development of future applications for liver tissue engineering using 3D bioprinting of human iPS-derived cells.

References

Armstrong, J. P., Burke, M., Carter, B. M., Davis, S. A., Perriman, A. W. 3D Bioprinting Using a Templated Porous Bioink. Adv Healthc Mater, v.5, n.14, p1724-30. 2016.

Attallah, A. M., Mosa, T. E., Omran, M. M., Abo-Zeid, M. M., El-Dosoky, I., Shaker, Y. M. Immunodetection of collagen types I, II, III, and IV for differentiation of liver fibrosis stages in patients with chronic HCV. J Immunoassay Immunochem, v.28, n.2, p155-68. 2007.

Baiocchini, A., Montaldo, C., Conigliaro, A., Grimaldi, A., Correani, V., Mura, F. Ciccosanti, F., Rotiroti, N., Brenna, A. *et al.* Extracellular Matrix Molecular Remodeling in Human Liver Fibrosis Evolution. PLoS One, v.11, n.3, pe0151736. 2016.

Bhatia, S. N., Underhill, G. H., Zaret, K. S., Fox, I. J. Cell and tissue engineering for liver disease. Sci Transl Med, v.6, n.245, p245sr2. 2014.

Bishop, E. S., Mostafa, S., Pakvasa, M., Luu, H. H, Lee, M. J, Wolf, J. M., Ameer G. A. He, T. C., Reid, R. R. 3-D bioprinting technologies in tissue engineering and regenerative medicine: Current and future trends. Genes Dis, v.4, n.4, p185-195. 2017.

Caires-Júnior, L., Goulart, E., Melo, U., Araujo, B., Alvizi, L., Soares-Schanoski, A., de Oliveira, D., Kobayashi, G., Griesi-Oliveira, K., and Musso, C. *et al.*. Discordant congenital Zika syndrome twins show differential in vitro viral susceptibility of neural progenitor cells. Nature Communications, v.9, n.1, p475. 2018.

Cameron, K., Tan, R., Schmidt-Heck, W., Campos, G., Lyall, M. J., Wang, Y., Lucendo-Villarin, B., Szkolnicka, D., Bates, N., Kimber, S. J., Hengstler, J. G., Godoy, P., Forbes, S. J., Hay, D. C. Recombinant Laminins Drive the Differentiation and Self-Organization of hESC-Derived Hepatocytes. Stem Cell Reports, v.5, n.6, p1250-1262. 2015.

Carnielli, C., Macedo, C., De Rossi, T., Granato, D., Rivera, C., Domingues, R., Pauletti, B, Yokoo, S., Heberle, H., *et al.*. Combining discovery and targeted proteomics reveals a prognostic signature in oral cancer. Nat Commun. v.9, n.1, p359. 2018.

Chen, E., Tan, C., Kou, Y., Duan, Q., Wang, Z., Meirelles, G., Clark, N., Ma'ayan A. Enrichr: interactive and collaborative HTML5 gene list enrichment analysis tool. BMC Bioinformatics, v.15, n.128. 2013.

Choi, S. S. & Diehl, A. M. Epithelial-to-mesenchymal transitions in the liver. Hepatology, v.50, n.6, p2007-13. 2009.

Chong, J., Soufan, O., Li, C., Caraus, I., Li, S., Bourque, G., Wishart, D. S., Xia, J.. MetaboAnalyst 4.0: towards more transparent and integrative metabolomics analysis. Nucleic Acid Res, v.46, W1, W486-W494. 2018.

Cicchini, C., Amicone, L., Alonzi, T., Marchetti, A., Mancone, C., Tripodi, M. Molecular mechanisms controlling the phenotype and the EMT/MET dynamics of hepatocyte. Liver Int, v.35, n.2, p302-10. 2015.

Fabregat, A., Jupe, S., Matthews, L., Sidiropoulos, K., Gillespie, M., Garapati, P., Haw, R., Jassal, B., Korninger, F., *et al*. The Reactome Pathway Knowledgebase. Nucleic Acids Res v.4, D649-D655. 2018.

Faulkner-Jones, A., Fyfe, C., Cornelissen, D. J., Gardner, J., King, J., Courtney, A., Shu, W. Bioprinting of human pluripotent stem cells and their directed differentiation into hepatocyte-like cells for the generation of mini-livers in 3D. Biofabrication, v.7, n.4, p044102. 2015.

Ge, P. S. & Runyon, B. A. Treatment of Patients with Cirrhosis. N Engl J Med, v. 375, n.8, p767-77. 2016.

Goldman, O. & Gouon-Evans, V. Human Pluripotent Stem Cells: Myths and Future Realities for Liver Cell Therapy. Cell Stem Cell, v.18, n.6, p703-6. 2016.

Husson, A., Brasse-Lagnel, C., Fairand, A., Renouf, S., Lavoinne, A. Argininosuccinate synthetase from the urea cycle to the citrulline-NO cycle. Eur J Biochem, v.270, n.9, p1887-99. 2003.

Jazedje, T., Bueno, D., Almada, B., Caetano, H., Czeresnia, C., Perin, P., Halpern, S., Maluf, M., Evangelista, L., *et al*.. Human fallopian tube mesenchymal stromal cells enhance bone regeneration in a xenotransplanted model. Stem Cell Rev, v.8, n.2, p355-6. 2012.

Kim, H. M., Kim, J. W., Choi, Y., Chun, H. S., Im, I., Han, Y. M., Song, C. W., Yoon, S., Park, H. J. Xeno-sensing activity of the aryl hydrocarbon receptor in human pluripotent stem cell-derived hepatocyte-like cells. Sci Rep, v.6, p21684. 2016.

Kizawa, H., Nagao, E., Shimamura, M., Zhang, G., Torii, H. Scaffold-free 3D bio-printed human liver tissue stably maintains metabolic functions useful for drug discovery. Biochem Biophys Rep, v.10, p186-191. 2017.

Kuleshov, M., Jones, M., Rouillard, A., Fernandez, N., Duan, Q., Wang, Z., Koplev, S., *et al*.. Enrichr: a comprehensive gene set enrichment analysis web server 2016 update. Nucleic Acids Res, v.8, p90-7. 2016.

Lamouille, S., Xu, J., Derynck, R.. Molecular mechanisms of epithelial-mesenchymal transition. Nat Rev Mol Cell Biol. v.15, n.3, p178-96. 2014.

Levy, G., Bomze, D., Heinz, S., Ramachandran, S. D., Noerenberg, A., Cohen M., Shibolet, O., Sklan, E., Braspenning, J., Nahmias, Y. Long-term culture and

expansion of primary human hepatocytes. Nat Biotechnol, v.33, n.12, p1264-1271. 2015.

Li, Q., Hutchins, A. P., Chen, Y., Li, S., Shan, Y., Liao, B., Zheng, D., Shi, X., Li, Y., Chan, W. Y., *et al*. A sequential EMT-MET mechanism drives the differentiation of human embryonic stem cells towards hepatocytes. Nat Commun, v.3, n.8, p15166. 2017.

Lyu, C., Shen, J., Wang, R., Gu, H., Zhang, J., Xue, F., Liu, X., Liu, W., *et al*. Targeted genome engineering in human induced pluripotent stem cells from patie nts with hemophilia B using the CRISPR-Cas9 system. Stem Cell Res Ther, v.9, n.1, p92. 2018.

Ma, X., Qu, X., Wei, Z., Yi-Shuan, L., Suli, Y., Hong, Z., Justin, L., Pengrui W., *et al*., Deterministically patterned biomimetic human iPS-derived hepatic model via rapid 3D bioprinting. PNAS, v.113, n.8, p2206-2211. 2016.

Mi, H & Thomas, P. PANTHER pathway: an ontology-based pathway database coupled with data analysis tools. Methods Mol Biol, v.563, p123-40. 2009.

Miller, E., Kobayashi, G., Musso, C., Allen, M., Ishiy, F., de Caires, L., Goulart, E., Griesi-Oliveira, K., Zechi-Ceide, R., and Richieri-Costa, A. *et al*. EIF4A3 deficient human iPSCs and mouse models demonstrate neural crest defects that underlie Richieri-Costa-Pereira syndrome. Human Molecular Genetics, v.26, p2177-2191. 2017.

Okita, K., Yamakawa, T., Matsumura, Y., Sato, Y., Amano, N., Watanabe, A., Goshima, N., and Yamanaka, S. An Efficient Nonviral Method to Generate Integration-Free Human-Induced Pluripotent Stem Cells from Cord Blood and Peripheral Blood Cells. Stem Cells v.31, p458-466. 2013.

Palakkan, A. A., Hay, D. C., Anil, K. P. R., Kumary, T. V., Ross, J. A. Liver tissue engineering and cell sources: issues and challenges. Liver Int, v.33, n.5, p666-76. 2013.

Rashidi, H., Luu, N. T., Alwahsh, S. M., Ginai, M., Alhaque, S., Dong, H., Tomaz R. A., Vernay, B., *et al*. 3D human liver tissue from pluripotent stem cells displays stable phenotype in vitro and supports compromised liver function in vivo. Arch Toxicol, v.92, n.10, p3117-3129. 2018.

Ruiz de Galarreta, M. & Lujambio, A. J Hepatol. Therapeutic editing of hepatocyte genome in vivo, v.67, n.4, p818-828. 2017.

Sriram, G., Tan, J., Islam, I., Rufaihah, A., Cao, T. Efficient differentiation of human embryonic stem cells to arterial and venous endothelial cells under feeder- and serum-free conditions. Stem Cell Research & Therapy, v.6. p261. 2015.

Szklarczyk, D., Morris, J., Cook, H., Kuhn, M., Wyder, S., Simonovic, M., Santos A., Doncheva, N., Roth, A., *et al.* The STRING database in 2017: quality-

controlled protein-protein association networks, made broadly accessible. Nucleic Acids Res, v.4, D362-D368. 2017.

Tang, H. W., Hu, Y., Chen, C. L., Xia, B., Zirin, J., Yuan, M., Asara, J. M., Rabinow, L., Perrimon, N. The TORC1-Regulated CPA Complex Rewires an RNA Processing Network to Drive Autophagy and Metabolic Reprogramming. Cell Metab, v.27, n.5, p1040-1054. 2018.

Wang, Y., Alhaque, S., Cameron, K., Meseguer-Ripolles, J., Lucendo-Villarin, B., Rashidi, H., Hay, D.C. Defined and Scalable Generation of Hepatocyte-like Cells from Human Pluripotent Stem Cells. J Vis Exp, v.121. 2017.

Xue, Z. F., Wu, X. M., Liu, M.. Hepatic regeneration and the epithelial to mesenchymal transition. World J Gastroenterol, v.19, n.9, p1380-6. 2013.

Yap, K. K., Dingle, A. M., Palmer, J. A., Dhillon, R. S., Lokmic, Z., Penington A. J, Yeoh, G. C, Morrison, W.A, Mitchell, G. M. Enhanced liver progenitor cell survival and differentiation in vivo by spheroid implantation in a vascularized tissue engineering chamber. Biomaterials, v.34, n.16, p3992-4001. 2013.

Zeisberg, M., Yang, C., Martino, M., Duncan, M. B., Rieder, F., Tanjore, H., Kalluri, R.. Fibroblasts derive from hepatocytes in liver fibrosis via epithelial to mesenchymal transition. J Biol Chem, v.282, n.32, p23337-47. 2007.

Zhao, Y., Zhu, R., Sun, Y. Epithelial-mesenchymal transition in liver fibrosis Biomed Rep, v.4, n.3, p269–274. 2016.

6. Acknowledgment

We would like to thank the funding agencies FAPESP/CEPID, CAPES, INCT and CNPq. Ernesto Goulart is a FAPESP grantee (2015/14821-1). We thank the Nuclear Magnetic Resonance (NMR) Facility at Brazilian Biosciences National Laboratory (LNBio), for the use of the NMR spectrometer (600MHz, Varian Inova). We acknowledge the Mass Spectrometry Facility at Brazilian Biosciences National Laboratory (LNBio), CNPEM, Campinas, Brazil for their support on mass spectrometry analysis. We thank Valdemir Melechco Carvalho from Fleury Laboratory for the support on the proteomic experiments. The authors have no conflict of interest to disclaim. This work is dedicated to Raúl Marcel González Garcia, *in memoriam*.

Figure Captions

Figure 1 – iPS cell differentiation in 2D. A) Schematic representation of 2D cell differentiation protocols. B) Step-wise hepatocyte differentiation gene expression panel for *CK18*, *G6PC*, *ALB* and *UGT1A1*, normalized with iPS at day 0 of the differentiation protocol. C) Representative flow cytometry graph for ALB/UGT1A1 at day 18. D) Representative IF staining of iPS-derived hepatocytes for CYP3A4, A1AT, ALB and ECAD at day 18 of hepatocyte differentiation (bar = 200 μm). E) Representative ICG uptake assay image after 1h and 4h after incubation with dye (bar = 400 μm). F) RT-qPCR gene expression for *GSTA1* and *GSTA4,* normalized with iPS at day 0 of the differentiation protocol. G) CYP induction assay RT-qPCR for *CYP1A1* and *CYP3A4*, induced with Omeprazol and Rifampicin. Data was normalized with 2D cultured iPS-derived hepatocyte at day 18 of differentiation protocol. H) Representative flow

cytometry staining for CD31/VECAD. I) IF staining of iECs for CD31/VECAD and Von-Willebrand factor (bar = 200 µm). J) Matrigel angiogenesis assay after 48h (bar = 400 µm). K) Acetylated-LDL uptake assay (bar = 200 µm). L) Step-wise RT-qPCR gene expression analysis of iECs for *PECAM1*, *EFNB2* and *KDR,* normalized with iPS at day 0 of the differentiation protocol. M) Mean fluorescence intensity (MFI) analysis of iEC neutrophil activation assay. N) Representative flow cytometry graph of iNCC-MSC cells stained for CD90/CD73 and CD31/CD45. O) IF staining of NCC-MSC for CD105 and F-actin (bar = 10 µm). P) RT-qPCR gene expression alaysis for BGLAP, COL2A1 and LPL after 28 days of MSC differentiation towards osteoblast, chondroblast and adipoblast, respectively, normalized with MSC at day 0 of the differentiation protocol. Q) Representative images of stained and control wells using Allizarin Red, Alcian Blue and Oil Red after 28 days of MSC differentiation towards osteoblast, chondroblast and adipoblast, respectively (bar = 100 µm). (n= 3, biological replicates. * = $p<0.05$, ** = $p<0.01$, *** = $p < 0.001$, unpaired Student t-test). DE = Definitive endoderm, HB = Hepatoblast, HT = Hepatocyte, Om = Omeprazol and Rf = Rifampicin.

Figure 2 - iPS cell differentiation in 3D. A) Schematic representation of 3D hepatic differentiation of iPS. B) Phase contrast images of every step of 3D hepatic differentiation (bar = 400 µm). C) Step-wise RT-qPCR gene expression analysis for *OCT4*, *FOXA2*, *AFP*, *HNF4*, *ALB*, *UGT1A1* and *CK19,* normalized with iPS at day 0 of the differentiation protocol. D) Size distribution of 3D hepatic spheroids after 18 days of culture. E) HE and picrossirius staining of 3D hepatic spheroids at day 18. Arrow indicates basal lamina. (bar = 100 µm). F) IF staining for OCT4 and SSEA4 at day 0 (bar = 50 µm). G) IF staining for CXCR4 and FOXA2 at day 3 (bar = 20 µm). H) IF

staining for ECAD and AFP at day 9 (bar = 50 μm). I) IF staining for ALB and CYP3A4 at day 18 (bar = 50 μm). J) IF staining for A1AT and HNF4 at day 18 (bar = 20 μm). K) IF staining for CK18 and CK19 at day 18 (bar = 20 μm). EB = Embryonic bodies.

Figure 3 – Bioink formulation testing. A) Printability of different composition of bioink using alginate and pluronic F27. B) Shape stability of different composition of bioink over 120h in presence of 1mM of calcium. C) SEM representative images of Alginate and Alginate/Pluronic blend. D) Porosity analysis from SEM images. E) Schematic representation of bioprinting experiments and data collection. F) Representative images of 3D bioprinting process and donut-shape hepatic constructs. **(**n= 3, biological replicates. * = $p<0.05$, ** = $p<0.01$, *** = $p < 0.001$, unpaired Student t-test).

Figure 4 – Cell survival and liver function assessment. A) Representative image of confocal microscopy of LIVE and DEAD assay at day 18 (bar = 20 μm). B) Live and Dead analysis over time. C) LDH activity in culture supernatant overtime. D) Ki-67 staining analysis overtime. E) UREA concentration in culture supernatant overtime. F) AFP concentration in culture supernatant overtime. G) ALB concentration in culture supernatant overtime. H) A1AT concentration in culture supernatant overtime. I) RT-qPCR gene expression analysis at day 18 for *CYP3A4*, *GSTA1*, *NR1/2*, *CYP1A1*, *CYP1A2*, *ALB*, *TDO2*, *AHR*, *CK18* and *MRP1* (n = 3, normalized with 2D cultured iPS-derived hepatocyte at day 18 of differentiation protocol. biological replicates. * = $p<0.05$, ** = $p<0.01$, unpaired Student t-test).

Figure 5 –Metabolomics and Proteomics analysis. A) Principal component analysis of identified metabolites in culture supernatant at day 18. B) Pathway enrichment analysis of Student t-test significantly different ($p < 0.05$) metabolites between tested groups. C) Top 50 enriched pathways ordered top-bottom for lowest p value. D) Most significantly different metabolites identified. E) Venn's diagram of proteomics analysis of printed hepatic constructs (top) and principal component analysis (bottom). F) Differentially expressed proteins identified comparing single cells against spheroid groups (Student t-test, $p<0.05$). G) Interactome map related to differently expressed proteins, showed in F, and filtered by major cluster of proteins. In blue, mitochondrial proteins and in red proteins related to amino-acid or fatty acid catabolism. H) KEGG pathway enrichment analysis and major protein hits (top) and top 10 enriched pathways (bottom), related to differently expressed proteins showed in F. I) RT-qPCR gene expression analysis at day 18 for *CDH1*, *CDH2*, *CDH6*, *CDH7*, *CDH11*, *VIM*, *TWIST1*, *SNAIL1* and *SNAIL2*, normalized with 2D cultured iPS-derived hepatocyte at day 18 of differentiation protocol. n= 3, biological replicates. * = $p<0.05$, ** = $p <0.01$, unpaired Student t-test). n= 3, biological replicates. * = $p<0.05$, ** = $p <0.01$, *** = $p < 0.001$, unpaired Student t-test). SC = single cell, SP = spheroid.

Supplemental information

1. Supplementary Tables

Supplementary Table 1 – Antibodies used for IF staining

Antibody	Catalog number	Host Specie	Assay dilution
Anti-A1AT	ab9373	Rabbit	1/100
Anti-AFP	PA5 21-004	Rabbit	1/100
Anti-ALB	ab10241	Mouse	1/100
Anti-CD105	ab156756	Mouse	1/100
Anti-CD31	ab119339	Mouse	1/100
Anti-CK18	ab32118	Rabbit	1/100
Anti-CK19	ab7754	Mouse	1/100
Anti-CXCR4	ab124824	Rabbit	1/100
Anti-CYP3A4	ab197053	Rabbit	1/100
Anti-ECAD	ab1416	Mouse	1/100
Anti-FOXA2	ab60721	Mouse	1/100
Anti-HNF4	ab41898	Mouse	1/100
Anti-OCT3/4	ab19857	Rabbit	1/100
Anti-SSEA4	ab16287	Mouse	1/100
Anti-VECAD	ab33168	Rabbit	1/100
Anti-Vimentin	ab8978	Mouse	1/100
Anti-vW	ab6994	Rabbit	1/100
Donkey anti-Mouse Alexa 546	A10036	N/A	1/1000
Goat anti-Mouse Alexa 488	11001	N/A	1/1000
Goat anti-Rabbit Alexa 488	11034	N/A	1/1000
Goat anti-Rabbit Alexa 546	A11010	N/A	1/1000

Supplementary Table 2 - Antibodies used for flow-cytometry staining

Antibody	Catalog number	Host Specie	Dilution
Anti-ALB	ab106582	Chicken	1/100
Anti-CD31	566177	Mouse	1/100
Anti-CD31	ab9498	Mouse	1/100
Anti-CD45	560973	Mouse	1/100
Anti-CD73	560847	Mouse	1/100
Anti-CD90	555596	Mouse	1/100
Anti-ICAM1	ab2213	Mouse	1/100
Anti-UGT1A1	ab194697	Rabbit	1/100
Anti-VECAD	ab33168	Rabbit	1/100
Goat Anti-Chicken Alexa 488	A0001	Goat	1/1000
Goat Anti-Mouse Alexa 488	11001	Goat	1/1000
Goat Anti-Mouse Alexa 647	ab 150115	Goat	1/1000
Goat Anti-Rabbit Alexa 488	11034	Goat	1/1000
Goat Anti-Rabbit Alexa 647	ab150075	Goat	1/1000

Supplementary Table 3 – Primers sequences list

Gene	Foward	Reverse
AFP	TGCAGCCAAAGTGAAGAGGGAAGA	CATAGCGAGCAGCCCAAAGAAGAA
AHR	ACAACCGATGGACTTGGGTC	GCTCTGTTCCTTCCTCATCTGT
ALB	AATGTGCTGATGACAGGGCG	CGGCAATGCAGTGGGATTTT
BGLAP	CACTCCTCGCCCTATTGGC	CCCTCCTGCTTGGACACAAAG
CDH1	CCATTCAGTACAACGCCCAACCC	CACAGTCACACACGCTGACCTC
CDH11	AGAGGTCCAATGTGGGAACG	GGTTGTCCTTCGAGGATACTGT
CDH2	TGCGGTACAGTGTAACTGGG	GAAACCGGGCTATCTGCTCG
CDH6	AGCTGCAGTTTCAGCCGCGA	AGGGTATCTCTGCTCGCCTTCC
CDH7	TCAAATACATCTTGTCAGGCGAA	TGGCATGAATATCCCCAGTGT
CK18	ACATCCGGGCCCAATATGAC	GGTGCTCTCCTCAATCTGCT

CK19	ACCAAGTTTGAGACGGAACAG	CCCTCAGCGTACTGATTTCCT
CO2A1	TGGACGCCATGAAGGTTTTCT	TGGGAGCCAGATTGTCATCTC
CXCR4	CAAGGCCCTCAAGACCACAG	TGTAGTAAGGCAGCCAACAGG
CYP1A1	CCTTGGAACCTTCCCTGATCC	GATCTTGGAGGTGGCTGAGGT
CYP1A2	CTGGACTTCTTCCCCATCCTTC	GTTCTTGTCAAAGTCCTGATAGTGC
CYP3A4	ATGGAAAAGTGTGGGGCTT	TCATGTCAGGATCTGTGATAGC
FOXA2	TGCACTCGGCTTCCAGTATG	CATGTTGCTCACGGAGGAGT
G6PC	CTACTACAGCAACACTTCCGTG	GGTCGGCTTTATCTTTCCCTGA
GST1A2	TGGACAAAGACAAGAGGAACC	ATAGCTTGACCTTCGAGTGC
GSTA1	CTGCCCGTATGTCCACCTG	AGCTCCTCGACGTAGTAGAGA
GSTA4	TTGGTACAGACCCGAAGCATT	CAGGGTTCTCTCCTTGAGGTT
HNF4	TGGACAAAGACAAGAGGAACC	ATAGCTTGACCTTCGAGTGC
LPL	AAGGCACCTGCGGTATTTGT	GATTCGCCCAGTTTCAGCCT
MRPI	CTGGACTGATGACCCCATCG	GCGATCCCTTGTGAAATGCC
NR1/2	AGCCTGCTCATAGGTTCTTGT	ACCTGTGATGCCGAACAACT
OCT3/4	TCCCATGCATTCAAACTGAGG	CCAAAAACCCTGGCACAAACT
SNAIL1	TCGGAAGCCTAACTACAGCGA	AGATGAGCATTGGCAGCGAG
SNAIL2	TCTGCGGCAAGGCGTTTTCCAG	GCAAATGCTCTGTTGCAGTGAGGG
TDO2	AGAGCTGGCCTACCTGAAGA	GCCCCTCAGCGTACTGATTT
TWIST1	CAATGACATCTAGGTCTCCGGGCCC	TACGCCTTCTCGGTCTGGAGGATG
UGT1A1	TGCAACCCTTGCCTCAGAAT	ATTCCTGGGATAGTGGATTTTGGT
VIM	GACAACCTGGCCGAGGACATCATG	AGACGTGCCAGAGACGCATTGTC

2. Supplementary Methods

2.1. iPS cell line generation and culture

The reprogramming protocol was performed with episomal vectors system (pCXLE-hOCT3/4-shP53-F, addgene plasmid 27077; pCXLE-hSK, addgene plasmid 27078; pCXLE-hUL, addgene plasmid 27080; gift from Shinya Yamanaka), according

to Okita *et al*. (Okita *et al*., 2013), and using the Amaxa human CD34+ cells Nucleofection kit (Lonza), following the manufacturer's instructions.

$CD71^{+}$-cells, which were isolated from donors' peripheral blood mononuclear cells or dermal fibroblast were nucleofected. After 3 days of nucleoporation, the cells were seeded on irradiated murine embryonic fibroblasts (Millipore – A24903) with embryonic stem cell medium (DMEM/F12 supplemented with 2mM GlutaMAX-I, 0.1 mM non-essential amino acids, 100 μM 2-mercaptoethanol, 20% of knockout serum replacement all provided by Life Technologies) and supplemented with 10 ng/mL of bFGF (Peprotech), 0.25 mM NaB, 0.5 mM VPA, 2 uM thiazovivin, 0.5 μM PD 0325901 and 2 μM SB 431542 (all provided by Tocris Bioscience). Typical iPS colonies were manually collected and seeded to hESC-qualified matrigel (Corning) - coated 60mm petri dishes (Corning) and cultured in Essential 8 medium (Gibco) supplemented with 100 μg/mL normocin (InvivoGen). All derived cell lines were checked for mycoplasma contamination periodically. In all procedures involving single-cell passaging, media were supplemented for 24h after passaging with 5 μM Rock inhibitor (Sigma-Aldrich).

DNA was extracted from iPS cell lines cultures with the use of NucleoSpin Tissue (Macherey-Nagel), following supplier's instructions. Multiplex ligation-dependent probe amplification (MLPA) was performed with subtelomeric kits (P036 and P070; MRC-Holland) to detect chromosomal abnormalities, as previously described (Caires-Júnior, *et al*. 2017). Teratoma formation was performing by injecting $3x10^{6}$ cells/300 μL of GFR hESC qualified matrigel (Corning) intramuscular in NOD-SCID mices and followed for up to 6 weeks.

2.2. iPS-derived cells characterization

2.2.1 Immunofluorescence (IF) staining

For IF staining, cell cultures were fixed with 4% PFA for 20 minutes followed by permeabilization with 0.01% Triton X-100 for 30 minutes and blockage using 5% BSA in PBS for 1h. After that, the cells were incubated overnight with primary antibodies at 4°C and subsequently incubated with secondary antibodies (see Supplementary Table 1) for 1h at room temperature. The final step was DAPI (Sigma) staining for 5 min at room temperature. Images were acquired using Carl Zeiss LSM 800, confocal microscope.

2.2.2. Flow cytometry

To evaluate culture uniformity cells were stained and analyzed by flow cytometry analysis. Fixation and permeabilization were performed using a Fix & Perm Kit (Invitrogen) according to the manufacturer's instructions. Cells were stained with conjugated primary antibody (see Supplementary Table 2) for 45 min in an ice bath, washed with 1× PBS, and then analyzed by Guava Flow cytometer (Merck). The experiment was performed collecting at least 10,000 events per group. After data acquisition, further analysis was performed using FlowJo software. Gate was set using isotype control.

2.2.3. Histological staining

For histological processing, the samples were fixed in 4% PFA for 1h at room temperature. Tissues were de-hydrated using ethanol/xylene gradient and embedded I

paraffin. Tissue section of 5µm were obtained and standard eosin/hematoxylin and picrossirius red staining was performed.

2.2.4. RT-qPCR

For RT-PCR , total RNA was isolated from cell cultures using the RNeasy Mini Kit (Qiagen), following the manufacturer's recommendations. Briefly, 1 µg of total RNA was converted into cDNA using Superscript II (Life Technologies) and oligo-dT primers according to the manufacturer's specifications. RT-qPCR reactions were performed with Power SYBR Green Master Mix (Life Technologies). Fluorescence was detected using the Applied Biosystem 7500 Real-Time PCR System, under standard temperature protocol. Primer pairs were either designed with PrimerBLAST (http://www.ncbi.nlm.nih.gov/tools/primer-blast/) or retrieved from PrimerBank (http://pga.mgh.harvard.edu/ primerbank/). Primers sequences are listed in Supplementary Table 3. Quantitative analyses were performed using a relative quantification curve with positive control and GAPDH as endogenous control.

2.2.5. ELISA

For ELISA, the cultures' supernatant were collected every other day and store at -80°C. The samples were thawed and centrifuged at 300g for 10 min to remove cellular debris. ELISA was performed according to manufacturer's instructions.

2.2.6. ICG uptake and release

Indocyanine green (ICG) (Sigma) was dissolved in DMSO at 100 mg/ml. ICG was added to culture media to a final concentration of 1 mg/ml and incubated for 1h min at 37°C. After brief washing with PBS, the cellular uptake of ICG was examined under a light microscope. Cells' culture media was replaced and incubated for 6h and the release of cellular ICG was examined.

2.2.7. CYP induction assay

Hepatocytes at day 18 of differentiation protocol were cultured for 48 hours with either 50 μM of Omeprazol, 25 μM of Rifampicin or a corresponding volume of DMSO. Cells were removed from the plate and centrifuged at 300g for 5 min. Cell pellets were rapidly frozen in liquid nitrogen. RT-qPCR was performed according to section 2.3.3.

2.2.8. Angiogenesis assay

Matrigel (Corning) was diluted with EGM-2 (Lonza) 1:1 on ice and before coating in a 24 well plate, 380 ul of diluted Matrigel were added to each well and incubated for 30 min at 37°C. Endothelial cells were plated at $5x10^5$ cells/well and cultured for 48h with EGM-2. The formation of a branched capillary bed was evaluated under phase contrast microscope.

2.2.9. Ac-LDL uptake

Alexa 488-labeled acetylated-LDL (Ac-LDL) (Thermo) was added to a final concentration of 10 μg/mL to the cell media and incubated for 2h in 37°C. Plates were washed twice with DPBS and cell media was refilled. Cellular uptake was evaluated in a fluorescence microscope (Nikon).

2.2.10. Neutrophil activation assay

Endothelial cells were cultured until they were 80% confluent. TNF-α (R&D) was added to cell media in a final concentration of 10ng/mL and incubated for 24h at 37°C. Control group received the same volume of PBS+0.1% BSA. Cells were detached from plate and incubated with anti-ICAM-1 for flow cytometry analysis, see section 2.3.2.

2.2.11. nMSC differentiation assay

For induction of mesenchymal differentiation, $2.5x10^5$ nMSC per well were plated on 12 well plates (Corning). After 24h, the cell media was replaced with supplemented Stempro Osteogenesis Differentiation Media (Thermo), Stempro Chondrogenesis Differentiation Media or Stempro Adipogenesis Differentiation Media. Cells were cultured for 21 days, with media changes every other day. Cells were fixed in 4% PFA for 30 minutes and stained accordingly to establish protocols (Miller *et al.*, 2017). Osteogenic differentiation was shown by formation of calcium-hydroxyapatite-positive areas (Alizarin Red staining). Chondrogenic differentiation was assessed with Alcian Blue blue staining to demonstrate extracellular matrix glycosaminoglycans. Adipogenic differentiation was confirmed by intracellular accumulation of lipid-rich

vacuoles stainable with oil red O (Sigma). Cells were stained with 0.16% oil red O for 20 minutes.

2.3. Proteomics

Briefly, for protein extraction and digestion, samples were treated with 8M urea, followed by protein reduction with dithiothreitol (5mM for 25 min at 56 °C) and alkylation with iodoacetamide (14mM for 30 min at room temperature). Urea was diluted to a final concentration of 1.6M with 50mM ammonium bicarbonate, and 1mM of calcium chloride was added to the samples for trypsin digestion for 16h at 37°C (2 µg of trypsin). The reaction was stopped with 0.4% formic acid, and peptides were desalted with C18 stage tips, dried in a vacuum concentrator, reconstituted in 0.1% formic acid and stored at −20 °C for subsequent analysis by LC-MS/MS.

The peptide mixture (total volume of 4.5 µL) was analyzed using an LTQ Orbitrap Velos (Thermo Fisher Scientific) mass spectrometer coupled to nanoflow liquid chromatography on an EASY-nLC system (Proxeon Biosystems) with a Proxeon nanoelectrospray ion source. Peptides were subsequently separated in a 2–90% acetonitrile gradient in 0.1% formic acid using a PicoFrit analytical column (20 cm × ID75, 5 µm particle size, New Objective) at a flow rate of 300 nL/min over 212 min, in which a gradient of 35% acetonitrile is reached in 175 min. The nanoelectrospray voltage was set to 2.2 kV, and the source temperature was set to 275 °C. The instrument methods employed for LTQ Orbitrap Velos were set up in DDA mode. Full scan MS spectra (m/z 300–1600) were acquired in the Orbitrap analyzer after accumulation to a target value of 1e6. Resolution in the Orbitrap was set to r = 60,000, and the 20 most intense peptide ions (top 20) with charge states ≥2 were sequentially isolated to a target

value of 5000 and fragmented in the high-pressure linear ion trap by CID (collision induced dissociation) with a normalized collision energy of 35%. Dynamic exclusion was enabled with an exclusion size list of 500 peptides, a exclusion duration of 60 s and a repetition count of 1. An activation Q of 0.25 and an activation time of 10 ms were used.

Twelve LC-MS/MS runs were performed. Raw data were processed using MaxQuant v1.3.0.3 software, and MS/MS spectra were searched against The Human UniProt database (released January 7, 2015, 89,649 sequences, and 35,609,686 residues) using the Andromeda search engine. As search parameters, a tolerance of 6 ppm was considered for precursor ions (MS search) and 0.5 Da for fragment ions (MS/MS search), with a maximum of two missed cleavages. A maximum of a 1% false discovery rate (FDR) was set for both the protein and peptide identification. Protein quantification was performed using the LFQ algorithm implemented in MaxQuant software, with a minimal ratio count of 2 and a window of 2 min for matching between runs. Statistical analysis was performed with Perseus v1.2.7.4 software, which is available in the MaxQuant package. Identified protein entries were processed, excluding reverse sequences and those identified “only by site” entries. Contaminants were not removed from the dataset because serum albumin is of interest in the study of LO. Protein abundance, which was calculated based on the normalized spectrum intensity (LFQ intensity), was log2-transformed, and the dataset was filtered by minimum valid values in at least one group. Missing values for the LFQ intensity were not imputed as random numbers, the mean and standard deviation of which were selected to best simulate low abundance values close to the noise level (imputation width = 0.3, shift = 1.8).

Significance was assessed by comparing all conditions and samples using ANOVA and Student's t test to identify differentially expressed proteins between specific groups (P value < 0.05). Exclusive and common proteins from each comparison are presented as a Venn diagram generated using the InteractiVenn tool. For data visualization, heat maps with z-score values of log2 LFQ intensities.

2.4 Scanning electron microscopy

After printing of tested materials, 3D constructs were fixed in 2.5% glutaraldehyde solution for 24 hours The material was incorporated with osmium tetroxide 1% for 1h. Next, tested materials were dehydrated using an alcohol gradient. After dehydration the 3D constructs were dryed using critical point dryer apparatus (Polaron Range CPD7591). The 3D constructs were placed in a post and coated with gold using gold plasma coater in an argonium atmosphere for 3 minutes with a 10-15cm distance between the support and the golden plate. Images were acquired using a Sigma VP, Carl Zeiss ®. Porosity of evaluated using ImageJ software.

2.5 Cell survival and functional analysis

Bioprinted constructs were checked for cell viability using LIVE/DEAD staining (Thermo) following manufacturer's instructions. Cells were incubated for 30 min at 37°C and washed once with DPBS. Image acquisition was made using Zeiss LSM 800. For LDH assay , the cultures supernatant was collected every other day. LDH assay (Thermo) was performed according to manufacturer's instructions.

3. Supplementary Figures Caption

Supplemental Figure 1 – Human iPS cell lines characterization. A) Representative phase contrast images of iPS cell lines. (bar = 400 μm). B) MLPA analysis of iPS cell lines. C) Representative images of HE staining of teratomas generated by iPS injection in nude mices after 6 weeks, indicating endodermal, mesodermal and ectodermal differentiation (bar = 100 μm).

Supplementary References

Caires-Júnior, L., Goulart, E., Melo, U., Araujo, B., Alvizi, L., Soares-Schanoski, A., de Oliveira, D., Kobayashi, G., Griesi-Oliveira, K., and Musso, C. *et al*.. Discordant congenital Zika syndrome twins show differential in vitro viral susceptibility of neural progenitor cells. Nature Communications, v.9, n.1, p475. 2018.

Miller, E., Kobayashi, G., Musso, C., Allen, M., Ishiy, F., de Caires, L., Goulart, E., Griesi-Oliveira, K., Zechi-Ceide, R., and Richieri-Costa, A. *et al*. EIF4A3 deficient human iPSCs and mouse models demonstrate neural crest defects that underlie Richieri-Costa-Pereira syndrome. Human Molecular Genetics, v.26, p2177-2191. 2017.

Figure 1

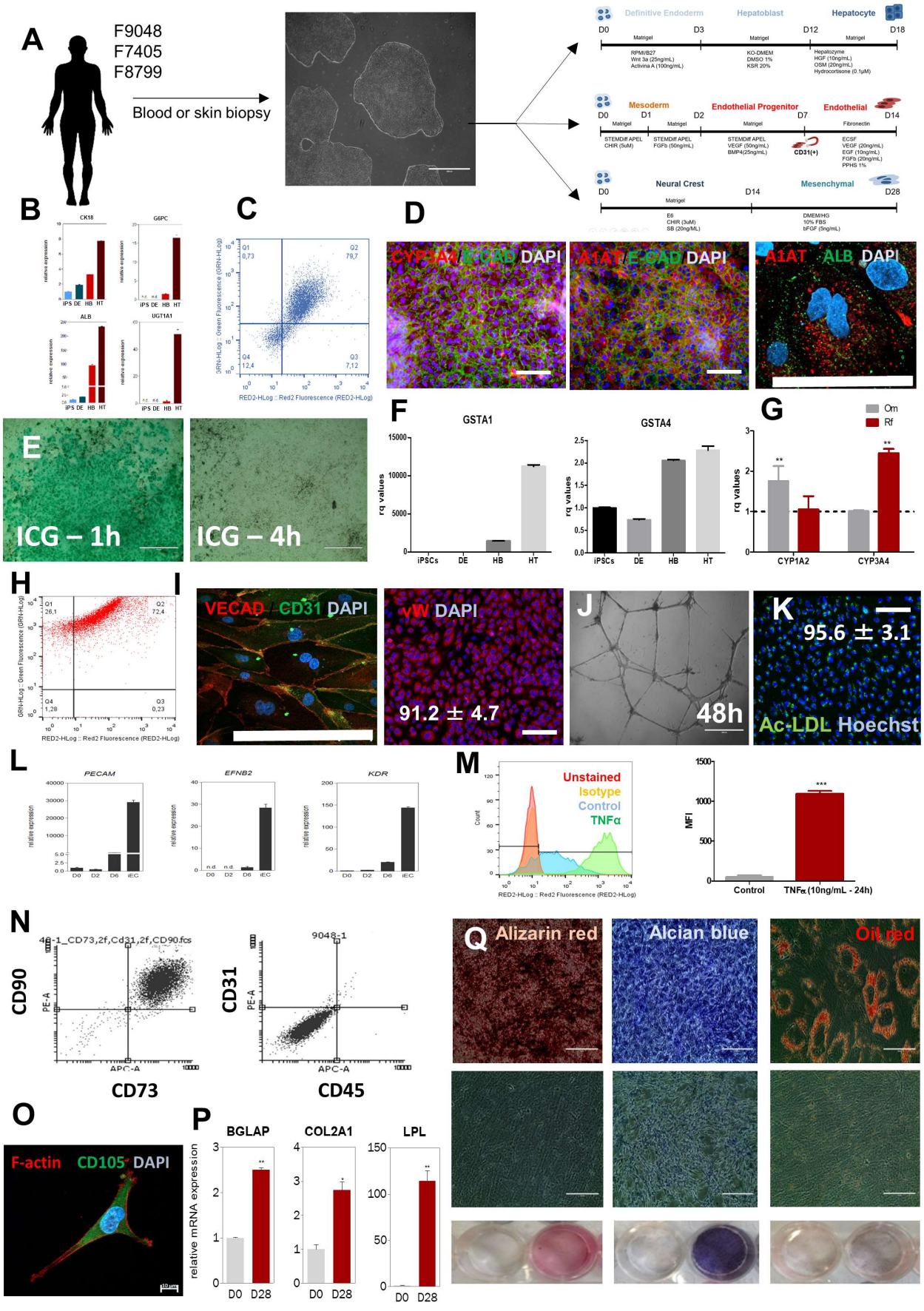
A
F9048
F7405
F8799
Blood or skin biopsy
Definitive Endoderm
Hepatoblast
Hepatocyte
D0
D3
D12
D18
Matrigel
RPMI/B27
Wnt 3a (25ng/mL)
Activina A (100ng/mL)
KO-DMEM
DMSO 1%
KSR 20%
Hepatozyme
HGF (10ng/mL)
OSM (20ng/mL)
Hydrocortisone (0.1µM)
Mesoderm
Endothelial Progenitor
Endothelial
D0
D1
D2
D7
D14
STEMDiff APEL
CHIR (5uM)
FGFb (50ng/mL)
VEGF (50ng/mL)
BMP4(25ng/mL)
CD31(+)
ECSF
VEGF (20ng/mL)
EGF (10ng/mL)
FGFb (20ng/mL)
PPHS 1%
Fibronectin
Neural Crest
Mesenchymal
D28
E6
CHIR (3uM)
SB (20ng/mL)
DMEM/HG
10% FBS
bFGF (5ng/mL)
B
CK18
G6PC
ALB
UGT1A1
iPS DE HB HT
C
Q1 0,73
Q2 79,7
Q4 12,4
Q3 7,12
RED2-HLog :: Red2 Fluorescence (RED2-HLog)
D
CYP3A4 E-CAD DAPI
A1AT E-CAD DAPI
A1AT ALB DAPI
E
ICG – 1h
ICG – 4h
F
GSTA1
GSTA4
rq values
iPSCs DE HB HT
G
Om
Rf
CYP1A2
CYP3A4
H
Q1 26,1
Q2 72,4
Q4 1,28
Q3 0,23
I
VECAD CD31 DAPI
vW DAPI
91.2 ± 4.7
J
48h
K
95.6 ± 3.1
Ac-LDL Hoechst
L
PECAM
EFNB2
KDR
relative expression
D0 D2 D6 iEC
M
Unstained
Isotype
Control
TNFα
Count
MFI
Control
TNFα (10ng/mL - 24h)
N
46-1_CD73,2f,Cd31,2f,CD90.fcs
9048-1
CD90
CD31
PE-A
APC-A
CD73
CD45
O
F-actin CD105 DAPI
P
BGLAP
COL2A1
LPL
relative mRNA expression
D0 D28
Q
Alizarin red
Alcian blue
Oil red

Figure 2

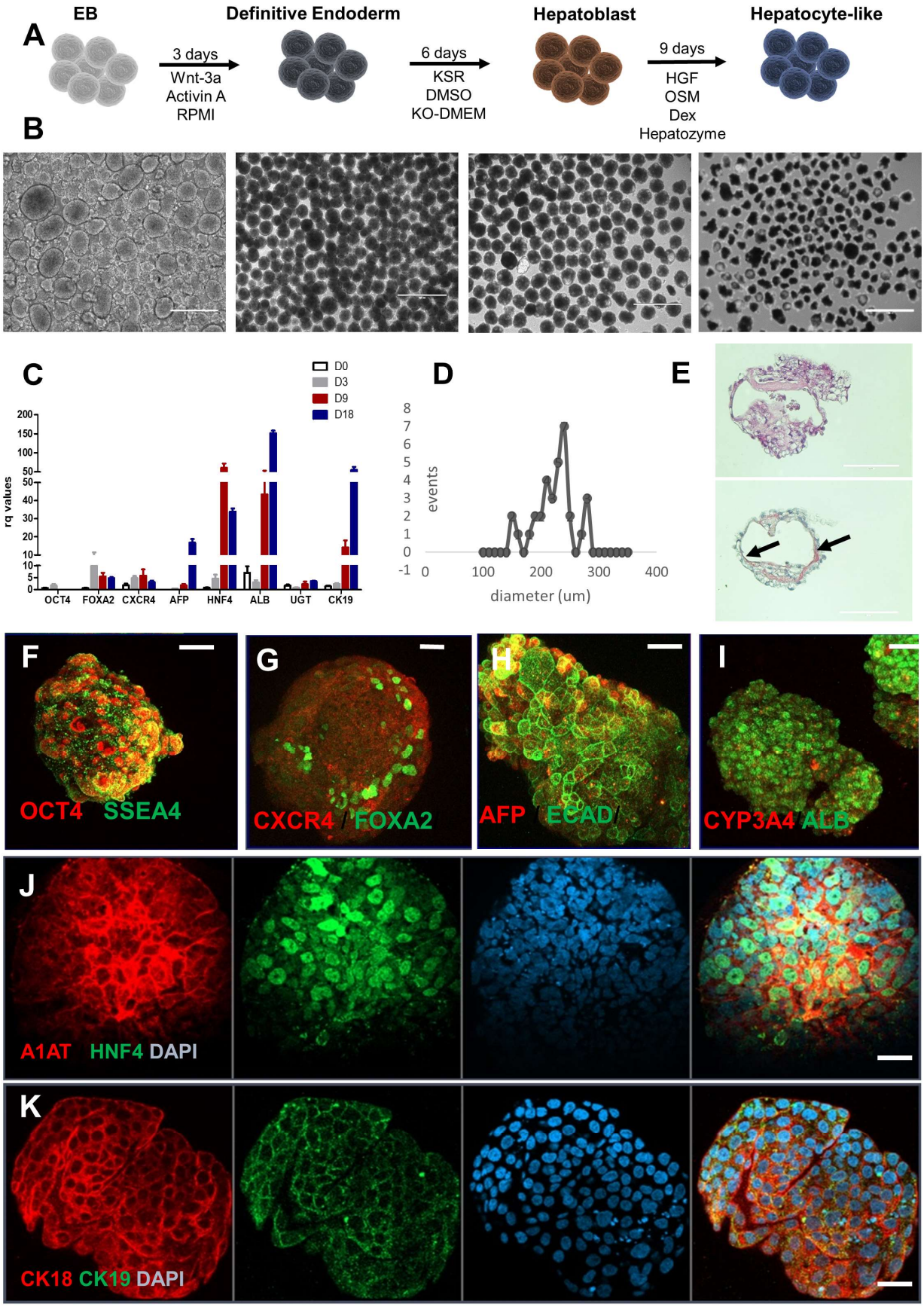
A
EB
3 days
Wnt-3a
Activin A
RPMI
Definitive Endoderm
6 days
KSR
DMSO
KO-DMEM
Hepatoblast
9 days
HGF
OSM
Dex
Hepatozyme
Hepatocyte-like
B
C
D0
D3
D9
D18
rq values
OCT4
FOXA2
CXCR4
AFP
HNF4
ALB
UGT
CK19
D
events
diameter (um)
E
F
OCT4 SSEA4
G
CXCR4 / FOXA2
H
AFP / ECAD
I
CYP3A4 / ALB
J
A1AT HNF4 DAPI
K
CK18 CK19 DAPI

Figure 3

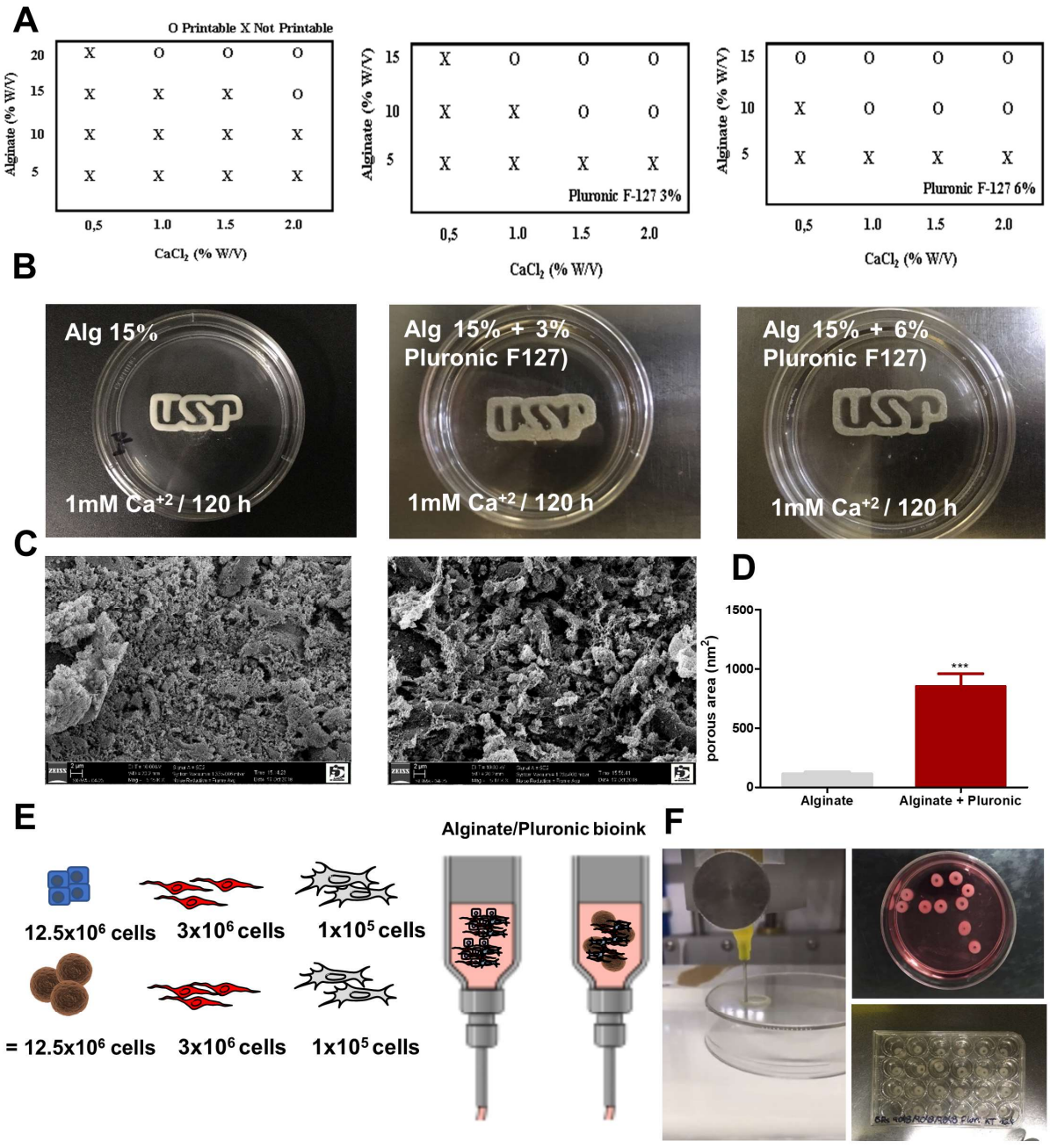
A
O Printable X Not Printable
Alginate (% W/V)
CaCl2 (% W/V)
Pluronic F-127 3%
Pluronic F-127 6%
B
Alg 15%
1mM Ca+2 / 120 h
Alg 15% + 3% Pluronic F127)
Alg 15% + 6% Pluronic F127)
C
D
porous area (nm2)
***
Alginate
Alginate + Pluronic
E
12.5x10⁶ cells
3x10⁶ cells
1x10⁵ cells
= 12.5x10⁶ cells
Alginate/Pluronic bioink
F

Figure 4

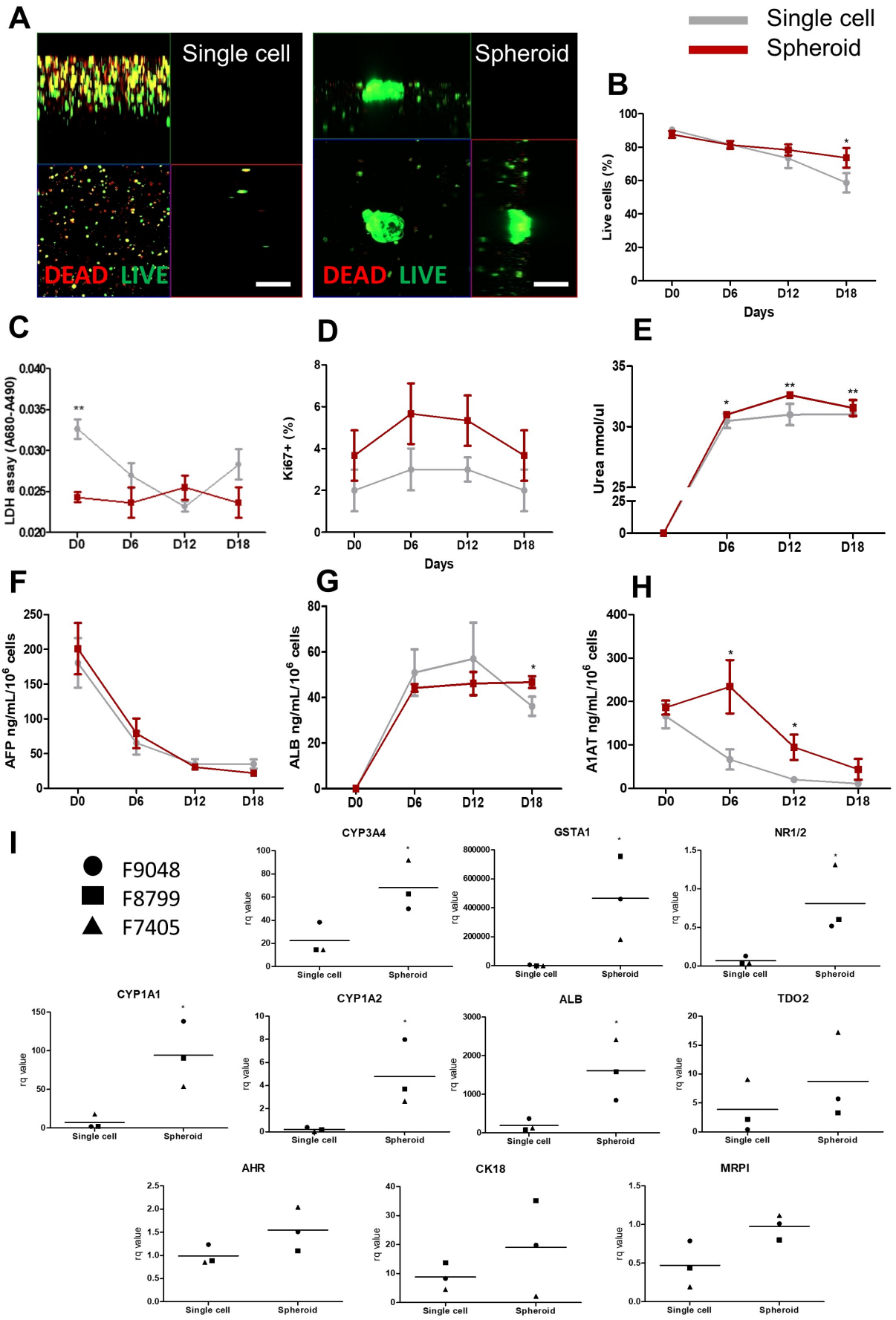
A
Single cell
Spheroid
DEAD LIVE
DEAD LIVE
Single cell
Spheroid
B
Live cells (%)
Days
D0 D6 D12 D18
C
LDH assay (A680-A490)
D
Ki67+ (%)
Days
E
Urea nmol/ul
F
AFP ng/mL/10^6 cells
G
ALB ng/mL/10^6 cells
H
A1AT ng/mL/10^6 cells
I
F9048
F8799
F7405
CYP3A4
GSTA1
NR1/2
CYP1A1
CYP1A2
ALB
TDO2
AHR
CK18
MRPI
rq value
Single cell
Spheroid

Figure 5

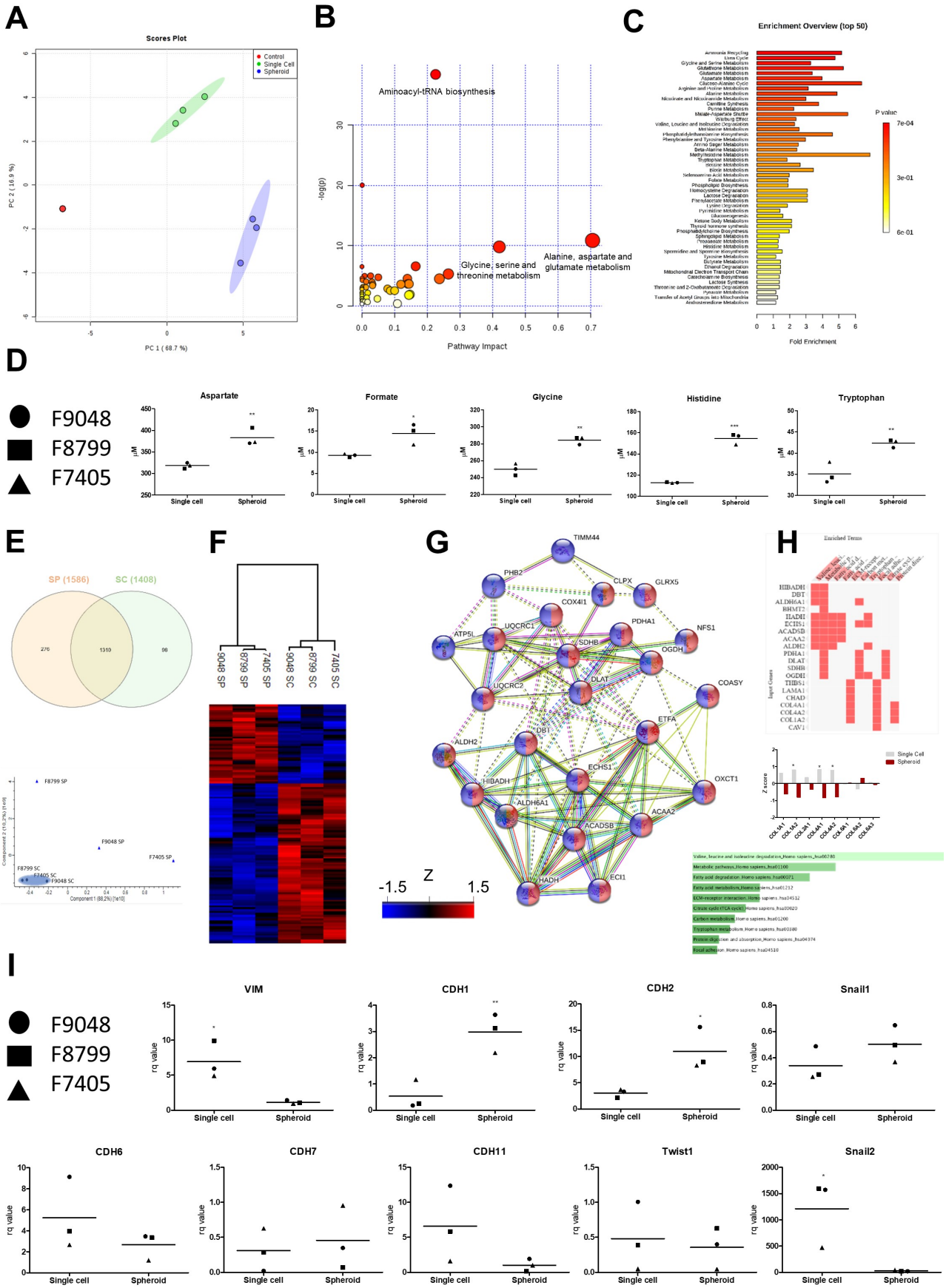
A
Scores Plot
Control
Single Cell
Spheroid
PC 1 (68.7 %)
PC 2 (16.9 %)
B
Aminoacyl-tRNA biosynthesis
Glycine, serine and threonine metabolism
Alanine, aspartate and glutamate metabolism
-log(p)
Pathway Impact
C
Enrichment Overview (top 50)
P value
7e-04
3e-01
6e-01
Fold Enrichment
D
F9048
F8799
F7405
Aspartate
Formate
Glycine
Histidine
Tryptophan
µM
Single cell
Spheroid
E
SP (1586)
SC (1408)
276
1310
98
F8799 SP
F9048 SP
F7405 SP
F8799 SC
F7405 SC
F9048 SC
F
9048 SP
8799 SP
7405 SP
9048 SC
8799 SC
7405 SC
G
TIMM44
PHB2
CLPX
GLRX5
COX4I1
ATP5L
UQCRC1
PDHA1
NFS1
SDHB
OGDH
DLAT
UQCRC2
COASY
ETFA
DBT
ALDH2
ECHS1
OXCT1
HIBADH
ALDH6A1
ACAA2
ACADSB
HADH
ECI1
Z
-1.5
1.5
H
Enriched Terms
Input Genes
HIBADH
DBT
ALDH6A1
BHMT2
ILADH
ECHS1
ACADSB
ACAA2
ALDH2
PDHA1
DLAT
SDHB
OGDH
THBS1
LAMA1
CHAD
COL4A1
COL4A2
COL1A2
CAV1
Z score
Single Cell
Spheroid
COL1A1
COL1A2
COL2A1
COL4A1
COL4A2
COL5A1
COL6A2
COL6A3
I
F9048
F8799
F7405
VIM
CDH1
CDH2
Snail1
CDH6
CDH7
CDH11
Twist1
Snail2
rq value
Single cell
Spheroid

Supplementary Figure 1

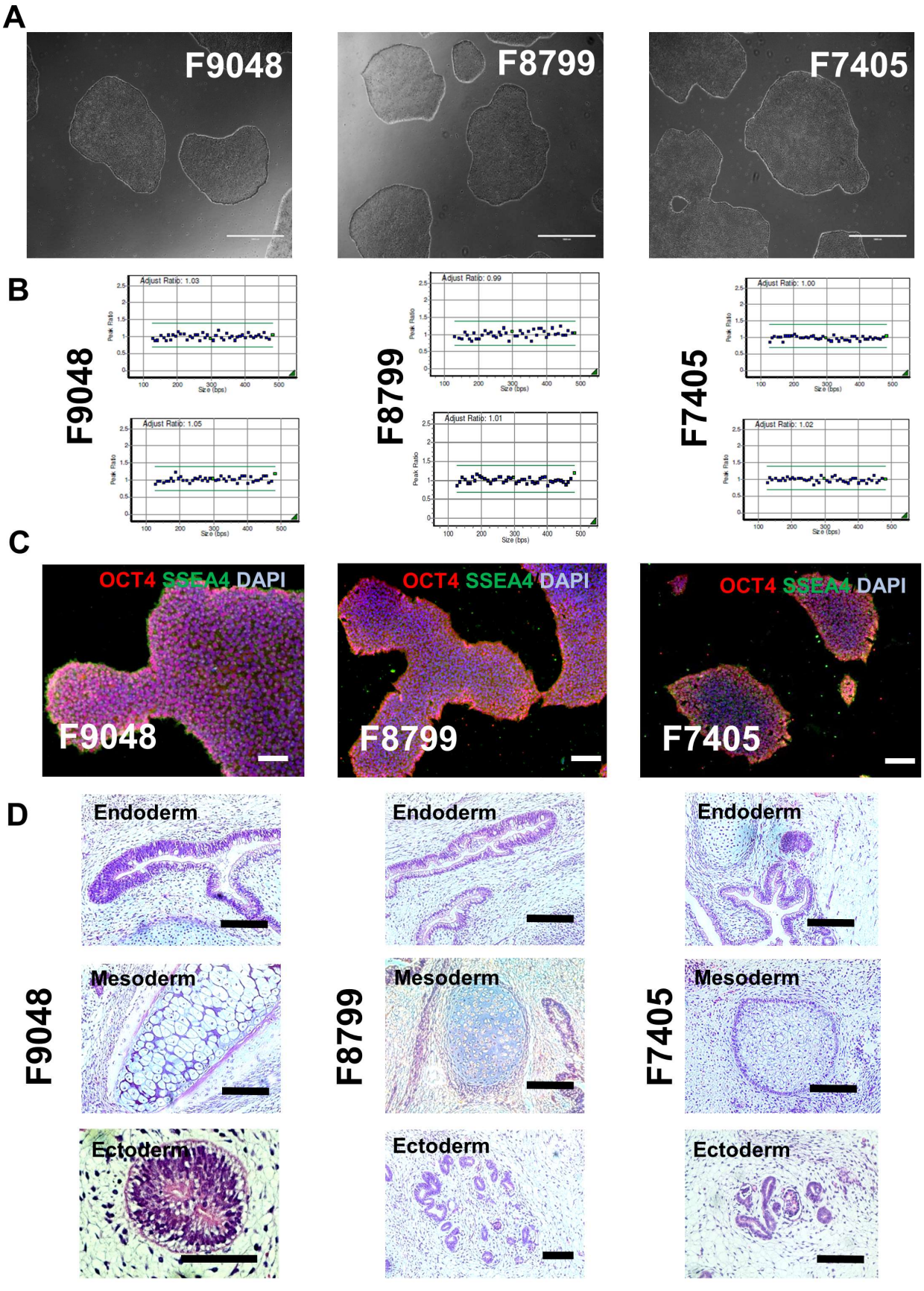

Capítulo 3:

Adult and iPS-derived non-parenchymal cells regulate liver organoid development through differential modulation of Wnt and TGF-β.

Capítulo 3: Artigo submetido – Organóides hepáticos

Submetido para a Revista: *Stem Cell Reports*

Adult and iPS-derived non-parenchymal cells regulate liver organoid development through differential modulation of Wnt and TGF-β

Authors: Ernesto Goulart[1], Luiz Carlos de Caires-Junior[1], Kayque Teles Alves-Silva[1], Bruno Henrique Silva Araujo[2], Gerson S. Kobayashi[1], Camila Manso Musso[1], Amanda Faria Assoni[1], Danyllo Oliveira[1], Elia Caldini[3], Jonathan A. Gerstenhaber[4], Maria Rita Passos-Bueno[1], Silvano Raia[5], Peter I. Lelkes[4], Mayana Zatz[1]*.

Affiliations:

[1]Centro de Estudos do Genoma Humano e Células Tronco, Departamento de Genética e Biologia Evolutiva, Instituto de Biociências, Universidade de São Paulo (USP), São Paulo, SP, Brazil.

[2]Brazilian Biosciences National Laboratory (LNBio), Brazilian Center for Research in Energy and Materials (CNPEM), Zip Code 13083-970, Campinas, São Paulo, Brazil.

[3]Laboratório de Biologia Celular, Departamento de Patologia, Faculdade de Medicina, Universidade de São Paulo – (USP), São Paulo, SP, Brazil.

[4]Department of Bioengineering, Temple University, Philadelphia, PA, United States

[5]Unidade do Fígado, Departamento de Cirurgia, Faculdade de Medicina, Universidade de São Paulo – (USP), São Paulo, SP, Brazil

***Corresponding author:** mayazatz@usp.br

Summary

Liver organoids (LO) technology holds great promises to be used in large-scale population-based drug screening and in future regenerative medicine strategies. Recently, some studies reported robust protocols for generating isogenic LO using liver parenchymal and non-parenchymal cells derived from induced pluripotent stem cells (iPS). However, using whole-iPS derived cells could impose great challenges for a translational perspective. Thus, here we evaluated the influence of isogenic versus heterogenic non-parenchymal cells (NPC) in the LO development. Here we show that using primary mesenchymal stromal cells (MSC) and iPS-derived endothelial cells (EC) LO produce significantly more albumin while have reduced TGF-β and Wnt signaling. Proteomics analysis revealed that major shifts in protein expression induced by the combination of non-parenchymal cells are related to integrin profile and TGF-β/Wnt signaling activity. Together this work enhances the current technology towards LO developmental and elucidates the role of important pathways aiming to push LO technology bench-to-bedside.

Keywords: Organoid, Liver, iPS, Hepatocyte, 3D culture.

Resumo

A tecnologia de organóides hepáticos (OH) é uma grande promessa de alternativa a ser usada em testes de drogas em larga escala, utilizando amostras representativas populacionais e em futuras estratégias de medicina regenerativa. Recentemente, alguns estudos demonstraram protocolos robustos para geração de OH isogênicos utilizando células parenquimatosas e não-parenquimatosas do fígado, derivadas de células-tronco

pluripotentes induzidas (iPS). No entanto, o uso de células derivadas de iPS, como um todo, pode impor grandes desafios para uma perspectiva translacional. Assim, este trabalho avaliou a influência da utilização de células não parenquimatosas isogênicas versus heterogênicas no desenvolvimento OH. Usando células tronco mensenquimais primárias (MSC), os OH produzem significativamente mais albumina. OH formados por células endoteliais derivadas de iPS e MSC primárias mostraram reduzida ativação da via TGF-β e Wnt. A análise proteômica revelou que grande parte das mudanças no perfil de expressão de proteínas, induzidas pela combinação de células não parenquimatosas testadas, estão relacionadas ao perfil de integrinas e à atividade de sinalização de TGF-β/Wnt. Assim, esse trabalho esclarece pontos críticos do desenvolvimento de OH e elucida aspectos importantes visando impulsionar o desenvolvimento da tecnologia de OH.

Palavras-chave: Organóides, Fígado, iPS, Hepatócitos, Cultura 3D.

Highlights:

- 1 - Primary adult MSC and iPS-derived EC improve LO maturation.
- 2 – Reduced TGF-beta signaling activity is a hallmark of more mature LO.
- 3 - Proteomics revealed major shifts induced by NPC, mostly related to integrin profile.

eTOC blurb: Goulart E. *et al*. show how different compositions of non-parenchymal cell sources can alters liver organoid development and final outcome. Adult primary cells or iPS-derived cells can modulate important developmental pathways that regulates liver organoid maturation.

1. Introduction

Liver organogenesis can be in part recapitulated by using organoid technology (Takebe *et al*., 2013). The combination of defined ratio of parenchymal progenitor cells (i.e., hepatoblast) and non-parenchymal cells (NPC) (i.e., endothelial cells and mesenchymal cells) recreates a cellular microenvironment akin to the early stages of liver bud development and allows for spontaneous tissue formation (Camp *et al*., 2017). The first attempts to bioengineer complex liver organoids (LOs) used hepatoblasts derived from human pluripotent stem cells (iPS) in conjunction with primary human NPC, such as human umbilical cord-derived endothelial cells (HUVEC) and adipose tissue-derived mesenchymal stem cells (MSCs), all derived from different donors (Takebe *et al*., 2013).

NPC contribute to liver development and homeostasis by secreting growth factors (e.g. TNF-α, IL-6, HGF, TGF-β and BMP2, 4, and 6, etc) that regulate hepatocyte proliferation, DNA synthesis, and hepatic cord formation (Gordillo *et al*., 2015; Shin and Monga, 2013; Loh *et al*., 2014). Asai and collaborators (Asai *et al*., 2017) showed the distinct contributions of primary lineages of endothelial cells (ECs) and MSCs secretome in LO development in vitro. More recently, some other groups reported a series of combined protocols for generating isogenic LOs obtained from whole iPS-derived cells, obtained from the same donor, or by using primary NPCs from the same donor (Takebe *et al*., 2017; Koui *et al*., 2017; Nie *et al*., 2018). Takebe and collaborators (Takebe *et al*., 2017) successfully generated LOs from human donors that could potentially be applied for high throughput personalized screening of liver toxicity.

However, large-scale differentiation of iPS into multiple cell lineages is challenging in terms of cost and efficiency as opposed to primary cell lineages. As a caveat, the use of standard commercial non-parenchymal cell lines will yield human LOs that are chimeric in nature. Here we propose to evaluate the effects of applying liver NPCs derived from iPS-derived fetal-like cells versus adult primary NPC cell lines to LO development and functionality.

2. Experimental Procedures

2.1. iPS cell line generation and culture and primary adult cell culture

Induced pluripotent stem cells (iPSs) were generated from three healthy human donors (F9048 = Male, 26; F8799 = Female, 28; F7405 = Male, 23), as previously described (Miller *et al*., 2017). The reprogramming and cell culture protocol are described in Supplementary Methods. Differentiation protocols and human primary adult cell culture methods are described in supplementary methods.

2.2. Liver organoid

Prior to cell seeding, Matrigel was diluted 1:1 on ice with cold EGM-2 and dispensed at 380 µl/well in a 24 well plate. Gelling was achieved by incubation in 37^0 C for at least 30 min. A mixture of IPS-derived cells ($1x10^6$ hepatoblast, $8x10^5$ ECs and $2x10^5$ MSCs, as per Takebe *et al*., 2013) was centrifuged for 5 min at 300 x g and resuspended in 2 mL of LO culture media (composed of 1:1 EGM-2/Hepatocye differentiation media, see supplementary methods). The cell mixture was seeded on top of the Matrigel bed. Media was changed every other day. In order to assess the rate of

mesenchymal condensation, pictures of the wells were taken every 12h. The confluent cell layer and the total covered area progressive condensation over time was evaluated using ImageJ software.

2.3. Proteomics

Proteomic sample processing and analysis followed a previously published protocol (Carnielli *et al*., 2018). For detailed information see the Supplementary Methods section. Pathway annotation of protein IDs was performed using the comprehensive EnrichR gene set enrichment analysis web server (Kuleshov *et al*., 2016; Chen *et al*., 2013), applying Reactome (Fabregat *et al*., 2018.) and Panther (Mi and Thomas, 2009) categorization with the significance threshold set at $p < 0.05$. Interactome analysis was performed using String (Szklarczyk *et al*., 2017) with k-means clustering in three groups.

2.4. Statistical Analysis

Statistical Analyses to assess LO functional analysis and development quality (Figures 2 and 4) was performed using one-way ANOVA with Tukeys' post-test. For all other statistical analyses, Student's two tailed t tests were used for pairwise comparisons. Data are presented as means ± SEM, or mean of at least three independent experiments, with at least two technical replicates. For the proteomics analyses, statistical tests were performed using Students t-test, using Perseus software and pathway enrichment analysis using EnrichR. Values of $p < 0.05$ were considered significant. GraphPad Prism software was used to perform all other statistical analyses.

3. Results

3.1. iPS cell differentiation

Aiming a broad applicability of our studies and reproducibility of the results, we carried out the experiments with 3 independent iPS cell lines, as mentioned in section 2.1. All data shown in Figure 1 are related to cell line F9048 and similar results were observed with the other cell lines (Supplementary Figure 1C). Figure 1A summarizes the groups tested in this study, using different combinations of NPCs with iPS-derived hepatocytes. Here, we have used "I" to indicate cells derived from iPS and "P" to indicate primary cell lines. Isogenic LO (i.e., containing all three cell lines derived from the same iPSs) is referred to as III. When using NPC derived from primary human cell lines, the group is referred to as IPP. When using human aortic endothelial cells (HAEC) and iPS-derived MSC, the group is referred as IPI. Finally, when using iPS-derived EC and dental pulp derived MSC (dpMSC), the group is referred as IIP.

The hepatic differentiation potential was evaluated and characterized in vitro. Figure 1B shows representative images of flow cytometric analyses. After three days of differentiation 58.5 ± 4.7% (n=3) of cells were $CXCR4^{+}/FOXA2^{+}$ (definitive endoderm). Despite starting out with a heterogeneous population, at day 9 of differentiation, a majority of cells (78 ± 5.8%, n=3) expressed hepatic progenitor markers, such as *HNF4A* and *AFP*. After terminal hepatocyte differentiation, 74.3 ± 7.1% (n=3) of the cells expressed the hepatic markers *ALB* and *UGT1A1* (Figure 1B). Phase contrast image showed homogenous hepatocyte morphology in a monolayer culture. Representative images of immunofluorescence (IF) staining for each step of hepatic differentiation are shown in Figure 1C. After three days, 62.8 ± 4.8% (n=3) of

cells were double positive for FOXA2 and CXCR4. After nine days, 77.4 ± 5.9% (n=3) were positive for HNF4a and AFP and at day 18, 88.6 ± 6.9% (n=3) of cell population were positive for ALB and UGT1A1. Also, at day 18, 90.2 ± 3.1% (n=3) cells stained positive for Periodic acid -Schiff (PAS) (Figure 1C).

For assessing endothelial differentiation, the iPS-derived cells were evaluated stepwise throughout the differentiation protocol. Figure 1D shows representative images of the flow cytometric analyses. The first step of the differentiation protocol (day 2) resulted in homogenous mesodermal differentiation, as inferred from the nearly ubiquitous co-expression of Brachyury T and GATA4 (92.4 ± 3.7, n=3). However, at the end of endothelial differentiation (day 7), only 13.1 ± 2.7% of the cell population was double-positive for endothelial markers CD34 and CD31. After magnetic sorting of the CD31+ cells and seeding a 60% confluent cell culture, the great majority of cells were positive for CD31 and a varying percentage of them were also positive for VECAD, (48.6 ± 22.8%, n=3). At the day 7 of endothelial differentiation 12.8 ± 2.2% of cells were positive for CD34. After cell sorting, 90.1% ± 6.7% of cells were double positive for CD31 and VECAD (Figure 1E). IF staining was performed in 90% confluent culture, which could explain the difference observed in flow cytometry analysis. ECs took up acetylated-LDL (95.3 ± 3.7%, n=3) and were able to generate capillary-like tubular structures in the Matrigel angiogenesis assay (Figure 1D and E).

For mesenchymal differentiation, flow cytometric analysis indicated that the majority of iNCC cells expressed HNK1 and P75 (79.0 ± 3.1%, n=3). Following mesenchymal terminal differentiation, essentially all the cells showed a typical MSC morphology, were positive for the majority of cell population which expressed CD73 and CD90 (95.1 ± 1.8%, n=3) and CD105 (Figure 1F). Also, iNCC staining revealed that the majority (80.3 ± 7.9%) of the cells were double-positive for P75 and Vimentin.

Similarly, most (85.2 ± 8.0%) iNCC-derived MSC were double positive for CD73 and Vimentin (Figure 1G). Additionally, 90.2 ± 5.9% of these MSCs were positive for CD105 (Figure 1G). Finally, we tested the ability of the iNCC-derived MSC to differentiate into osteogenic, chondrogenic, and adipogenic lineages. Figure 1H shows representative, low-magnification bright field images and photographs of cell culture wells, and negative controls, stained for Alizarin Red, Alcian Blue, and Oil Red, respectively, after 28 days exposure to the various MSC differentiation induction protocols.

3.2. Liver organoids functional analysis

Liver Organoid (LO) formation was evaluated by assessing the tissue condensation rate, (i.e. mesenchymal condensation rate) (Takebe *et al*. 2017). As seen in Figure 2A, the rate of mesenchymal condensation was essentially identical for all cell lines and all experimental groups. No apparent morphological differences were observed in histological staining in the three cell lines and between groups (Figure 2B shows representative H&E images of the III group). Analysis of gene expression by RT-qPCR after 12 days of LO culture revealed increased expression of important hepatic phase I xenobiotic biotransformation enzymes in IIP, such as *CYP1A1* and *CYP1A2*, but not *CYP3A4*, and also an increased expression of the phase II enzyme GSTA1. The data also indicate an increased expression of important hepatic maturation markers, such as *ALB* and *TDO2*. ELISA analysis of the LO culture supernatants revealed a significantly increased (6.7 fold) amount of secreted albumin by day 12 in the IIP group, as compared to other groups (Figure 2D). Also, for the same time point, we observed a significant reduction of AFP secretion in the supernatants of group IIP, as compared to

groups IPP and IPI (Figure 2E). No statistical differences were observed at day 6 (Supplementary Figure 1E). Also, we did not observe any differences in A1AT and LDH media production in all groups and in different time points (Supplementary Figure 1E).

3.3. LO developmental pathways analysis

Western blotting analysis of important cell signaling pathways related to liver development are displayed in Figure 3A (experiment performed twice, independently). Densitometry analysis revealed significantly reduced activity (i.e., reduced ratio of phosphorylated/total protein) of SMAD2 (Figure 3B) in III, as compared to IPP and IPI, but not to IIP. ERK1/2 activity was increased exclusively in III (Figure 3C). β-Catenin expression was reduced in IIP, as compared to all groups (Figure 3D). No statistically significant differences across all groups were found in the activities of Jagged-1 and SMAD1.5.7 (Figure 3E and F). To confirm the western blotting findings, we performed an additional set of experiments using combinations of Wnt and TGF-β agonists (i.e. CHIR99021 and TGF-β1, respectively) and antagonist (i.e. DKK, WIF1 and SB431542, respectively) during LO maturation (Figure 3G) for 10 days. Combinations of both agonists, 10 μM CHIR99021 + 20 ng/mL of TGF- β1 significantly reduced the albumin gene expression, while the antagonists, 100 ng/mL of DKK, 200 ng/mL WIF1 plus 10 μM SB431542 significantly increased albumin gene expression (Figure 4J).

3.4. Proteomics

Proteomic profiling revealed significant differences in LO groups at day 12. Of the approximately 2100 proteins identified in each group, the vast majority of the protein IDs (2031) were identified (Figure 4A). Principal component analysis showed the absence of clustering amongst all samples tested (Figure 4B). Figure 4C shows a heat map of differentially expressed proteins, when applying ANOVA with $p<0.05$ thresholds. Hierarchical clustering shows that the most different group was IPP, while the most similar among all groups were III and IPI. Figure 4D highlights the integrin signaling as the most enriched pathway identified. Figure 4E shows the interactome from ANOVA-tested, differentially expressed proteins, filtered by the most enriched GO according to biological function. The two major clusters of nodes are located around FN1 and the integrin alpha subunits V and 5, first shell of interactors, and TGFBI (i.e. TGF-β induced protein) and CTNNB1 (i.e. β-catenin), confirming Western Blotting findings. Gene expression analysis of *ITGAV* by RT-qPCR confirmed reduced expression in groups III and IIP, as oppose of what was observed in *ITGB1*. Secretome analysis of 2D co-culture of NPCs are displayed in Figures 4F-H. Figure 4F shows the heat-map generated by ANOVA with $p<0.05$ thresholds. Hierarchical clustering shows that IP is more similar to primary NPCs and that II is more similar to PI. Pathway enrichment analysis of the secretome of NPCs (Figure 4G) highlights the role of integrins/extracellular matrix (ECM), TGF-β, and IGF, which are filtered and displayed in the heat-map in Figure 4H. The interactome of ANOVA-tested, differentially expressed proteins, filtered for ECM and IGF signaling, is shown in Figure 4H.

4. Discussion

A major aim of this study was to elucidate the role and efficacy of NPCs, derived either from iPS or from primary cell culture, in the development and functionally of LOs. Human iPS used in this study were characterized by flow cytometry and gene expression (in Figure S2A and B). We successfully differentiated all three iPS cell lines towards hepatoblasts, arterial ECs and iNCC-derived MSCs. The differential contribution, if any, of arterial, venous, or lymphatic ECs in the development of LO remains to be elucidated. Thus, we used iPS-derived arterial ECs, with commercially available HAECs serving as the correspondent adult cell line. For mesenchymal cells, we used iNCC-derived MSC, with dpMSC as the primary adult cell counterpart.

We succeeded in deriving functional hepatoblasts, as assessed by the expression of HNF4a and AFP. The potential of our hepatoblasts to differentiate into hepatocyte was inferred from expression pattern of mature hepatic markers such as UGT1A1 and CK18 and by PAS staining (Figure 1B and C).

Arterial endothelial cell commitment was inferred from the expression of general endothelial markers, such as *CD31* and *VECAD*, together with that of specific arterial ECs markers such as *NOTCH4* and the very low levels of expression of *PDPN* and *EPHB4*, which are markers of lymphatic and venous phenotype, respectively (Figure S1B). The functionality of our iPS-derived ECs was demonstrated by their ability to take up acetylated LDL and to generate capillaries in Matrigel.

Neural crest differentiation was confirmed by the expression of HNK1 and CD75 (Figure 1F). iNCC-derived MSC expressed stromal-mesenchymal markers such as CD105, CD90 and CD73 (Figures 1F and G). Following *in vitro* induction, the mesenchymal differentiation was confirmed by the osteogenic staining with Alizarin Red (calcium deposits), chondrogenic staining with Alcian Blue (glycosaminoglycans)

and adipogenic staining with Oil Red (lipid droplets), (Figure 1H). This result indicates that we have successfully derived competent multipotent mesenchymal cells, and not fibroblasts.

LO generation was compared between all tested groups. No differences were observed in the mesenchymal condensation rate and in the morphology between all tested groups (Figure 2A and B). Even though we noted some intrinsic variations between the tested cell lines, our RT-qPCR data at day 12 (Figure2C) revealed that important genes related to hepatic xenobiotic metabolism of phase I (i.e. *CYP1A2* and *CYP1A1*) and II (i.e. *GSTA1*) were overexpressed in IIP. These data suggest that the hepatic metabolic rate was higher in the presence of dpMSC associated with iPS derived ECs (i.e. group IIP) and reduced in the presence of adult arterial ECs. ALB and TDO2 gene expression were also significantly elevated in group IIP, which suggests increased hepatic maturation. In addition, IIP produced more albumin at day 12 (Figure 2C), with reduced AFP gene expression and secretion, as compared to IPI and IPP, but not to III. A concomitant increase in albumin and reduction of AFP secretion is one of the most important hallmarks of hepatocyte maturation (Ang *et al*., 2018; Roll and Willenbring, 2010; Peters *et al*., 2016). The secretion of AA1T and LDH was not altered between the groups and at the time points tested (Supplementary Figure F).

To evaluate the influence of NPC in key signaling pathways relevant to LO formation, we performed a series of Western Blots (Figure 4A). The protein activity analysis revealed that the III and IIP groups exhibited significantly lower activity of TGF-β (Figure 4B). Also, the IIP group showed significantly reduced Wnt activity (Figure 4D), while the III group exhibited increased ERK1/2 activity (Figure 4C). Activated ERK1/2 inhibits GSK3B through c-Met or IGF receptor signaling (Etnyre *et al*., 2014), which could explain high β-catenin in III. No differences were observed in

the signaling of Notch and BMP4 (Figure 4E and F). Figure 4H compiles the information obtained from our Western Blot analyses. TGF-β inhibition increased LO albumin production *in vitro* by inducing hepatoblast differentiation towards hepatocytes, thereby suppressing cholangiocyte differentiation (Ng *et al*., 2018). Also, TGF-β is positively correlated with lower $O2_{(g)}$ levels and activation of HIF1A during liver organogenesis (Ayabe *et al*., 2018). In addition, Wnt signaling inhibition is known to induce hepatocyte differentiation in 3D culture (Pettinato *et al*., 2016). The combined inhibition of Wnt and TGF-β significantly reduced the expression of albumin, as opposed of what was observed, when these two pathways were activated (Figure 3G).

In order to confirm and evaluate the impact of previous Western Blotting analysis, we performed a proteomic profiling of the various LOs. We observed intrinsic and differential protein expression patterns assigned by differential contribution of NPC to LO development (Figure 4A-E). While sharing most of protein IDs (Figure S1A), the NPC composition tested significant influenced LO developmental pathways (Figure S1B).

Most differentially enriched pathways were related to integrin signaling (Figure 4C-E). The fibronectin receptor ITGAV (integrin receptor αV) was one of the major hits identified in our pathway enrichment analysis, as well as the integrin alpha subunit 5 (ITGA5). ITGAV expression is induced by TGF-β and acts promoting epithelial-mesenchymal transition (Mamuya and Duncan, 2012) and fibrosis (Henderson *et al*., 2013). Integrin subunits α5 and β1 are necessary for bile duct epithelial tract formation during liver development (Tanimizu *et al*., 2012). Also, integrin β1 is important for sustaining hepatocyte viability in native ECM and has been implicated in liver regeneration (Speicher T *et al*., 2014; Pinkse GG *et al*., 2004). Importantly, specific integrin subunit combinations during liver organogenesis, such as α5β1, help to

generate the different hepatic structures, and are influenced by surrounding sinusoids, vascular development and local ECM (Shiojiri N and Sugiyama Y, 2004). In our studies, Decorin, a well-known endothelial-produced repressor of liver fibrosis and local inhibitor of TGF-β (Baghy *et al*. 2012) and c-Met (Goldini *et al*., 2009) was significantly more expressed in group IIP (Figure 4H). The reduced secretion of IGFBP5 by dpMSC (Figure 4H), a MAPK signaling activator overexpressed during fibrosis (Yasuoka *et al*., 2009), could explain the high ERK1/2 in III and reduced β-catenin in IIP. dpMSC produces more ECM, except for collagen type IV, but their role in LO maturation remains unclear.

Collectively, the expression of integrin β1, but not αV, and reduced TGF-β and Wnt signaling observed in the combination of iPS-derived EC and dpMSC, might explain the observed differences in hepatocyte function in the various LOs. Our data suggests that high TGF-β activity induced by HAEC (Figure 3B), increased expression of ITGAV and induced ECM remodeling that impairs hepatocyte function. Additionally, we suggest that Wnt signaling repression in IIP is due to reduced secretion of IGFBP5 by dpMSC.

5. Conclusion

Our data indicates that reduced activity of TGF-β and Wnt is contributes for the increased albumin secretion and hepatic function observed in the combination of dpMSC and iPS-derived ECs as NPCs. These differential growth factor stimuli generate substantial changes in integrin and ECM profiles that regulate liver development. In translational terms, this work provides important insights for assessing future strategies

to advance organoid technologies aiming at high-throughput drug screening platforms and regenerative therapy approaches.

References

Ang, L., Tan, A., Autio, M., Goh, S., Choo, S., Lee, K., Tan, J., Pan, B., Lee, J., Lum, J., *et al*.. A Roadmap for Human Liver Differentiation from Pluripotent Stem Cells. Cell Rep, v.22, p2190-2205. 2018.

Asai, A., Aihara, E., Watson, C., Mourya, R., Mizuochi, T., Shivakumar, P., Phelan, K., Mayhew, C., Helmrath, M., *et al*. Paracrine signals regulate human liver organoid maturation from induced pluripotent stem cells. Development, v.144, p1056-1064. 2017.

Ayabe, H., Anada, T., Kamoya, T., Sato, T., Kimura, M., Yoshizawa, E., Kikuchi, S., Ueno, Y., Sekine, K., *et al*. Optimal Hypoxia Regulates Human iPS-Derived Liver Bud Differentiation through Intercellular TGFB Signaling. Stem Cell Reports, v.11, p306-316. 2018

Baghy, K., Iozzo, R. V., Kovalszky, I. Decorin–TGFβ Axis in Hepatic Fibrosis and Cirrhosis. Journal of Histochemistry & Cytochemistry, v.60, n.4, p262–268. (2012)

Camp, J., Sekine, K., Gerber, T., Loeffler-Wirth, H., Binder, H., Gac, M., Kanton, S., Kageyama, J., Damm, G., and Seehofer, D. *et al*. Multilineage communication regulates human liver bud development from pluripotency. Nature, v.546, 533–538. 2017.

Carnielli, C., Macedo, C., De Rossi, T., Granato, D., Rivera, C., Domingues, R., Pauletti, B., Yokoo, S., Heberle, H., *et al.* Combining discovery and targeted proteomics reveals a prognostic signature in oral cancer. Nat Commun. v.9, n.1, p359. 2018.

Chen, E., Tan, C., Kou, Y., Duan, Q., Wang, Z., Meirelles, G., Clark, N., Ma'ayan, A. Enrichr: interactive and collaborative HTML5 gene list enrichment analysis tool. BMC Bioinformatics, v.15, n.128. 2013.

Etnyre, D., Stone, A. L., Fong, J. T., Jacobs, R. J., Uppada, S. B., Botting, G. M., Rajanna, S. *et al*.. Targeting c-Met in melanoma. Cancer Biology & Therapy, v.15, n.9, p1129–1141. 2014.

Fabregat, A., Jupe, S., Matthews, L., Sidiropoulos, K., Gillespie, M., Garapati, P., Haw, R., Jassal, B., Korninger, F., *et al*. The Reactome Pathway Knowledgebase. Nucleic Acids Res v.4, D649-D655. 2018.

Goldoni, S., Humphries, A., Nyström, A., Sattar, S., Owens, R. T., McQuillan, D. J. *et al.* Decorin is a novel antagonistic ligand of the Met receptor. The Journal of Cell Biology, v.185, n.4, p743–754. 2009.

Gordillo, M., Evans, T., Gouon-Evans, V. Orchestrating liver development. Development, v.142, p2094-2108. 2015.

Henderson, N., Arnold, T., Katamura, Y., Giacomini, M., Rodriguez, J. D., McCarty, J. H., Pellicoro, A. *et al*. Targeting of αv integrin identifies a core molecular pathway that regulates fibrosis in several organs. Nature Medicine, v.19, n.12, p1617–1624. 2013.

Koui, Y., Kido, T., Ito, T., Oyama, H., Chen, S., Katou, Y., Shirahige, K., Miyajima, A. An In Vitro Human Liver Model by iPS-Derived Parenchymal and Non-parenchymal Cells. Stem Cell Reports 9, 490-498. (2017)

Kuleshov, M., Jones, M., Rouillard, A., Fernandez, N., Duan, Q., Wang, Z., Koplev, S., Jenkins, S., Jagodnik, K., *et al*..Enrichr: a comprehensive gene set enrichment analysis web server 2016 update. Nucleic Acids Res v.8, W90-7. 2016.

Loh, K., Ang, L., Zhang, J., Kumar, V., Ang, J., Auyeong, J., Lee, K., Choo, S., Lim, C., and Nichane, M. *et al.* Efficient Endoderm Induction from Human Pluripotent Stem Cells by Logically Directing Signals Controlling Lineage Bifurcations. Cell Stem Cell, v.14, p237-252. 2014.

Mamuya, F. A., & Duncan, M. K. aV integrins and TGF-β-induced EMT: a circle of regulation. Journal of Cellular and Molecular Medicine, v.16, n.3, p445–455. 2012.

Mi H & Thomas P. PANTHER pathway: an ontology-based pathway database coupled with data analysis tools. Methods Mol Biol, v.563, p123-40. 2009.

Miller, E., Kobayashi, G., Musso, C., Allen, M., Ishiy, F., de Caires, L., Goulart, E., Griesi-Oliveira, K., Zechi-Ceide, R., Richieri-Costa, A. *et al*. EIF4A3 deficient human iPSCs and mouse models demonstrate neural crest defects that underlie Richieri-Costa-Pereira syndrome. Human Molecular Genetics v.26, p2177-2191. 2017.

Ng, S., Saeb-Parsy, K., Blackford, S., Segal, J., Serra, M., Horcas-Lopez, M., No D., Mastoridis, S., Jassem, W., *et al*. Human iPS derived progenitors bioengineered into liver organoids using an inverted colloidal crystal poly (ethylene glycol) scaffold. Biomaterials, v.182, p299-311. 2018.

Nie, Y., Zheng, Y., Ogawa, M., Miyagi, E., Taniguchi, H. Human liver organoids generated with single donor-derived multiple cells rescue mice from acute liver failure. Stem Cell Research & Therapy v.9. 2018.

Okita, K., Yamakawa, T., Matsumura, Y., Sato, Y., Amano, N., Watanabe, A., Goshima, N., Yamanaka, S. An Efficient Nonviral Method to Generate Integration-Free Human-Induced Pluripotent Stem Cells from Cord Blood and Peripheral Blood Cells. Stem Cells, v.31, p458-466. 2013.

Peters, D., Henderson, C., Warren, C., Friesen, M., Xia, F., Becker, C., Musunuru, K Cowan, C.. Asialoglycoprotein receptor 1 is a specific cell-surface marker for isolating hepatocytes derived from human pluripotent stem cells. Development, v.143, 1475-81. 2016.

Pettinato, G., Ramanathan, R., Fisher, R., Mangino, M., Zhang, N., Wen, X.. Scalable Differentiation of Human iPSs in a Multicellular Spheroid-based 3D Culture into Hepatocyte-like Cells through Direct Wnt/β-catenin Pathway Inhibition. Sci Rep v.6, p32888. 2016.

Pinkse, G. G., Voorhoeve, M. P., Noteborn, M., Terpstra, O. T. , Bruijn, J. A., De Heer, E. Hepatocyte survival depends on beta1-integrin-mediated attachment of hepatocytes to hepatic extracellular matrix. Liver Int, v.24, n.3, p218-26. 2004.

Roll, G. & Willenbring H. Transplanted nonviable human hepatocytes produce appreciable serum albumin levels in mice. Stem Cell Res, v.5, p267-70. 2010.

Shin, D. & Monga, S. Cellular and Molecular Basis of Liver Development. Comprehensive Physiology, v.3, n.2, p799-815. 2013.

Shiojiri, N. & Sugiyama, Y. Immunolocalization of extracellular matrix components and integrins during mouse liver development, v.40, n.2, p346-55. 2004.

Si-Tayeb, K., Lemaigre, F. Duncan, S. Organogenesis and development of the liver. Dev Cell. v.18, n.2, p175-89. 2010.

Speicher, T., Siegenthaler, B., Bogorad, R. L., Ruppert, R, Petzold, T., Padrissa-Altes, S, Bachofner, M., Anderson, D. G., Koteliansky, V., Fässler, R., Werner, S.. Knockdown and knockout of β1-integrin in hepatocytes impairs liver regeneration through inhibition of growth factor signalling. Nat Commun. v.21, n.5, p3862. 2014.

Szklarczyk, D., Morris, J., Cook, H., Kuhn, M., Wyder, S., Simonovic, M., Santos, A., Doncheva, N., Roth, A., Bork, P., Jensen L, Von Mering, C. The STRING database in 2017: quality-controlled protein-protein association networks, made broadly accessible. Nucleic Acids Res v.4, D362-D368. 2017.

Takebe, T., Sekine, K., Enomura, M., Koike, H., Kimura, M., Ogaeri, T., Zhang, R., Ueno, Y., Zheng, Y., Koike, N. *et al.* Vascularized and functional human liver from an iPS-derived organ bud transplant. Nature v.499, p481–484. 2013.

Takebe, T., Sekine, K., Kimura, M., Yoshizawa, E., Ayano, S., Koido, M., Funayama, S., Nakanishi, N., Hisai, T., Kobayashi, T. *et al*. Massive and Reproducible Production of Liver Buds Entirely from Human Pluripotent Stem Cells. Cell Reports, v.21, p2661-2670. 2017.

Tanimizu, N., Kikkawa, Y., Mitaka, T., Miyajima, A. α1- and α5-containing laminins regulate the development of bile ducts via β1 integrin signals. J Biol Chem, v.287, p28586-97. 2012.

Yasuoka, H., Hsu, E., Ruiz, X. D., Steinman, R. A., Choi, A. M. K., Feghali-Bostwick, C. A.. The Fibrotic Phenotype Induced by IGFBP-5 Is Regulated by MAPK Activation and Egr-1-Dependent and -Independent Mechanisms. The American Journal of Pathology, v.175, n.2, p605–615. 2009.

6. Acknowledgments

We would like to thank the funding agencies FAPESP/CEPID, CAPES, INCT and CNPq. Ernesto Goulart is a FAPESP grantee (2015/14821-1). We acknowledge the Mass Spectrometry Facility at Brazilian Biosciences National Laboratory (LNBio), CNPEM, Campinas, Brazil for their support on mass spectrometry analysis. We thank Valdemir Melechco Carvalho from Fleury Laboratory for the support on the proteomic experiments. Authors have no conflict of interest to disclaim. This work is dedicated to Raúl Marcel González Garcia, *in memoriam*.

Figure Captions

Figure 1 – iPS cells differentiation.

(A) Graphical summary of experimental groups and design. (B) Step-wise flow-cytometry characterization of hepatocyte differentiation *in vitro*. Representative image of gated analyses for $FOXA2^+/CXCR4^+$ at day 3, $AFP^+/HNF4a^+$ at day 9, $UGT1A1^+/ALB^+$ at day 18, and phase contrast image of cellular morphology at day 18. (C) IF staining for FOXA2/CXCR4 at day 3, AFP/HNF4a at day 9, and UGT1A1/ALB and PAS staining of hepatoytes at day 18 and confluent fibroblast culture PAS staining negative control (n = 3, biological replicates. Data displayed as mean ± SEM, bar = 50 μm). (D) Step-wise flow-cytometry characterization of endothelial differentiation *in vitro*. Representative images of gated analyses for $BRACHYURY^+/GATA4^+$ at day 2, $CD34^+/CD31^+$ at day 6, $VECAD^+/CD31^+$ at day 10, and phase contrast image of cellular morphology at day 10. (E) IF staining for CD34 at day 2, VECAD/CD31 and Ac-LDL uptake at day 10 and angiogenesis assay at day 12 (n = 3, biological replicates. Data displayed as mean ± SEM, bar = 50 μm) (F) Step-wise flow-cytometry characterization

of iNCC-MSC differentiation *in vitro*. Representative image of gated analyses for P75+/HNK1+ at day 18, CD73+/CD90+ and and IF staining for CD105/F-Actin and phase contrast image at day 28. (G) IF staining for P75/VIMENTIN at day 18, CD73/VIMENTIN and CD105 at day 28 and representative images for MSC differentiation assay after 28 days of induction and stained for Allizarin Red, Alcian Blue and Oil red (n = 3, biological replicates. Data displayed as mean ± SEM, bar = 50 μm).

Figure 2 – Liver organoid functional analysis. (A) Representative image of liver organoids culture of all cell lines and tested conditions after 72h of mesenchymal condensation in a 24-well plate and area analysis overtime (n = 3, biological replicates. Data displayed as mean ± SEM). (B) HE-staining for III groups of all cell lines (bar = 50 μm). (C) RT-qPCR gene expression analysis of hepatic markers at day 12, normalized with 2D cultured iPS-derived hepatocyte at day 18 of differentiation protocol. (D) Normalized albumin secretion at day 6 and day 12 (D) Urea secretion at day 6 and 12. (E) AFP secreation at day 12. (n = 3, biological replicates. Data displayed as great mean and individual scatter plots. One-way Anova with Tukeys` post-hoc, * = $p < 0.05$, ** = $p < 0.01$, *** = $p < 0.01$).

Figure 3 – Liver organoid cell signaling analysis. (A) Representative Western blotting gels for all evaluated proteins. (B) pSMAD2/SMAD2 analysis. (C) p-ERK1/2/ERK1/2 analysis. (D) β-Catenin analysis. (E) Jagged-1 analysis. (F) p-SMAD1.5.7/SMAD1.5.7 analysis. (G) Albumin gene expression after IPP organoid culture in presence of TGF-β and Wnt antagonist and agonist for 10 days. Data was normalized with untreated iPP organoid. (H) Graphical representation of Western

blotting results. (n = 6, biological replicates. Data displayed as great mean and individual scatter plots. One-way Anova with Tukeys` post-hoc, * = $p < 0.05$, ** = $p < 0.01$ and *** = $p < 0.001$).

Figure 4 – Liver organoid proteomic analysis. (A) Venn-diagram of all identified proteins in all groups. (B) Principal component analysis of all tested samples. (C) Heat-map of Z-scores from differentially expressed protein IDs in LO after one-way Anova test ($p<0.05$). (D) Pathway enrichment analysis using EnrichR related to C. (E) String interactome graph of protein from list from C, filtered by most enriched GO biological process, colored differently accordingly to kmeans clustering. RT-qPCR for *ITGAV* and *ITGB1* (n = 3, biological replicates, normalized with 2D cultured iPS-derived hepatocyte at day 18 of differentiation protocol). Data displayed as great mean and individual scatter plots. One-way ANOVA with Tukeys` post-hoc, * = $p < 0.05$ and ** = $p < 0.01$). Filtered heat-map for TGF, Wnt and for integrin signaling. (F) Heat-map of Z-scores from differentially expressed protein IDs in LO secretome after one-way Anova test ($p<0.05$) (G) Pathway enrichment analysis using EnrichR related to F. (H) String interactome graph of protein list from F, filtered by most enriched GO biological process and filtered heatmap for proteins related to ECM organization and IGF are colored differently accordingly to kmeans clustering

Supplemental information

1. Supplementary Tables

Supplementary Table 1 – Antibodies used for IF staining

Antibody	Catalog number	Host Specie	Assay dilution
anti-AFP	ab133617	Rabbit	1/100
Anti-CD105	ab156756	Mouse	1/100
Anti-CD31	ab119339	Mouse	1/100
Anti-CD34	ab81289	Rabbit	1/100
Anti-CD45	ab10558	Rabbit	1/100
Anti-CD73	ab175396	Rabbit	1/100
Anti-CK18	ab32118	Rabbit	1/100
anti-CXCR4	ab124824	Rabbit	1/100
Anti-FOXA2	ab60721	Mouse	1/100
Anti-HNF4	ab41898	Mouse	1/100
Anti-OCT3/4	ab19857	Rabbit	1/100
Anti-P75	ab52987	Rabbit	1/100
anti-SSEA4	ab16287	Mouse	1/100
Anti-UGT1A1	ab129729	Mouse	1/100
Anti-VECAD	ab33168	Rabbit	1/100
Anti-Vimentin	ab8978	Mouse	1/100
Donkey anti-Mouse Alexa 546	A10036	N/A	1/1000
Goat anti-Mouse Alexa 488	11001	N/A	1/1000
Goat anti-Rabbit Alexa 488	11034	N/A	1/1000
Goat anti-Rabbit Alexa 546	A11010	N/A	1/1000

Supplementary Table 2 - Antibodies used for flow-cytometry staining

Antibody	Catalog number	Host Specie	Assay dilution
anti-AFP	PA5 21-004	Rabbit	1/100
Anti-UGT1A1	ab194697	Rabbit	1/100
Anti-HNF4	ab41898	Mouse	1/100
Anti-ALB	ab106582	Chicken	1/100
Anti-CD105	ab156756	Mouse	1/100
Anti-CD34	ab81289	Rabbit	1/100
Anti-CD31	ab119339	Mouse	1/100
Anti-VECAD	ab33168	Rabbit	1/100
Anti-Brachyury T	ab140661	Mouse	1/100
Anti-GATA2	LS-C166381	Rabbit	1/100
Anti-HNK1	ab187274	Mouse	1/100
anti-Mouse Alexa 647	ab 150115	Goat	1/1000
anti-Rabbit Alexa 647	ab150075	Goat	1/1000
Goat anti-Mouse Alexa 488	11001	Goat	1/1000
Goat anti-Rabbit Alexa 488	11034	Goat	1/1000
Goat anti-Chicken Alexa 488	A0001	Goat	1/1000
Anti-P75	ab52987	Rabbit	1/100

Supplementary Table 3 - Antibodies used for Western Blotting

Antibody	Catalog number	Host Specie	Assay dilution
Anti Jaaged 1	sc-390177	Mouse	1/1000
Anti -p-SMAD2	138D4	Rabbit	1/1000

Anti SMAD2	#5339	Rabbit	1/1000
Anti p-ERK1/2	#4377	Rabbit	1/1000
Anti ERK1/2	#4695	Rabbit	1/1000
Anti p-SMAD1.5.7	#9511S	Rabbit	1/1000
Anti SMAD5	#9517P	Rabbit	1/1000
Anti β-catenin	#9582P	Rabbit	1/1000
Anti β-actin	ab49900	Mouse	1/40000
Anti-Rabbit HRP	7074S	Goat	1/5000
Anti-Mouse HRP	7076S	Goat	1/5000

Supplementary Table 4 – Primers sequences list

Gene	Foward	Reverse
OCT3/4	TCCCATGCATTCAAACTGAGG	CCAAAAACCCTGGCACAAACT
EphB4	ACGGGGTATCCTCCTTAGCC	GTACCTCTCGGTCAGTGGTG
Notch4	GCACTGCCAGAGATCCTCAT	CCCTAGCTCTGCCTCACACT
Podoplanin	ACCAGTCACTCCACGGAGAAA	GGTCACTGTTGACAAACCATCT
NANOG	TGGACACTGGCTGAATCCTTC	CGTTGATTAGGCTCCAACCAT
CXCR4	CAAGGCCCTCAAGACCACAG	TGTAGTAAGGCAGCCAACAGG
T	CTGGGTACTCCCAATGGGG	GGTTGGAGAATTGTTCCGATGA
PAX2	CCAAAGTTCAGCAGCCTTTCC	ATTGGAGGCGCTGGAAACAG
LIN28	AGCGCAGATCAAAAGGAGACA	CCTCTCGAAAGTAGGTTGGCT
CYP1A1	CCTTGGAACCTTCCCTGATCC	GATCTTGGAGGTGGCTGAGGT
CYP1A2	CTGGACTTCTTCCCCATCCTTC	GTTCTTGTCAAAGTCCTGATAGTGC
GSTA1	CTGCCCGTATGTCCACCTG	AGCTCCTCGACGTAGTAGAGA
ALB	AATGTGCTGATGACAGGGCG	CGGCAATGCAGTGGGATTTT
TDO2	AGAGCTGGCCTACCTGAAGA	GCCCCTCAGCGTACTGATTT
CYP3A4	ATGGAAAAGTGTGGGGCTT	TCATGTCAGGATCTGTGATAGC
ITGAV	GCTGTCGGAGATTTCAATGGT	TCTGCTCGCCAGTAAAATTGT
ITGB1	CCTGAGAGTGATGCTACTCCA	CACCCTGGTTGTGCCAAAAAT

2. Supplementary Methods

2.1. iPS cell line generation and culture

Cell reprogramming was performed according to Okita *et al*. (2013), using an episomal vector system (pCXLE-hOCT3/4-shP53-F, addgene plasmid 27077; pCXLE-hSK, addgene plasmid 27078; pCXLE-hUL, addgene plasmid 27080) and using the Amaxa human $CD34^+$ cells Nucleofection kit (Lonza), following the manufacturer's recommendations.

Briefly, $CD71^+$-cells, which were isolated from donors' peripheral blood mononuclear cells or dermal fibroblast were nucleofected. Three days after nucleoporation using Lonza Nucleofector 2b, cells were seeded on irradiated murine embryonic fibroblasts (Millipore – A24903) and cultured in maintenance medium, which was composed of DMEM/F12 supplemented with 2mM GlutaMAX-I, 0.1mM non-essential amino acids, 100 µM 2-mercaptoethanol, 20% of knockout serum replacement (all provided by Life Technologies), 10 ng/mL of bFGF (Peprotech), 0.25 mM NaB, 0.5 mM of valproic acid, 2 µM thiazovivin, 0.5uM PD 0325901 and 2µM SB 431542; all provided by Tocris Bioscience). Typical circular hiPS colonies were transferred to 35 mm circular dishes (Corning) coated with 10 µg/cm^2 hESC-qualified Matrigel™ (Corning), incubated for 30 min at 37ºC and cultured in Essential 8 medium (Gibco) supplemented with 100µg/mL normocin (InvivoGen) with daily complete media change. All derived cell lines were checked periodically for mycoplasma contamination. In all procedures involving single-cell passaging were performed using Accutase for 3-5 min (Gibco), cells were seeded $2.5x10^4$ cells/cm^2. After seeding, media were supplemented with 5 µM of Y-27632 (Sigma-Aldrich) upon seeding and maintained for 24h. Total DNA was extracted from iPS cultures using a NucleoSpin

Tissue kit (Macherey-Nagel), following the supplier's instructions. Multiplex ligation-dependent probe amplification (MLPA) analysis was performed with subtelomeric kits (P036 and P070; MRC-Holland) to detect chromosomal imbalances, as previously described (Caires-Júnior *et al*., 2018).

2.2. iPS cell differentiation

Hepatocyte differentiation was performed accordingly previously published protocols *(*Cameron *et al*., 2015*).* Briefly, single cell iPSs were seeded at cell density of $2.5x10^4$ cells/cm^2 in Matrigel coated plates and culture for three days, with daily media changes, in endodermal induction media (RPMI 1640 (from Gibco), supplemented with 2% B27 (Gibco), 100 ng/mL of Activin A - R&D, 25 ng/mL of Wnt3a - R&D, 1% GlutaMAX – Gibco and 100 ug/mL of Normocin (Invivogen). Subsequently, the cells were cultured for 6 days in hepatoblast induction media, with media changes every other day (KO-DMEM (Gibco), supplemented with 20% knockout serum replacement (Life Technologies), 1% DMSO, 1% Glutamax and 100 ng/mL of normocin). Hepatocyte induction was carried for another 9 days, in media comprised of Hepatozyme (Gibco), supplemented with 10 ng/mL of HGF, 20 ng/mL (R&D) of Oncostatin M (R&D), 10 nM of hydrocortisone (Sigma-Aldrich) and 1% GlutaMAX, with media changes every other day.

Endothelial differentiation was carried out following the protocol of Sriram *et al*., (2015), with few modifications. First, iPSs were plated at $1.5x10^4$ /cm^2 and cultured for three days. For the next 5 days, basal media was comprised of Stempro-34 (Gibco) as basal media, supplemented daily with the following differentiation factors: On the first day, with 5 μM CHIR99021 and on the second day, basal media was supplemented

with 50 ng/mL FGF-2. For the last three days, the basal media was supplemented with 50 ng/mL VEGF and 25 ng/mL BMP4. All recombinant agents were obtained from R&D systems. On the last day of differentiation, cells were detached using Accutase for 5 min and sorted magnetically using anti-CD31 microbeads (Miltenyi), following the manufacturer's instructions. $CD31^+$ cells were plated in 60mm Matrigel-coated dishes (Corning) and cultured for no more than 6 passages in serum-free human endothelial media (Gibco) supplemented with 10 ng/mL VEGF, 20 ng/mL FGF-2, 10 ng/mL EGF and 1% of human platelet lysate (Sigma).

Procedures for induced neural crest cell (iNCC) derivation were based on previously published methodology (Miller *et al*., 2017). iPSs were seeded as single cells at 1×10^4 cells/cm^2 onto 60-mm Matrigel-coated dishes and cultured in Essential 8 (E8) media. Two days post-seeding, the E8 media was changed to iNCC differentiation medium, composed of Essential 6™ Medium (Life Technologies) supplemented with 8 ng/ml FGF-2, 20 µM SB431542 (TOCRIS), 1 µM CHIR99021 and 100 µg/ml Normocin. The differentiation medium was changed a daily basis. After ~2–4 days, neural crest-like cells were seen detaching from the borders of individual colonies. The cultures were split before reaching confluence, using Accutase. Cells were re-seeded into new 60-mm Matrigel-coated dishes in fresh iNCC differentiation medium. Cells were passaged using Accutasewhen they reached 80% confluency at 1:3 ratio whenever necessary, for 15 days. Differentiated iNCCs were cultivated for up to eight passages in iNCC differentiation medium, which was completely changed daily. Neural mesenchymal cell (nMSC) populations were obtained through culturing iNCCs with mesenchymal stem cell medium, as previously described (Miller *et al*., 2017). In brief, iNCCs were seeded at 2×10^4cells/cm^2 onto non-coated 60-mm tissue culture dishes in nMSC medium (DMEM/F12 supplemented with 10% FBS, 2 mM GlutaMAX, 0.1 mM

non-essential amino acids and 100 µg/ml Normocin. Cells were differentiated for 6 days and passaged with TrypLE™ Express (Life Technologies) when reached 80% confluency at 1:3 ratio. nMSC cultures were expanded in nMSC medium for up to 6 passages, with medium changes every 3 days.

2.3. Human primary cell culture

Human aortic endothelial cells (HAEC) were purchased from Thermo Fisher (C0065C, passage three). HAEC were seeded at $1.5x10^4$ cells/cm^2 and cultured in EGM-2 (Lonza) with complete media changes every other day. Cells were split 1:3 when reached 80% confluency using Trypsin 0.05% (Life Technologies) and cultured for no longer then 10 passages. Dental-pulp MSC (dpMSC), obtained from our cell bank reservoir, have been previously described and fully characterized (Ishiy *et al*., 2015). dpMSCs were cultured in DMEM/F12 supplemented with 10% FBS and 1% non-essential amino acids (Gibco).

2.4. iPS-derived cells characterization

2.4.1. Immunofluorescence staining

Cell cultures were fixed with 4% PFA for 20 minutes followed by permeabilization with 0.01% Triton X-100 for 30 minutes and blockage using 5% BSA in PBS for 1 h. After that, the cells were incubated overnight with primary antibodies (see supplementary Table 1) at 4 °C and subsequently incubated with secondary antibodies (see supplementary Table 1) for 1 h at room temperature. The final step was DAPI (Sigma) staining for 5 min at room temperature.

2.4.2. Flow cytometry

Cells were stained for flow cytometry analysis to evaluate culture uniformity. Fixation and permeabilization were performed using a Fix & Perm Kit (Invitrogen) according to the manufacturer's instructions. Cells were stained with conjugated primary antibody (see supplementary Table 2) for 45 min in an ice bath, washed with 1× PBS, and then analyzed by Guava Flow cytometer (Merck). The experiment was performed collecting at least 10,000 events per group. After data acquisition, further analysis was performed using FlowJo software. Gate was set using isotype control.

2.4.3. PAS staining

Hepatocytes were fixed with 4% para-formaldehyde for 20 min at room temperature. Periodic acid of Schiff staining was performed following manufacturer's instructions (Sigma).

2.4.5. Angiogenesis assay

Matrigel (Corning) was diluted with EGM-2 (Lonza) 1:1 on ice. For coating a 24 well plate, 380 ul of diluted Matrigel were add to each well and incubated for 30 min at 37ºC. Endothelial cells were plated at $5x10^5$ cells/well and cultured for 48h with EGM-2. The formation of a branched capillary bed was evaluated under phase contrast microscope.

2.4.6. Ac-LDL uptake

Alexa 488-labeled acetylated-LDL (Ac-LDL) (Thermo) was add to a final concentration of 10 ug/mL to the cell media and incubated for 2h in 37ºC. Plates were washed twice with DPBS and cell media was refilled. Cellular uptake was evaluated in a fluorescence microscope (Nikon).

2.4.7. nMSC differentiation assay

For induction of mesenchymal differentiation, $2{,}5x10^5$ nMSC per well were plated on 12 well plate (Corning). After 24h, the cell media was replaced with either supplemented Stempro Osteogenesis Differentiation Media (Thermo), Stempro Chondrogenesis Differentiation Media or Stempro Adipogenesis Differentiation Media.

2.5. RT-qPCR

Total RNA was isolated from cell culture or organoids using the RNeasy Mini Kit (Qiagen), following the manufacturer's recommendations. Briefly, 1 µg of total RNA was converted into cDNA using Superscript II (Life Technologies) and oligo-dT primers according to the manufacturer's specifications. RT-qPCR reactions were performed with Power SYBR Green Master Mix (Life Technologies). Fluorescence was detected using the Applied Biosystem 7500 Real-Time PCR System, under standard temperature protocol. Primer pairs were either designed with PrimerBLAST (http://www.ncbi.nlm.nih.gov/tools/primer-blast/) or retrieved from PrimerBank (http://pga.mgh.harvard.edu/ primerbank/). Primers are listed in supplementary Table 4.

Quantitative analyses were performed using a relative quantification curve with positive control and GAPDH as endogenous control.

2.6. ELISA

Culture supernatant was collected every other day and store at -80C until further analysis. The samples were thaw and centrifuged at 300g for 10 min to remove cellular debris. ELISA was performed accordingly to manufacturer's instructions.

2.7. Western Blotting

The whole-organoid protein lysates were extracted, and western blotting analysis was performed. Protein lysates (5 μg) were electroblotted on polyvinylidene difluoride (PVDF) membranes (GE Healthcare) and probed with respective primary antibodies overnight at 4 °C (Supplementary table 3). The next day, membranes were incubated with related peroxidase (HRP)-conjugated secondary antibodies (Supplementary table 3. Proteins were visualized using chemiluminescence substrate. Finally, blots were scanned using ImageQuant and analyzed by ImageJ software. Normalized band intensities against corresponding β-actin were calculated for precise comparison.

2.8. Urea and LDH

Culture supernatant was collected every other day. LDH assay (Thermo) and Urea quantification assay (Sigma) was performed accordingly to manufacturer's instructions.

Cells were cultured for 21 days, with media changes every other day. Cells were fixed in 4% PFA for 30 minutes and stained accordingly to establish protocols (Jazedje *et al*., 2012) Osteogenic differentiation was shown by formation of calcium-hydroxyapatite-positive areas (Alizarin Red staining). Chondrogenic differentiation was assessed with toluidine blue staining to demonstrate extracellular matrix mucopolysaccharides. Confirmation of adipogenic differentiation by intracellular accumulation of lipid-rich vacuoles stainable with oil red O (Sigma). Cells were stained with 0.16% oil red O for 20 minutes.

2.9. Proteomics

Proteomics was performed in LO at day 12. For secretome analysis, paired combinations of endothelial cells and MSCs were plated at equal ratios and at high confluence (80%). Cells were culture for 24h using 50/50 mixture of endothelial/MSC, washed 3X with Dulbecco modified PBS and cultured for 48h in serum-free high glucose DMEM. Media was collected, filtered through a 20 μm membrane and concentrated using 3 kDa filters (Millipore). Briefly, for protein extraction and digestion, samples were treated with 8M urea, followed by protein reduction with dithiothreitol (5mM for 25 min at 56 °C) and alkylation with iodoacetamide (14mM for 30 min at room temperature). Urea was diluted to a final concentration of 1.6M with 50mM ammonium bicarbonate, and 1mM of calcium chloride was added to the samples for trypsin digestion for 16h at 37°C (2 μg of trypsin). The reaction was stopped with 0.4% formic acid, and peptides were desalted with C18 stage tips, dried in a vacuum concentrator, reconstituted in 0.1% formic acid and stored at −20 °C for subsequent

analysis by LC-MS/MS. The peptide mixture (total volume of 4.5 µL) was analyzed using an LTQ Orbitrap Velos (Thermo Fisher Scientific) mass spectrometer coupled to nanoflow liquid chromatography on an EASY-nLC system (Proxeon Biosystems) with a Proxeon nanoelectrospray ion source. Peptides were subsequently separated in a 2–90% acetonitrile gradient in 0.1% formic acid using a PicoFrit analytical column (20 cm × ID75, 5 µm particle size, New Objective) at a flow rate of 300 nL/min over 212 min, in which a gradient of 35% acetonitrile is reached in 175 min. The nanoelectrospray voltage was set to 2.2 kV, and the source temperature was set to 275 °C. The instrument methods employed for LTQ Orbitrap Velos were set up in DDA mode. Full scan MS spectra (m/z 300–1600) were acquired in the Orbitrap analyzer after accumulation to a target value of 1e6. Resolution in the Orbitrap was set to r = 60,000, and the 20 most intense peptide ions (top 20) with charge states ≥2 were sequentially isolated to a target value of 5000 and fragmented in the high-pressure linear ion trap by CID (collision induced dissociation) with a normalized collision energy of 35%. Dynamic exclusion was enabled with an exclusion size list of 500 peptides, an exclusion duration of 60 s and a repetition count of 1. An activation Q of 0.25 and an activation time of 10 ms were used.

Twelve LC-MS/MS runs were performed. Raw data were processed using MaxQuant v1.3.0.3 software, and MS/MS spectra were searched against The Human UniProt database (released January 7, 2015, 89,649 sequences, and 35,609,686 residues) using the Andromeda search engine. As search parameters, a tolerance of 6 ppm was considered for precursor ions (MS search) and 0.5 Da for fragment ions (MS/MS search), with a maximum of two missed cleavages. A maximum of a 1% false discovery rate (FDR) was set for both the protein and peptide identification. Protein quantification was performed using the LFQ algorithm implemented in MaxQuant

software, with a minimal ratio count of 2 and a window of 2 min for matching between runs. Statistical analysis was performed with Perseus v1.2.7.4 software, which is available in the MaxQuant package. Identified protein entries were processed, excluding reverse sequences and those identified “only by site” entries. Contaminants were not removed from the dataset because serum albumin is of interest in the study of LO. Protein abundance, which was calculated based on the normalized spectrum intensity (LFQ intensity), was log2-transformed, and the dataset was filtered by minimum valid values in at least one group. Missing values for the LFQ intensity were not imputed as random numbers, the mean and standard deviation of which were selected to best simulate low abundance values close to the noise level (imputation width = 0.3, shift = 1.8).

Significance was assessed by comparing all conditions and samples using ANOVA and Student’s t test to identify differentially expressed proteins between specific groups (P value < 0.05). Exclusive and common proteins from each comparison are presented as a Venn diagram generated using the InteractiVenn tool. For data visualization, heat maps with z-score values of log2 LFQ intensities.

The mass spectrometry proteomics data have been deposited to the ProteomeXchange Consortium via the PRIDE partner repository with the dataset identifier PDX013190

2.10. Ethics statement

The experimental procedures involving samples from human subjects were approved by the Ethics Committee of Instituto de Biociências at Universidade de São Paulo, Brazil (Protocol number 1.294.118).

3. Supplementary Figures Caption

Supplementary Figure 1 – Cellular characterization

(A) Representative phase contrast images of iPS cell lines in culture (bar = 200 um). (B) Representative data from F9048 iPS characterization. RT-qPCR for *PAX2*, *CXCR4*, *T*, *LIN28*, *NANOG* and *OCT3/4*. Also, flow-cytometry for OCT4 and SSEA4. (C) Representative flow cytometry panel of cell lines F8799 and F7405 stained for terminal differentiation markers of hepatocyte (ALB and UGT1A1), endothelial (VECAD and CD31) and MSC (CD90 and CD73). (D) HAEC cell line stained for CD31 and VECAD (bar = 50 μm) and dp-MSC cell line stained for CD105 (bar = 50 μm). (E) Representative data from F9048 RT-qPCR of iPS-derived endothelial cells for *NOTCH4*, *PDPN* and *EPHB4* genes. (F) A1AT and Urea concentration in media supernatant of cultured LO at day 6 and day12.

Supplementary References

Caires-Júnior, L., Goulart, E., Melo, U., Araujo, B., Alvizi, L., Soares-Schanoski, A., de Oliveira, D., Kobayashi, G., Griesi-Oliveira, K., and Musso, C. *et al*. (2018). Discordant congenital Zika syndrome twins show differential in vitro viral susceptibility of neural progenitor cells. Nature Communications 9.

Cameron K, Tan R, Schmidt-Heck W, Campos G, Lyall MJ, Wang Y, Lucendo-Villarin B, Szkolnicka D, Bates N, Kimber SJ, Hengstler JG, Godoy P, Forbes SJ, Hay DC. Recombinant Laminins Drive the Differentiation and Self-Organization of hESC-Derived Hepatocytes. Stem Cell Reports. 2015 Dec 8;5(6):1250-1262.

Ishiy, F., Fanganiello, R., Griesi-Oliveira, K., Suzuki, A., Kobayashi, G., Morales, A., Capelo, L., and Passos-Bueno, M. (2015). Improvement of In Vitro Osteogenic Potential through Differentiation of Induced Pluripotent Stem Cells from Human Exfoliated Dental Tissue towards Mesenchymal-Like Stem Cells. Stem Cells International 2015, 1-9.

Jazedje T, Bueno D, Almada B, Caetano H, Czeresnia C, Perin P, Halpern S, Maluf M, Evangelista L, Nisenbaum M, Martins M, Passos-Bueno M and Zatz M. (2012). Human fallopian tube mesenchymal stromal cells enhance bone regeneration in a xenotransplanted model. Stem Cell Rev 8(2):355-6

Miller, E., Kobayashi, G., Musso, C., Allen, M., Ishiy, F., de Caires, L., Goulart, E., Griesi-Oliveira, K., Zechi-Ceide, R., and Richieri-Costa, A. *et al*. (2017). EIF4A3 deficient human iPSs and mouse models demonstrate neural crest defects that underlie Richieri-Costa-Pereira syndrome. Human Molecular Genetics 26, 2177-2191.

Sriram, G., Tan, J., Islam, I., Rufaihah, A., and Cao, T. (2015). Efficient differentiation of human embryonic stem cells to arterial and venous endothelial cells under feeder- and serum-free conditions. Stem Cell Research & Therapy 6.

Figure 1

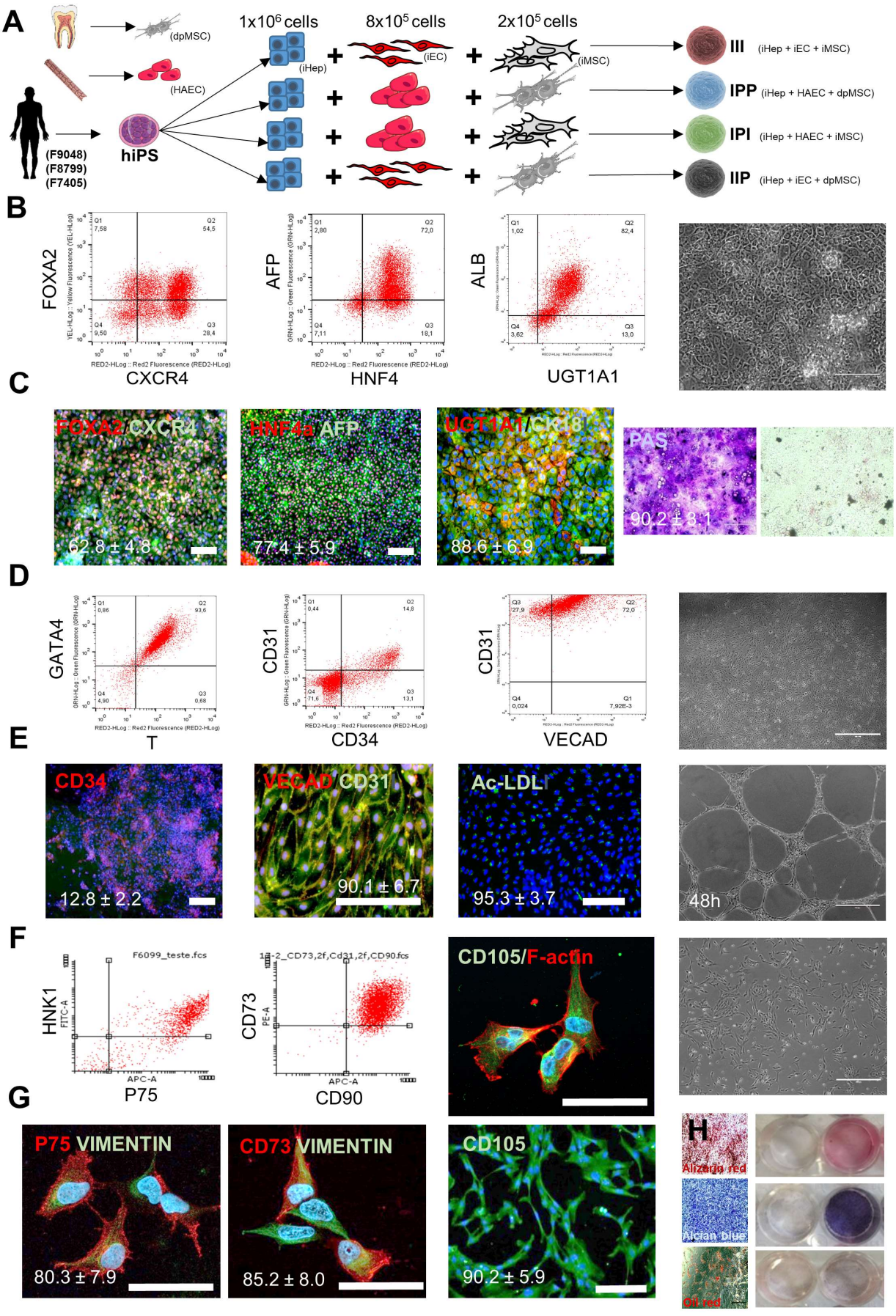
A
(dpMSC)
(HAEC)
(F9048)
(F8799)
(F7405)
hiPS
1x10^6 cells
8x10^5 cells
2x10^5 cells
(iHep)
(iEC)
(iMSC)
III (iHep + iEC + iMSC)
IPP (iHep + HAEC + dpMSC)
IPI (iHep + HAEC + iMSC)
IIP (iHep + iEC + dpMSC)
B
FOXA2
CXCR4
AFP
HNF4
ALB
UGT1A1
C
FOXA2/CXCR4
62.8 ± 4.8
HNF4a/AFP
77.4 ± 5.9
UGT1A1/CK18
88.6 ± 6.9
PAS
90.2 ± 3.1
D
GATA4
T
CD31
CD34
CD31
VECAD
E
CD34
12.8 ± 2.2
VECAD/CD31
90.1 ± 6.7
Ac-LDL
95.3 ± 3.7
48h
F
HNK1
P75
CD73
CD90
CD105/F-actin
G
P75/VIMENTIN
80.3 ± 7.9
CD73/VIMENTIN
85.2 ± 8.0
CD105
90.2 ± 5.9
H
Alizarin red
Alcian blue
Oil red

Figure 2

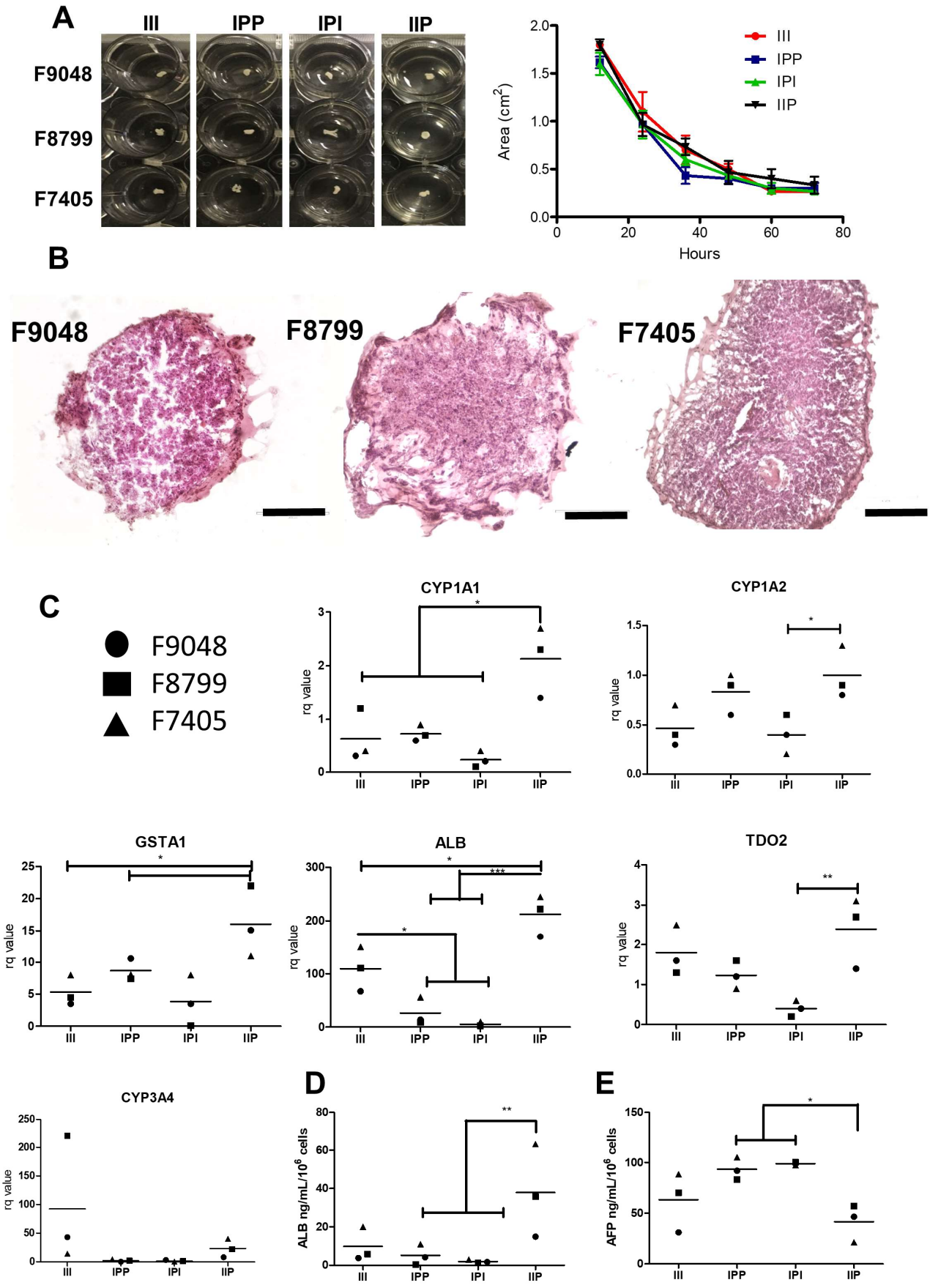
A
III
IPP
IPI
IIP
F9048
F8799
F7405
Area (cm2)
Hours
III
IPP
IPI
IIP
B
F9048
F8799
F7405
C
F9048
F8799
F7405
CYP1A1
CYP1A2
GSTA1
ALB
TDO2
CYP3A4
rq value
D
ALB ng/mL/10^6 cells
E
AFP ng/mL/10^6 cells

Figure 3

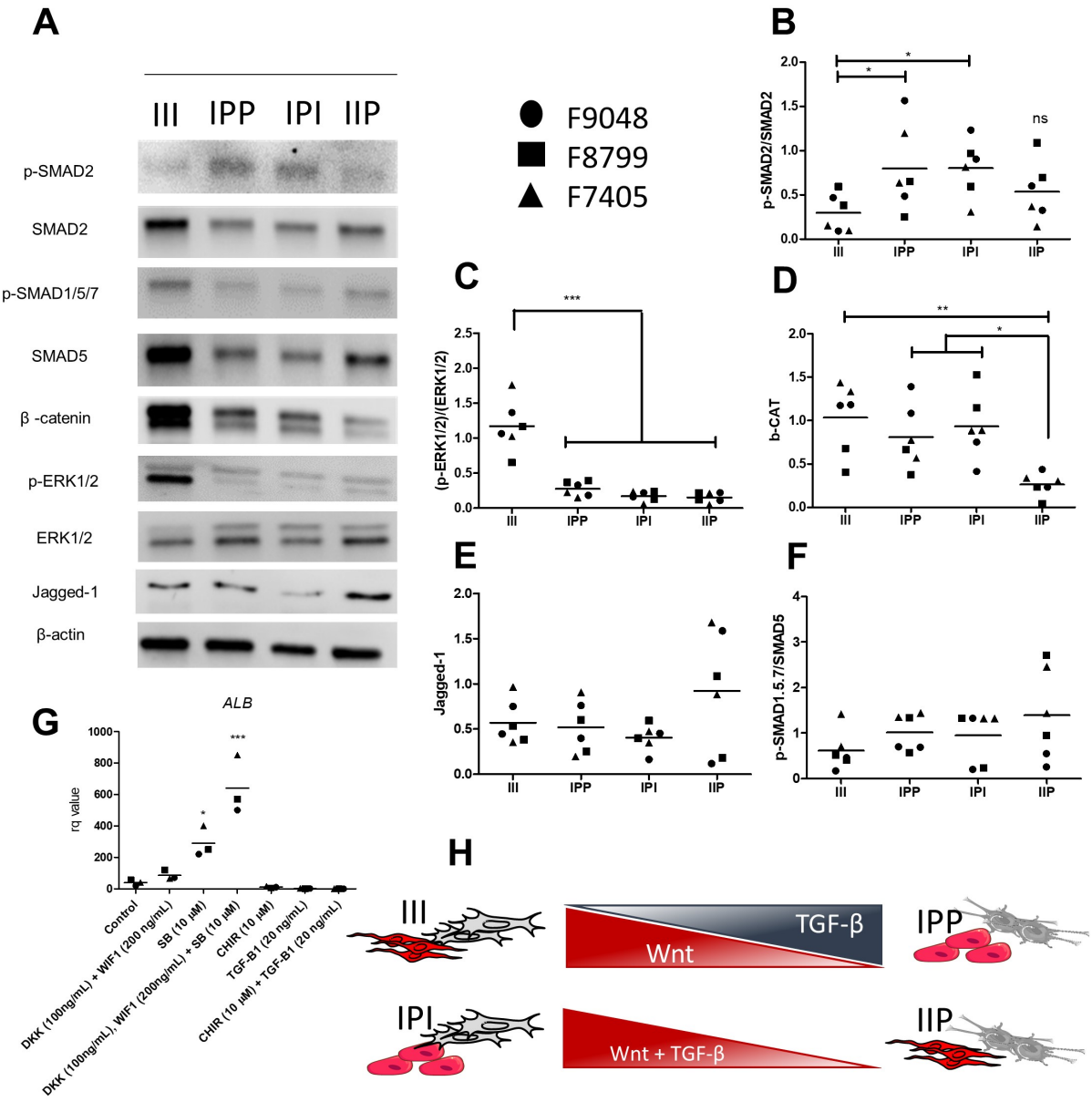
A
III
IPP
IPI
IIP
p-SMAD2
SMAD2
p-SMAD1/5/7
SMAD5
β -catenin
p-ERK1/2
ERK1/2
Jagged-1
β-actin
F9048
F8799
F7405
B
p-SMAD2/SMAD2
ns
C
(p-ERK1/2)/(ERK1/2)
D
b-CAT
E
Jagged-1
F
p-SMAD1.5.7/SMAD5
G
ALB
rq value
Control
DKK (100ng/mL) + WIF1 (200 ng/mL)
SB (10 μM)
DKK (100ng/mL), WIF1 (200ng/mL) + SB (10 μM)
CHIR (10 μM)
TGF-B1 (20 ng/mL)
CHIR (10 μM) + TGF-B1 (20 ng/mL)
H
III
IPP
IPI
IIP
TGF-β
Wnt
Wnt + TGF-β

Figure 4

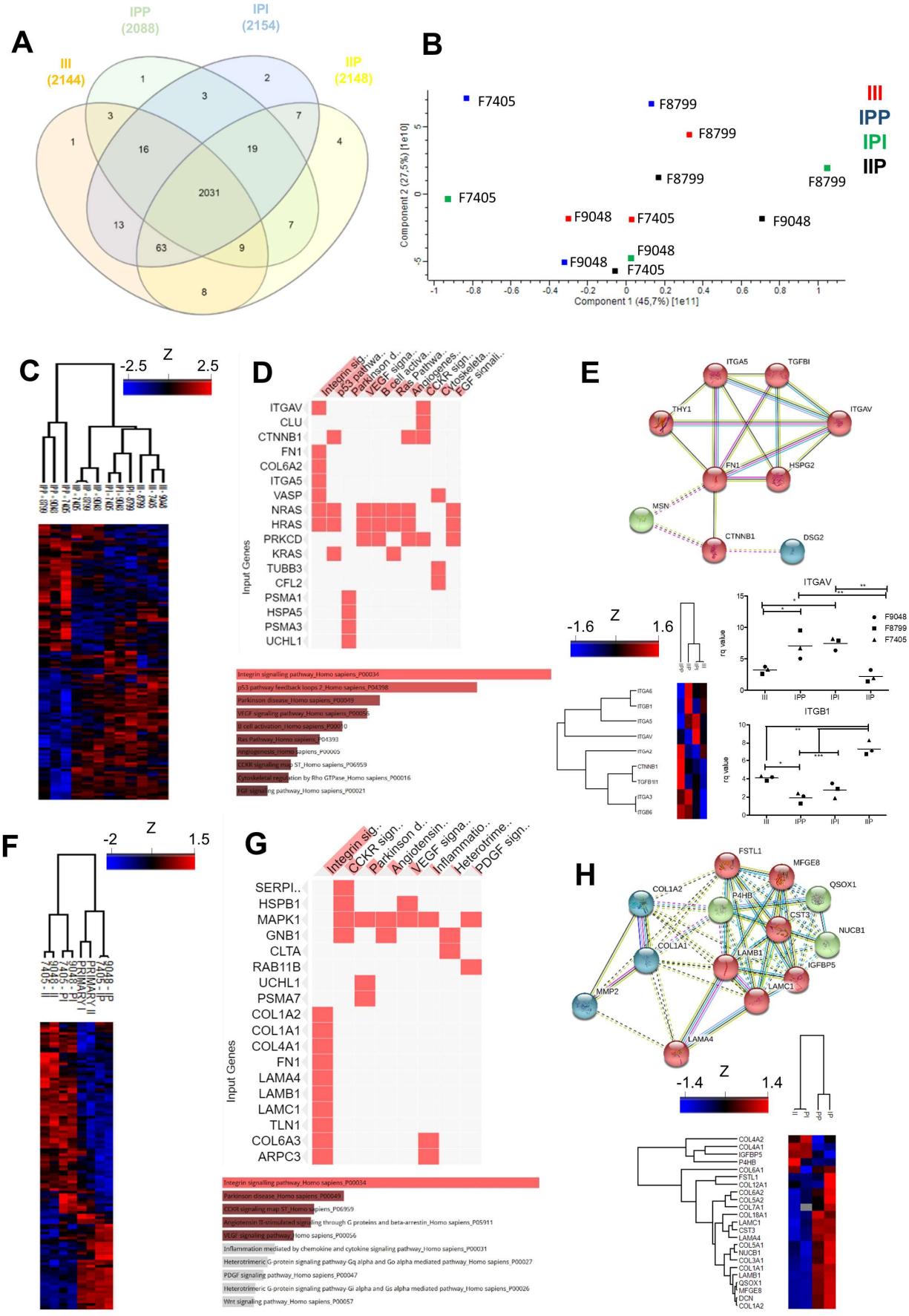
A
IPP (2088)
IPI (2154)
III (2144)
IIP (2148)
1
2
3
3
7
1
4
16
19
2031
13
7
63
9
8
B
F7405
F8799
F8799
F8799
F8799
F7405
F9048
F7405
F9048
F9048
F9048
F7405
III
IPP
IPI
IIP
Component 2 (27,5%) [1e10]
Component 1 (45,7%) [1e11]
C
Z
-2.5
2.5
D
Integrin sig..
p53 pathwa..
Parkinson d..
VEGF signa..
B cell activa..
Ras Pathwa..
Angiogenes..
CCKR sign..
Cytoskeleta..
FGF signali..
ITGAV
CLU
CTNNB1
FN1
COL6A2
ITGA5
VASP
NRAS
HRAS
PRKCD
KRAS
TUBB3
CFL2
PSMA1
HSPA5
PSMA3
UCHL1
Input Genes
Integrin signalling pathway_Homo sapiens_P00034
p53 pathway feedback loops 2_Homo sapiens_P04398
Parkinson disease_Homo sapiens_P00049
VEGF signaling pathway_Homo sapiens_P00056
B cell activation_Homo sapiens_P00010
Ras Pathway_Homo sapiens_P04393
Angiogenesis_Homo sapiens_P00005
CCKR signaling map ST_Homo sapiens_P06959
Cytoskeletal regulation by Rho GTPase_Homo sapiens_P00016
FGF signaling pathway_Homo sapiens_P00021
E
ITGA5
TGFBI
THY1
ITGAV
FN1
HSPG2
MSN
CTNNB1
DSG2
Z
-1.6
1.6
ITGA6
ITGB1
ITGA5
ITGAV
ITGA2
CTNNB1
TGFB1I1
ITGA3
ITGB6
ITGAV
ITGB1
rq value
F9048
F8799
F7405
III
IPP
IPI
IIP
F
Z
-2
1.5
9048 - II
7405 - II
PRIMARY II
9048 - PI
PRIMARY I
7405 - PI
9048 - IP
7405 - IP
G
Integrin sig..
CCKR sign..
Parkinson d..
Angiotensin..
VEGF signa..
Inflammatio..
Heterotrime..
PDGF sign..
SERPI..
HSPB1
MAPK1
GNB1
CLTA
RAB11B
UCHL1
PSMA7
COL1A2
COL1A1
COL4A1
FN1
LAMA4
LAMB1
LAMC1
TLN1
COL6A3
ARPC3
Input Genes
Integrin signalling pathway_Homo sapiens_P00034
Parkinson disease_Homo sapiens_P00049
CCKR signaling map ST_Homo sapiens_P06959
Angiotensin II-stimulated signaling through G proteins and beta-arrestin_Homo sapiens_P05911
VEGF signaling pathway_Homo sapiens_P00056
Inflammation mediated by chemokine and cytokine signaling pathway_Homo sapiens_P00031
Heterotrimeric G-protein signaling pathway-Gq alpha and Go alpha mediated pathway_Homo sapiens_P00027
PDGF signaling pathway_Homo sapiens_P00047
Heterotrimeric G-protein signaling pathway-Gi alpha and Gs alpha mediated pathway_Homo sapiens_P00026
Wnt signaling pathway_Homo sapiens_P00057
H
FSTL1
MFGE8
COL1A2
QSOX1
P4HB
CST3
NUCB1
COL1A1
LAMB1
IGFBP5
MMP2
LAMC1
LAMA4
Z
-1.4
1.4
III
IPI
IPP
IIP
COL4A2
COL4A1
IGFBP5
P4HB
COL6A1
FSTL1
COL12A1
COL6A2
COL5A2
COL7A1
COL18A1
LAMC1
CST3
LAMA4
COL5A1
NUCB1
COL3A1
COL1A1
LAMB1
QSOX1
MFGE8
DCN
COL1A2

Supplementary Figure

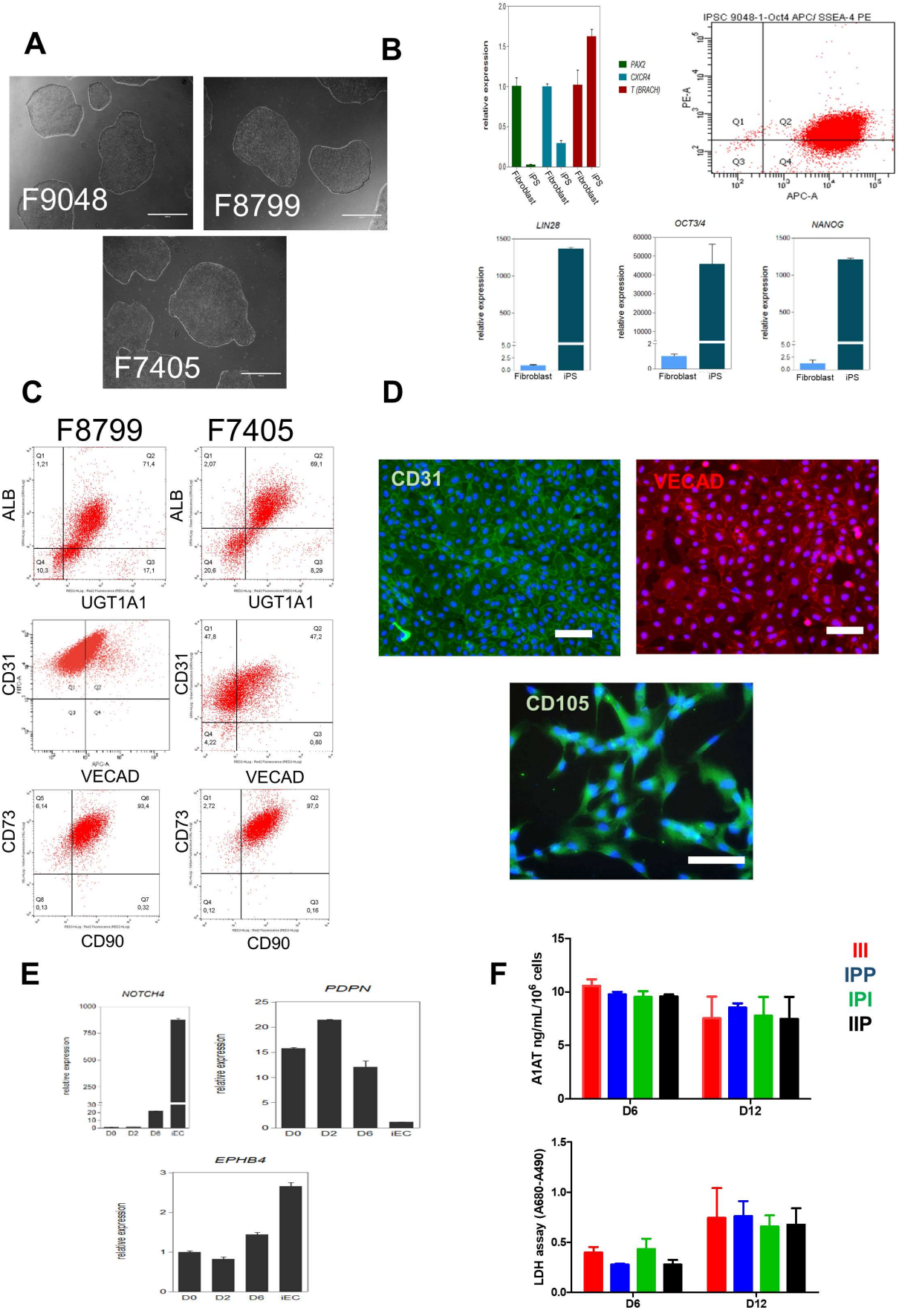

Capítulo 4:

Development of a liver vascular shunt using iPS-derived cells and a decellularized aortic scaffold

Capítulo 4: Fígado acessório aórtico

Artigo em preparação

Development of a liver vascular shunt using iPS-derived cells and a decellularized aortic scaffold

Authors: Ernesto Goulart[1], Luiz Carlos de Caires-Junior[1], Kayque Teles Alves-Silva[1], Gerson S. Kobayashi[1], Camila Manso Musso[1], Bruno Henrique Silva Araujo[2], Adriana Paes Leme[2], Amanda Faria Assoni[1], Valdemir Melechco Carvalho, Danyllo Oliveira[1] Tadeu Rangel[4], Elia Caldini[3], Silvano Raia[4], Peter I. Lelkes[5], Mayana Zatz[1]*.

Affiliations:

[1]Centro de Estudos do Genoma Humano e Células Tronco, Departamento de Genética e Biologia Evolutiva, Instituto de Biociências, Universidade de São Paulo (USP), São Paulo, SP, Brazil.

[2]Brazilian Biosciences National Laboratory (LNBio), Brazilian Center for Research in Energy and Materials (CNPEM), Zip Code 13083-970, Campinas, São Paulo, Brazil.

[3]Laboratório de Biologia Celular, Departamento de Patologia, Faculdade de Medicina, Universidade de São Paulo – (USP), São Paulo, SP, Brazil.

[4]Unidade do Fígado, Departamento de Cirurgia, Faculdade de Medicina, Universidade de São Paulo – (USP), São Paulo, SP, Brazil

[5]Department of Bioengineering, Temple University, Philadelphia, PA, United States

***Corresponding author:** mayazatz@usp.br

Abstract

The liver is a central organ for metabolism and hemostasis. If not treated, several chronic and acute liver diseases resulting from toxic exposures or congenital diseases cause evolves a significant loss of hepatic function and a fibrotic process known as cirrhosis. Portal hypertension, usually associated with cirrhosis represents a severe co-morbidity. Currently, the only therapeutic option for patients with severe portal hypertension is a transjugular intrahepatic portal-systemic shunt, which is associated with the development of hepatic encephalopathy due to reduced first passage hepatic metabolism. Here we report a method to generate an accessory functional hepatic tissue that could serve as a vascular by-pass using decellularized rat thoracic aorta as scaffold. Following the decellularization process histological analysis showed no residual cellular components, less than 50ng of residual DNA per milligram of tissue, preserved ultrastructure and extra-cellular matrix proteins, such as collagen I and IV, pan-Laminin and fibronectin. *In vitro* differentiation of human induced pluripotent stem cells (iPS) towards hepatocytes, endothelial and mesenchymal stem cells were confirmed by functional analysis. Recellularization in a bioreactor-assisted system showed hepatic function over time in culture. In short, although recellularization distribution should be improved to achieve an even cellular distribution, we show new strategy to generate an accessory hepatic tissue. This strategy may be used in the future as an alternative for patients with severe portal hypertension with associated hepatic encephalopathy.

Keywords: Decellularization, Liver, iPS, Hepatocyte, Portal hypertention.

Resumo

O fígado é um órgão central no metabolismo. Várias doenças hepáticas, crônicas e agudas, resultantes de exposições tóxicas ou doenças congênitas evoluem, se não tratadas, por uma perda significativa da função hepática e um processo fibrótico conhecido como cirrose. A hipertensão portal, usualmente associada a pacientes cirróticos, é uma comorbidade grave. Atualmente a única opção terapêutica para pacientes com hipertensão portal grave é a aplicação de *shunt* porto-sistêmico intra-hepático transjugular (TIPSS). O procedimento de TIPSS está associado ao desenvolvimento de encefalopatia hepática, devido à redução do metabolismo hepático de primeira passagem. Neste estudo, relatamos um método para gerar um tecido hepático funcional acessório que serviria como um *by-pass* vascular. Aortas torácicas de ratos Wistar descelularizadas foram utilizadas como arcabouços. O processo de descelularização mostrou a remoção dos componentes celulares residuais por análise histológica, DNA residual <50ng/mg de tecido e preservação da ultraestrutura das principais proteínas da matriz extra-celular, como colágeno I e IV, pan-laminina e fibronectina. A diferenciação *in vitro* de células-tronco pluripotentes induzidas (iPS) em hepatócitos, células-tronco mesenquimais e endoteliais foi confirmada por análise funcional. A recelularização em um sistema de cultura assistido por biorreator demonstrou a função hepática do tecido gerado ao longo do tempo. No entanto, a recelularização apresentou uma distribuição celular irregular. Neste trabalho, nós desenvolvemos uma nova estratégia para gerar um tecido hepático acessório totalmente funcional que ainda precisa de melhorias. Essa estratégia pode ser usada, no futuro, como uma alternativa para pacientes com hipertensão portal grave associada a um quadro de encefalopatia hepática.

Palavras-chave: Descelularização, Fígado, IPS, Hepatócito, Hipertensão portal.

1. Introduction

The liver is a central organ regulating several physiological processes, such as biotransformation of compounds absorbed and distributed in the enterohepatic system, bile, serum albumin and coagulation factors production, ammonia detoxification among others.

It is known that the liver has an incredible regenerative capacity. Nevertheless, under severe conditions, this regenerative capacity is overcome (Mitaka, 1998; Runge *et al*., 2000). Currently, liver transplantation is the only definitive therapy for patients in the final stage of chronic liver disease (Murray & Carithers, 2005) but available donors are very limited (Asgari *et al*.,2013). Severe liver disease could be initiated by many factors, including hepatic viral infections (viral hepatitis), drug-induced hepatocyte cell death, hepatocellular carcinoma, autoimmune and congenital diseases. The chronic injuries to the liver may evolve to a progressive fibrotic process in response to local inflammation, called liver cirrhosis. Cirrhotic patients usually develop portal hypertension due to increased blood perfusion resistance in the fibrotic liver sinusoidal bed (Suk & Kim, 2015). This condition leads to formation of varices in the portal system, which can cause severe abdominal bleeding.

Additionally, trans-jugular intrahepatic portosystemic shunt (TIPSS) is one of the most used approaches to address severe cases of portal hypertension. However, since this methodology deviates significant amount of un-metabolized blood from the liver to the systemic circulation, (i.e. by-pass of the first passage liver metabolism) patients usually develop hepatic encephalopathy (Suk & Kim, 2015). A potential solution to circumvent this problem is the development of new tissue engineering strategies.

In recent years, organs' decellularization has shown to be able to produce a non-antigenic three-dimensional acellular biological matrix, using only the extracellular matrix and the complex three-dimensional organization of the donnor tissue (Uygun *et al*., 2010; Langer & Vacanti, 1993; Badylak, 2007; Ott *et al*., 2008). The resulted acellular matrixes could be used as scaffolds for subsequent recellularization using healthy and mature cells from the future recipient, eliminating thus the risk for organ rejection. Previous studies have already used primary hepatocytes, established and/or commercial cell lines, progenitor cells and/or embryonic stem cells (ESCs) to repopulate the decellularized hepatic scaffold (Uygun *et al*., 2010; Ren *et al*., 2014; Baptista *et al*., 2011). These works were not post-transplantation successfully due to failures in the revascularization of the organ, leading to edema, vascular extravasation, and severe thromboembolic events. To our knowledge, no other study so far was able to show prolonged animal survival using the whole organs decellularization/recellularization approach.

The application of iPS (induced pluripotent stem cells) as a potential cell source changed the paradigm and incentivized research projects involving tissue engineering (Takahashi *et al*., 2007). The differentiation of iPS cells into hepatocytes, endothelial and mesenchymal cells has been performed by administration of growth factors, overexpression of transcription factors (viral vectors) or co-cultures with other cell types (Kondo *et al*., 2014). Protocols for differentiation of iPS into mature hepatocytes, functional and mesenchymal endothelial cells have been extensively developed (Ying *et al*., 2014; Jing *et al*., 2013). Recently it has been shown that hepatocytes derived from iPS are able to recelularize acellular hepatic scaffolds (Kanagavel, 2014). As for the differentiation of functional endothelial cells and mesenchymal cells (i.e. non-

parenchymal cells), several protocols have already been able to generate fully functional cells *in vitro* (Adams *et al*., 2013).

In this study, we tested whether it is possible to build Wistar rat acellular vascular scaffold with hepatocytes, endothelial cells and mesenchymal cells obtained from the same donor iPS cell line, which could potentially ameliorate portal hypertension while providing hepatic first passage metabolism to portal blood, at the same time. If this system demonstrates liver function *in vitro,* it could serve in the future as potential liver accessory organ to treat patients with severe portal hypertension and hepatic encephalopathy.

2. Materials and Methods

2.1. Animals and Ethics

Two-month old male Wistar rats (150-200g) of isogenic strains were used in this work. Animals were kept in the Human Genome and Stem Cell Research Center Animal facility (HUG-CELL), with food and water *ad libitum* and 12 hours of day light cycle, with approval of the research ethics committee of the Biosciences Institute from the University of São Paulo, (Protocol number 229/2015). A total of 30 animals (n = 30) were anesthetized with xylazine (10 mg/kg)/ketamine (90 mg/kg) for dissection of the total thoracic portion of the aorta, used for decellularization procedures. Euthanasia was carried by exsanguination.

2.2. Aorta decellulatization

Anesthetized animals were heparinized (i.v. heparin injection 100U/kg) and the thoracic portion of the aorta was dissected, with costal branches ligated. Blood from the tissue was drained by perfusion of 0.09% saline solution added with 100U/ml heparin. To perform the decellularization process, the aortic tissue was perfused with 1% (v/v) solution of Triton X-100 + 0.05% (m/v) NaOH for 48 hours under a constant hydrodynamic pressure of 120 mmHg and free flow rate. After this step, the same procedure was performed with infusion of distilled water for 30 minutes. Finally, the organ was perfused with PBS pH=7.4 at 5 ml/min for 1 hour. The decellularized tissue was then kept in sterile PBS solution under refrigeration (4°C) for up to 14 days (Ren *et al*., 2014).

2.3. Histology analysis and tissue DNA quantification

At the end of the decellularization protocol, tissue samples were fixed with 4% formaldehyde for 24 hrs and dehydrated in ethanol gradient, and then soaked in xylol. Samples were mounted in paraffin cassettes for subsequent microtomy and histological staining. Hematoxylin and eosin (H&E) staining, Picrossirius Red staining, Alcian Blue staining and Reduced Resorcin-Fuchsin staining were performed in collaboration with the Laboratory of Cell Biology LIM59, University of Sao Paulo Medical School.The residual tissue DNA was extracted by the Qiagen DNeasy Blood and Tissue kit and quantified accordingly to manufacturer's instructions.

2.4. Scanning electron microscopy and micro-CT-scan

Scanning electron microscopy was performed using Sigma VP, Carl Zeiss® scanning electron microscope. Control and decellularized aortic tissues were fixed in 2.5% glutaraldehyde solution for 24 hours. The material was incorporate with osmium tetroxide 1% for 1h. Next, tested materials were dehydrated using an alcohol gradient. After dehydration the tissue samples were dryed using critical point dryer apparatus (Polaron Range CPD7591). The materials were placed in a post and coated with gold using gold plasma coater in an argonium atmosphere for 3 minutes with a 10-15cm distance between the support and the golden plate.

Micro CT analysis was performed using the Skyscan 1176. Acquisition was made using a voltage of 44kV and 397 μA with resolution at 18 μm. Samples were previously incubated in a 320 mg/mL iodine solution for 1 hour at room temperature.

2.5. Proteomics

Proteomic was performed in normal and decellularized aortic tissue samples which were processed and analyzed following a previously published protocol (Carnielli *et al*., 2018). Briefly, for protein extraction and digestion, samples were treated with 8M urea, followed by protein reduction with dithiothreitol (5mM for 25 min at 56 °C) and alkylation with iodoacetamide (14mM for 30 min at room temperature). Urea was diluted to a final concentration of 1.6M with 50mM ammonium bicarbonate, and 1mM of calcium chloride was added to the samples for trypsin digestion for 16h at 37°C (2 μg of trypsin). The reaction was stopped with 0.4% formic acid, and peptides were desalted with C18 stage tips, dried in a vacuum concentrator, reconstituted in 0.1% formic acid and stored at −20 °C for subsequent analysis by LC-MS/MS. The peptide mixture (total volume of 4.5 μL) was analyzed using an LTQ

Orbitrap Velos (Thermo Fisher Scientific) mass spectrometer coupled to nanoflow liquid chromatography on an EASY-nLC system (Proxeon Biosystems) with a Proxeon nanoelectrospray ion source. Peptides were subsequently separated in a 2–90% acetonitrile gradient in 0.1% formic acid using a PicoFrit analytical column (20 cm × ID75, 5 μm particle size, New Objective) at a flow rate of 300 nL/min over 212 min, in which a gradient of 35% acetonitrile is reached in 175 min. The nanoelectrospray voltage was set to 2.2 kV, and the source temperature was set to 275 °C. The instrument methods employed for LTQ Orbitrap Velos were set up in DDA mode. Full scan MS spectra (m/z 300–1600) were acquired in the Orbitrap analyzer after accumulation to a target value of 1e6. Resolution in the Orbitrap was set to r = 60,000, and the 20 most intense peptide ions (top 20) with charge states ≥2 were sequentially isolated to a target value of 5000 and fragmented in the high-pressure linear ion trap by CID (collision induced dissociation) with a normalized collision energy of 35%. Dynamic exclusion was enabled with an exclusion size list of 500 peptides, an exclusion duration of 60 s and a repetition count of 1. An activation Q of 0.25 and an activation time of 10 ms were used. Raw data were processed using MaxQuant v1.3.0.3 software, and MS/MS spectra were searched against The Human UniProt database (released January 7, 2015, 89,649 sequences, and 35,609,686 residues) using the Andromeda search engine. As search parameters, a tolerance of 6 ppm was considered for precursor ions (MS search) and 0.5 Da for fragment ions (MS/MS search), with a maximum of two missed cleavages. A maximum of a 1% false discovery rate (FDR) was set for both the protein and peptide identification. Protein quantification was performed using the LFQ algorithm implemented in MaxQuant software, with a minimal ratio count of 2 and a window of 2 min for matching between runs. Statistical analysis was performed with Perseus v1.2.7.4 software, which is available in the MaxQuant package. Identified

protein entries were processed, excluding reverse sequences and those identified “only by site” entries. Contaminants were not removed from the dataset because serum albumin is of interest in the study of LO. Protein abundance, which was calculated based on the normalized spectrum intensity (LFQ intensity), was log2-transformed, and the dataset was filtered by minimum valid values in at least one group. Missing values for the LFQ intensity were not imputed as random numbers, the mean and standard deviation of which were selected to best simulate low abundance values close to the noise level (imputation width = 0.3, shift = 1.8). Pathway annotation of protein IDs was performed using the comprehensive EnrichR gene set enrichment analysis web server (Kuleshov *et al*., 2016), applying Gene Ontology (The Gene Onthology Consortium, 2019) and Jensen_COMPARTMENT (Binder *et al*., 2014) categorization with the significance threshold set at $p<0.05$.

2.6. Immunohistochemistry

After a protocol of antigen recovery with 1M sodium citrate at 95°C for 15 minutes, some tissue sections were used for immunohistochemistry with the following antibodies: anti-collagen IV, anti-collagen I, anti-fibronectin (Abcam), anti-pan -laminin (Baptista *et al*. 2011; De Kock *et al*. 2011; Barakat *et al*. 2012).

2.7. iPS culture, reprogramming and *in vitro* differentiation protocol

iPS were generated from CD71+-cells, isolated from peripheral blood mononuclear cells of a healthy human donors (F8799 = Female, 28), and culture as previously described by our group (Miller *et al*., 2017).

Hepatocyte differentiation in 2D was performed according robust published protocols (Cameron *et al*., 2015; Wang *et al*., 2017). Briefly, cells were cultured for three days, with daily media changes, in endodermal induction media (RPMI 1640 - Gibco, supplemented with 2% B27 - Gibco, 100 ng/mL of Activin A - R&D, 25 ng/mL of Wnt3a - R&D, 1% GlutaMAX – Gibco and 100 µg/mL of Normocin - Invivogen). For the next 6 days, cells were cultured in hepatoblast induction media, with media changes every other day (KO-DMEM - Gibco, added with 20% knockout serum replacement, 1% DMSO, 1% Glutamax and 100 ng/mL of normocin). The hepatocyte induction was carried out for 9 days with media changes every other day, and the media was comprised of Hepatozyme (Gibco), supplemented with 10 ng/mL of HGF, 20 ng/mL (R&D) of Oncostatin M (R&D), 10 nM of hydrocortisone (Sigma-Aldrich) and 1% GlutaMAX.

Endothelial differentiation was carried out following Cao *et al*. (Sriram *et al*., 2015), 2015 protocol, with few modifications. First, iPSs were plated at 1.5×10^4 /cm^2 and cultured for three days. For the next 5 days, basal media was comprised of supplemented Stempro 34 (Gibco) added with differentiation factor with daily media changes. In the first day, basal media was supplemented with 5 µM of CHIR99021. In the second day, media was added with 50 ng/mL of FGF-2. For the last three days, media was added with 50 ng/mL of VEGF and 25 ng/mL of BMP4. All recombinant factors was obtained from R&D systems. In the last day of differentiation, cells were magnetically sorted using anti-CD31 microbeads (Miltenyi), following manufacturer's instructions. Positives cells were plated in 60mm Matrigel coated dishes (Corning) and cultured for no more than 6 passages in human endothelial serum free media (Gibco) added with 10 ng/mL of VEGF, 20 ng/mL of FGF-2, 10 ng/mL of EGF and 1% of human platelet lysate.

Procedures for iNCC derivation were based on previously published methodology (Miller *et al*., 2015). Single cells iPS were seeded onto 60-mm Matrigel-coated dishes at 1×10^4 cells/cm^2. Two days post-seeding, medium was changed to iNCC differentiation medium, composed of Essential 6™ Medium (Life Technologies) supplemented with 8 ng/ml FGF-2, 20 µM SB431542 (TOCRIS), 1 µM CHIR99021 and 100 µg/ml Normocin. Differentiation medium was changed daily.. After ~2–4 days, neural crest-like cells were seen detaching from colony borders. The cells were split before reaching confluence, using Accutase. Cells were re-seeded into new 60mm Matrigel-coated dishes in fresh iNCC differentiation medium. Cells were passed whenever they reached 80% confluency, for 15 days. Differentiated iNCCs were cultivated for up to eight passages in iNCC differentiation medium, replenished daily. nMSC populations were obtained through culturing of iNCCs with mesenchymal stem cell medium, as previously described (Miller *et al.*, 2017). In brief, iNCCs were seeded at 2×10^4 cells/cm^2 onto non-coated 60-mm tissue culture dishes in nMSC medium (DMEM/F12 supplemented with 10% FBS, 2 mM GlutaMAX, 0.1 mM non-essential aminoacids and 100 µg/ml Normocin. Cells were differentiated for 6 days and passaged with TrypLE™ Express (Life Technologies) when needed. nMSC cultures were expanded in nMSC medium for up to 6 passages, with medium changes every 3 days.

2.8. Immunnofluorescence and flow-cytometry

For immunofluorescence analysis, cell cultures were fixed with 4% PFA for 20 minutes followed by permeabilization with 0.01% Triton X-100 for 30 minutes and blockage using 5% BSA in PBS for 1h. After that, the cells were incubated overnight with primary antibodies at 4°C and subsequently incubated with secondary antibodies

(see Supplementary Table 1) for 1h at room temperature. The final step was DAPI or Hoechst (Sigma) staining for 5 min at room temperature. Images were acquired using Nikon Eclipse microscope. The antibodies used in this study are described in Supplementary Table 1.

For flow cytometry analysis, Fixation and permeabilization were performed using a Fix & Perm Kit (Invitrogen) according to the manufacturer's instructions. To evaluate culture uniformity, cells were stained with conjugated primary antibody (see Supplementary Table 2) for 45 min in an ice bath, washed with 1× PBS, and then analyzed by Guava Flow cytometer (Merck). The experiment was performed collecting at least 10,000 events per group. After data acquisition, further analysis was performed using FlowJo software. Gate was set using isotype control.

2.9. LDL uptake, Basolateral-apical transport and amgiogenis assays

Alexa-488-labeled LDL (LDL) (Thermo) was added to a final concentration of 10 μg/mL to the cell media and incubated for 2h in 37°C. Plates were washed twice with DPBS and cell media was refilled. CDFDA (Sigma) was added to a final concentration of 10 μM to the cell media and incubated for 30 min in 37°C. Plates were washed twice with DPBS and cell media was refilled. Cellular uptake and transportation was evaluated in a fluorescence microscope (Nikon).

Matrigel (Corning) was diluted with EGM-2 (Lonza) 1:1 on ice. For coating a 24 well plate, 380 μl of diluted Matrigel were added to each well and incubated for 30 min at 37°C. Endothelial cells were plated at $5x10^5$ cells/well and cultured for 48h with EGM-2. The formation of a branched capillary bed was evaluated under phase contrast microscope.

2.10. RT-qPCR

Total RNA was isolated from cell culture using the RNeasy Mini Kit (Qiagen), following the manufacturer's recommendations. Briefly, 1µg of total RNA was converted into cDNA using Superscript II (Life Technologies) and oligo-dT primers according to the manufacturer's specifications. RT-qPCR reactions were performed with Power SYBR Green Master Mix (Life Technologies). Fluorescence was detected using the Applied Biosystem 7500 Real-Time PCR System, under standard temperature protocol. Primer pairs were either designed with PrimerBLAST (http://www.ncbi.nlm.nih.gov/tools/primer-blast/) or retrieved from PrimerBank (http://pga.mgh.harvard.edu/ primerbank/). Primers sequences are listed in Supplementary Table 3. Quantitative analyses were performed using a relative quantification curve with positive control and GAPDH as endogenous control. Primers sequences are listed in Supplementary Table 3.

2.11. Recellularization

Decellularized aorta tissue was placed in the bioreactor and perfused with culture media (Hepatic differentiation media 1:1 EGM-2) for 1 hour at 37°C. Matrigel was diluted 1:100 in culture media and perfused into the decellularized aorta for another hour. Since terminally differentiated hepatocyte in 2D are not suitable after passaging and have very poor ability to migrate we decided to print the liver construct using hepatoblasts. A final concentration of $2x10^7$ cells/cm of aortic section was obtained from a mixture of 75% hepatoblast, 20% iEC and 10% nMSC. Cells were injected into the aorta lumen in a final volume of 5 mL of cell suspension at 0.5 mL/min with 1 rpm.

Rotation was stopped for 12 hours with no perfusion. Finally, tissue was gently washed with 50 mL of culture media at 5 mL/mL and then cultured for 16 days at 5 mL/min at 80 mmHg and 5 rpm, with complete media changes every 3 days.

2.12. ELISA

Culture supernatant was collected every other day and stored at -80°C. The samples were thawed and centrifuged at 300g for 10 min to remove cellular debris. ELISA was performed accordingly to manufacturer's instructions.

2.13. Statistical analysis

Statistical Analyses was performed using two-tailed unpaired Student's t test. Data are shown as means ± SEM. Values of $p < 0.05$ were considered significant. GraphPad Prism software was used to perform the statistical analysis.

3. Results

iPS differentiation towards hepatocytes was confirmed by IF staining for hepatic markers UGT1A1 and CK19 at day 18 of the differentation protocol (Figure 1A). Also, 76,2% of cells expressed ALB (Figure 1E). Cultured iPS- derived hepatocytes were able to uptake LDL and to transport CDFDA into bile canaliculi. (Figure 1D and E). Gene expression of phase I biotransformation enzymes CYP1A1 and CYP3A4, and HNF1A and TDO2 during the in vitro differentiation confirmed the commitment towards hepatic phenotype (Figure 1F). iPS-derived endothelial cells stained positive for CD31 and

VECAD (Figure 1B) and are able to form capillaries in matrigel angiogenesis assay (Figure 1G). MSC-derived cells express P75, Vimentin and CD105 (Figure 1C and H).

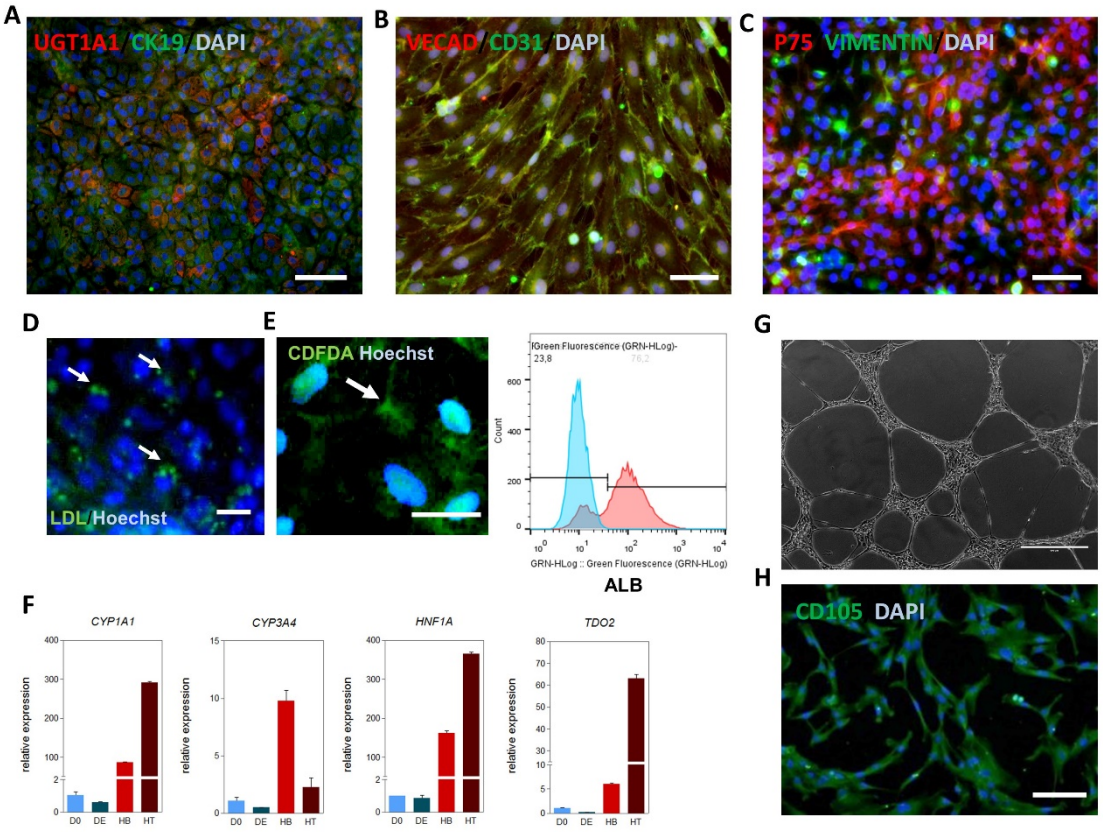

Figure 1: Characterization of *in vitro* iPS differentiation protocols. (A) IF staining for hepatic UGT1A1 and CK19 in iPs-derived hepatocytes. (B) IF staining for endothelial markers CD31 and VECAD in iPS-derived endothelial cells. (C) IF staining for mesenchymal markers P75 and Vimentin in iPS-derived MSC. (D) Hepatocyte LDL uptake. Arrow indicates stained intracelular vesicles. (E) CDFDA bile canaliculi staining. Arrow indicates bile canaliculi. (F) Step-wise RT-qPCR for hepatic markers CYP1A1, CYP3A4, HNF1A and TDO2 during differentiation. Bar = 50 µm. D0 = iPS, DE = Definitive endoderm, HB = Hepatoblast, HT = Hepatocyte.

The decellularization protocol of rat aortic tissue was characterized and validated (Figure 2). Histological staining by HE, Picrosirius and Alcian Blue revealed that the decellularization process was efficient in removing all cell nuclei, but preserving the residual extracellular matrix structure, as expected, including localization of collagen type I in aorta adventitia, the elastin fibers in the tunica media and residual

glyconsaminoglycans (Figure 2A-H). No apparent difference was observed in micro CT-scan comparing control and decellularized tissue (Figure 2I and J). Scanning electron microscopy showed that the collagens fibers in the tunica adventitia become more porously and loose as the cells are removed (Figure 2M and N). Tunica intima was preserved and the *vasa vasorum* became visible in the decellularized tissue (Figure 2M and N), which could facilitate cell migration during recellularization protocol. Tunica media became compacted with dispersed fibers between elastic sheets, as the cells were removed (Figure Q and U).

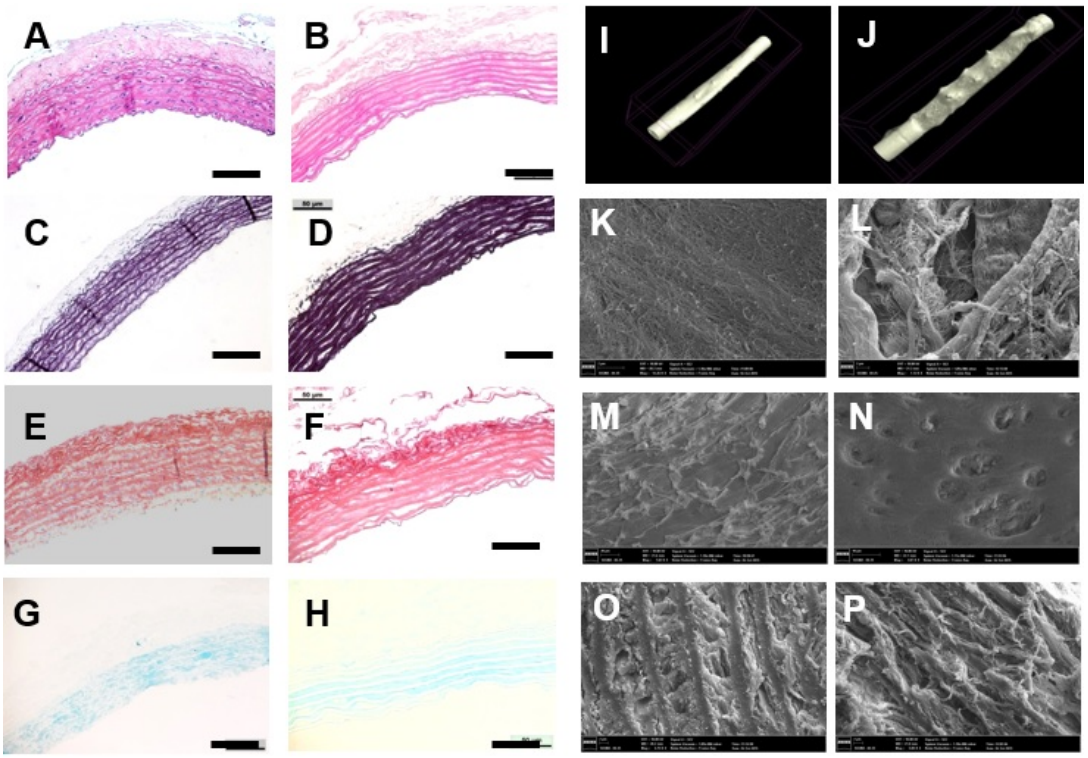

Figure 2: Characterization of rat aorta decellularization protocol. (A and B) H&E of normal and decellularized tissue respectively. (C and D) Reduced Resorcin-fuchsin staining of normal and decellularized tissue, respectively. (E and F) Picrossirius Red staining of normal and decellularized tissue, respectively. (G and H) Alcian blue staining of normal and decellularized tissue respectively. (I and J) Micro CT-scan of normal and decellularized tissue, respectively. (K and L) Scanning eletron microscopy of tunica adventitia of normal and decellularized tissue, respectively. (N and O) Scanning eletron microscopy of tunica intima of normal and decellularized tissue, respectively. (P and Q) Scanning eletron microscopy of tunica media of normal and decellularized tissue, respectively. Bar = 50 µm.

The analysis of the protein composition of the decellularized aortic matrix was

performed by immunohistochemistry (IHC) for the main extracellular matrix proteins, i.e. collagen I, collagen IV, fibronectin and laminin. It was observed that, in general, the presence and the localization of these proteins were maintained: Collagen I (tunica intima and adventitia), collagen IV (tunica media), fibronectin (tunica adventitia, media and intima) and laminin (tunica media) as shown in Figure 3A-H. The total residual tissue DNA at the end of the decellularization protocol was lower than immunogenicity threshold proposed in the literature of 50 ng DNA/mg tissue (9), as shown in Figure 3I.

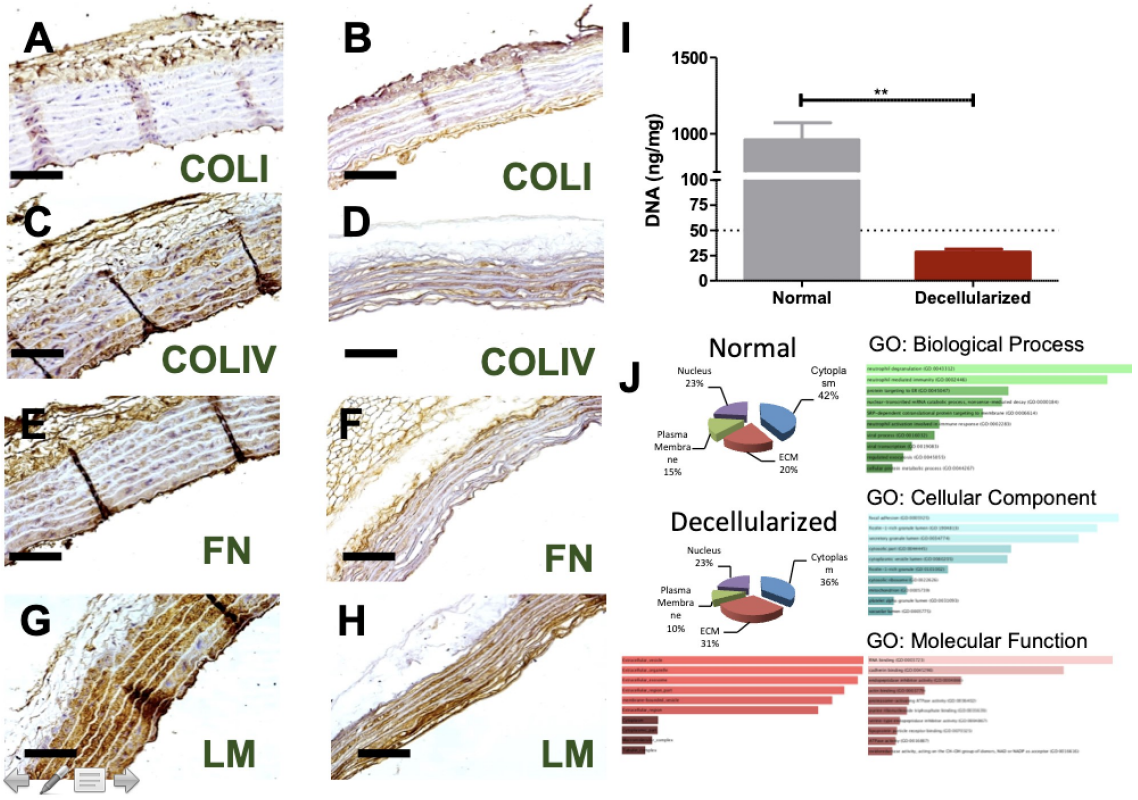

Figure 3: Evaluation of decellularized aortic tissue. A-H) Immunehistochemistry (IHC) of the main extra-cellular matrix proteins, the left the natural tissue and the direct the tissue at the end of the decellularization protocol. (A and B) IHC for Collagen I, of normal and decellularized tissue, respectively. (C and D) IHC for Collagen IV, of normal and decellularized tissue, respectively. (E and F) IHC for fibronectin, of normal and decellularized tissue, respectively. (G and H) IHC for pan-Laminin of normal and decellularized tissue, respectively. I) Residual DNA quantification. Bar = 50 µm. n=10 biological replicates. J) Proteomics analysis indicated by their localization and decellularized matrix top 10 siginificantly enriched pathways applying JENSEN_compartment, GO: biological Process, GO: Cellular Component and GO:Molecular function. **= $p<0.01$, Student t-test. COLI = Collagen type I, COLIV = Collagen type IV, FN = Fibronectin and LM = pan-Laminin.

It was observed that after 16 days of bioreactor-assisted culture the cells were able to form a tissue composed of a thick layer of cells, forming a hepatic neo-media with a discrete penetration of cells in the elastic lamina (Figure 4C and D). Also, the cells pushed the elastic tissue, thereby forming a neo-adventitia (Figure 4C). However, an homogeneous dispersion of the cells in the neo-tunica media along the aortic scaffold was not observed (Figure 4D). Tissue IF staining at day 16 showed a positive staining for the neo-media hepatic marker CK18 and for the neo-intima endotelial marker CD31, showing a preferential migration of endothelial cells during the recellularization process (Figure 4E). A1AT secretion was comparable to human primary hepatocyte levels already at the hepatoblast stage (Figure 4E). In addition, the quantification of hepatic proteins in the culture perfusate confirmed the terminal differentiation of seeded hepatoblasts. This was observed by the secretion of ALB starting at the seventh day after recellularization in perfusion culture, followed by a reduction of AFP, APOB100 and Urea secretion, reaching primary hepatocyte levels (Figure 4F).

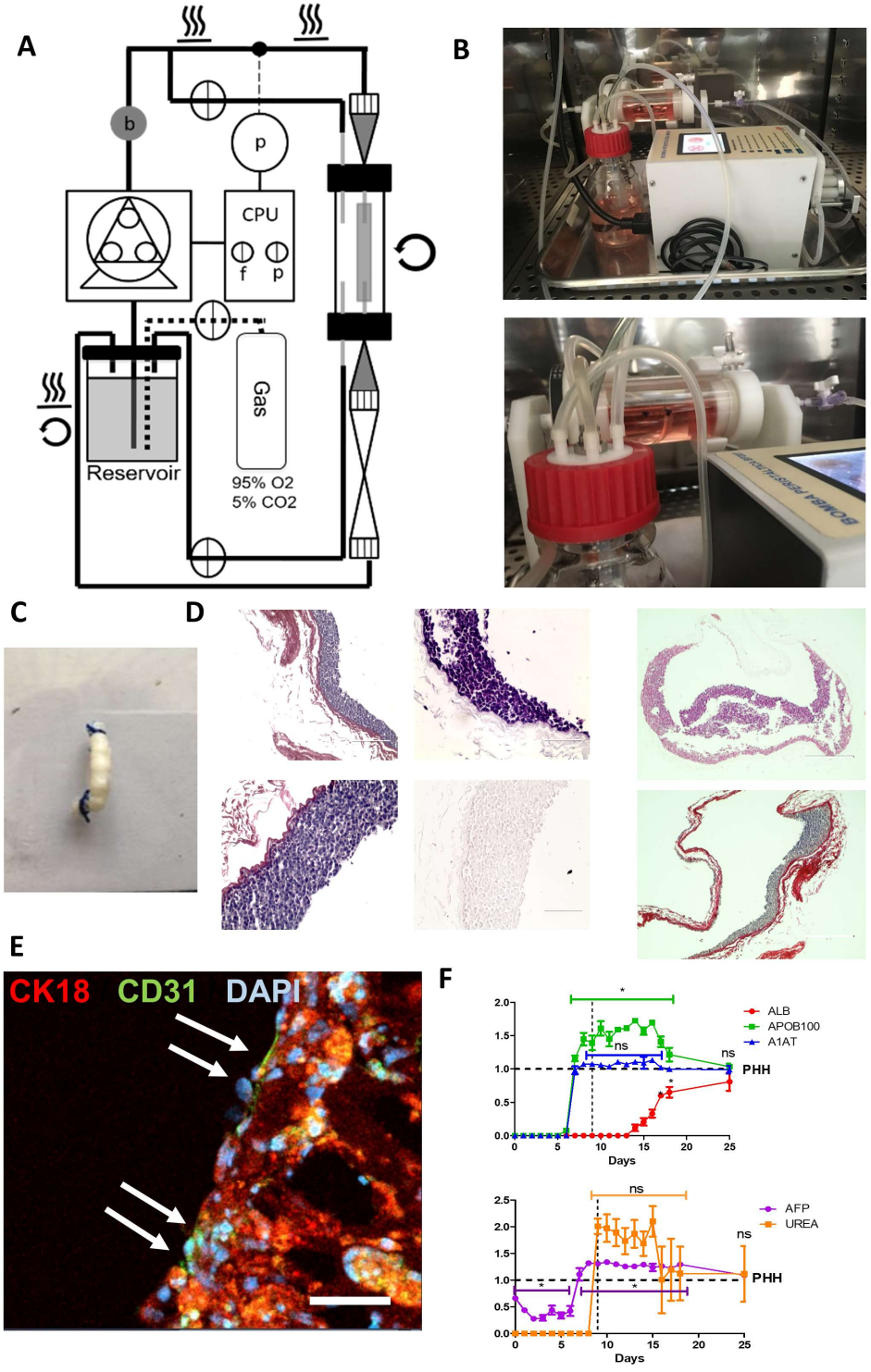

Figure 4: Recellularization of aortic scaffold. A) Schematic representation of the bioreactor design. B) Tissue culture in bioreactor-assisted condition, designed for this study. C) Photograph of the aortic tissue produced at the end of 16 days bioreactor-assisted culture experiment. D) Reduced Resorcin Fuchsin staining of recellularized aorta graft. E) IF staining of liver-aortic graft at day 16 for hepatic marker CK18 and endothelial CD31, Arrows indicate endothelial cells lined along the vascular lumen. F) ELISA and urea quantification assay from culture supernatant or perfusate. Data was normalized with 24 hours human primary hepatocyte culture supernatant at passage 2. Bar = 200 µm. *= $p<0.05$, Student t-test.

4. Discussion

iPS differentiation was achieved with success. Figure 1 shows that our protocol is able to generate fully functional hepatocyte that stained positive for CK18, UGT1A1 and ALB, and also express important hepatic markers such as *CYP1A1, CYP3A4 TDO2* and *HNF1A* (Figure 1A and F). Derived hepatocytes were also able to perform the endocytosis of LDL, the major carrier of cholesterol, (Figure 1D) showing that these cells express characteristic hepatic LDL receptors (Van de Sluis, *et al*. 2017). In addition, CDFDA assay showed that the cells were able to transform and transport the fluorescent-labeled molecule into the bile canaliculi, generated spontaneously in cell cultures (Figure 1E). Endothelial cells derived from iPS stained positive for CD31 and VECAD (Figure 1B and G) and were able to generate a thin capillary bed in matrigel angiogenesis assay, confirming the cellular phenotype. iPS-derived MSC stained positive for P75 and Vimentin, which confirms the neural crest origin of MSC differentiated cells (Miller *et al*., 2015) (Figure 1C). Also, MSC express mesenchymal marker CD105 (Figure 1H).

Rat thoracic aorta decellularization was characterized by histological analysis. H&E stain shows the complete removal of cellular component form the tissue (Figure 2A-B). Reduced Resorcin-Fuchsin staining showed the preservation of elastic laminae in tunica media after decellularization (Figure 2C and D). Picrossirrius red staining showed the preservation of collagen fibers in the tunica adventitia after the decellularization protocol (Figure 2E and F). Alcian blue shows that glycosaminoglycans are still present in the tunica media of decellularized tissue (Figure 2G and H). Micro CT-Scan showed the preservation of costal vascular branches and the vascular barrier property of decellularized tissue, observed by the ability to retain the

contrast agent intraluminal (Figure 2I an J). Scanning electron microscopy confirmed that the decellularization process makes the tunica adventitia fibers become looser, the elastic laminae in tunica media more compacted and the *vasa vasorum* communications in the tunica adventitia exposed. (Figure 2J-Q)

We also investigated whether the main extracellular matrix proteins were preserved at the end of the decellularization protocol. It was observed that all proteins tested by IHC were still present in their native tissue compartment at the end of the protocol (Figure 3A-H). Laminin and collagen IV are components of the basement membrane of epithelial cells and are also present surrounding the membrane of smooth muscle cells, the main cellular type of the tunica media (Hedin *et al*., 1988). On the other hand, collagen I and fibronectin are structural components of the intima and adventitia, and have the primary function of assisting in the mechanical resistance of the vascular wall (Beenakker *et al*., 2012) Additionally, DNA content was significantly reduced after the decellularizartion protocol (Figure 3I) which was considered complete when no cell nucleus were visible by H&E histological examination and when the residual DNA content was <50 ng/mg tissue (Soto-Gutierrez *et al*. 2011; Baptista *et al*. 2011; De Kock *et al*. 2011; Crapo *et al*., 2011).

As the decellularization process can remove important components for cell adhesion through the interaction of integrins with extracellular matrix proteins, the evaluation of the protein composition of decellularized matrices is very important to predict the success of recellularization protocols (Li *et al*., 2016). After decellularized, extracellular matrix protein ID was increased (Figure 3J) but most proteins ID identified are related to extracellular vesicles and proteins related to neutrophil degranulation (Figure 3J). This data indicates that the decellularized tissue contains many extracellular vesicles within its matrixes. It is not clear, however, if these reminiscent proteins are

capable of triggering immune response once transplanted.

Finally, the recellularization was performed and tissues were cultured in bioreactor-assisted perfusion protocol. Recellularized grafts were able to produce hepatic proteins such as ALB, AFP and A1AT in concentrations similar to primary human hepatocytes in culture (Figure 4F). Although the results are encouraging, the non-homogeneous dispersion of the cells in the tissue (most cells were deposited in the lower portion of the vascular lumen and into the elastic lamina) indicate that process requires improvement.

In short, we show that is possible to generate a functional liver accessory organ using an acelular aortic scaffold in combination with completely iPS-derived cells. However, the recellularization process needs to be optimized. In addition, future *in vivo* studies of the liver accessory shunt in an animal model of portal hypertension is needed to confirm the effectiveness of our approach.

Acknowledgments

We would like to thank the funding agencies FAPESP, CAPES and CNPq. Ernesto Goulart is a FAPESP grantee (2015/14821-1). We would like to thank LNBio/CNPEM and Fleury laboratory for the proteomics analysis. Authors have no conflict of interest to disclaim. This work is dedicated to Raúl Marcel González Garcia, *in memoriam*.

Supplemental information

Supplementary Tables

Supplementary Table 1 – Antibodies used for IF staining

Antibody	Catalog number	Host Specie	Assay dilution
Anti-CD105	ab156756	Mouse	1/100
Anti-CD31	ab119339	Mouse	1/100
Anti-CK18	ab32118	Rabbit	1/100
Anti-CK19	SAB4501670	Rabbit	1/100
Anti-P75	ab52987	Rabbit	1/100
Anti-UGT1A1	ab129729	Mouse	1/100
Anti-VECAD	ab33168	Rabbit	1/100
Anti-Vimentin	ab8978	Mouse	1/100
Donkey anti-Mouse Alexa 546	A10036	N/A	1/1000
Goat anti-Mouse Alexa 488	11001	N/A	1/1000
Goat anti-Rabbit Alexa 488	11034	N/A	1/1000
Goat anti-Rabbit Alexa 546	A11010	N/A	1/1000

Supplementary Table 2 - Antibodies used for flow-cytometry staining

Antibody	**Catalog number**	**Host Specie**	**Assay dilution**
Anti-ALB	ab106582	Chicken	1/100
Goat anti-Chicken Alexa 488	A0001	Goat	1/1000

Supplementary Table 3 – Primers sequences list

Gene	Foward	Reverse
HNF1A	GCAGCAGTTCACCCATGCAG	CGCCCCTTCTTGGTTGGTAG
CYP1A1	CCTTGGAACCTTCCCTGATCC	GATCTTGGAGGTGGCTGAGGT
TDO2	AGAGCTGGCCTACCTGAAGA	GCCCCTCAGCGTACTGATTT
CYP3A4	ATGGAAAAGTGTGGGGCTT	TCATGTCAGGATCTGTGATAGC

References

Adams, W. J., Zhang, Y., Cloutier, J., Kuchimanchi, P., Newton, G., Sehrawat, S., Aird, W. C., Mayadas, T. N., Luscinskas, F.W., García-Cardeña, G. Functional Vascular Endothelium Derived from Human Induced Pluripotent Stem Cells. Stem Cell Reports, v.1, p105-113. 2013.

Asgari, S. Moslem, M., Bagheri-Lankarani, K., Pournasr, B., Miryounesi, M., Baharvand, H. Differentiation and transplantation of human induced pluripotent stem cell-derived hepatocyte-like cells. Stem Cell Rev and Rep, v.9, p493–504. 2013.

Badylak, S. F. The extracellular matrix as a biologic scaffold material. Biomaterials, v.28, n.25, p3587-93. 2007.

Baptista, P. M., Siddiqui, M. M., Lozier, G., Rodriguez, S. R., Atala, A., Soker, S. The use of whole organ decellularization for the generation of a vascularized liver organoid. Hepatology v.53, n.2, p604-617. 2011.

Barakat, O., Abbasi, S., Rodriguez, G., Rios, J., Wood, R. P., Ozaki, C., Holley, L. S., Gauthier, P. K. Use of decellularized porcine liver for engineering humanized liver organ. J Surg Res, v.173, n.1, p11-25. 2012.

Binder, J. X., Pletscher-Frankild, S., Tsafou, K., Stolte, C., O'Donoghue, S. I., Schneider, R., Jensen, L. J. COMPARTMENTS: unification and visualization of protein subcellular localization evidence. Database (Oxford), v.2014, bau012. 2014.

Beenakker, J.W., Ashcroft, B. A., Lindeman, J. H., Oosterkamp, T. H. Mechanical properties of the extracellular matrix of the aorta studied by enzymatic treatments. Biophys J.v.102, n.8, p1731-7. 2012.

Cameron, K., Tan, R., Schmidt-Heck, W., Campos, G., Lyall, M. J., Wang, Y., Lucendo-Villarin, B., Szkolnicka, D., Bates, N., *et al*. Recombinant Laminins Drive the Differentiation and Self-Organization of hESC-Derived Hepatocytes. Stem Cell Reports, v.5, n.6, p1250-1262. 2015

Carnielli, C., Macedo, C., De Rossi, T., Granato, D., Rivera, C., Domingues, R., Pauletti, B., Yokoo, S., Heberle, H., *et al*. Combining discovery and targeted proteomics reveals a prognostic signature in oral cancer. Nat Commun, v.9, n.1, p359. 2018.

Crapo, P. M., Gilbert T. W., Badylak S. F. An overview of tissue and whole organ decellularization processes. Biomaterials v. 32, n.12, p3233-43. 2011.

De Kock, J., Ceelen, L., De Spiegelaere, W., Casteleyn, C., Claes, P., Vanhaecke, T., Rogiers, V. Simple and quick method for whole-liver decellularization: a

novel in vitro three-dimensional bioengineering tool? Arch Toxicol, v.85, n.6, p607-612. 2011.

Hedin, U., Bottger, B. A., Forsberg, E., Johansson, S., Thyberg, J. Diverse effects of fibronectin and laminin on phenotypic properties of cultured arterial smooth muscle cells. J Cell Biol. v.107, n.1, p307-19. 1988.

Jing, S., Schwartz, R. E., Ross, N. T., Logan, D. J., Thomas, D., Duncan, S. A., North, T. E., Goessling, W., Carpenter, A. E., et al. Identification of small molecules for human hepatocyte expansion and iPS differentiation. Nature chemical biology, v.9, p514-521. 2013.

Kanagavel, V. *et al*. Organ engineering using decellularized liver scaffold recellularized with iPSC-derived hepatocytes. The FASEB Journal (28):398-410 (2014).

Kondo, Y., Yoshihashi, S., Mimori, K., Ogihara, R., Kanehama, Y., Maki, Y., Enosawa, S., Kurose, K., Iwao, T., *et al*. Selective culture method for hepatocyte-like cells differentiated from human induced pluripotent stem cells. Drug Metabolism and Pharmacokinetics (DMPK), v.29, n.5, p407-13. 2014.

Kuleshov, M., Jones, M., Rouillard, A., Fernandez, N., Duan, Q., Wang, Z., Koplev, S., Jenkins, S., Jagodnik, K., *et al*. Enrichr: a comprehensive gene set enrichment analysis web server 2016 update. Nucleic Acids Res, v.8, W90-7. 2016.

Langer, R. & Vacanti J. P. Tissue engineering. Science, v.260, n.5110, p920-926. 1993.

Li, Q., Uygun, B. E., Geerts, S., Ozer, S., Scalf, M., Gilpin, S. E., Ott, H. C., Yarmush M. L., Smith, *et al*. Proteomic analysis of naturally-sourced biological scaffolds. Biomaterials, v.75, p37-46. 2016.

Mi, H. & Thomas P. PANTHER pathway: an ontology-based pathway database coupled with data analysis tools. Methods Mol Biol, v.563, p123-40. 2009.

Miller, E., Kobayashi, G., Musso, C., Allen, M., Ishiy, F., de Caires, L., Goulart, E., Griesi-Oliveira, K., Zechi-Ceide, R., and Richieri-Costa, A. *et al*. EIF4A3 deficient human iPSCs and mouse models demonstrate neural crest defects that underlie Richieri-Costa-Pereira syndrome. Human Molecular Genetics, v.26, p2177-2191. 2017.

Mitaka, T. The current status of primary hepatocyte culture. Int. J. Exp. Pathol, v.79, p393- 409. 1998.

Murray, K. F. & Carithers-Junior, R. L. AASLD Practice guidelines: evaluation of the patient for liver transplantation. Hepatology, v.41, n.6, p1-26. 2005.

Ott, H. C., Matthiesen, T. S., Goh, S. K., Black, L. D., Kren, S. M., Netoff, T. I., Taylor, D. A. Perfusion-decellularized matrix: using nature's platform to engineer a bioartificial heart. Nat Med, v.14, n.2, p213-221. 2008.

Ren, H., Shi, X., Tao, L., Xiao, J., Han, B., Zhang, Y., Yuan, X., Ding, Y. Evaluation of two decellularization methods in the development of a whole-organ decellularized rat liver scaffold. Liver International, v.33, n.3, p448-58. 2014.

Runge, D., Michalopoulos, G. K., Strom, S. C., Runge, D. M. Recent advances in human hepatocyte culture systems. Biochem. Biophys. Res. Commun, v.274, p1-3. 2000.

Soto-Gutierrez, A., Zhang, L., Medberry, C., Fukumitsu, K., Faulk, D., Jiang, H., Reing, J., Gramignoli, R, Komori, J., *et al*.. A whole-organ regenerative medicine approach for liver replacement. Tissue Eng Part C Methods, v.17, n.6, p677-686. 2011.

Sriram, G., Tan, J., Islam, I., Rufaihah, A., Cao, T.. Efficient differentiation of human embryonic stem cells to arterial and venous endothelial cells under feeder- and serum-free conditions. Stem Cell Research & Therapy, v.6., n.261. 2015.

Suk, K. T. & Kim, D. J. Staging of liver fibrosis or cirrhosis: The role of hepatic venous pressure gradient measurement. World J Hepatol, v.7, n.3, p607–615. 2015.

Takahashi, K., Tanabe, K., Ohnuki, M., Narita, M., Ichisaka, T., Tomoda, K., Yamanaka, S. Induction of pluripotent stem cells from adult human fibroblasts by defined factors. Cell, v.131, p961-872. 2007.

The Gene Onthology Consortium. The Gene Ontology Resource: 20 years and still GOing strong. Nucleic Acids Res, v.47, n.D1, D330-D338. 2019

Uygun, B. E., Soto-Gutierrez, A., Yagi, H., Izamis, M. L., Guzzardi, M. A., Shulman, C., Milwid, J., Kobayashi, N., *et al*. Organ reengineering through development of a transplantable recellularized liver graft using decellularized liver matrix. Nat Med, v.16, n.7, p814-820. 2010.

Van de Sluis, B., Wijers, M., Herz, J. News on the molecular regulation and function of hepatic LDLR and LRP1. Curr Opin Lipidol, v.28, n.3, p241–247. 2017.

Wang, Y., Alhaque, S., Cameron, K., Meseguer-Ripolles, J., Lucendo-Villarin, B., Rashidi H., Hay, D. C. Defined and Scalable Generation of Hepatocyte-like Cells from Human Pluripotent Stem Cells. J Vis Exp, v.2, n.121. 2017

Ying, A., Mich-Basso, J. D., Lin, B., Yang, L. High Efficient Differentiation of Functional hepatocytes from Porcine Induced Pluripotent Stem Cells. Plos One, v.9, n.6, e100417. 2014.

Capítulo 5:
Discussão geral e conclusões

Capítulo 5: Discussão geral e conclusões

Esta tese buscou, por meio de três abordagens diferentes, contribuir para o progresso das mais modernas tecnologias de engenharia tecidual hepática, utilizando para tal células derivadas de iPS. Primeiramente, vamos discutir os resultados obtidos durante a validação dos protocolos de diferenciação celular *in vitro* em hepatócitos, células endoteliais e MSC, que serviram como fonte celular para as abordagens utilizadas. Na sequência, será realizada uma discussão ampla sobre os resultados obtidos nos capítulos 2, 3 e 4.

Este trabalho utilizou três linhagens de células iPS diferentes, obtidas de doadores saudáveis, estabelecidas e armazenadas no biobanco do Centro de Estudos do Genoma Humano e Células Tronco da Universidade de São Paulo. As linhagens celulares foram testadas para avaliar a pluripotência, pela expressão dos marcadores OCT4 e SSEA4 e pela capacidade de gerar teratomas em animais imunodeficientes. A estabilidade cromossômica das linhagens foi testada por kit de MLPA com sondas subteloméricas. Os resultados indicam que todas as linhagens celulares utilizadas neste estudo eram comprovadamente pluripotentes e não apresentavam aneuploidias. Usando protocolos publicados na literatura, fomos capazes de gerar hepatócitos totalmente funcionais (tanto em 2D, quanto em 3D), células endoteliais e MSC, todas derivadas dos mesmos doadores.

Como já discutido no Capítulo 1, é importante ressaltar que hepatócitos terminalmente diferenciados não são capazes de sobreviver, ou preservar o fenótipo celular após poucas passagens (2-3), além de possuírem baixa capacidade de migração (Shulman & Nachmias, 2013). Assim sendo, decidimos imprimir as construções hepáticas e recelularizar o tecido aórtico usando hepatoblastos. O protocolo de produção

de organóides hepáticos utiliza, da mesma forma, uma mistura de hepatoblasto, células endoteliais e MSCs. Neste estágio da diferenciação, as células progenitoras hepáticas ainda possuem alta capacidade migratória, proliferativa e de adesão ao substrato, o que facilita sua aplicação. A diferenciação terminal foi alcançada durante a cultura *in vitro* das construções impressas, da maturação hepática dos organóides e do tecido aórtico funcionalizado.

As três linhagens celulares de iPS foram diferenciadas em hebatoblastos. Após indução da diferenciação em endoderme definitiva (via ativação de TGF-β e Wnt), representada pela expressão dos marcadores característicos FOXA2 e CXCR4, conseguimos derivar hepatoblastos funcionais. A expressão de HNF4A e AFP confirma a diferenciação em progenitor hepático. HNF4A é um fator de transcrição importante no controle da expressão de genes envolvidos na especificação e funcionalidade do fenótipo hepático, como o fator de transcrição HNF1A e os receptores nucleares PXR e CAR, que por sua vez controlam a expressão de enzimas metabólicas de fase I, como o CYP3A4, CYP2D6, etc (Hokakoski & Negishi, 2000). AFP é a globulina plasmática fetal produzida pelo fígado. Ao final da gestação e até os primeiros meses de vida a produção de AFP é substituída pela produção de albumina (Bader *et al*., 2004).

O potencial de diferenciação dos hepatoblastos em hepatócitos foi confirmado, após indução da diferenciação *in vitro*, pelo perfil de expressão de marcadores hepáticos, como A1AT, ALB, CYP3A4, ECAD, (Capítulo 2, Figura 1D), UGT1A1 (enzima de conjugação do metabolismo de fase II, utilizada para a conjugação da bilirrubina), CK18 (citoqueratina hepática) e pela coloração positiva no protocolo de ácido periódico de Schiff (PAS), que evidencia estoques intracelulares de glicogênio (resultado da oxidação de grupamentos glicóis em aldeídos, que após reação com reagente de Shiff, forma um precipitado rosa avermelhado) (Capítulo 3, Figura 1B e C).

A função hepática também foi avaliada pela captação e liberação do corante indocianina verde (ICG), comprovando o transporte basolateral e apical de hepatócitos. Estas células têm a capacidade de absorver o corante verde ICG pelo transportador OATP-C expresso exclusivamente na membrana basolateral do hepatócito e rapidamente excretar o composto pelo transportador apical do canalículo biliar MRP2 (Shimanada *et al.*, 2015). (Capítulo 2, Figura 1E). Foi observada a expressão gênica da enzima do metabolismo de fase I, *GSTA1* e *GSTA4* presentes no final da diferenciação hepática (Capítulo 2, Figura 1F). Quando os hepatócitos foram tratados com Omeprazol e Rifampicina, a indução da expressão gênica de *CYP1A2* e *CYP3A4*, respectivamente, foi confirmada (Capítulo 2, Figura 1G), o que comprova a capacidade de indução metabólica destas células, fenômeno hepático característico. Notavelmente, tanto a diferenciação hepática 2D como 3D compartilham o perfil de expressão de expressão gênica e protêica ao longo do protocolo (Capítulo 2, Figura 2A-C e Figura 2F-K). Observa-se que a diferenciação 3D gera esferóides celulares que possuem uma dispersão de tamanho homogênea (Capítulo 2, Figura 2D) e são ocos, formados por uma camada única de células epitelizadas e depositadas sobre uma fina camada de matriz extracelular (Capítulo 2, Figura 2E).

Para induzir a diferenciação em células endoteliais, primeiramente as células iPS foram diferenciadas em um fenótipo de mesoderme, induzida pela ativação de Wnt e FGF. A confirmação da diferenciação mesodermal foi avaliada pela expressão de GATA2 e BRACHYURY T, ambos fatores de transcrição característicos deste fenótipo celular (Lugus *et al*., 2007). Os resultados indicaram uma alta eficiência na indução da diferenciação mesodermal.

A diferenciação de células endoteliais foi inferida a partir da expressão de marcadores endoteliais gerais, como CD31 e CD34 (proteínas expressas em progenitores endoteliais), respectivamente um receptor vascular de adesão de plaquetas

e uma glicoproteína vascular. Já a co-expressão de VECAD e CD31 indica um fenótipo de células endoteliais maduras, sendo VECAD uma caderina vascular. A expressão gênica de marcadores específicos de células endoteliais arteriais como *NOTCH4* e níveis muito baixos de expressão de *PDPN* e *EPHB4* (marcadores de fenótipo linfático e venoso, respectivamente) (Kume, 2010) (Capítulo 2, Figura Suplementar 1E), confirmam um fenótipo arterial.

Como a diferenciação para células endoteliais apresentou, ao final do dia 6, um rendimento muito baixo (aproximadamente 15% de população duplo positivas para CD31 e CD34), foi realizada uma separação magnética para células CD31 positivas. Após 12 dias em cultura, as células apresentaram uma população homogênea para os marcadores de células endoteliais, VECAD e CD31. Como estas células são capazes de proliferar por até 5 passagens, foi possível expandir as culturas celulares após a separação magnética para gerar a quantidade suficiente de células para os experimentos subsequentes. A funcionalidade das células endoteliais derivadas foi demonstrada pela sua capacidade de absorver LDL acetilado (comprovando a atividade de *scavenger* vascular) (Capítulo 2, Figura 1K), de gerar capilares em Matrigel no ensaio de angiogênese (Capítulo 2, Figura 1J), pela expressão do fator de Von-Willebrand (Capítulo 2, Figura 1I), importante fator da cascata de coagulação. Por último, quando tratadas por 24h com 10 ng/mL TNF-α, citocina pró-inflamátoria, as células endoteliais superexpressaram significativamente ICAM1 simulando ativação/recrutamento neutrofílico (Capítulo 2, Figura 1M). Como explicado anteriormente, o painel de expressão gênica para os marcadores vasculares *PECAM1*, *NOTCH4*, *EFNB2* e *KDR* confirmou o fenótipo arterial (Capítulo 2, Figura 1L). Não está clara a contribuição diferencial, se houver, entre as células endoteliais arteriais, venosas ou linfáticas no desenvolvimento de tecidos por engenharia tecidual, em especial nas abordagens

utilizadas neste estudo. Assim, derivamos células arteriais, usando a linhagem comercial HAECs como a linhagem celular adulta correspondente.

Por fim, visando obter células MSC, utilizamos um protocolo desenvolvido pelo nosso grupo para a diferenciação em crista neural e posterior indução da diferenciação mesenquimal. A diferenciação em crista neural foi confirmada pela expressão de HNK1 e CD75 (Capítulo 2, Figura 1N). As MSC derivadas de iNCC expressam marcadores estromais-mesenquimais, como CD105, CD90 e CD73 (Capítulo 2, Figura 1N e O) e possuem potencial de diferenciação mesenquimal, observado após indução *in vitro* da diferenciação com protocolos comerciais (Gibco). Após 28 dias de diferenciação o potencial multipotente das células foi confirmado por ensaios de coloração e expressão gênica. O potencial osteogênico foi confirmado pela coloração com Vermelho de Alizarina (indicador de estoques de cálcio) e expressão de importante marcador osteogênico *BGLAP* (Capítulo 2, Figura 1P e Q). O potencial condrogênico foi confirmado pela coloração com Alcian Blue (coloração de glicosaminoglicanoa) e expressão de marcador de condrogênese tardia *COL2A1* (Capítulo 2, Figura 1P e Q). O potencial adipogênico confirmado pela coloração com Oil Red (coloração de vesículas lipídicas), e expressão de marcador de adipogênese tardia, *LPL* (Capítulo 2, Figura 1P e Q). Este resultado indica que derivamos com sucesso células mesenquimais multipotentes competentes e não fibroblastos. Para as células mesenquimais, usamos células mesenquimais de polpa dentária (dpMSC) como cultura de células primárias adultas correspondente, visto que possuem a mesma origem embrionária das iNCC-MSC.

O Capítulo 2 desta tese avaliou a utilização de células derivadas de células iPS para a bioimpressão 3D de tecido hepático, comparando a impressão de hepatócitos em dispersão celular individual (*single cell*) ou em agregados tridimensionais (esferóides).

A produção da biotinta, composta pela mistura de hidrogel de alginato/plurônico F-127, produziu uma matriz estável com maior porosidade em comparação com hidrogel de alginato, como descrito anteriormente na literatura (Armstrong *et al*., 2016). Além disso, a mistura dos dois polímeros aumentou a capacidade de impressão das construções utilizando concentrações reduzidas de cálcio e dos próprios polímeros (Capítulo 2, Figura 3A). A microscopia eletrônica de varredura revelou que a mistura de alginato/plurônico aumentou a porosidade média do material em comparação com o hidrogel de alginato, o que pode indicar uma melhor capacidade de difusão de nutrientes e metabólitos atravéz material (Capítulo 2, Figura 3B-D).

Quando impressas em 3D, as construções hepáticas contendo esferóides apresentaram sobrevida prolongada, redução da morte celular após a impressão, aumento da produção de uréia e secreção prolongada de albumina e A1AT ao longo do tempo de cultura (Capítulo 2, Figura 4A-H). Além disso, a construção impressa utilizando hepatócitos dispersos em *single cell* reduziu a expressão de importantes marcadores hepáticos e enzimas funcionais, o que indica uma perda significativa do fenótipo hepático (Capítulo 2, Figura 4I). A análise metabólica revelou um padrão distinto de metabólitos no sobrenadante da cultura no 18º dia. As vias mais enriquecidas estão relacionadas ao ciclo hepático da uréia e ao metabolismo de nitrogênio, indicando redução da atividade metabólica hepática em construções impressas com dispersão celular em *single-cell*. Os níveis de aspartato foram significativamente maiores nos esferóides (Capítulo 2, Figura 5C e D). Isso pode indicar um aumento da atividade da aspartato transaminase hepática, o que poderia explicar o aumento da secreção de uréia como ilustrado na Figura 4E (Capítulo 2), uma vez que o aspartato é fundamental no ciclo da uréia (Hussun *et al*., 2003). A análise proteômica mostrou que as proteínas identificadas que eram estatisticamente diferentes entre os grupos testados estão

relacionadas a vias do metabolismo de compostos nitrogenados e de ácidos graxos, indicando que o grupo impresso com esferóides era metabolicamente mais ativo que o grupo impresso em *single cell* (Capítulo 2, Figura 5E-H). A fim de avaliar como as construções impressas utilizando dispersão celular em *single-cell* perdem rapidamente o fenótipo hepático, realizamos uma série de RT-qPCR para importantes genes envolvidos na transição epitélio-mesênquima (EMT) (Capítulo 2, Figura 5I). No dia 18, a dispersão celular em *single-cell* reduziu a expressão dos marcadores epiteliais *CDH1* e *CDH2* e aumentou a expressão de *Vimentina* e *SNAIL2*, o que indica uma perda do fenótipo epitelial durante a diferenciação terminal e um aumento no fenótipo mesenquimatoso. Embora as caderinas mesenquimais *CDH6*, *CDH7* e *CDH11* não tenham alcançado significância estatística, o aumento da expressão de Vimentina e *SNAIL2* é indicativo de um aumento do fenótipo celular mesenquimal dentro das construções impressas (Kim *et al*., 2016). Sabe-se que, em diferentes lesões crônicas no fígado, os hepatócitos podem sofrer EMT parcial ou total e iniciar a fibrogênese (Baiocchini *et al*., 2016, Attallah *et al*., 2007). Esse processo contribui para o desenvolvimento de cirrose e consequente redução da função hepática (Baiocchini *et al*., 2016, Attallah *et al*., 2007).

Analisando em conjunto, estes dados indicam que a bioimpressão dos tecidos hepáticos utilizando esferóides tem função e viabilidade celular prolongada, em comparação com a dispersão em *single cell*. Nossos dados corroboram os achados de trabalhos anteriores, que demonstraram que células progenitoras hepáticas podem sobreviver por mais tempo em câmaras de perfusão vascularizadas quando implantadas como esferóides (Yap *et al*., 2013). Além disso, esses dados corroboram os achados de Rashidi e colaboradores (Rashidi *et al*., 2018) que mostram que os esferóides hepáticos 3D podem sustentar a função hepática em cultura por mais de um ano. Embora ainda

não esteja claro como os esferóides hepáticos podem sustentar o fenótipo celular por tanto tempo, acreditamos que nosso trabalho contribui para a noção bem estabelecida de que para o funcionamento do parênquima epitelial, fornecer um microambiente que mantenha as células epitelizadas é crucial (Xue *et al*., 2013; Choi & Diehl, 2009). Nossos resultados indicam que células hepáticas derivadas de iPS quando cultivadas em um microambiente 3D de baixa densidade celular, que não permite a sinalização dependente de contato célula-célula, induz EMT e um fenótipo pró-fibrótico, que não possui funcionalidade hepática adequada, reduzindo sua viabilidade celular ao longo do tempo.

O Capítulo 3 desta tese, avaliou a influência da composição celular de organóides hepáticos com diferentes combinações de células adultas e derivadas de iPS. A geração de organóides hepáticos foi comparada variando a composição de células não parenquimáticas (NPC). Não foram observadas diferenças na taxa de condensação mesenquimal e na morfologia entre todos os grupos testados (Capítulo 3, Figura 2A e B). Os dados de RT-qPCR no dia 12 (Capítulo 3, Figura 2C) revelaram que, embora seja notável uma variação intrínseca entre as linhagens celulares testadas, genes importantes relacionados ao metabolismo da fase I hepático (i.e. *CYP1A2* e *CYP1A1*) e II (i.e. *GSTA1*) foram superexpressos no grupo IIP. Estes dados indicam que a taxa metabólica hepática é maior na presença de MSC adultas associada a células endoteliais derivadas de iPS e reduzida na presença de endoteliais adultas. A expressão dos genes *ALB* e *TDO2* também são significativamente elevadas no grupo IIP, o que sugere um aumento da maturação hepática. Além disso, um aumento significativo na secreção de albumina no sobrenadante de cultura foi observado no grupo IIP no dia 12 (Capítulo 3, Figura 2C) em comparação com IPI e IPP, mas não em comparação com o grupo III. A expressão do gene *AFP* foi significativamente reduzida no grupo IIP em comparação

com IPI e IPP, mas não comparado ao grupo III. O aumento da secreção de albumina e a redução da secreção de AFP é um dos marcadores mais comumente utilizado para indicar a maturação de hepatócitos (Ang *et al*., 2018; Roll & Willenbring, 2010; Peters *et al*., 2016). A secreção de AA1T e LDH não se mostrou alterada entre os grupos nos dias testados (Capítulo 3, Figura Suplementar 1F).

Para avaliar a influência das NPCs nas vias de sinalização relevantes para o desenvolvimento de organóides hepáticos, foi realizada uma série de ensaios de Western Blotting (Capítulo 3, Figura 3A) para as principais vias utilizadas durante este processo. A análise da atividade proteica revelou que os grupos III e IIP, que produziram mais albumina em comparação aos grupos IPI e IPP, exibiram atividade significativamente menor do TGF-β (Capítulo 3, Figura 3B). Além disso, o grupo IIP apresenta uma atividade significativamente menor de Wnt (Capítulo 3, Figura 3D). O grupo III possui atividade de ERK1/2 aumentada (Capítulo 3, Figura 3C). Acredita-se que o FGF, secretado pela mesoderme adjacente, seja o principal ativador da sinalização de MAPK durante esse período do desenvolvimento embrionário (Si-Tayeb *et al*., 2011).

Nenhuma diferença foi observada na sinalização de Notch e BMP4 (Capítulo 3, Figura 3E e F, respectivamente). Combinados, esses dados indicam que as células NPCs possuem contribuições diferentes no desenvolvimento de organóides hepáticos, e regulam importantes sinais celulares envolvidos no desenvolvimento hepático, como TGF-β e Wnt. A Figura 3H (Capítulo 3) compila as informações obtidas na análise de Western Blotting. Trabalhos prévios demonstraram que a inibição do TGF-β aumenta a produção *in vitro* de albumina de organoides hepáticos, induz a maturação de hepatócito e está correlacionada com os níveis de O2 durante a organogênese do fígado (Ayabe *et al*., 2018; Ng *et al*., 2018). Além disso, sabe-se que a inibição da sinalização de Wnt induz a diferenciação de hepatócitos e reprime a diferenciação em colangiócito em

cultura 3D (Pettinato *et al*., 2016). A inibição combinatória de Wnt e TGF-β aumentou significativamente a expressão de albumina, o oposto do observado quando essas duas vias foram ativadas (Capítulo 3, Figura 3D).

A fim de avaliar o resultado da contribuição diferencial da NPCs durante o desenvolvimento de organóides hepáticos e identificar as principais diferenças e reguladores da função hepática, realizamos um perfil proteômico global dos tecidos gerados. Mesmo compartilhando a maioria das proteínas identificadas (Capítulo 3, Figura 4A), as fontes de células NPCs mostraram influênciar significativamente o tecido final (Capítulo 3, Figura 4B). Após obter uma lista de proteínas diferencialmente expressas, observamos que a maioria das vias enriquecidas estão relacionadas à organização da matriz extracelular e à sinalização da integrinas (Capítulo 3, Figura 4C-E). O receptor de ligação à fibronectina ITGAV (integrina receptor alfa V) e ITGA5 (integrina receptor alfa 5) foram um dos principais achados identificados na análise de enriquecimento de vias. Sabe-se que as subunidades de integrina α5 (ITGA5) e a β1 (ITGB1) são necessárias para a formação do trato do epitélio do ducto biliar no desenvolvimento do fígado (Tanimizu *et al*., 2012). A integrina β1 é fundamental para manter a viabilidade dos hepatócitos na matriz extracelular nativa e está implicada na regeneração hepática (Speicher *et al*., 2014; Pinkse *et al*., 2004). É importante ressaltar que a diversidade de combinações de subunidades de integrina durante a organogênese do fígado ajuda a gerar as diferentes estruturas hepáticas, influenciadas pelo desenvolvimento sinusoidal e vascular periférico e a pela matriz extracelular local (Shiojiri & Sugiyama, 2004). Coletivamente, a expressão de integrina beta1, mas não alfa V, resultado da sinalização celular atribuida a células endoteliais derivadas de iPS e dpMSC, podem explicar as diferenças observadas na função dos hepatócitos nos

organóides. É importante ressaltar que a transcrição das subunidades da integrina é induzida e regulada pela via de TGF-β (Munger & Sheppard, 2011).

Assim, nossos dados indicam que o efeito combinatório da atividade reduzida de TGF-β e Wnt é responsável pelo aumento da maturação hepática, observada na combinação de dpMSC e células endoteliais arteriais derivadas de iPS como fonte de células NPCs para geração de organóides hepáticos. Curiosamente, mesmo que as MSC constituam apenas a minoria da composição celular total no modelo de organóides hepáticos (i.e. 10%), a sua presença tem um impacto significativo na função e maturação destas estruturas.

Por último, o Capítulo 4, demonstra o desenvolvimento de uma nova abordagem para o tratamento da hipertensão portal, utilizando a recelularização de um arcabouço aórtico com células derivadas de iPS. A descelularização da aorta torácica de rato foi caracterizada por análise histológica. O processo de descelularização se mostrou eficiente visto que preserva os constituintes da matriz extracelular e é capaz de remover todo o conteúdo celular do tecido (Capítulo 4, Figura 2A-P e Figura 3A-H). Além disso, o conteúdo de DNA residual foi significativamente reduzido após o protocolo de descelularização (Capítulo 4, Figura 3I), o que é um indicativo do sucesso do procedimento, mesmo com a presença de resíduos celulares evidenciados pelo estudo de proteômica (Capítulo 4, Figura 3J).

Finalmente, o ensaio de recelularização, realizado com um protocolo de perfusão assistida por biorreator, desenvolvido neste trabalho, foi caracterizado *in vitro*. Os tecidos gerados foram capazes de produzir proteínas hepáticas, como ALB, AFP e A1AT em concentrações semelhantes aos de hepatócitos humanos primários em cultura (Capítulo 4, Figura 4F). Embora os resultados sejam encorajadores, a dispersão não homogênea das células no tecido (a maioria das células foi depositada na porção inferior

do lúmen vascular e também na lâmina elástica), indicam que o processo precisa ser melhorado (Capítulo 4, Figura 4C-E).

Como mostrado no Capítulo 2, usando uma biotinta de alginato/plurônico, demonstramos que a impressão 3D utilizando hepatócitos cultivados em sistema tridimensional (esferóides) e células NPCs, todas derivadas de células iPS, permite aumentar significativamente a função hepática e a sobrevida do tecido. Além disso, a dispersão unicelular de células do parênquima hepático induz EMT e um conversão celular em um fenótipo pró-fibrótico. Estas observações provêm informações importantes que podem contribuir significativamente para o desenvolvimento de futuras aplicações de engenharia tecidual hepática usando bioimpressão 3D de células derivadas de iPS humanas.

Além disso, no Capítulo 3, mostramos que a fonte celular de células NPCs desempenha um papel significativo no desenvolvimento de organóides hepáticos, e afeta a funcionalidade final do tecido gerado, por alterar vias de sinalização que regulam a maturação hepática. A análise proteômica gerou informações relevantes sobre como a células NPCs obtida de tecidos adultos, ou de iPS, afetam a formação dos organóides hepáticos. Coletivamente, nossos dados corroboram as descobertas de estudos anteriores sobre como diferentes fontes de células NPCs podem influenciar a função de organóides hepáticos e fornece contribuições para explicar os mecanismos envolvidos durante a crucial etapa de maturação hepática. Observamos que tal regulação ocorre através da sinalização diferencial de TGF-β e Wnt, que produzem mudanças substanciais no perfil de integrinas que regulam a organogênese hepática. Este trabalho pode ser útil na avaliação de estratégias futuras para unir a tecnologia de organóides com a triagem em larga escala de drogas e, também, em abordagens de medicina regenerativa.

Por último, no Capítulo 4, os resultados indicam que é possível gerar um fígado funcional acessório usando um arcabouço aórtico acelular em combinação com células derivadas de iPS. No entanto, o processo de recelularização precisa ser otimizado. Além disso, futuros estudos *in vivo* em um modelo animal de hipertensão portal são necessários para confirmar a eficácia da nossa abordagem.

Em conclusão, este trabalho conseguiu prover importantes informações que podem ajudar no desenvolvimento das atuais tecnologias de engenharia tecidual. Espera-se que os mecanismos aqui descritos possam ser devidamente validados e aprofundados em estudos futuros.

Referências

Ang, L., Tan, A., Autio, M., Goh, S., Choo, S., Lee, K., Tan, J., Pan, B., Lee, J., *et al*. A Roadmap for Human Liver Differentiation from Pluripotent Stem Cells. Cell Rep, v.22, p2190-2205. 2018.

Armstrong, J. P., Burke, M., Carter, B. M., Davis, S. A., Perriman, A. W. 3D Bioprinting Using a Templated Porous Bioink. Adv Healthc Mater, v.5, n.14, p1724-30. 2016.

Attallah, A. M., Mosa, T. E., Omran, M. M., Abo-Zeid, M. M., El-Dosoky, I., Shaker, Y. M. Immunodetection of collagen types I, II, III, and IV for differentiation of liver fibrosis stages in patients with chronic HCV. J Immunoassay Immunochem, v.28, n.2, p155-68. 2007.

Bader, D., Riskin, A., Vafsi, O., Tamir, A., Peskin, B., Israel, N., Merksamer, R., Dar, H., David, M. Alpha-fetoprotein in the early neonatal period--a large study and review of the literature. Clin Chim Acta, v.349, n1-2, p15-23. 2004.

Baiocchini, A., Montaldo, C., Conigliaro, A., Grimaldi, A. Correani, V., Mura, F. Ciccosanti, F., Rotiroti, N., Brenna, A., *et al*. Extracellular Matrix Molecular Remodeling in Human Liver Fibrosis Evolution. PLoS One, v.11, n.3, e0151736. 2016.

Choi, S. S. & Diehl, A. M. Epithelial-to-mesenchymal transitions in the liver. Hepatology, v.50, n.6, p2007-13. 2009.

Honkakoski, P. & Negishi, M. Regulation of cytochrome P450 (CYP) genes by nuclear receptors. Biochem J, v.47, n.2, p321–337. 2000.

Husson, A., Brasse-Lagnel, C., Fairand, A., Renouf, S., Lavoinne, A. Argininosuccinate synthetase from the urea cycle to the citrulline-NO cycle. Eur J Biochem, v.270, n.9, p1887-99. 2003.

Kim H. M., Kim, J. W., Choi, Y., Chun, H. S., Im, I., Han, Y. M., Song, C. W., Yoon, S., Park, H. J. Xeno-sensing activity of the aryl hydrocarbon receptor in human pluripotent stem cell-derived hepatocyte-like cells. Sci Rep, v.6, n.21684. 2016.

Kume, T. Specification of arterial, venous, and lymphatic endothelial cells during embryonic development. Histol Histopathol, v.25, n.5, p637–646. 2010.

Lamouille, S., Xu, J., Derynck, R. Molecular mechanisms of epithelial-mesenchymal transition. Nat Rev Mol Cell Biol, v.15, n.3, p178-96. 2014.

Lugus J. J., Chung, Y. S., Mills, J. C., Kim, S. I., Grass, J., Kyba, M., Doherty, J. M., Bresnick, E. H., Choi, K. GATA2 functions at multiple steps in hemangioblast development and differentiation. Development, v.134 n.2, p393-405. 2007.

Munger, J. & Sheppard, D. Cross talk among TGF-β signaling pathways, integrins, and the extracellular matrix. Cold Spring Harb Perspect Biol, v.3, a005017. 2011.

Peters, D., Henderson, C., Warren, C., Friesen, M., Xia, F., Becker, C., Musunuru, K., Cowan, C. Asialoglycoprotein receptor 1 is a specific cell-surface marker for isolating hepatocytes derived from human pluripotent stem cells. Development, v.143, p1475-81. 2016.

Pinkse, G. G., Voorhoeve, M. P., Noteborn, M., Terpstra, O. T., Bruijn, J. A., De Heer, E. Hepatocyte survival depends on beta1-integrin-mediated attachment of hepatocytes to hepatic extracellular matrix. Liver Int, v.24, n.3, p.218-26. 2004.

Rashidi, H., Luu, N. T., Alwahsh, S. M., Ginai, M., Alhaque, S., Dong, H., Tomaz, R. A., Vernay, B., Vigneswara, V., *et al*. 3D human liver tissue from pluripotent stem cells displays stable phenotype in vitro and supports compromised liver function in vivo. Arch Toxicol, v.92, n.10, p3117-3129. 2018.

Roll, G. & Willenbring, H. Transplanted nonviable human hepatocytes produce appreciable serum albumin levels in mice. Stem Cell Res, v.5, p267-70. 2010.

Shimada, S., Ohtsubo, S., Ogasawara, K., Kusano, M. Macro- and microscopic findings of ICG fluorescence in liver tumors. World Journal of Surgical Oncology, v.13, n.1). 2015.

Shiojiri, N. & Sugiyama, Y. Immunolocalization of extracellular matrix components and integrins during mouse liver development. Hepatology, v.40, n.2, p346-55. 2004.

Shulman, M. & Nahmias, Y. Long-Term Culture and Coculture of Primary Rat and Human Hepatocytes. Methods Mol Biol, v.945, p287–302. 2013.

Speicher, T., Siegenthaler, B., Bogorad, R. L., Ruppert, R., Petzold, T., Padrissa-Altes, S., Bachofner, M., Anderson, D. G., Koteliansky, V., *et al*. Knockdown and knockout of β1-integrin in hepatocytes impairs liver regeneration through inhibition of growth factor signalling. Nat Commun, v.21, n.5, p3862. 2014.

Tanimizu, N., Kikkawa, Y., Mitaka, T., Miyajima, A. α1- and α5-containing laminins regulate the development of bile ducts via β1 integrin signals. J Biol Chem. v.287, p28586-97. 2012.

Xue, Z. F., Wu, X. M., Liu, M. Hepatic regeneration and the epithelial to mesenchymal transition. World J Gastroenterol, v.19, n.9, p1380-6. 2013.

Yap K. K., Dingle, A. M., Palmer, J. A., Dhillon, R. S., Lokmic, Z., Penington, A. J., Yeoh, G. C., Morrison, W. A., Mitchell, G. M. Enhanced liver progenitor cell survival and differentiation in vivo by spheroid implantation in a vascularized tissue engineering chamber. Biomaterials, v.34, n.16, p3992-4001. 2013.

6. Resumo

Atualmente, a única alternativa viável para pacientes que possuem um quadro de doença hepática em estágio final é o transplante total ou parcial de fígado. Devido à crescente defasagem entre doadores disponíveis e pacientes em fila de espera, o desenvolvimento de abordagens de engenharia tecidual hepática (ETH) se tornou uma necessidade crescente. As células pluripotentes induzidas (iPS) são uma atraente alternativa para servirem como fonte celular para aplicações de engenharia tecidual por serem capazes de produzir todos os fenótipos celulares. Dentre as principais abordagens de EHT podemos citar as técnicas de bioimpressão 3D, organóides hepáticos e descelularização/recelularização. Este trabalho buscou avaliar a utilização de células iPS no desenvolvimento das três tecnologias descritas. Visando avaliar como imprimir um tecido hepático funcional com células iPS, testamos a impressão com hepatócitos dispersos em células únicas em comparação com a impressão de esferóiedes hepáticos. Os esferóides hepáticos mostraram maior viabilidade e funcionalidade hepática por preservarem o fenótipo epitelial ao longo do tempo. A composição de células não parenquimáticas derivadas de iPS ou células primárias para a formação de organóides hepáticos foi testada neste trabalho. Os resultados indicam que, utilizando células mesenquimais primárias e endoteliais derivadas de iPS, obtém-se uma maturação hepatica mais eficiênte devido a inibição das vias de sinalização TGF-β e modulação da via Wnt. A recelularização do tecido aórtico descelularizado de ratos com células derivadas de iPS mostrou ser capaz de prover função hepática em cultura assistida por biorreator, porém os resultados indicam a necessidade de aprimoramento do protocolo de recelularização. Este trabalho comprovou a viabilidade da aplicação de células iPS nas abordagens EHT testadas e contribuiu para o desenvolvimento de alternativas terapêuticas viáveis para pacientes em fila de espera de transplante hepático.

7. Abstract

Currently, the only feasible alternative for patients with end-stage liver disease is total or partial liver transplantation. Due to the growing gap between available donors and patients in waiting list, the development new tissue engineering technologies have become a growing need. Induced pluripotent cells (iPS) are an attractive alternative to serve as cell source for tissue engineering applications due to their ability to differentiate into all cellular phenotypes. Among the main liver tissue engineering technologies, 3D bioprinting, hepatic organoids and decellularization/recellularization of biological matrixes have generated much expectation. Thus, this work aimed to evaluate the use of iPS cells in the development of the aforementioned technologies. In order to evaluate how to bioprint a functional liver tissue using iPS-derived cells, we tested the effect of printing a single cell dispersion of hepatocytes versus printing hepatic spheroids. Hepatic spheroids showed greater viability and liver function, due to preserved epithelial phenotype over time. The composition of non-parenchymal cells using iPS-derived cells or primary adult cells for hepatic organoid formation was tested. The results indicated that, using primary mesenchymal cells and iPS-derived endothelial cells, we obtained a more efficient hepatic maturation due to the inhibition of TGF-β and modulation Wnt signaling pathway. Recellularization of rat aortic decellularized scaffold with iPS-derived cells displayed hepatic function over time in a bioreactor-assisted culture, but the results indicate the need for improvements in the recellularization protocol. In conclusion, this work demonstrated the feasibility of use of iPS-derived cells for liver tissue engineering approaches and contributed to the development of the investigated technologies in order to generate future therapeutic alternatives for patients in waiting list for liver transplantation.

8. Anexos

8.1. Resultados e padronizações adicionais

8.1.1. Padronização da diferenciação celular in vitro de hepatócitos e células endoteliais

Visando avaliar o rendimento e a eficiência dos protocolos usados para diferenciar as linhagens de células iPS em hepatócitos e células endoteliais, foi realizado um estudo da expressão das proteínas marcadoras de cada etapa dos protocolos adotados, por imunofluorecência. O objetivo foi avaliar a progressão da mudança de fenótipo celular e possíveis contaminantes celulares de fenótipos em amadurecimento, ou seja, que ainda não terminaram sua completa diferenciação na etapa seguinte.

Metodologia

As culturas celulares foram fixadas com PFA a 4% durante 20 minutos, seguida por permeabilizaçãoo com Triton X-100 a 0,01% durante 30 minutos e bloqueio utilizando BSA a 5% (m/v) em PBS durante 1h. Depois disso, as células foram incubadas durante *overnight* com anticorpos primários a 4°C e subsequentemente incubadas com anticorpos secundários (ver Tabela 1) durante 1 h à temperatura ambiente. Ao final foi realizada a coloração com DAPI (Sigma) durante 5 min à temperatura ambiente. As imagens foram adquiridas usando o microscópio Nikon Eclipse. Os anticorpos utilizados neste estudo estão descritos na Tabela 1.

Resultados e Discussão

Os resultados mostrados a seguir confirmam a direcionalidade do processo de diferenciação e a inexistência de células pluripotentes ao final dos protocolos, importante para confirmar a segurança das eventuais aplicações em humanos destas células. Observa-se que a maioria das células perdem a epxressão completa dos marcadores de pluripotência no dia 9. Já os marcadores de células de endoderme definitiva não são mais expressos ao final do protocolo de diferenciação. Em contraste, ainda é observada uma expressão residual dos marcadores de células progenitoras hepáticas (AFP e HNF4) ao final do dia 18.

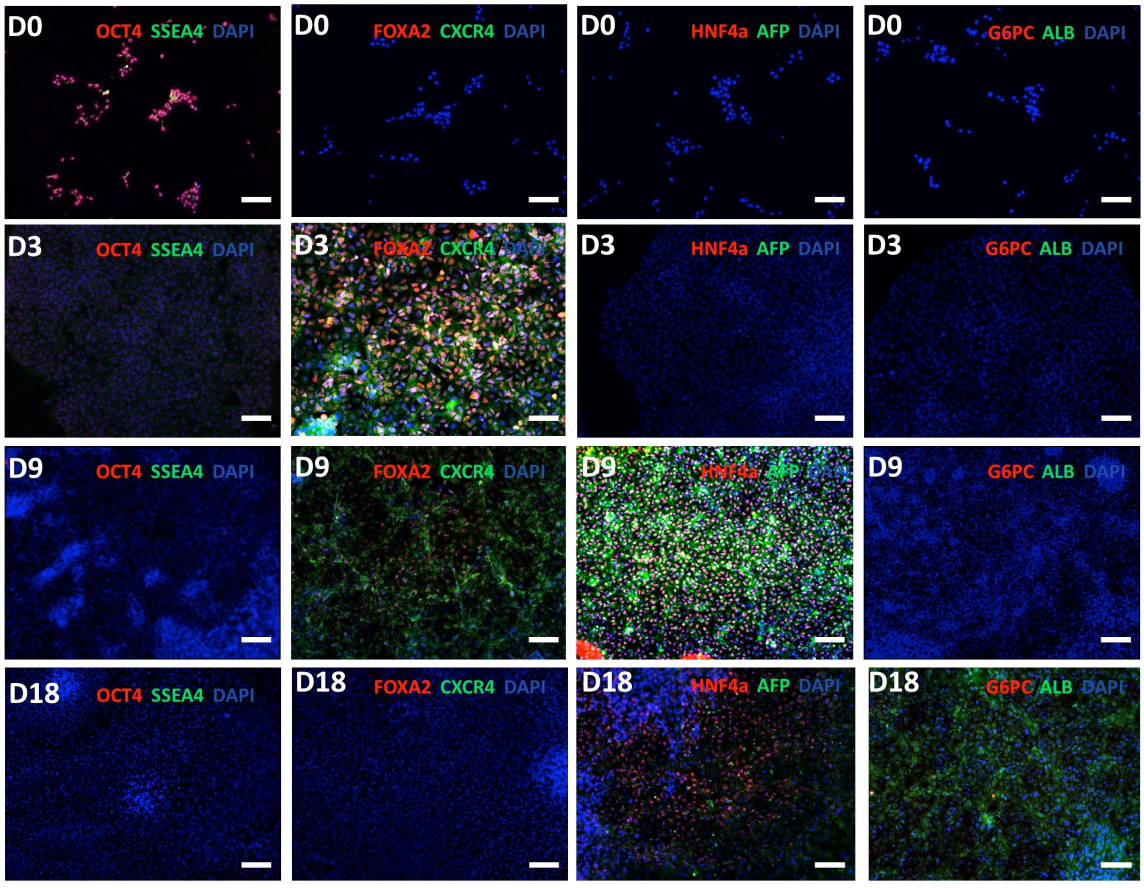

Figura 1: Expressão das proteínas marcadoras da das etapadas da diferenciação de hepatócitos em cultura. Linhas representam os marcadores das etapadas de diferenciação, em cada dia. Os marcadores utilizados foram: Pluripotência (SSEA4 e OCT4), Endoderme Definitiva (CXCR4, FOXA2), Hepatoblasto (AFP e HNF4) e Hepátócito (ALB e G6PC). Nas colunas estãos os dias representativos do final do processo de diferenciação para cada par de marcadores. Barra = 50 µm.

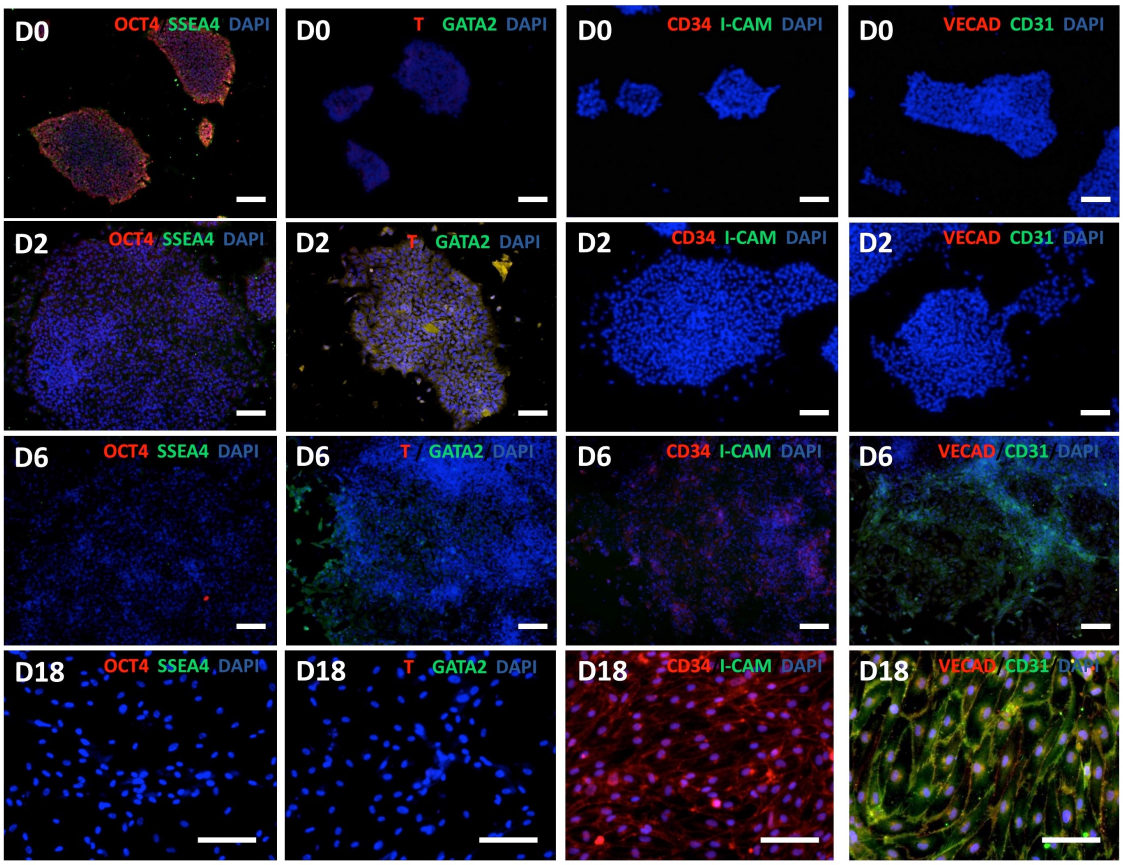

Figura 2: Expressão das proteínas marcadoras da das etapadas da diferenciação de células endoteliais em cultura. Linhas representam os marcadores das etapadas de diferenciação, em cada dia. Os marcadores utilizados foram: Pluripotência (SSEA4 e OCT4), Mesoderme (T, GATA2), Progenitor Endotelial (CD34 e ICAM-1) e Células Endoteliais (CD31 e VECAD). Nas colunas estãos os dias representativos do final do processo de diferenciação para cada par de marcadores. Barra = 50 µm.

Tabela 1: Lista de Anticorpos

Antibody	Catalog number	Host Specie	Assay dilution
Anti-CD34	ab86950	Rabbit	1/100
Anti-AFP	PA5 21-004	Rabbit	1/100
Anti-ALB	ab10241	Mouse	1/100
Anti-G6PC	ab156756	Mouse	1/100
Anti-CD31	ab119339	Mouse	1/100
Anti-T	ab167337	Mouse	1/100
Anti-GATA2	LS-C166381	Mouse	1/100

Anti-CXCR4	ab124824	Rabbit	1/100
Anti-FOXA2	ab60721	Mouse	1/100
Anti-HNF4	ab41898	Mouse	1/100
Anti-OCT3/4	ab19857	Rabbit	1/100
Anti-SSEA4	ab16287	Mouse	1/100
Anti-VECAD	ab33168	Rabbit	1/100
Donkey anti-Mouse Alexa 546	A10036	N/A	1/1000
Goat anti-Mouse Alexa 488	11001	N/A	1/1000
Goat anti-Rabbit Alexa 488	11034	N/A	1/1000
Goat anti-Rabbit Alexa 546	A11010	N/A	1/1000

8.1.2. Padronização de modelo murino de hipertensão portal

Visando a aplicação da tecnologia gerada no Capítulo 4 desta tese, avaliamos o modelo murinho de ligadura total de ducto biliar, como um possível modelo de hipertensão portal. Este trabalho foi realizado em parceria com o LIM29, Laboratório de Nefrologia Celular, Genética e Molecular, coordenado pela Profa. Dra. Irene Noronha e por seus alunos Rafael, Priscila e Cleonice, da Faculdade de Medicina da USP.

Metodologia

Ratos Wistar machos com 60 dias de vida (150-200g) de linhagens isogênicas foram utilizados neste trabalho. Os animais foram mantidos no biotério da Faculdade de Medicina da USP, com alimentação e água *ad libitum* e ciclo de luz de 12 horas, com aprovação do comitê de ética em pesquisa do Instituto de Biociências da Universidade de São Paulo (Protocolo número 229/2015). Um total de 16 animais (n = 16) foram utilizados. Os animais foram anestesiados com isoflurano para cirurgia de ligadura completa do ducto biliar comum (BDL) ou apenas abertura da cavidade peritoneal (*Sham*). Após o procedimento cirúrgico, os animais recuperados foram mantidos em isolamento. A sobrevida dos animais foi registrada. Amostra de sangue total foram coletadas no dia 0, 7 e 14 para análise bioquímica de ALT, AST, GGT, e billirrubina total, direrata e indireta, de acordo com as instruções do fabricante. Um total de 3 animais de cada grupo foram sacrificados no dia 7 e 14 para aferição da pressão portal e obteção de amostras para histologia e coloração de Tricrômio de Massons. A eutanásia foi realizada por exsanguinação após anestesia com xilazina (10 mg/kg)/cetamina (90 mg/kg).

Resultados e Discussão

Os resultados indicam que o modelo de ligadura de ducto biliar é capaz de, em apenas 7 dias, induzir um quadro de hipertensão portal, associado a um processo fibrótico colestático grave. A deposição de fibras colágenas peri-ductais, observado pela coloração do tricrômio de Massons, e o aumento das enzimas AST e gGT e bilirrubina direta comprovam a significativa lesão hepática. Este modelo parece ser um bom modelo a ser utilizado como uma opção para testar a eficiência do *by-pass* hepático desenvolvido no Capítulo 4, devido ao rápido resultado gerado e com mínimas intervenções necessárias.

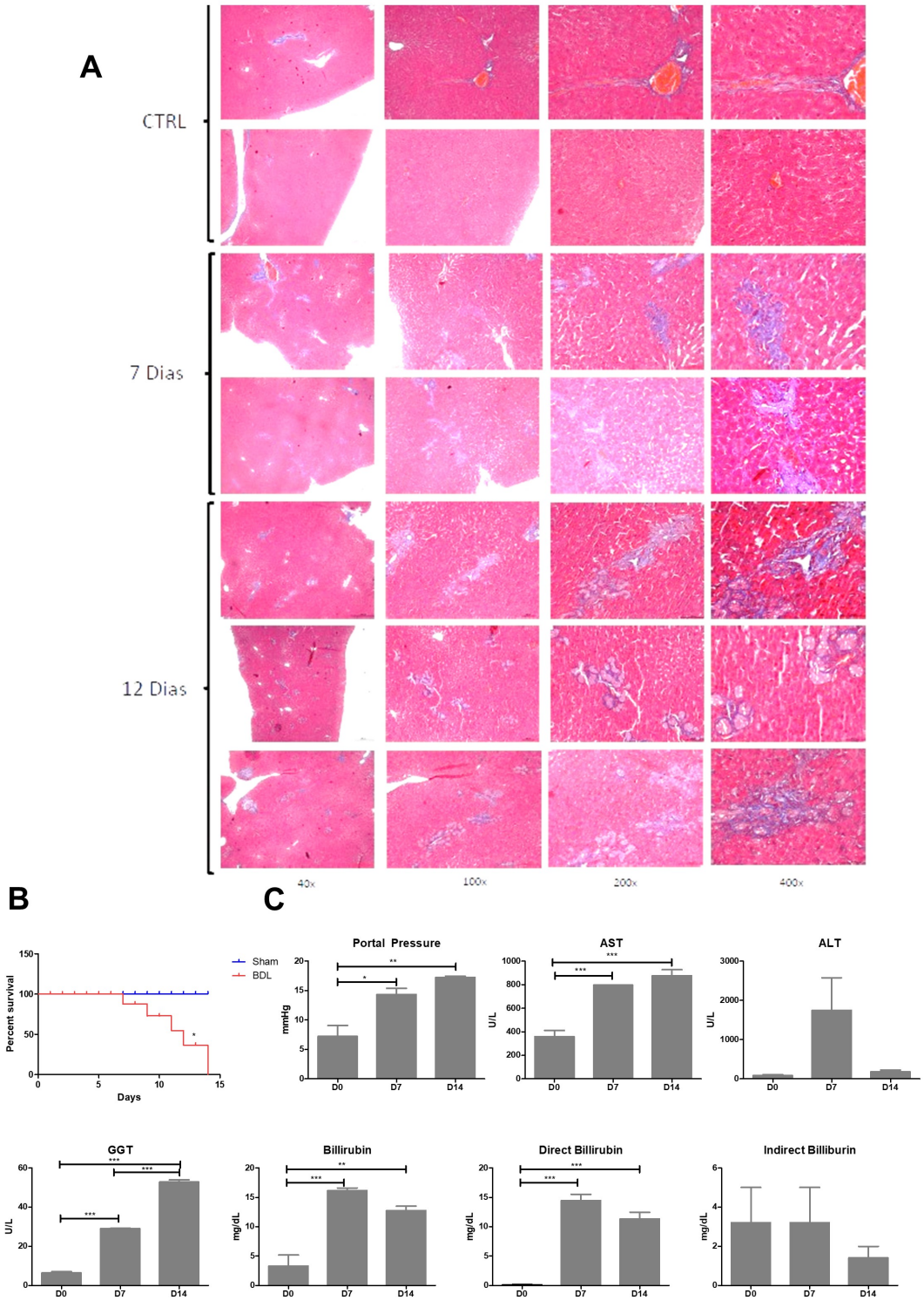

Figura 3: Caracterização do modelo de ligadura de ducto biliar comum em Ratos Wistar. (A) Imagens representativas da coloração de Tricrômio de Massons, em várias magnificações. (B) Curva de sobrevida, * = p<0.05, teste de Kaplan-Meier. (C) Análise da aferição da pressão portal e de parâmetros bioqúmicos de lesão hepática, pela quantificação sérica das enzimas ALT, AST, GGT e Billirubina total, direta e indireta. Barra = 50 µm, * = p<0.05, **= p<0.01, ***=p<0.001, ANOVA one-way com pós-teste de Tukey.

8.2. Produção científica

Encontram-se anexados a seguir os trabalhos científicos publicados em revistas indexadas, frutos de colaborações realizadas durante o período do desenvolvimento desta tese (2015-2019).

Artigo 1*: Revascularization of decellularized lung scaffolds: principles and progress.* (2015) American Journal of Physiology-Heart and Circulatory Physiology (Fator de Impacto 2017: 3,57/Qualis Ciências Biológica I - C). **Participação: Co-autor.**

Am J Physiol Lung Cell Mol Physiol 309: L1273–L1285, 2015.
First published September 25, 2015; doi:10.1152/ajplung.00237.2015.

CALL FOR PAPERS | *Bioengineering the Lung: Molecules, Materials, Matrix, Morphology, and Mechanics*

Revascularization of decellularized lung scaffolds: principles and progress

Collin T. Stabler,[1] Shimon Lecht,[1] Mark J. Mondrinos,[2] Ernesto Goulart,[3] Philip Lazarovici,[4] and Peter I. Lelkes[1]

[1]*Department of Bioengineering, College of Engineering, Temple University, Philadelphia, Pennsylvania;* [2]*Department of Bioengineering, School of Engineering and Applied Science, University of Pennsylvania, Philadelphia, Pennsylvania;* [3]*Human Genome and Stem Cell Research Center, Institute of Biosciences, University of São Paulo, São Paulo, Brazil; and* [4]*Institute for Drug Research, School of Pharmacy, Faculty of Medicine, The Hebrew University of Jerusalem, Jerusalem, Israel*

Submitted 14 July 2015; accepted in final form 23 September 2015

Stabler CT, Lecht S, Mondrinos MJ, Goulart E, Lazarovici P, Lelkes PI. Revascularization of decellularized lung scaffolds: principles and progress. *Am J Physiol Lung Cell Mol Physiol* 309: L1273–L1285, 2015. First published September 25, 2015; doi:10.1152/ajplung.00237.2015.—There is a clear unmet clinical need for novel biotechnology-based therapeutic approaches to lung repair and/or replacement, such as tissue engineering of whole bioengineered lungs. Recent studies have demonstrated the feasibility of decellularizing the whole organ by removal of all its cellular components, thus leaving behind the extracellular matrix as a complex three-dimensional (3D) biomimetic scaffold. Implantation of decellularized lung scaffolds (DLS), which were recellularized with patient-specific lung (progenitor) cells, is deemed the ultimate alternative to lung transplantation. Preclinical studies demonstrated that, upon implantation in rodent models, bioengineered lungs that were recellularized with airway and vascular cells were capable of gas exchange for up to 14 days. However, the long-term applicability of this concept is thwarted in part by the failure of current approaches to reconstruct a physiologically functional, quiescent endothelium lining the entire vascular tree of reseeded lung scaffolds, as inferred from the occurrence of hemorrhage into the airway compartment and thrombosis in the vasculature in vivo. In this review, we explore the idea that successful whole lung bioengineering will critically depend on *1*) preserving and/or reestablishing the integrity of the subendothelial basement membrane, especially of the ultrathin respiratory membrane separating airways and capillaries, during and following decellularization and *2*) restoring vascular physiological functionality including the barrier function and quiescence of the endothelial lining following reseeding of the vascular compartment. We posit that physiological reconstitution of the pulmonary vascular tree in its entirety will significantly promote the clinical translation of the next generation of bioengineered whole lungs.

lung tissue engineering; decellularization and recellularization; lung extracellular matrix; pulmonary vasculature; endothelium

ACCORDING TO THE American Center for Disease Control, chronic lower respiratory diseases (CLRDs) are currently the third leading cause of all deaths in the United States (37). The progressive nature of CLRD pathophysiology can only be partially controlled pharmacologically and inevitably leads to critical loss of gas-exchange capacity (i.e., end-stage organ failure), which is the prime indication for lung transplantation. Unfortunately, the number of patients added to the waiting list for lung transplants in the United States has consistently exceeded the number of transplants performed annually (116). The long-term survival rate of these transplant recipients at 5 years is 53% and at 10 years 31%, with current lung transplantation techniques focusing on bronchial artery revascularization (BAR) to improve long-term outcomes (112). Extracorporeal membrane oxygenation (ECMO)-based medical devices provide temporary relief in a clinical setting and often serve as a bridge to transplantation. However, the long-term use of these medical devices is offset by numerous shortcomings, such as thrombogenicity of the blood-contacting surfaces, limited gas-exchange surface area, and lack of endogenous metabolic and fibrinolytic activities (34). Given the chronic shortage of lungs suitable for transplantation (116) and the limitations of current ECMO devices (30), there is an unmet clinical need for innovative solutions to lung repair and/or replacement (114), such as tissue engineering a whole lung.

Recent studies suggest that decellularized cadaveric whole lungs, otherwise unsuitable for transplantation, or even individual lung lobes, might serve as a source for engineering replacement lungs and/or as organotypic scaffolding material (13, 28). "Whole organ engineering," which entails removal of cellular constituents (decellularization) and the subsequent recellularization, i.e., reseeding with the appropriate cocktail of tissue-specific cells, has the potential for increasing the number of available organs for clinical use, provided the functionality of the recellularized organ can be restored (6, 7, 19, 104, 131). During the decellularization process, a combination of reagents, usually detergents, is used to ablate the cells of a given organ, leaving behind an endogenous three-dimensional scaffold composed of insoluble extracellular matrix (ECM) proteins. Among the unresolved issues of the decellularization process is the incomplete removal of cellular components, which leaves behind residual fragments of cytosol, organelles, nuclei, and cell membranes, all of which can be immunogenic (8, 69). For a recent critical review of decellularization and some of the related issues see Ref. 47. The feasibility of the decellularization/recellularization (D/R) approach and its in vivo applicability was demonstrated in the initial in vivo studies that revealed a limited functionality of tissue-engineered left lung lobes in rodent models (29, 74, 80, 103).

Address for reprint requests and other correspondence: P. I. Lelkes, Temple Univ., Engineering Bldg. Rm. 811 1947 N. 12th St., Philadelphia, PA 19122 (e-mail: pilelkes@temple.edu).

Artigo 2: *EIF4A3 deficient human iPSCs and mouse models demonstrate neural crest defects that underlie Richieri-Costa-Pereira syndrome.* (2017) Human molecular genetics (Fator de Impacto 2017: 4,9/Qualis Ciências Biológicas I - A1). **Participação: <u>Co-autor</u>.**

OXFORD

Human Molecular Genetics, 2017, Vol. 0, No. 0 1–15

doi: 10.1093/hmg/ddx078
Advance Access Publication Date: 2 March 2017
Original Article

ORIGINAL ARTICLE

EIF4A3 deficient human iPSCs and mouse models demonstrate neural crest defects that underlie Richieri-Costa-Pereira syndrome

Emily E. Miller[1,†], Gerson S. Kobayashi[2,†], Camila M. Musso[2], Miranda Allen[1], Felipe A.A. Ishiy[2], Luiz Carlos de Caires Jr[2], Ernesto Goulart[2], Karina Griesi-Oliveira[2], Roseli M. Zechi-Ceide[3], Antonio Richieri-Costa[3], Debora R. Bertola[2], Maria Rita Passos-Bueno[2,*] and Debra L. Silver[1,4,5,6,*]

[1]Department of Molecular Genetics and Microbiology, Duke University Medical Center, Durham, NC, USA, [2]Department of Genetics and Evolutionary Biology, Human Genome and Stem Cell Research Center, Institute of Biosciences, University of Sao Paulo, Sao Paulo, Brazil, [3]Department of Clinical Genetics, Hospital for Rehabilitation of Craniofacial Anomalies (HRCA), University of São Paulo, Bauru, Brazil, [4]Department of Neurobiology, [5]Department of Cell Biology and [6]Duke Institute for Brain Sciences, Duke University Medical Center, Durham, NC, USA

*To whom correspondence should be addressed at: Rua do Matão, 277, Institute of Biosciences, University of Sao Paulo, Sao Paulo, SP, 05508090, Tel: +55 11 30919910; Fax: +551130917740; Email: passos@ib.usp.br; 224 CARL Building, 213 Research Drive, Durham, NC 27710, USA. Tel: +1 9196687909; Fax: +1 9196842790; Email: debra.silver@duke.edu

Abstract

Biallelic loss-of-function mutations in the RNA-binding protein EIF4A3 cause Richieri-Costa–Pereira syndrome (RCPS), an autosomal recessive condition mainly characterized by craniofacial and limb malformations. However, the pathogenic cellular mechanisms responsible for this syndrome are entirely unknown. Here, we used two complementary approaches, patient-derived induced pluripotent stem cells (iPSCs) and conditional *Eif4a3* mouse models, to demonstrate that defective neural crest cell (NCC) development explains RCPS craniofacial abnormalities. RCPS iNCCs have decreased migratory capacity, a distinct phenotype relative to other craniofacial disorders. *Eif4a3* haploinsufficient embryos presented altered mandibular process fusion and micrognathia, thus recapitulating the most penetrant phenotypes of the syndrome. These defects were evident in either ubiquitous or NCC-specific *Eif4a3* haploinsufficient animals, demonstrating an autonomous requirement of *Eif4a3* in NCCs. Notably, RCPS NCC-derived mesenchymal stem-like cells (nMSCs) showed premature bone differentiation, a phenotype paralleled by premature clavicle ossification in *Eif4a3* haploinsufficient embryos. Likewise, nMSCs presented compromised *in vitro* chondrogenesis, and Meckel's cartilage was underdeveloped *in vivo*. These findings indicate novel and essential requirements of EIF4A3 for NCC migration and osteochondrogenic differentiation during craniofacial development. Altogether, complementary use of iPSCs and mouse models pinpoint unique cellular mechanisms by which *EIF4A3* mutation causes RCPS, and provide a paradigm to study craniofacial disorders.

[†]Joint first authors.
Received: January 18, 2017. **Revised:** February 21, 2017. **Accepted:** February 28, 2017

Artigo 3: *Immunoglobulin therapy ameliorates the phenotype and increases lifespan in the severely affected dystrophin–utrophin double knockout mice*. (2017) European Journal of Human Genetics (Fator de Impacto 2017: 3,63/Qualis Ciências Biológicas I - A1). **Participação: <u>Co-autor</u>.**

European Journal of Human Genetics
https://doi.org/10.1038/s41431-017-0017-y

ARTICLE

Immunoglobulin therapy ameliorates the phenotype and increases lifespan in the severely affected dystrophin–utrophin double knockout mice

Bruno Ghirotto Nunes[1] · Flávio Vieira Loures[2] · Heloisa Maria Siqueira Bueno[1] · Erica Baroni Cangussu[1] · Ernesto Goulart[1] · Giuliana Castello Coatti[1] · Elia Garcia Caldini[3] · Antonio Condino-Neto[2] · Mayana Zatz[1]

Received: 4 May 2017 / Revised: 13 September 2017 / Accepted: 14 September 2017

Abstract
Duchenne muscular dystrophy (DMD) is an X-linked recessive disorder, caused by mutations in the dystrophin gene, affecting 1:3500–5000 boys worldwide. The lack of dystrophin induces degeneration of muscle cells and elicits an immune response characterized by an intensive secretion of pro-inflammatory cytokines. Immunoglobulins modulate the inflammatory response through several mechanisms and have been widely used as an adjuvant therapy for autoimmune diseases. Here we evaluated the effect of immunoglobulin G (IG) injected intraperitoneally in a severely affected double *knockout* (dko) mouse model for Duchenne muscular dystrophy. The IG dko treated mice were compared regarding activity rates, survival and histopathology with a control untreated group. Additionally, dendritic cells and naïve lymphocytes from these two groups and WT mice were obtained to study *in vitro* the role of the immune system associated to DMD pathophysiology. We show that IG therapy significantly enhances activity rate and lifespan of dko mice. It diminishes muscle tissue inflammation by decreasing the expression of costimulatory molecules MHC, CD86 and CD40 and reducing Th1-related cytokines IFN-γ, IL-1β and TNF-α release. IG therapy dampens the effector immune responses supporting the hypothesis according to which the immune response accelerates DMD progression. As IG therapy is already approved by FDA for treating autoimmune disorders, with less side-effects than currently used glucocorticoids, our results may open a new therapeutic option aiming to improve life quality and lifespan of DMD patients.

Artigo 4: *Down syndrome iPSC-derived astrocytes impair neuronal synaptogenesis and the mTOR pathway in vitro.* (2017) Molecular neurobiology (Fator de Impacto 2017: 5,07/Qualis Ciências Biológicas I - A1). **Participação: Co-autor.**

Mol Neurobiol
https://doi.org/10.1007/s12035-017-0818-6

Down Syndrome iPSC-Derived Astrocytes Impair Neuronal Synaptogenesis and the mTOR Pathway In Vitro

Bruno H. S. Araujo[1,2] · Carolini Kaid[3] · Janaina S. De Souza[4] · Sérgio Gomes da Silva[5,6] · Ernesto Goulart[3] · Luiz C. J. Caires[3] · Camila M. Musso[3] · Laila B. Torres[7] · Adriano Ferrasa[8,9] · Roberto Herai[9] · Mayana Zatz[3] · Oswaldo K. Okamoto[3] · Esper A. Cavalheiro[1]

Received: 17 June 2017 / Accepted: 2 November 2017

Abstract Several methods have been used to study the neuropathogenesis of Down syndrome (DS), such as mouse aneuploidies, post mortem human brains, and in vitro cell culture of neural progenitor cells. More recently, induced pluripotent stem cell (iPSC) technology has offered new approaches in investigation, providing a valuable tool for studying specific cell types affected by DS, especially neurons and astrocytes. Here, we investigated the role of astrocytes in DS developmental disease and the impact of the astrocyte secretome in neuron mTOR signaling and synapse formation using iPSC derived from DS and wild-type (WT) subjects. We demonstrated for the first time that DS neurons derived from hiPSC recapitulate the hyperactivation of the Akt/mTOR axis observed in DS brains and that DS astrocytes may play a key role in this dysfunction. Our results bear out that 21 trisomy in astrocytes contributes to neuronal abnormalities in addition to cell autonomous dysfunctions caused by 21 trisomy in neurons. Further research in this direction will likely yield additional insights, thereby improving our understanding of DS and potentially facilitating the development of new therapeutic approaches.

Keywords Down syndrome · Induced pluripotent stem cell · mTOR pathway · Astrocyte

Introduction

Down syndrome (DS) is the most common cause of genetic intellectual disability (ID), and its worldwide

Artigo 5: *Discordant congenital Zika syndrome twins show differential in vitro viral susceptibility of neural progenitor cells.* (2018) Nature communications (Fator de Impacto 2017: 12,35 /Qualis Ciências Biológicas I - C). **Participação: <u>Co-primeiro autor</u>.**

nature COMMUNICATIONS

ARTICLE

Corrected: Publisher correction

DOI: 10.1038/s41467-017-02790-9 OPEN

Discordant congenital Zika syndrome twins show differential in vitro viral susceptibility of neural progenitor cells

Luiz Carlos Caires-Júnior *et al.*#

Congenital Zika syndrome (CZS) causes early brain development impairment by affecting neural progenitor cells (NPCs). Here, we analyze NPCs from three pairs of dizygotic twins discordant for CZS. We compare by RNA-Seq the NPCs derived from CZS-affected and CZS-unaffected twins. Prior to Zika virus (ZIKV) infection the NPCs from CZS babies show a significantly different gene expression signature of mTOR and Wnt pathway regulators, key to a neurodevelopmental program. Following ZIKV in vitro infection, cells from affected individuals have significantly higher ZIKV replication and reduced cell growth. Whole-exome analysis in 18 affected CZS babies as compared to 5 unaffected twins and 609 controls excludes a monogenic model to explain resistance or increased susceptibility to CZS development. Overall, our results indicate that CZS is not a stochastic event and depends on NPC intrinsic susceptibility, possibly related to oligogenic and/or epigenetic mechanisms.

Author contributions

L.C.C.-J., E.G., U.S.M., B.H.S.A., L.A., A.S.S., K.G.-O., R.M.A., J.K., E.C.-N., H.N., L.C.dS. F., P.L.H., M.R.P.-B., and M.Z. conceptualized the study; L.C.C.-J., E.G., U.S.M., and B.H. S.A. wrote the original draft; U.S.M., L.A., V.V.dL., H.V.dL., J.R.M.dO., N.M.R.A., A.M., S.S., J.G.C.M., S.D.P, R.P.dA., A.J.B.B., T.F., M.R.P.-B., and M.Z. collected samples and resources for the study; L.C.C.-J., E.G., U.S.M., B.H.S.A., L.A., A.S.S., K.G.-O., G.S.K., D. F.dO., C.M.M., R.M.A., S.F.S.-P., G.L.Y., S.E., M.S.N., L.F.dS., M.S.A., S.V.-A., R.A.S., and H.N. performed experiments and data analysis; L.C.C.-J., E.G., U.S.M., B.H.S.A., S.V.-A., M.R.P.-B., and M.Z. were responsible for writing, reviewing, and editing of the manuscript; M.R.P.-B. and M.Z. coordinated the study.

Additional information

Supplementary Information accompanies this paper at https://doi.org/10.1038/s41467-017-02790-9.

Competing interests: The authors declare no competing financial interests.

Reprints and permission information is available online at http://npg.nature.com/reprintsandpermissions/

Publisher's note: Springer Nature remains neutral with regard to jurisdictional claims in published maps and institutional affiliations.

Luiz Carlos Caires-Júnior[1], Ernesto Goulart[1], Uirá Souto Melo[1], Bruno Henrique Silva Araujo[2,3], Lucas Alvizi[1], Alessandra Soares-Schanoski[4], Danyllo Felipe de Oliveira[1], Gerson Shigeru Kobayashi[1], Karina Griesi-Oliveira[1,5], Camila Manso Musso[1], Murilo Sena Amaral[4], Lucas Ferreira daSilva[6], Renato Mancini Astray[4], Sandra Fernanda Suárez-Patiño[4], Daniella Cristina Ventini[4], Sérgio Gomes da Silva[5,7], Guilherme Lopes Yamamoto[1], Suzana Ezquina[1], Michel Satya Naslavsky[1], Kayque Alves Telles-Silva[1], Karina Weinmann[1], Vanessa van der Linden[8], Helio van der Linden[9], João Ricardo Mendes de Oliveira[10], Nivia Maria Rodrigues Arrais[11], Adriana Melo[12], Thalita Figueiredo[1], Silvana Santos[13], Joanna Goes Castro Meira[14], Saulo Duarte Passos[15], Roque Pacheco de Almeida[16], Ana Jovina Barreto Bispo[16], Esper Abrão Cavalheiro[3], Jorge Kalil[4], Edécio Cunha-Neto[17], Helder Nakaya[18], Robert Andreata-Santos[19], Luis Carlos de Souza Ferreira[19], Sergio Verjovski-Almeida[4,6], Paulo Lee Ho[4], Maria Rita Passos-Bueno[1] & Mayana Zatz[1]

[1]Department of Genetics and Evolutionary Biology, Human Genome and Stem Cell Research Center, Biosciences Institute, University of São Paulo (USP), São Paulo - SP 05508-900, Brazil. [2]Brazilian Biosciences National Laboratory (LNBio) Brazilian Center for Research in Energy and Materials (CNPEM) Campinas - SP 13083-970 Brazil. [3]Neuroscience laboratory, Department of Neurology and Neurosurgery, Federal University of São Paulo —UNIFESP/EPM, São Paulo - SP 04039-002, Brazil. [4]Butantan Institute, São Paulo - SP 05503-900, Brazil. [5]Albert Einstein Hospital, São Paulo - SP 05652-900, Brazil. [6]Department of Biochemistry, Institute of Chemistry, University of São Paulo (USP), São Paulo - SP 05508-900, Brazil. [7]Universidade de Mogi das Cruzes, Mogi das Cruzes - SP 08780-911, Brazil. [8]AACD, Recife - PE 50080-810, Brazil. [9]Rehabilitation Center—Dr. Henrique Santillo, Goiânia - GO 74653-230, Brazil. [10]Neuropsychiatry Department and KeizoAsami Laboratory, Federal University of Pernambuco (UFPE), Recife - PE 50670-901, Brazil. [11]Department of Pediatrics, Federal University of Rio Grande do Norte (UFRN), Natal- RN 59010-180, Brazil. [12]ISEA, Campina Grande- PB 58400-220, Brazil. [13]Department of Biology, Paraíba State University (UEPB), Campina Grande - PB 58429-500, Brazil. [14]Federal University of Bahia (UFBA), Salvador - BA 40170-115, Brazil. [15]Infectious pediatric laboratory, Medicine School of Jundiaí, Jundiaí - SP 13202-550, Brazil. [16]Division of Immunology and Molecular Biology Laboratory, Federal University of Sergipe (UFS), Aracaju - SP 49100-000, Brazil. [17]Heart Institute, Faculty of Medicine, University of São Paulo (USP), São Paulo - SP 05403-900, Brazil. [18]Department of Clinical and Toxicological Analyses, School of Pharmaceutical Sciences, University of São Paulo (USP), São Paulo - SP 05508-900, Brazil. [19]Vaccine Development Laboratory, Department of Microbiology, Institute of Biomedical Science, University of São Paulo (USP), São Paulo - SP 05508-900, Brazil. Luiz Carlos de Caires Junior, Ernesto Goulart, Uirá Souto Melo, and Bruno Henrique Silva Araujo contributed equally to this work. Maria Rita Passos-Bueno and Mayana Zatz jointly supervised this work.

Artigo 6: *Zika virus selectively kills aggressive human embryonal CNS tumor cells in vitro and in vivo.* (2018) Cancer Research (Fator de Impacto 2017: 9,13/Qualis Ciências Biológicas I - A1). **Participação: Co-primeiro autor.**

Published OnlineFirst April 26, 2018; DOI: 10.1158/0008-5472.CAN-17-3201

Translational Science

Cancer Research

Zika Virus Selectively Kills Aggressive Human Embryonal CNS Tumor Cells *In Vitro* and *In Vivo*

Carolini Kaid[1], Ernesto Goulart[1], Luiz C. Caires-Júnior[1], Bruno H.S. Araujo[2], Alessandra Soares-Schanoski[3], Heloisa M.S. Bueno[1], Kayque A. Telles-Silva[1], Renato M. Astray[3], Amanda F. Assoni[1], Antônio F.R. Júnior[1], Daniella C. Ventini[3], Ana L.P. Puglia[3], Roselane P. Gomes[3], Mayana Zatz[1], and Oswaldo K. Okamoto[1]

Abstract

Zika virus (ZIKV) is largely known for causing brain abnormalities due to its ability to infect neural progenitor stem cells during early development. Here, we show that ZIKV is also capable of infecting and destroying stem-like cancer cells from aggressive human embryonal tumors of the central nervous system (CNS). When evaluating the oncolytic properties of Brazilian Zika virus strain ($ZIKV^{BR}$) against human breast, prostate, colorectal, and embryonal CNS tumor cell lines, we verified a selective infection of CNS tumor cells followed by massive tumor cell death. $ZIKV^{BR}$ was more efficient in destroying embryonal CNS tumorspheres than normal stem cell neurospheres. A single intracerebroventricular injection of $ZIKV^{BR}$ in BALB/c nude mice bearing orthotopic human embryonal CNS tumor xenografts resulted in a significantly longer survival, decreased tumor burden, fewer metastasis, and complete remission in some animals. Tumor cells closely resembling neural stem cells at the molecular level with activated Wnt signaling were more susceptible to the oncolytic effects of $ZIKV^{BR}$. Furthermore, modulation of Wnt signaling pathway significantly affected $ZIKV^{BR}$-induced tumor cell death and viral shedding. Altogether, these preclinical findings indicate that $ZIKV^{BR}$ could be an efficient agent to treat aggressive forms of embryonal CNS tumors and could provide mechanistic insights regarding its oncolytic effects.

Significance: Brazilian Zika virus strain kills aggressive metastatic forms of human CNS tumors and could be a potential oncolytic agent for cancer therapy. *Cancer Res; 78(12); 3363–74.*

Introduction

The recent outbreak of Zika virus (ZIKV), especially throughout South and Central Americas, revealed an unprecedented impact of gestational infection on neurodevelopment, resulting in severe central nervous system (CNS) development effects in neonates, such as microcephaly and other associated abnormalities (1). Recent studies showed that ZIKV prominently infects neural stem and progenitor cells (NPC) and disrupts key cellular processes, e.g., survival, proliferation, and differentiation (2, 3), leading to massive cell death and growth reduction.

Notably, aggressive CNS embryonal tumors with high incidence in infants are originated from NPC aberrations, affecting key cell signaling pathways that regulate neurogenesis, such as the mTOR/Wnt pathway (4). These tumors are comprised by cells with neural stem–like features, also known as cancer stem cells (CSC), which are highly tumorigenic and resistant to classical cancer therapies (5). CNS tumors enriched in stem-like cancer cells are very difficult to treat and usually associated with poor prognosis (6). Available therapies have a low efficiency and severe adverse effects that include endocrine, motor, and cognitive deficits.

Oncolytic viral therapy has emerged as an alternative approach to treat aggressive, fast-growing forms of cancer. Oncolytic viruses are defined as native or genetically modified viruses that are able to directly infect and lyse tumor cells (7). Because ZIKV infects preferentially NPC, we hypothesized that $ZIKV^{BR}$ could act as an oncolytic agent in particular against aggressive and metastatic human CNS embryonal tumors.

Materials and Methods

Human and animal samples

The study followed the International Ethical Guideline for Biomedical Research (CIOMS/OMS, 1985) and was approved by the Institutional Animal Experimentation Ethics Committee (CEUA-USP 290/2017; CEUA-Instituto Butantan 3473210817). A total of 66 animals were included in the present study. Animals with 30% weight loss and/or visible tumor and/or ataxia and/or

[1]Human Genome and Stem Cell Research Center, Department of Genetics and Evolutionary Biology, Biosciences Institute, University of São Paulo (USP), São Paulo, Brazil. [2]Brazilian Biosciences National Laboratory (LNBio), Brazilian Center for Research in Energy and Materials (CNPEM), Campinas, São Paulo, Brazil. [3]Butantan Institute, São Paulo, Brazil.

Note: Supplementary data for this article are available at Cancer Research Online (http://cancerres.aacrjournals.org/).

C. Kaid, E. Goulart, and L.C. Caires-Júnior contributed equally to this article.

M. Zatz and O.K. Okamoto are senior authors of this article.

O.K. Okamoto is the lead contact of this article.

Corresponding Authors: Oswaldo K. Okamoto, University of São Paulo, São Paulo, SP 05508-900, Brazil. Phone: 55-11-30488357; E-mail: keith.okamoto@usp.br; and Mayana Zatz, Phone: 55-11-30910850; E-mail: mayazatz@usp.br

doi: 10.1158/0008-5472.CAN-17-3201

Artigo 7: *10q23. 31 microduplication encompassing PTEN decreases mTOR signalling activity and is associated with autosomal dominant primary microcephaly.* (2018) Journal of medical genetics (Fator de Impacto: 5,75/Qualis Ciências Biológica I - A1).

Participação: Co-autor.

SHORT REPORT

10q23.31 microduplication encompassing *PTEN* decreases mTOR signalling activity and is associated with autosomal dominant primary microcephaly

Danyllo Oliveira,[1] Gabriela Ferraz Leal,[2,3] Andréa L Sertié,[4] Luiz Carlos Caires Jr,[1] Ernesto Goulart,[1] Camila Manso Musso,[1] João Ricardo Mendes de Oliveira,[5] Ana Cristina Victorino Krepischi,[1] Angela Maria Vianna-Morgante,[1] Mayana Zatz[1]

[1]Department of Genetics and Evolutionary Biology, Human Genome and Stem-Cell Research Center, Institute of Biosciences, University of São Paulo, São Paulo, Brazil
[2]Fernando Figueira Integral Medicine Institute, Recife, Brazil
[3]Amaury de Medeiros Health Center, University of Pernambuco, Recife, Brazil
[4]Hospital Albert Einstein, São Paulo, Brazil
[5]Neuropsychiatry Department, Federal University of Pernambuco, Recife, Brazil

Correspondence to
Professor Mayana Zatz, Department of Genetics and Evolutionary Biology, Human Genome and Stem-Cell Research Center, University of Sao Paulo, SP03178-200, Brazil; mayazatz@usp.br

Received 4 May 2018
Revised 7 August 2018
Accepted 29 August 2018

ABSTRACT

Background Hereditary primary microcephaly (MCPH) is mainly characterised by decreased occipitofrontal circumference and variable degree of intellectual disability. MCPH with a dominant pattern of inheritance is a rare condition, so far causally linked to pathogenic variants in the *ALFY*, *DPP6*, *KIF11* and *DYRK1A* genes.

Objective This study aimed at identifying the causative variant of the autosomal dominant form of MCPH in a Brazilian family with three affected members.

Methods Following clinical evaluation of two sibs and their mother presenting with autosomal dominant MCPH, array comparative genome hybridisation was performed using genomic DNA from peripheral blood of the family members. Gene and protein expression studies were carried out in cultured skin fibroblasts.

Results A 382 kb microduplication at 10q23.31 was detected, encompassing the entire *PTEN*, *KLLN* and *ATAD1* genes. *PTEN* haploinsufficiency has been causally associated with macrocephaly and autism spectrum disorder and, therefore, was considered the most likely candidate gene to be involved in this autosomal dominant form of MCPH. In the patients' fibroblasts, *PTEN* mRNA and protein were found to be overexpressed, and the phosphorylation patterns of upstream and downstream components of the mammalian target of rapamycin (mTOR) signalling pathway were dysregulated.

Conclusions Taken together, our results demonstrate that the identified submicroscopic 10q23.31 duplication in a family with MCPH leads to markedly increased expression of *PTEN* and reduced activity of the mTOR signalling pathway. These results suggest that the most probable pathomechanism underlying the microcephaly phenotype in this family involves downregulation of the mTOR pathway through overexpression of *PTEN*.

To cite: Oliveira D, Leal GF, Sertié AL, *et al*. *J Med Genet* Epub ahead of print: [please include Day Month Year]. doi:10.1136/jmedgenet-2018-105471

INTRODUCTION

Hereditary primary microcephaly (MCPH), characterised by occipitofrontal circumference (OFC) two or three SD below the population mean,[1 2] is a genetically heterogeneous disorder whose overall incidence varies across different populations, from 1.3 to 150 per 100 000 newborns. The population prevalence of this condition is directly related to the rates of endogamy, since most cases of MCPH have an autosomal recessive mode of inheritance.[1 3] Nevertheless, families have been reported, in which MCPH has either autosomal dominant or X linked inheritance.[1 4]

Patients with MCPH often display varying degrees of intellectual disability (ID), which is correlated to the level of brain hypoplasia. Despite being structurally smaller, the patients' brains usually exhibit normal cytoarchitecture,[2] suggesting that the genes implicated in MCPH have an important role in determining human brain size. For instance, the *ASPM* gene, associated with autosomal recessive MCPH, has been reported as undergoing positive selection for cortical size expansion during recent primate evolution.[5]

The main processes through which MCPH-linked genes regulate brain growth involve those associated with neural progenitor cells (NPCs) divisions. During neocortical development, these cells, particularly concentrated at ventricular zone (VZ) and subventricular zone (SVZ) of the developing telencephalon, undergo both symmetric and asymmetric divisions, which maintain the stem cell pool and generate newborn neurons that, through radial migration, originate the cortical plate.[6] Accurate positioning of centrosomes and spindles is essential for proper NPCs division and cortical development, since vertical cleavage planes perpendicular to the VZ and SVZ usually result in symmetric divisions, while horizontal cleavages lead to asymmetric divisions.[6] Most of the known pathogenic variants responsible for autosomal recessive MCPH are in genes encoding centrosomal proteins or proteins required for spindle formation and function, such as *ASPM*, *CEP152*, *CEP235*, *CENPJ* and *CDK5RAP2*. In addition, disruption of chromatin dynamics and condensation, caused by pathogenic variants in the *PCH1* and *MCPH1* genes, has also been implicated in the pathogenesis of autosomal recessive MCPH.[7]

Patients with autosomal dominant MCPH[4] usually show moderate-to-mild ID or no cognitive impairment. The term 'silent microcephaly' has been proposed to refer to this entity without any neurological or dysmorphic manifestations.[4] Recently, linkage studies and exome sequencing identified a pathogenic variant in the *ALFY* gene, which encodes an autophagy scaffold protein, segregating along with microcephaly through three generations of a family.[8] Functional studies using animal models showed that the mutated protein